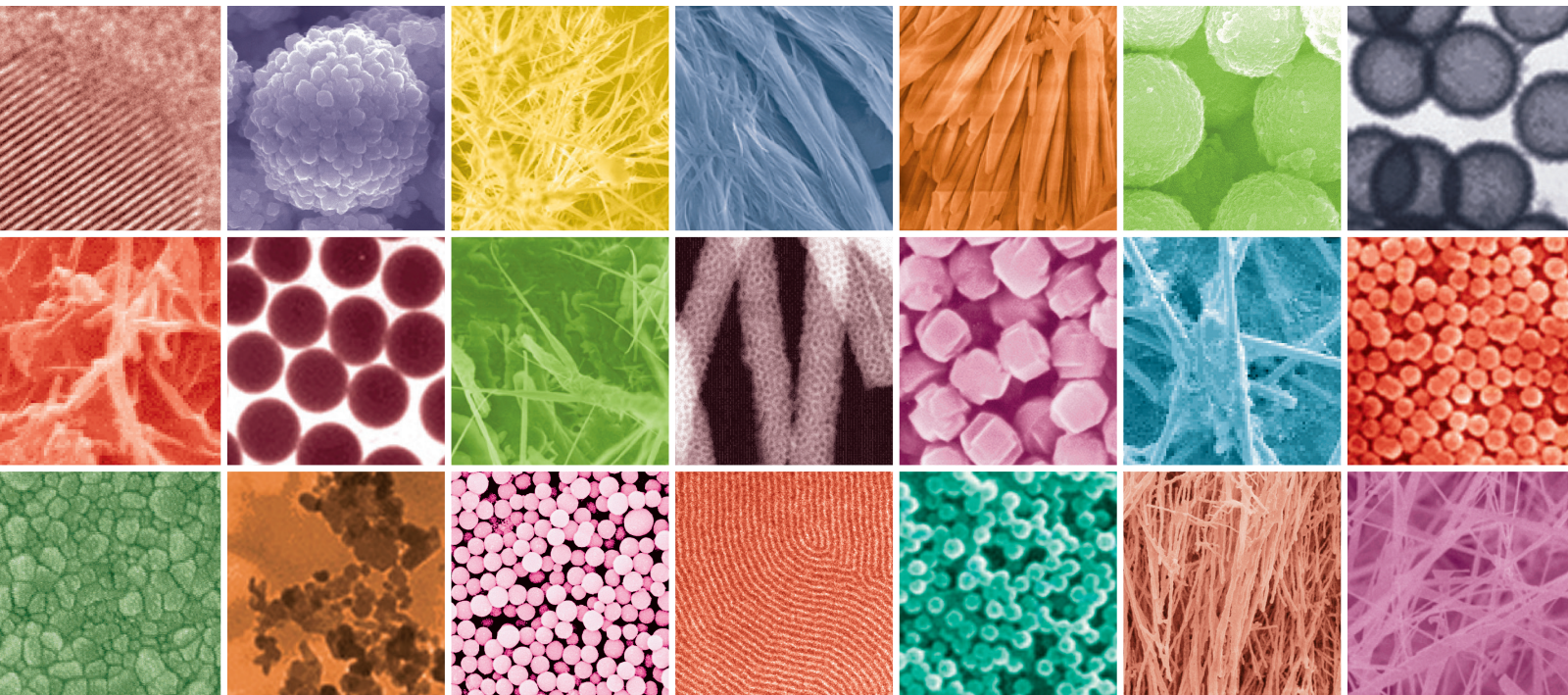


# Electrospun Polymer Nanomaterials: Preparation, Characterization, and Application

Journal of  
Nanomaterials

Guest Editors: Aihua He, Ruigang Liu, Huarong Nie, and Yaqin Huang





---

**Electrospun Polymer Nanomaterials:  
Preparation, Characterization,  
and Application**

**Electrospun Polymer Nanomaterials:  
Preparation, Characterization,  
and Application**

Guest Editors: Aihua He, Ruigang Liu, Huarong Nie,  
and Yaqin Huang



---

Copyright © 2014 Hindawi Publishing Corporation. All rights reserved.

This is a special issue published in "Journal of Nanomaterials." All articles are open access articles distributed under the Creative Commons Attribution License, which permits unrestricted use, distribution, and reproduction in any medium, provided the original work is properly cited.

## Editorial Board

- Katerina E. Aifantis, USA  
Nageh K. Allam, USA  
Margarida Amaral, Portugal  
Jordi Arbiol, Spain  
Xuedong Bai, China  
Lavinia Balan, France  
Stefano Bellucci, Italy  
Enrico Bergamaschi, Italy  
Theodorian Borca-Tasciuc, USA  
M. Bououdina, Bahrain  
C. Jeffrey Brinker, USA  
Christian Brosseau, France  
Yibing Cai, China  
Chuanbao Cao, China  
Xuebo Cao, China  
Victor M. Castao, Mexico  
Albano Cavaleiro, Portugal  
Bhanu P. S. Chauhan, USA  
Yuan Chen, Singapore  
Wei Chen, China  
Tupei Chen, Singapore  
Shafiq Chowdhury, USA  
Kwang-Leong Choy, UK  
Jin-Ho Choy, Korea  
Yu-Lun Chueh, Taiwan  
Cui Chunxiang, China  
M. A. Correa-Duarte, Spain  
Majid Darroudi, Iran  
Shadi A. Dayeh, USA  
Yong Ding, USA  
Bin Dong, China  
Zehra Durmus, Turkey  
Joydeep Dutta, Oman  
Ali Eftekhari, USA  
Farid El-Tantawy, Egypt  
Claude Estourns, France  
Andrea Falqui, Saudi Arabia  
Xiaosheng Fang, China  
Bo Feng, China  
Alan Fuchs, USA  
Lian Gao, China  
Peng Gao, China  
P. K. Giri, India  
R. E. Gorga, USA  
Jean M. Greneche, France
- Changzhi Gu, China  
Hongchen Chen Gu, China  
Mustafa O. Guler, Turkey  
John Z. Guo, USA  
Lin Guo, China  
Zaiping Guo, Australia  
Smrati Gupta, Germany  
Michael Harris, USA  
Jr-Hau He, Taiwan  
Nguyen D. Hoa, Vietnam  
Zhongkui Hong, China  
Michael Z. Hu, USA  
Nay Ming Huang, Malaysia  
Shaoming Huang, China  
Qing Huang, China  
David Hui, USA  
Young-K. Jeong, Republic of Korea  
Sheng-Rui Jian, Taiwan  
Xin Jiang, Germany  
Wanqin Jin, China  
Rakesh K. Joshi, UK  
Myung-Hwa Jung, Korea  
Zhenhui Kang, China  
Jeong-won Kang, Korea  
H. Karimi-Maleh, Iran  
F. Karimzadeh, Iran  
Antonios Kelarakis, UK  
Alireza Khataee, Iran  
Ali Khorsand Zak, Iran  
Dojin Kim, Korea  
Jang-Kyo Kim, Hong Kong  
Wonbaek Kim, Korea  
Do Kyung Kim, Korea  
Sanjeev Kumar, India  
Sushil Kumar, India  
Subrata Kundu, India  
Alan K. T. Lau, Hong Kong  
Burtrand Lee, USA  
Jun Li, Singapore  
Benxia Li, China  
Xing-Jie Liang, China  
Meiyong Liao, Japan  
Shijun Liao, China  
Gong-Ru Lin, Taiwan  
Wei Lin, USA
- Tianxi Liu, China  
Jun Liu, USA  
Zainovia Lockman, Malaysia  
Songwei Lu, USA  
Daniel Lu, China  
Jue Lu, USA  
Ed Ma, USA  
Malik Maaza, South Africa  
Gaurav Mago, USA  
Morteza Mahmoudi, Iran  
Santanu K. Maiti, India  
D. Mangalaraj, India  
Sanjay R. Mathur, Germany  
V. Mittal, United Arab Emirates  
Paulo Cesar Morais, Brazil  
Mahendra A. More, India  
Jae-Min Myoung, Korea  
Rajesh Naik, USA  
Weihai Ni, China  
Koichi Niihara, Japan  
Sherine Obare, USA  
Won-Chun Oh, Republic of Korea  
Atsuto Okamoto, Japan  
Abdelwahab Omri, Canada  
U. Paik, Republic of Korea  
Edward A. Payzant, USA  
Kui-Qing Peng, China  
O. Perales-Perez, Puerto Rico  
A. Phuruangrat, Thailand  
Wenxiu Que, China  
Mahendra Rai, India  
S. Sinha Ray, South Africa  
Ugur Serincan, Turkey  
Huaiyu Shao, Japan  
Donglu Shi, USA  
Bhanu P. Singh, India  
Vladimir Sivakov, Germany  
Yanlin Song, China  
Marinella Striccoli, Italy  
Jing Sun, China  
Bohua Sun, South Africa  
Xuping Sun, Saudi Arabia  
Nyan-Hwa Tai, Taiwan  
Saikat Talapatra, USA  
Bo Tan, Canada



---

Nairong Tao, China  
Titipun Thongtem, Thailand  
Somchai Thongtem, Thailand  
Ion Tiginyanu, Moldova  
Alexander Tolmachev, Ukraine  
Valeri P. Tolstoy, Russia  
Ramon Torrecillas, Spain  
Tsung-Yen Tsai, Taiwan  
Takuya Tsuzuki, Australia  
Tamer Uyar, Turkey  
Raquel Verdejo, Spain  
Mat U. Wahit, Malaysia  
Zhenbo Wang, China  
Ruibing Wang, Canada

Shiren Wang, USA  
Cheng Wang, China  
Yong Wang, USA  
Jinquan Wei, China  
Ching-Ping Wong, Hong Kong  
Xingcai Wu, China  
Guodong Xia, Hong Kong  
Ping Xiao, UK  
Zhi Li Xiao, USA  
Shuangxi Xing, China  
Yangchuan Xing, USA  
Nanping Xu, China  
Doron Yadlovker, Israel  
Yingkui Yang, China

Piaoping Yang, China  
Yoke K. Yap, USA  
Ramin Yousefi, Iran  
Khaled Youssef, USA  
Kui Yu, Canada  
William W. Yu, USA  
Haibo Zeng, China  
Tianyou Zhai, China  
Bin Zhang, China  
Renyun Zhang, Sweden  
Yanbao Zhao, China  
Lianxi Zheng, Singapore  
Chunyi Zhi, Hong Kong

# Contents

**Electrospun Polymer Nanomaterials: Preparation, Characterization, and Application,**

Aihua He, Ruigang Liu, Huarong Nie, and Yaqin Huang

Volume 2014, Article ID 540831, 2 pages

**The Effect of Surfactants on the Diameter and Morphology of Electrospun Ultrafine Nanofiber,**

Jian-Yi Zheng, Ming-Feng Zhuang, Zhao-Jie Yu, Gao-Feng Zheng, Yang Zhao, Han Wang,

and Dao-Heng Sun

Volume 2014, Article ID 689298, 9 pages

**Fabrication of Ultrafine Carbon Fibers Possessing a Nanoporous Structure from Electrospun Polyvinyl Alcohol Fibers Containing Silica Nanoparticles,** Koichi Sawada, Shinji Sakai, and Masahito Taya

Volume 2014, Article ID 487943, 6 pages

**CLSVOF Method to Study the Formation Process of Taylor Cone in Crater-Like Electrospinning of Nanofibers,** Yong Liu, Jia Li, Yu Tian, Xia Yu, Jian Liu, and Bao-Ming Zhou

Volume 2014, Article ID 635609, 12 pages

**Electrohydrodynamic Direct-Write Orderly Micro/Nanofibrous Structure on Flexible Insulating Substrate,**

Jiang-Yi Zheng, Hai-Yan Liu, Xiang Wang, Yang Zhao, Wei-Wei Huang, Gao-Feng Zheng,

and Dao-Heng Sun

Volume 2014, Article ID 708186, 7 pages

**Alternating Current Electrohydrodynamic Printing of Microdroplets,** Gao-Feng Zheng, Hai-Yan Liu,

Rong Xu, Xiang Wang, Juan Liu, Han Wang,

and Dao-Heng Sun

Volume 2014, Article ID 596263, 7 pages

**Fabrication of Aligned Carbon Nanotube/Polycaprolactone/Gelatin Nanofibrous Matrices for Schwann Cell Immobilization,** Shiao-Wen Tsai, Chun-Chiang Huang, Lih-Rou Rau, and Fu-Yin Hsu

Volume 2014, Article ID 498131, 8 pages

**Tunable Structures and Properties of Electrospun Regenerated Silk Fibroin Mats Annealed in Water Vapor at Different Times and Temperatures,** Xiangyu Huang, Suna Fan,

Alhadi Ibrahim Mohammed Altayp, Yaopeng Zhang, Huili Shao, Xuechao Hu, Minkai Xie,

and Yuemin Xu

Volume 2014, Article ID 682563, 7 pages

**Effects of Electrode Reversal on the Distribution of Naproxen in the Electrospun Cellulose Acetate Nanofibers,** Zhuang Li, Hongliang Kang, Ning Che, Zhijing Liu, Pingping Li, Weiwei Li, Chao Zhang,

Chun Cao, Ruigang Liu, and Yong Huang

Volume 2014, Article ID 360658, 8 pages

**Assessment of Morphology, Activity, and Infiltration of Astrocytes on Marine EPS-Imbedded Electrospun PCL Nanofiber,** Seul Ki Min, Cho Rong Kim, Sung Hoon Kim, and Hwa Sung Shin

Volume 2014, Article ID 302725, 8 pages

**Coaxial Electrospinning with Mixed Solvents: From Flat to Round Eudragit L100 Nanofibers for Better Colon-Targeted Sustained Drug Release Profiles,** Deng-Guang Yu, Ying Xu, Zan Li, Lin-Ping Du,

Ben-Guo Zhao, and Xia Wang

Volume 2014, Article ID 967295, 8 pages

## Editorial

# Electrospun Polymer Nanomaterials: Preparation, Characterization, and Application

Aihua He,<sup>1</sup> Ruigang Liu,<sup>2</sup> Huarong Nie,<sup>3</sup> and Yaqin Huang<sup>4</sup>

<sup>1</sup> Key Laboratory of Rubber-Plastics, Ministry of Education/Shandong Provincial Key Laboratory of Rubber-Plastics, School of Polymer Science and Engineering, Qingdao University of Science and Technology, Qingdao, Shandong 266042, China

<sup>2</sup> State Key Laboratory of Polymer Physics and Chemistry, Beijing National Laboratory of Molecular Sciences, Institute of Chemistry, Chinese Academy of Sciences, Beijing 100190, China

<sup>3</sup> Department of Bioengineering, University of Washington, Seattle, WA 98195, USA

<sup>4</sup> Beijing Laboratory of Biomedical Materials, Beijing University of Chemical Technology, Beijing 10029, China

Correspondence should be addressed to Aihua He; [aihuahe@iccas.ac.cn](mailto:aihuahe@iccas.ac.cn)

Received 12 July 2014; Accepted 12 July 2014; Published 26 August 2014

Copyright © 2014 Aihua He et al. This is an open access article distributed under the Creative Commons Attribution License, which permits unrestricted use, distribution, and reproduction in any medium, provided the original work is properly cited.

Electrospinning is a facile technology for the fabrication of nanostructured materials. With the varied solution properties and electrospun parameters, different nanostructures can be achieved for specific purpose. Up to now, a large amount of polymers has been electrospun for numerous potential applications including biomedical tissue scaffolds, drugs delivery, and semiconductor nanowire synthesis. To put forward the development of this technique and the applications of electrospun nanomaterials, a number of important issues have been addressed such as the fabrication and applications of electrospun nanofibers, advances in electrospun functional nanofibers, and electrospun nanoporous materials. In this special issue, we have invited ten papers that address such issues.

One of the papers of this special issue describes the fabrication of diclofenac sodium (DS) loaded Eudragit L100 nanofibers by a modified coaxial electrospinning for colon-targeted sustained release, which helps to avoid the clogging problem of spinneret in electrospinning. Another paper presents an interesting attempt to use PCL nanofiber containing marine seaweeds-extracellular polymeric substance for neural tissue repair. Another paper is about the technology of orderly printing of microdroplets by means of electrohydrodynamic print (EHDP) with alternating current, which would accelerate the application of inkjet printing in the field of micro-/nanosystem production.

One of the papers addresses the introduction of CNTs in aligned electrospun polycaprolactone/gelatin nanofibrous matrices as the growth environments of Schwann cells for peripheral nerve repair. The effects of diameters, alignment, and the content of CNTs in the nanofibers on cell behaviors are discussed. Another paper describes direct write of orderly micro-/nanofibrous structure by electrohydrodynamic system on insulate substrate, which is an interesting attempt to promote the application of EDW technology on the flexible electronics. Another paper simulates a novel electrospinning method, crater-like electrospinning, by two-phase computational fluid dynamics for a deep understanding of two-phase flow and microfluid jets production in electrospinning process. Another paper presents tunable structure of electrospun regenerated silk fibroin mats by annealing in water vapor for the improved mechanical properties, which is contributed to the extension of posttreatment of electrospun matrix.

One of the papers proposes using two opposite emitting electrode electrospinning setups to get naproxen (NAP)/cellulose acetate hybrid nanofibers. The distribution and release behavior of the drugs in the nanofibers are dependent on the electrode polarity. Another paper illustrates the fabrication of ultrafine carbon fibers with a nanoporous structure by the template method based on the electrospun of silica nanoparticles (NPs) embedded in PVA nanofibers, thermal annealing, chemical vapor deposition, and

alkali treatment, which provides an indication of fabricating inorganic nanofibers by electrospinning polymer nanofibers. Another paper addresses the effect of surfactants on the diameter and morphology of electrospun nanofibers, which shows us a new route to increase the uniformity of electrospun nanofibers and thereby the industrial applications.

*Aihua He  
Ruigang Liu  
Huarong Nie  
Yaqin Huang*

## Research Article

# The Effect of Surfactants on the Diameter and Morphology of Electrospun Ultrafine Nanofiber

Jian-Yi Zheng,<sup>1</sup> Ming-Feng Zhuang,<sup>1</sup> Zhao-Jie Yu,<sup>1</sup> Gao-Feng Zheng,<sup>1</sup> Yang Zhao,<sup>1</sup> Han Wang,<sup>2</sup> and Dao-Heng Sun<sup>1</sup>

<sup>1</sup> Department of Mechanical and Electrical Engineering, Xiamen University, Xiamen 361005, China

<sup>2</sup> Guangdong Provincial Key Laboratory of Micro/Nano Manufacturing Technology and Equipment, Guangdong University of Technology, Guangzhou 510006, China

Correspondence should be addressed to Yang Zhao; zhaoy@xmu.edu.cn

Received 27 February 2014; Revised 29 May 2014; Accepted 29 May 2014; Published 24 June 2014

Academic Editor: Ruigang Liu

Copyright © 2014 Jian-Yi Zheng et al. This is an open access article distributed under the Creative Commons Attribution License, which permits unrestricted use, distribution, and reproduction in any medium, provided the original work is properly cited.

Different surfactants are introduced to study the diameter and morphology transformation characteristics of electrospun nanofiber. Surfactants increase the net charge density and instability motion of charged jet. The instability motion provides a good way to stretch the charged jets into finer ones, by which the beaded structures are also prevented. Ultrafine nanofiber with average diameter less than 65 nm can be fabricated. The nanofiber diameter decreases with the increase of surfactant concentration in polymer solution. The nanofibers with anionic surfactant sodium dodecyl sulfate (SDS) have the smallest diameter. The cationic surfactant hexadecyl trimethyl ammonium bromide (HTAB) plays the best role to prevent the formation of beaded structures in nanofibers, and helps to increase the uniformity of electrospun nanofiber. The effects of surfactants on the nanofiber diameter and morphology have been studied, which would promote the industrial application of ultrafine polymeric nanofibers.

## 1. Introduction

Ultrafine polymeric nanofibers have wide application in the fields of micro/nanosystem and flexible electronics. At present, quick and low cost fabrication are the main aspects for the development and industrial application of ultrafine polymeric nanofibers, which have attracted a lot of attentions in recent years [1, 2]. As a unique and simple nano/micromanufacturing technology, electrospinning does not require stencil-plate, photo etching, or ultra clean chamber. Nanofiber with diameter ranges from several nanometers to several micrometers [3] can be electrospun at normal pressure and temperature. Electrospinning also has good materials compatibility that meets the development demands of polymeric, flexible, and bio-nano/microsystem. By now, hundreds of materials have been electrospun into nanofibers through electrospinning [4, 5], such as polymer, glass, metal, and protein. Electrospun nanofiber has extremely high surface area and outstanding mechanical and physical properties, which are suitable for a wide range application

fields, such as drug delivery [6, 7], sensing materials [8, 9], catalyze template [10], and ion battery membrane [11, 12]. Decreasing the diameter and promoting the uniformity of electrospun nanofiber are the key roles for their industrial application.

During the electrospinning process, the high voltage is applied to stretch viscoelastic solution into the cone shape named as “Taylor Cone.” When the electrical field force overcomes the surface tension, a jet is ejected from the cone tip. The charge repulsion force that stems from the accumulated charges imports disturbances into the ejection and motion process of polymer jet. The instability motion is the important factor to stretch and thin the charged jet [13]. Attributed to the bending and whipping instability, electrospinning nanofiber deposited randomly on collector as nonwoven.

The morphology of electrospun nanofiber is an important factor to investigate the rheology behaviors of charged jet in the ejection process. With the inadequate stretching of liquid jet, there are usual beaded structures appearing along

the electrospun nanofiber. The beaded structures stem from the competition surface tension of liquid jet [14], in which the solution viscosity, surface tension, and net charges are the main influencing factors [15]. Repulsion force among electrospinning jets increases with the increase of charge density and provided an effective way to increase the uniformity and decrease the diameter of electrospun nanofiber. The surfactants have been introduced to decrease the surface tension and increase the net charge density. As such, Lin et al. [16] used cationic surfactants to increase the jet charge density; then instability motion can be enhanced and the beaded nanofibers were also overcome; Jia and Qin [17] used surfactants to change the surface tension of electrospinning solution; then the thermal performance and inner structure of nanofibers can be adjusted. The influences of surfactants on the diameter and morphology should be studied further to promote its application.

In this work, different surfactants were introduced to decrease the nanofiber diameter and prevent the formation of beaded structures in electrospun nanofiber. The surfactants would increase the net charge density and enlarge the repulsion force among charged jets. Then, the instability motion was also enhanced by the charge repulsion force. The transformation characteristics of nanofiber diameter and morphology were studied.

## 2. Experiments Details

**2.1. Experiment Setup.** The electrospinning setup based on conventional pole-type nozzle configuration was built up in this work. The high voltage source (DW-P403-IAC, Tianjing Dongwen High Voltage Power Supply Plant, China) was used to provide electrical field between steel nozzle spinneret (inner diameter was 232  $\mu\text{m}$  and outer diameter was 500  $\mu\text{m}$ , Shanghai Kindly Enterprise Development Group, China) and aluminum paper collector (thickness 0.04 mm, Zhongshan Sinon Daily Products Co., Ltd., China). The anode of the high voltage source was connected to the steel nozzle spinneret, and the cathode was connected to the grounded collector. The precision syringe pump (Harvard 11 Pico Plus, USA) was used to transfer polymer solution from syringe to spinneret.

**2.2. Electrospinning Solution.** Polyvinylidene fluoride (PVDF, average molecular weight = 141,000 g/mol, DuPont, USA) solution was used as electrospinning solution. PVDF powder was added to the mixed blends of acetone (Sinopharm Chemical Reagent Co. Ltd., China) and N, N-dimethylformamide (DMF, Sinopharm Chemical Reagent Co. Ltd., China). The weight ratio of acetone to DMF in the blending solvent was 2 : 3. The PVDF concentration in the solution was 12 wt%.

Anionic surfactant sodium dodecyl sulfate (SDS), non-ionic surfactants Triton X-100, and cationic surfactants hexadecyl trimethyl ammonium bromide (HTAB) were added to the PVDF solution to investigate the effect of surfactants on the diameter and morphology of electrospun nanofiber, respectively. All of these three surfactants were purchased from Sinopharm Chemical Reagent Co., Ltd. China, which

were used without any further purification. The surfactant concentrations in the PVDF solution were  $3.5 \times 10^{-3}$  mol/L,  $1.75 \times 10^{-2}$  mol/L, and  $3.5 \times 10^{-2}$  mol/L, respectively.

**2.3. Electrospinning Process.** In the experiment, the PVDF solution was transferred to the nozzle spinneret by the precision syringe pump at a flow rate of 200  $\mu\text{L/hr}$ . High voltage of 13 kV was applied at the nozzle spinneret, and the distance between spinneret to collector was 15 cm. The electrospun nanofibers were observed and measured by a SEM (LEO 1530 field emission scanning electron microscope). Before the observation of SEM, the samples were sputter-coated with a gold layer of about 10 nm thickness.

## 3. Results and Discussion

**3.1. Solution Characteristics.** Firstly, the characteristics of polymer solution with surfactants were tested. The viscosity of PVDF solution was 153 mPa·s, which was the same as the polymer solution without surfactant. Surfactants can increase the free charges in polymer solution and conductivity of solution. The conductivity of polymer solution increased from 138  $\mu\text{s/cm}$  to 860  $\mu\text{s/cm}$ , as SDS surfactant concentration increased from  $3.5 \times 10^{-3}$  mol/L to  $3.5 \times 10^{-2}$  mol/L. And the conductivity of polymer solution increased from 167  $\mu\text{s/cm}$  to 1104  $\mu\text{s/cm}$ , as HTAB surfactant concentration increased from  $3.5 \times 10^{-3}$  mol/L to  $3.5 \times 10^{-2}$  mol/L. The relationship between conductivity of polymer solution and surfactant concentration was shown in Figure 1. But the Triton X-100 did not change the conductivity, since the Triton X-100 was nonionic surfactant and did not increase the free charges in polymer solution. Figure 1 showed that the conductivity did not increase with the surfactant concentration. The conductivity of PVDF solution with Triton X-100 was 9  $\mu\text{s/cm}$ , which was the same as the polymer solution without surfactant.

**3.2. Beaded Nanofiber without Surfactants.** Then, PVDF solution without surfactants was used as electrospinning solution. Due to the fast evaporation of solvent, the charged jets cannot be stretched adequately into fine and uniform ones. Liquid jet would be shrank into beaded structure by the surface tension, as shown in Figure 2. The beaded nanofibers with a diameter range from 30 nm to 170 nm, and the average diameter was 67.02 nm. The standard deviation of electrospinning nanofiber was 31.62 nm. Attributed to the large surface tension and small stretching ratio, the electrospinning nanofiber had large diameter distribution. The beaded structure on the electrospinning nanofibrous web also had large diameter distribution, which ranged from 422 nm to 6.28  $\mu\text{m}$ . And the average diameter of beaded structure was 2.06  $\mu\text{m}$ . The diameter distribution range of nanofiber electrospun from PVDF solution without surfactant was shown in Figure 3. Decreasing the surface tension and solution viscosity provided a good way to overcome the beaded structure. On the other hand, increasing the net charge density and electrical field forced applied on the charged jet would also promote the stretching and uniformity of charged jet.

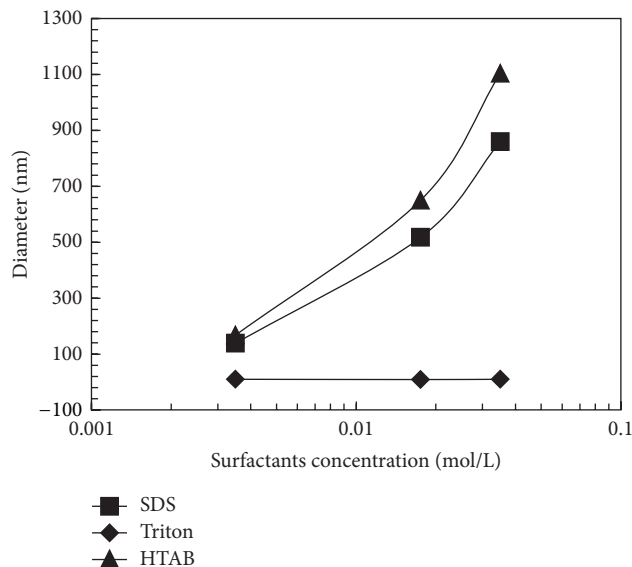


FIGURE 1: The relationship between solution conductivity and surfactant concentration in the solution.

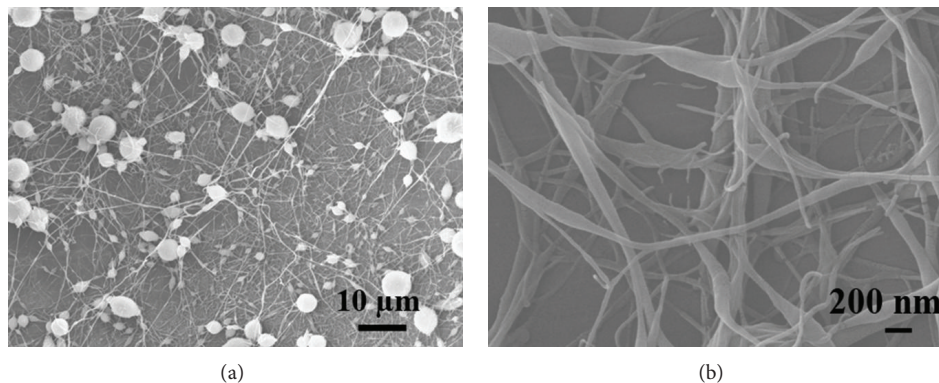


FIGURE 2: Beaded PVDF nanofiber electrospun from PVDF solution without surfactants. (a) Electrospun beaded PVDF nanofiber. (b) Close view of beaded nanofiber with magnification of 22,000x.

The diameter and morphology of electrospun nanofiber was observed and measured by SEM. The average diameter was calculated from more than 50 data points in 10 samples.

**3.3. Uniform Nanofiber with Surfactants.** And then, the effects of surfactant on the diameter and morphology were investigated by adding the surfactants to the polymer solution. The nanofibers electrospun from PVDF solution with surfactants of SDS, Triton X-100, and HTAB were shown in Figures 4–6, respectively. With the increase of surfactant concentration, both the conductivity of polymer solution and the net charge density of electrospinning jet can be increased [18]. The electrical field force applied on the charged jet increased with the increase of net charge density, which also enhanced the instability whipping and spiral motion

of charged jets. The instability motion of charged jet was an important role to promote the stretching process of electrospinning jet, decrease the diameter of liquid jet, and prevent the formation of beaded structures in the nanofibers [19]. Therefore, higher surfactant concentration in polymer solution led to less beaded structures and more uniform nanofiber. Figures 4–6 showed that the surfactants played a good factor to prevent the formation of beaded structure and increase the uniformity of electrospun nanofiber.

Then, the effects of surfactant concentration on the nanofiber diameter and distribution were studied. The relationships between nanofiber diameter and surfactant concentration in solution were shown in Figure 7. With the help of surfactant, the average nanofiber diameter was less than 65 nm. As surfactant concentration in polymer solution

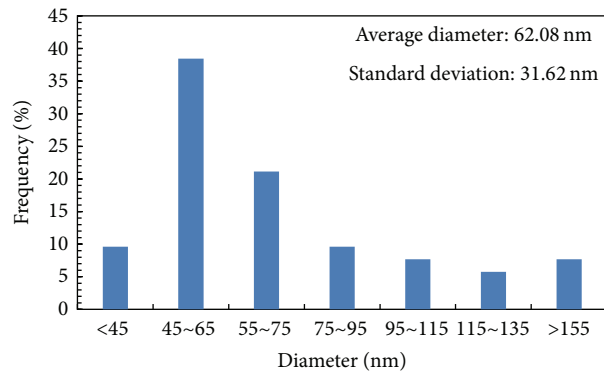


FIGURE 3: The diameter distribution range of nanofiber gained from PVDF solution without surfactant.

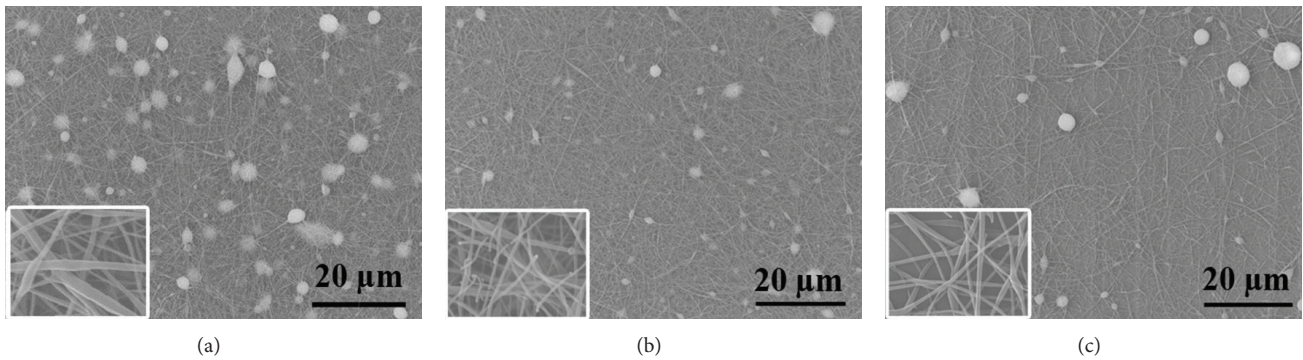


FIGURE 4: Electrospun nanofiber gained from PVDF solution with anionic surfactants of SDS. The concentration of SDS in the solution is (a)  $3.5 \times 10^{-3}$  mol/L, (b)  $1.75 \times 10^{-2}$  mol/L, and (c)  $3.5 \times 10^{-2}$  mol/L.

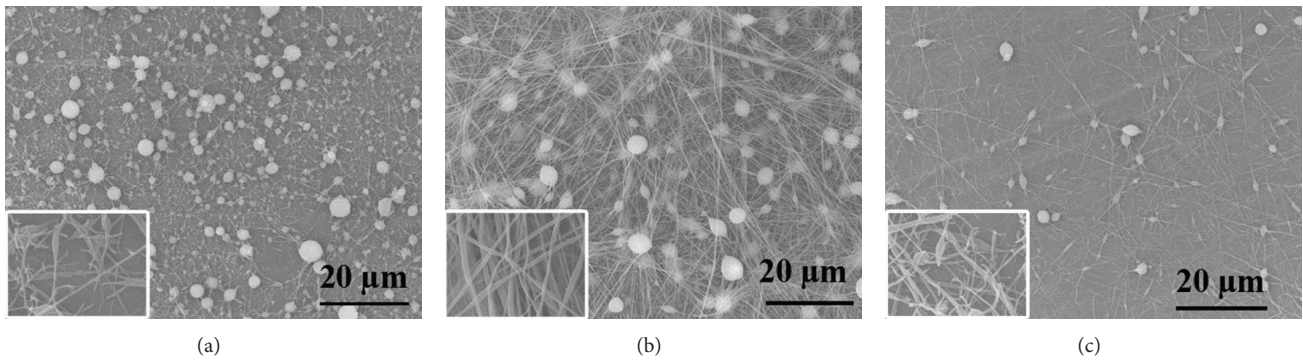


FIGURE 5: Electrospun nanofiber gained from PVDF solution with nonionic surfactants of Triton X-100. The concentration of Triton X-100 in the solution is (a)  $3.5 \times 10^{-3}$  mol/L, (b)  $1.75 \times 10^{-2}$  mol/L, and (c)  $3.5 \times 10^{-2}$  mol/L.

increased from  $3.5 \times 10^{-3}$  mol/L to  $3.5 \times 10^{-2}$  mol/L, the diameter of PVDF nanofiber with SDS decreased from 51.68 nm to 39.89 nm, the diameter of PVDF nanofiber with Triton X-100 decreased from 63.91 nm to 40.62 nm, and the diameter of PVDF nanofiber with HTAB decreased from 60.19 nm

to 41.61 nm. Figures 8–10 showed the diameter distribution range of nanofiber electrospun from PVDF solution with surfactant. The diameter of nanofiber ranged from 30 nm to 70 nm. The surfactant concentration in solution was  $3.5 \times 10^{-3}$  mol/L in Figure 8. The surfactant concentration in

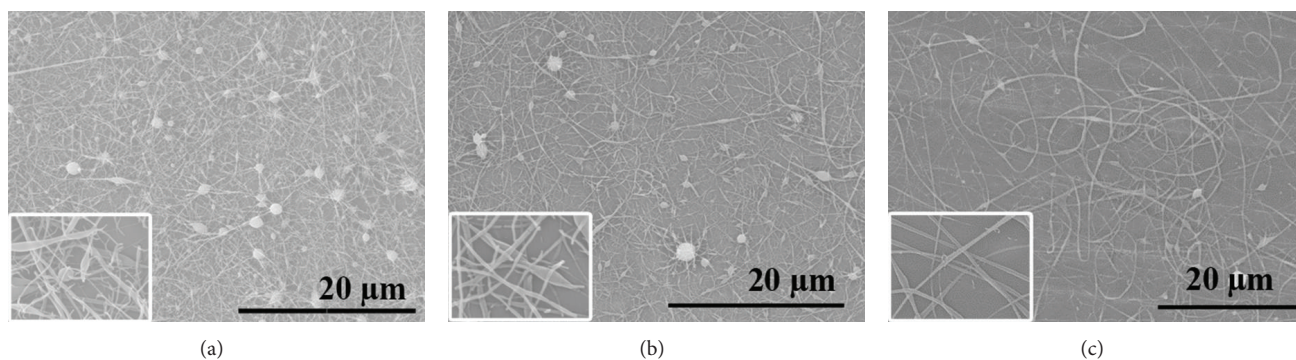


FIGURE 6: Electrospun nanofiber gained from PVDF solution with cationic surfactants of HTAB. The concentration of HTAB in the solution is (a)  $3.5 \times 10^{-3}$  mol/L, (b)  $1.75 \times 10^{-2}$  mol/L, and (c)  $3.5 \times 10^{-2}$  mol/L.

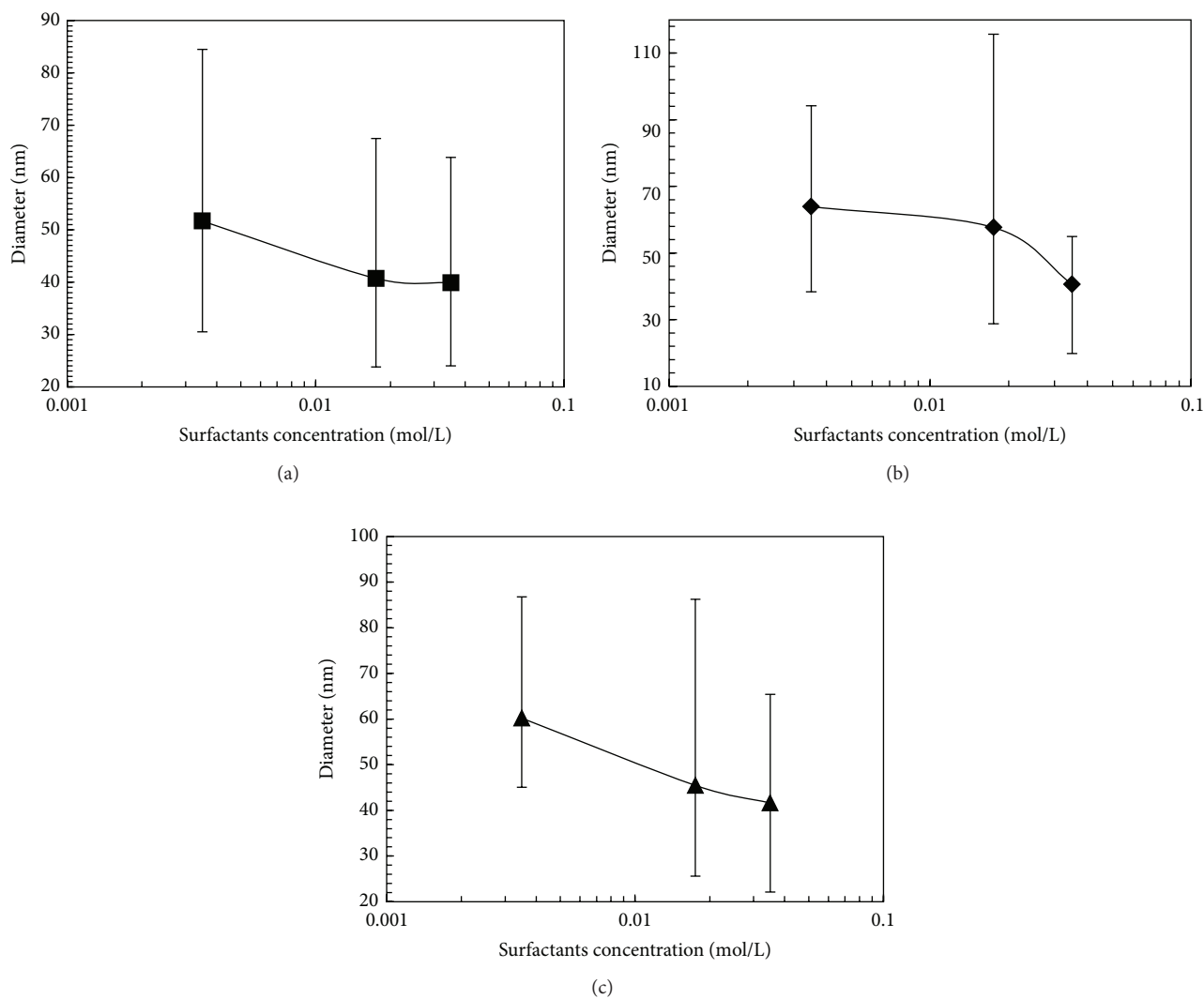


FIGURE 7: The relationship between nanofiber diameter and surfactant concentration in the solution: (a) SDS, (b) Triton X-100, and (c) HTAB.

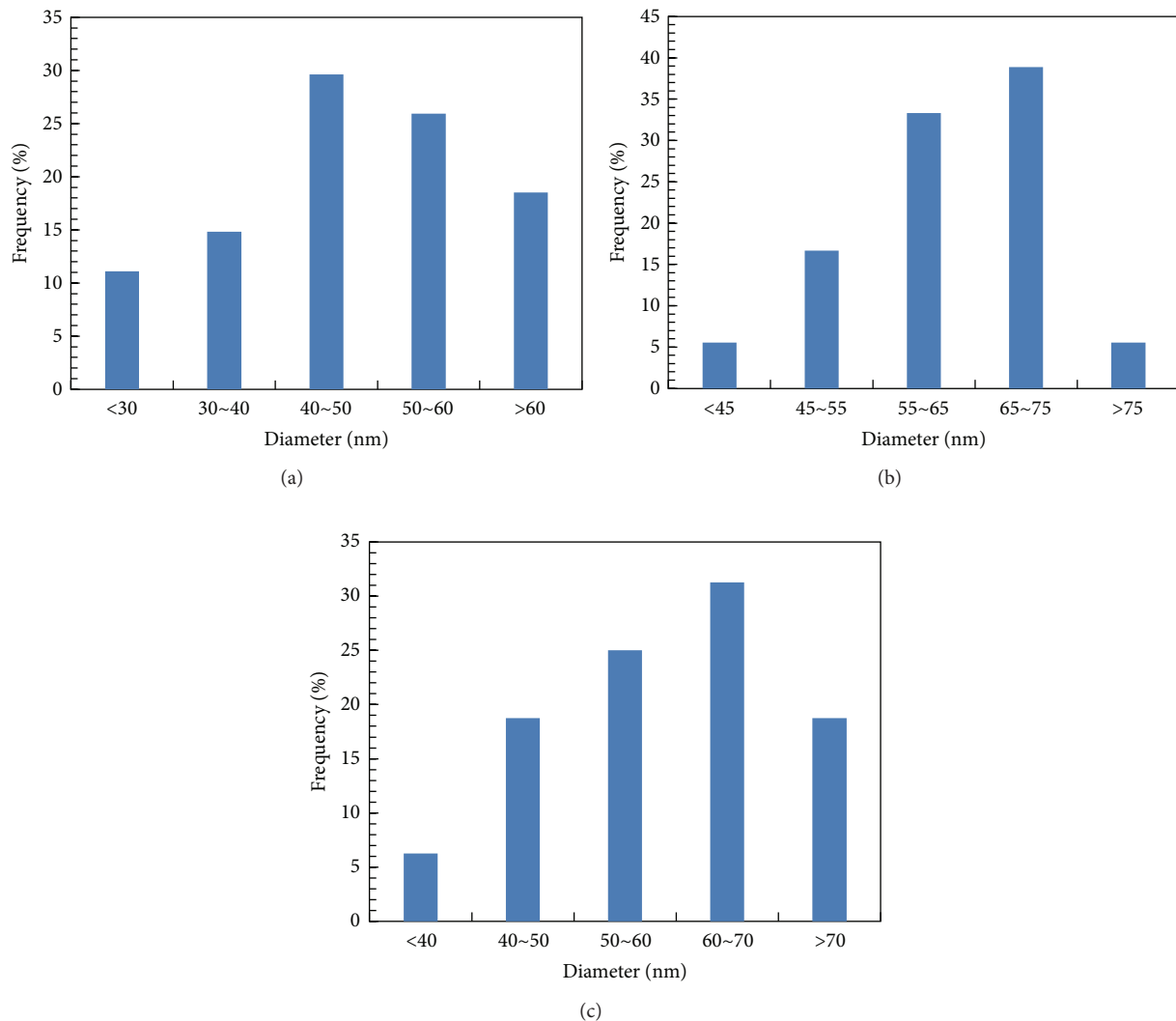


FIGURE 8: The diameter distribution of nanofiber gained from PVDF solution with surfactants: (a) SDS: average diameter is 51.68 nm and standard deviation is 13.81 nm; (b) Triton X-100: average diameter is 63.91 nm and standard deviation is 11.09 nm; (c) HTAB: average diameter is 60.19 nm and standard deviation is 13.71 nm. The surfactant concentration in solution was  $3.5 \times 10^{-3}$  mol/L.

solution was  $1.75 \times 10^{-2}$  mol/L in Figure 9. The surfactant concentration in solution was  $3.5 \times 10^{-2}$  mol/L in Figure 10. Both of nanofiber diameter and diameter distribution range decreased with the increase of surfactant concentration.

Different surfactants had played different roles in the rheology behaviors of charged jet. The nanofibers gained from PVDF solution with anionic surfactant SDS were shown in Figure 4. There were the least beaded structures in Figure 4(b), when surfactant concentration of SDS was  $1.75 \times 10^{-2}$  mol/L. When surfactant concentration of solution was  $3.5 \times 10^{-2}$  mol/L, nanofibers electrospun from PVDF solution had large beaded structure, as shown in Figure 4(c). Then, the diameter of beaded structure in Figure 4(c) was larger than that in Figures 4(a) and 4(b). The nanofibers gained from PVDF solution with nonionic surfactant of Triton X-100

were shown in Figure 5. Large surfactant concentration led to less beaded structures and smaller diameter. The nanofibers gained from PVDF solution with surfactant of HTAB in Figure 6 had less and smaller beaded structures than that in Figures 4 and 5. The relationship in Figure 7 showed that the nanofiber with the surfactant of SDS had the smallest diameter, attributed to larger charge repulsion force among liquid jets.

In this work, the anode of the high voltage source was connected to the steel nozzle spinneret. When injected from the spinneret, the liquid jet also carried away the positive charge accumulated on the spinneret. The cationic surfactant of HTAB would play a good way to provide excess positive charge to the liquid jet during the injection process. On the other hand, polymer solution with HTAB had the highest

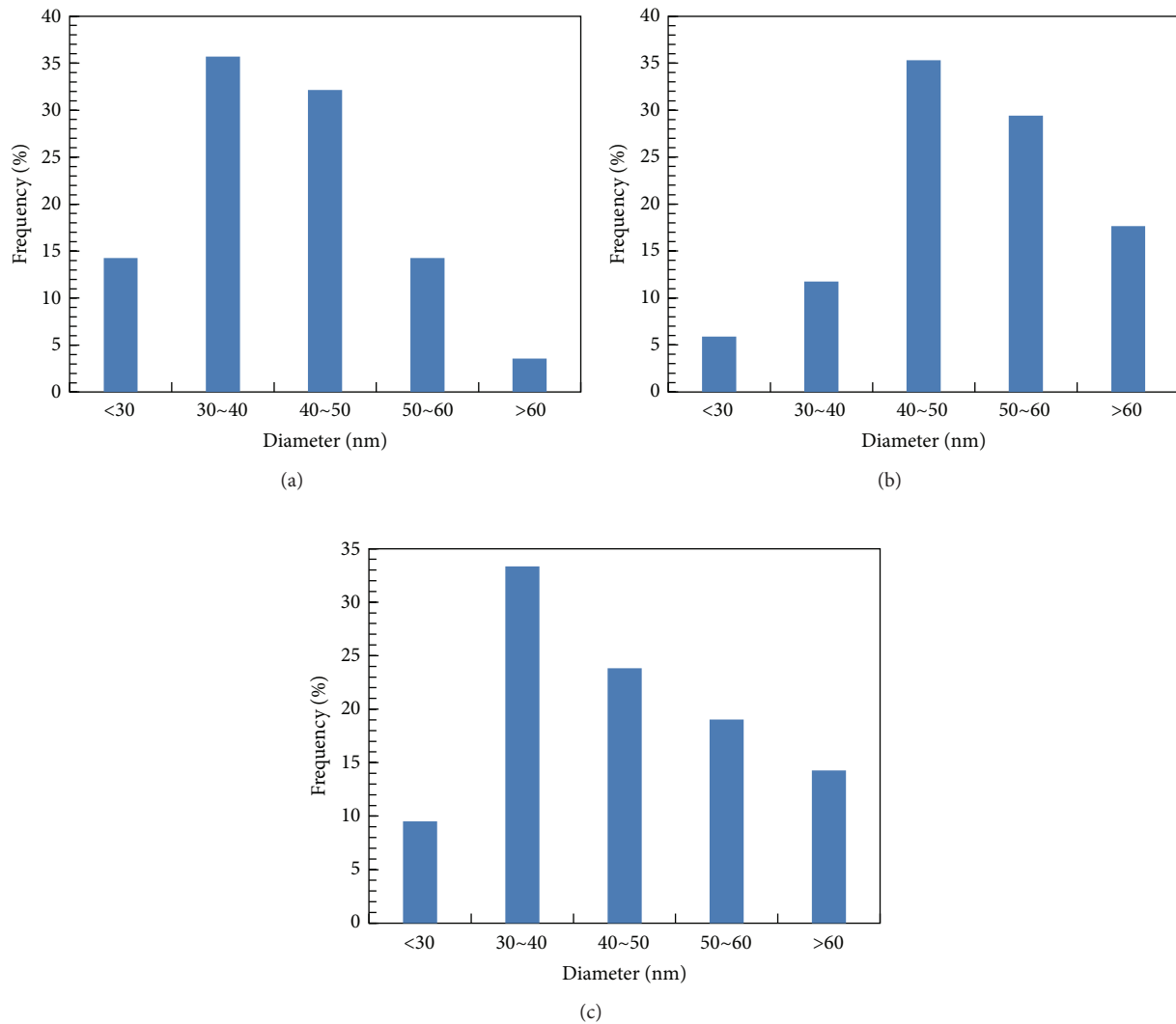


FIGURE 9: The diameter distribution of nanofiber gained from PVDF solution with surfactants: (a) SDS: average diameter is 40.71 nm and standard deviation is 10.02 nm; (b) Triton X-100: average diameter is 56.51 nm and standard deviation is 22.95 nm; (c) HTAB: average diameter is 45.55 nm and standard deviation is 15.15 nm. The surfactant concentration in solution was  $1.75 \times 10^{-2}$  mol/L.

conductivity that would increase the free charges in solution. And then, the net charge density can be increased to enhance the instability motion of charged jet. Thus, the nanofiber electrospun from PVDF solution with cationic surfactant of HTAB had the smallest and least beaded structure in nanofiber.

#### 4. Conclusion

Different surfactants were introduced to investigate the rheology behaviors of charged jet electrospun from PVDF solution. With the help of surfactants, net charge density in electrospinning jet was increased to enhance the charge repulsion force and the instability motion of charged jet.

Charged jets can be stretched adequately into finer and uniform ones by the larger electrical field force. With the help of surfactants, electrospinning nanofiber with average diameter less than 65 nm can be fabricated, which was finer than nanofiber electrospun from PVDF solution without surfactant. The nanofiber diameter and diameter distribution range decreased with the increase of surfactant concentration in solution. Attributed to the larger net charge density, the cationic surfactant of HTAB would provide a great way to prevent forming beaded structures.

The effects of surfactant on the transform characteristics of nanofiber diameter and morphology were studied, which would provide a good way to promote the industrial application of polymeric nanofibers.

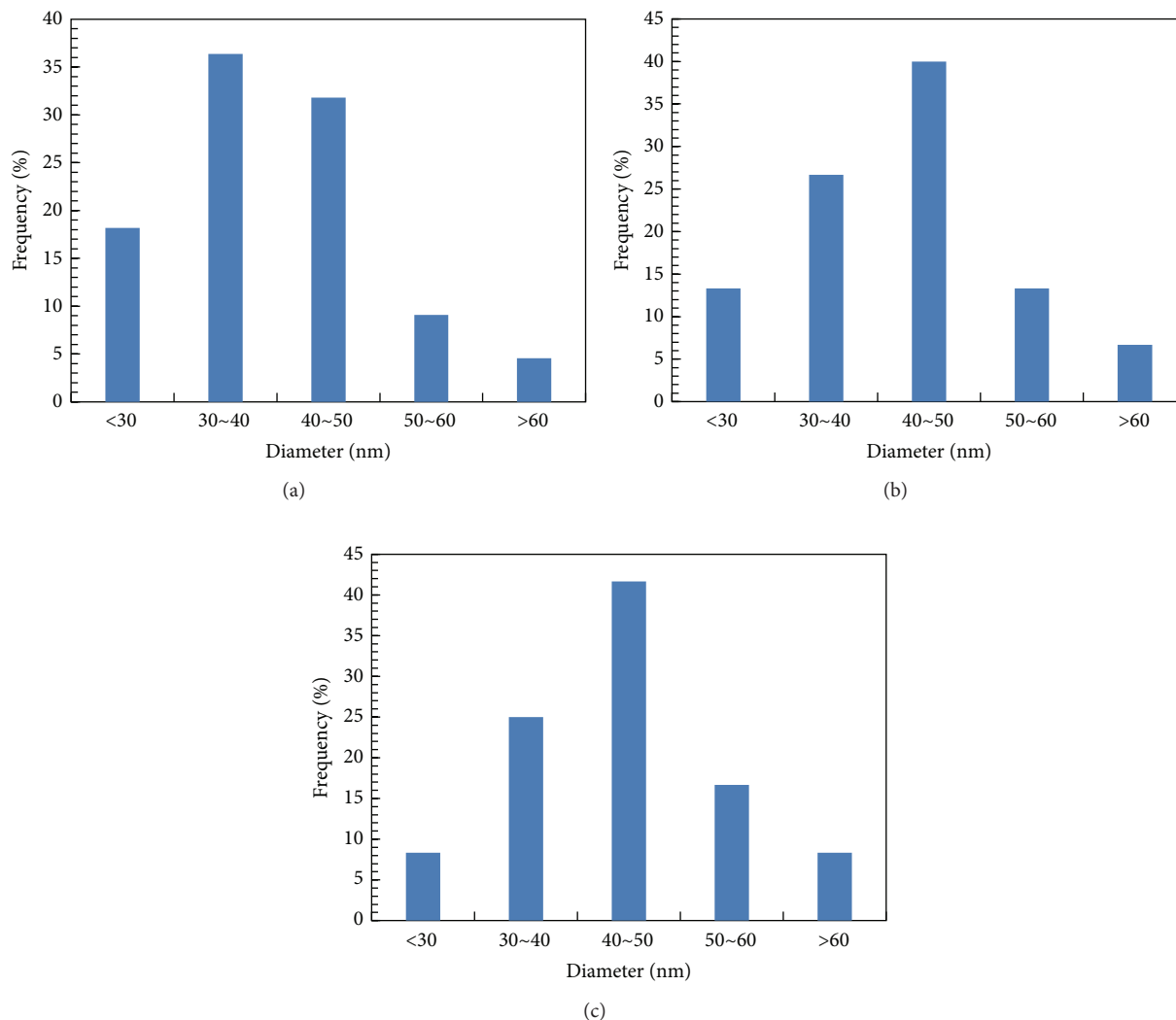


FIGURE 10: The diameter distribution of nanofiber gained from PVDF solution with surfactants: (a) SDS: average diameter is 39.89 nm and standard deviation is 9.99 nm; (b) Triton X-100: average diameter is 40.62 nm and standard deviation is 10.24 nm; (c) HTAB: average diameter is 41.61 nm and standard deviation is 12.88 nm. The surfactant concentration in solution was  $3.5 \times 10^{-2}$  mol/L.

## Conflict of Interests

The authors declare that there is no conflict of interests regarding the publication of this paper.

## Acknowledgments

This work is supported by the National Natural Science Foundation of China (nos. 51035002 and 51305371), Major Science and Technology Projects of Fujian Province of China (no. 2012H6022), and Opening fund of Guangdong Provincial Key Laboratory of Micro-Nano Manufacturing Technology and Equipment (no. GDMNML2013-01).

## References

- [1] J. C. Bolsée, W. D. Oosterbaan, L. Lutsen, D. Vanderzande, and J. Manca, "The importance of bridging points for charge transport in webs of conjugated polymer nanofibers," *Advanced Functional Materials*, vol. 23, no. 7, pp. 862–869, 2013.
- [2] Y. Xia, P. Yang, Y. Sun et al., "One-dimensional nanostructures: synthesis, characterization, and applications," *Advanced Materials*, vol. 15, no. 5, pp. 353–389, 2003.
- [3] W. Feng, Z. Wu, Y. Li, Y. Feng, and X. Yuan, "The fabrication and electrochemical properties of electrospun nanofibers of a multiwalled carbon nanotube grafted by chitosan," *Nanotechnology*, vol. 19, no. 10, Article ID 105707, 2008.
- [4] L. Persano, A. Camposeo, C. Tekmen, and D. Pisignano, "Industrial upscaling of electrospinning and applications of polymer nanofibers: a review," *Macromolecular Materials and Engineering*, vol. 298, no. 5, pp. 504–520, 2013.
- [5] W. Qian, D. G. Yu, and Y. Li, "Triple-component drug-loaded nanocomposites prepared using a modified coaxial electrospinning," *Journal of Nanomaterials*, vol. 2013, Article ID 826471, 7 pages, 2013.

- [6] C. Dott, C. Tyagi, L. K. Tomar et al., "A mucoadhesive electrospun nanofibrous matrix for rapid oramucosal drug delivery," *Journal of Nanomaterials*, vol. 2013, Article ID 924947, 19 pages, 2013.
- [7] Y. Zhang, S. Wu, J. Xu et al., "Preparation and performance characterization of electrospun drug loaded poly(vinyl alcohol)/chitosan nanofibrous membrane," *Journal of Zhejiang University*, vol. 42, no. 6, pp. 644–648, 2013.
- [8] W. G. Chen, Q. Zhou, L. N. Xu et al., "Improved methane sensing properties of Co-doped SnO<sub>2</sub> electrospun nanofibers," *Journal of Nanomaterials*, vol. 2013, Article ID 173232, 9 pages, 2013.
- [9] C. Wang, D. Chen, and L. Cheng, "Progress in the application of conducting polymer in glucose biosensor," *Journal of Biomedical Engineering*, vol. 30, no. 5, pp. 1112–1116, 2013.
- [10] H. Wang, D. Wu, D. Li et al., "Fabrication of continuous highly ordered mesoporous silica nanofibre with core/sheath structure and its application as catalyst carrier," *Nanoscale*, vol. 3, no. 9, pp. 3601–3604, 2011.
- [11] Y. E. Miao, G. N. Zhu, H. Hou, Y. Y. Xia, and T. Liu, "Electrospun polyimide nanofiber-based nonwoven separators for lithium-ion batteries," *Journal of Power Sources*, vol. 226, pp. 82–86, 2013.
- [12] L. Han, C. Lu, P. Chen, W. Qi, and Q. Yu, "The effects of in situ generated titanium dioxide on the mechanical and electrochemical properties of electrospun polyvinylidene fluoride separator for lithium-ion battery," *Acta Polymerica Sinica*, no. 11, pp. 1319–1325, 2012.
- [13] V. Pillay, C. Dott, and Y. E. Choonara, "A review of the effect of processing variables on the fabrication of electrospun nanofibers for drug delivery applications," *Journal of Nanomaterials*, vol. 2013, Article ID 789289, 22 pages, 2013.
- [14] R. Asmatulu, M. Ceylan, and N. Nuraje, "Study of superhydrophobic electrospun nanocomposite fibers for energy systems," *Langmuir*, vol. 27, no. 2, pp. 504–507, 2011.
- [15] K. H. Lee, H. Y. Kim, H. J. Bang, Y. H. Jung, and S. G. Lee, "The change of bead morphology formed on electrospun polystyrene fibers," *Polymer*, vol. 44, no. 14, pp. 4029–4034, 2003.
- [16] T. Lin, H. Wang, H. Wang, and X. Wang, "The charge effect of cationic surfactants on the elimination of fibre beads in the electrospinning of polystyrene," *Nanotechnology*, vol. 15, no. 9, pp. 1375–1381, 2004.
- [17] L. Jia and X. H. Qin, "The effect of different surfactants on the electrospinning poly(vinyl alcohol) (PVA) nanofibers," *Journal of Thermal Analysis and Calorimetry*, vol. 112, no. 2, pp. 595–605, 2013.
- [18] K. Ziani, C. Henrist, C. Jérôme, A. Aqil, J. I. Maté, and R. Cloots, "Effect of nonionic surfactant and acidity on chitosan nanofibers with different molecular weights," *Carbohydrate Polymers*, vol. 83, no. 2, pp. 470–476, 2011.
- [19] W. Li, G. Zheng, X. Wang et al., "Directly electrospun ultrafine nanofibres with Cu grid spinneret," *Journal of Physics D: Applied Physics*, vol. 44, no. 13, Article ID 135502, 2011.

## Research Article

# Fabrication of Ultrafine Carbon Fibers Possessing a Nanoporous Structure from Electrospun Polyvinyl Alcohol Fibers Containing Silica Nanoparticles

Koichi Sawada, Shinji Sakai, and Masahito Taya

*Division of Chemical Engineering, Department of Materials Engineering Science, Graduate School of Engineering Science, Osaka University, 1-3 Machikaneyama-cho, Toyonaka, Osaka 560-8531, Japan*

Correspondence should be addressed to Shinji Sakai; [sakai@cheng.es.osaka-u.ac.jp](mailto:sakai@cheng.es.osaka-u.ac.jp) and Masahito Taya; [taya@cheng.es.osaka-u.ac.jp](mailto:taya@cheng.es.osaka-u.ac.jp)

Received 25 February 2014; Revised 2 May 2014; Accepted 3 May 2014; Published 16 June 2014

Academic Editor: Ruigang Liu

Copyright © 2014 Koichi Sawada et al. This is an open access article distributed under the Creative Commons Attribution License, which permits unrestricted use, distribution, and reproduction in any medium, provided the original work is properly cited.

Ultrafine carbon fibers with a nanoporous structure were fabricated by the template method using silica nanoparticles (NPs) embedded in fibers of approximate diameter 500 nm, electrospun from an aqueous solution of polyvinyl alcohol,  $\text{CoCl}_2$ , silica NPs, and *N,N*-dimethylformamide. Black, conductive fibers were obtained by heat treatment in air and a chemical vapor deposition reaction under methanol vapor for more than 5 h. Transmission electron microscopy (TEM) demonstrated that the fabricated fibers after silica removal had a porous structure originating from 15 nm diameter silica NPs. Energy dispersive X-ray analysis combined with TEM confirmed the removal of silica from the fibers by NaOH treatment at 80°C. Total surface area and total pore volume of the fibers after silica removal, determined by nitrogen adsorption measurement, were 318 m<sup>2</sup>/g and 1.67 cm<sup>3</sup>/g, respectively. The sheet resistivities of the fabricated fibers were 35.1–477 Ω/□, which were relatively high, compared with that reported for polyacrylonitrile-based fibers carbonized at 800°C. D and G bands detected in the Raman spectrum of the NaOH-treated fibers showed that the prepared carbon fibers were more crystalline than natural carbonaceous materials.

## 1. Introduction

Carbon materials have attractive properties, such as surface hydrophobicity, chemical inertness, large surface area to volume ratios, and thermal stability. These properties enable their use in various applications, including catalysts [1], energy devices [2], sensors [3], and water and air cleaning elements [4, 5]. Recently, ultrafine carbon fibers fabricated from electrospun fibers have attracted great interest because they can be obtained as nonwoven fabrics consisting of continuous fibers with diameters ranging from several hundred nm to sub μm and such fabrics show high porosity and interconnectivity [6]. Ultrafine carbon fibers have been fabricated by carbonization of electrospun fibers made from carbon precursors such as polyacrylonitrile (PAN) and pitch [6].

Much effort has been given to control the structure, texture, and conductivity of fibers to expand the availability of the materials [6]. Amongst the properties of fibrous materials,

the pore structure plays a key role in applications. However, the conventional electrospinning process only generates solid ultrafine fibers, without pores. Therefore, posttreatment methods have been developed to create desirable pores in the carbon fibers [7, 8]. For this purpose, two processes have been reported. One is the treatment of carbon fibers with steam or carbon dioxide at 700–1000°C, a so-called “activation” process [8]. The other is to induce phase separation using a hard or soft template. Kim et al. fabricated porous PAN-based carbon fibers by phase separation. Porous carbon fibers were prepared via electrospinning of PAN and poly(methyl methacrylate) (PMMA), followed by carbonization with decomposition of PMMA [9]. In a recent report, Liu et al. fabricated porous carbon fibers by phase separation via electrospinning of PAN and  $\text{CaCO}_3$  nanoparticles (NPs) and subsequent carbonization, followed by acid treatment to remove the  $\text{CaCO}_3$  template. The carbon fibers possessed a nanoporous structure, resulting in a high surface area and pore volume. These characteristics were reported to play a key

role in a catalytic application and to be potentially useful in other applications [10].

In the current study, the fabrication of carbon fibers with a controlled nanoporous structure is proposed by combining a chemical vapor deposition (CVD) reaction and phase separation using electrospun poly(vinyl alcohol) (PVA) fibers containing 15 nm silica NPs as pore templates. Figure 1 illustrates the stepwise procedure proposed in this study to prepare nanoporous carbon fibers, which includes the treatments of electrospun fibers with heat and CVD and removal of silica NPs. The fibers are electrospun from a solution composed of PVA,  $\text{CoCl}_2$ , silica NPs, and *N,N*-dimethylformamide (DMF) as a cosolvent that facilitates electrospinning. Cobalt is known to catalyze carbon deposition during the CVD reaction [11]. In the present study, a cobalt compound was added to the electrospinning solution to facilitate carbon deposition inside the fibers, for maintaining the continuous nanofibrous structure after removal of the silica NPs. Heat treatment produces a fiber preparation containing cobalt and silica NPs. Subsequent removal of the silica NPs by NaOH endows the resultant carbon fibers with a nanoporous structure.

## 2. Materials and Methods

**2.1. Materials.** PVA (MW: 146,000–186,000 Da) was purchased from Polysciences, Inc. (Warrington, PA, USA) and  $\text{CoCl}_2 \cdot 6\text{H}_2\text{O}$ , DMF, and methanol were products from Wako Pure Chemical Industries Ltd. (Osaka, Japan). Colloidal silica (trade name: Snowtex), a sol of 30 wt% silica NPs with an average diameter of 15 nm, was provided by Nissan Chemical Industries Ltd. (Tokyo, Japan).

**2.2. Electrospinning of PVA/ $\text{CoCl}_2$ /Silica NP Mixture Solution.** An aqueous solution of 15 wt% PVA was prepared by autoclaving a suspension of PVA powder in distilled water at 120°C for 20 min. An aqueous solution of 1 wt%  $\text{CoCl}_2 \cdot 6\text{H}_2\text{O}$  (3.9 g) was added dropwise to the colloidal silica sol (8.4 g) under vigorous stirring using a magnetic stirrer. This solution was mixed with the PVA solution (8.5 g) and DMF (1.7 g) and then electrospun at a tip-to-collector distance of 15 cm, with a solution flow rate of 2.0 mL/min and applied voltage of 20 kV.

**2.3. Formation of Nanoporous Structure by Template Method.** The electrospun fibers were calcined at 500°C under air flow for 5 h after elevating the temperature at 5°C/min. Subsequently, the resultant fibers were subjected to CVD reaction in a quartz tube furnace (60 cm in length). Methanol vapor was delivered by bubbling nitrogen gas through a glass trap containing pure methanol at 200 cm<sup>3</sup>/min and ambient temperature. The methanol/nitrogen gas mixture was then introduced into the furnace and the CVD reaction was performed at 600°C for the prescribed period. Finally, the silica NPs were removed to form a nanoporous structure in the carbon fibers by soaking the fibers in a 10 wt% NaOH aqueous solution for 24 h at 80°C. After treatment, the fibers were rinsed with a large amount of distilled water and lyophilized.

**2.4. Morphological Characterization by TEM-EDX.** Morphologies and element mapping of the electrospun fibers were characterized with a transmission electron microscope-energy dispersive X-ray (TEM-EDX) instrument (H-800EDX, Hitachi Co., Tokyo, Japan) operated at 200 kV. The fibers were dispersed in water by sonication and deposited on a TEM copper grid.

**2.5. Pore Structural Characterization.** The pore structure of the fibers was investigated by measuring the nitrogen adsorption/desorption isotherms at −196°C with an automatic volumetric sorption analyzer (Autosorb-1, Quantachrome Co., Boynton Beach, FA, USA). The total surface area ( $S_{\text{BET}}$ ) and pore volume ( $V_{\text{total}}$ ) were calculated by the Brunauer-Emmett-Teller (BET) method and the Brunauer-Joyner-Halenda (BJH) method, respectively.

**2.6. Sheet Resistivity Measurement.** Sheet resistivity of the fibers was evaluated by a four-point probe resistivity measurement with a resistivity meter (RT-70V/RG-5, Napson Co., Chiba, Japan). The fibrous mats were cut and shaped into rectangles that were 1 cm square on each side, with an average thickness of 35 μm, and placed on a glass substrate.

**2.7. Raman Spectroscopy Measurement.** Raman spectroscopy was carried out to evaluate the quality and crystallinity of carbon fibers using a confocal Raman microscope (LabRAM HR-800, Horiba, Ltd., Kyoto, Japan) at a wavelength of 532 nm.

## 3. Results and Discussion

**3.1. Electrospinning and TEM-EDX Characterization.** Ultra-fine PVA fibers of about 500 nm in diameter containing  $\text{CoCl}_2$  and silica NPs were obtained by electrospinning. The white color of fibers as spun (Figure 2(a)) apparently became light blue after calcination in air at 500°C for 5 h (Figure 2(b)). From the TEM observations of fibers as spun and after calcination, it was found that the electron transparency inside the fibers increased somewhat after calcination and the presence of silica particles became more distinct (Figures 2(a) and 2(b)). This result indicates that the calcination treatment yielded fibers predominantly containing silica NPs (Figure 2(b)). As seen in Figures 2(b) and 2(c), no significant structural difference was observed by TEM between the fibers before and after the CVD reaction. However, a color change from white to black after the CVD reaction was obvious, which indicates the deposition of carbon in/on the fibers (Figure 2(c)). A black mat was obtained even after silica removal with NaOH treatment for 24 h. Electron transparency of the fibers was significantly increased after the NaOH treatment (Figures 2(c) and 2(d)). This result indicates that after the NaOH treatment, the fibers had a nanoporous structure originating from the silica NPs.

Next, the silica removal was confirmed by an EDX spectrometer equipped with TEM. Figures 3(a)–3(f) show scanning transmission electron microscopic (STEM) images and the results of element mapping for Si and Co. As seen

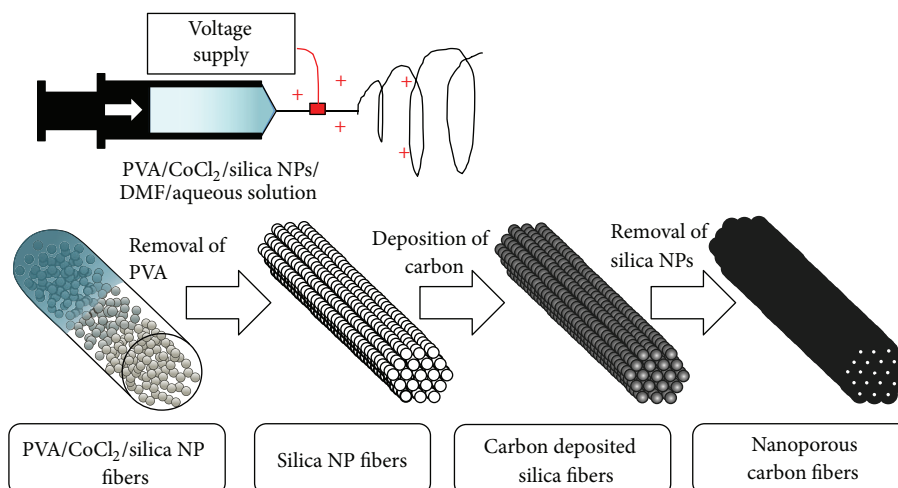


FIGURE 1: Schematic drawing of the stepwise procedure for fabrication of nanoporous carbon fibers by combined electrospinning, CVD reaction, and phase separation.

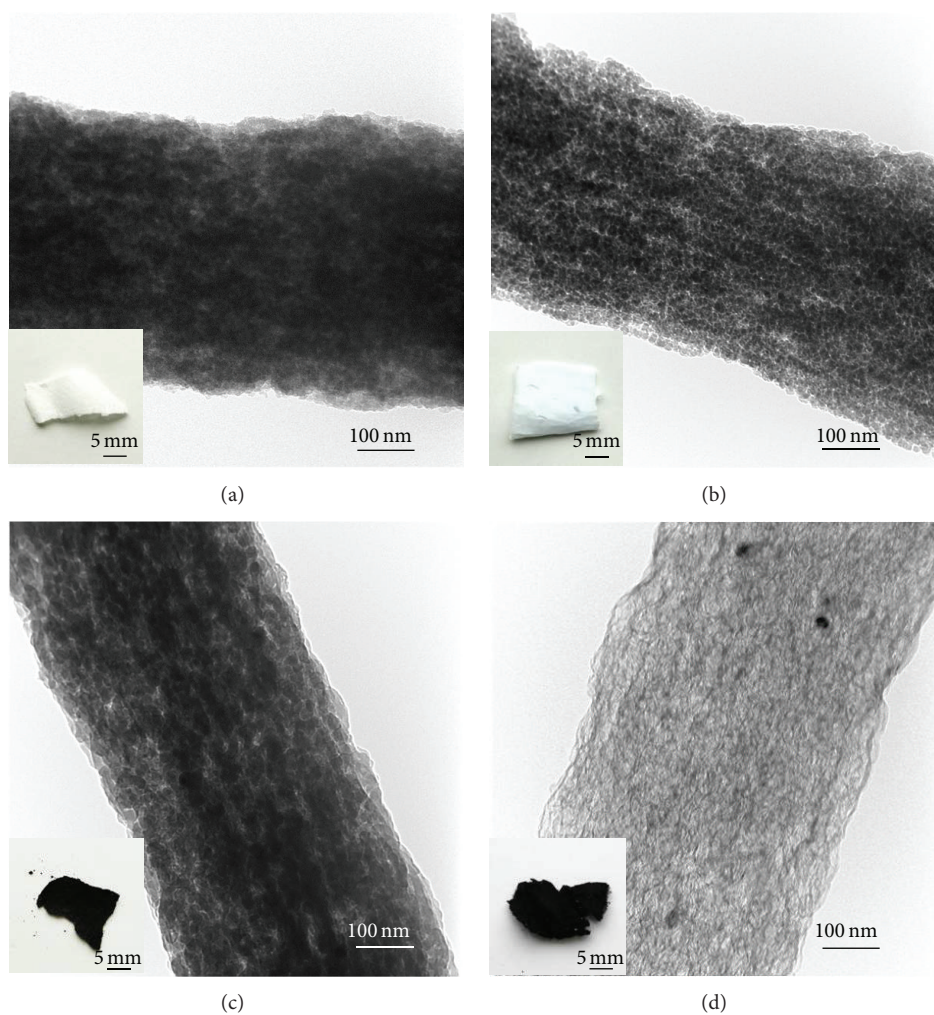


FIGURE 2: Photographs and TEM images of the PVA/ $\text{CoCl}_2$ /silica NP fibers as spun (a), after heat treatment at 500°C for 5 h in air (b), after CVD reaction at 600°C for 24 h (c), and after NaOH treatment at 80°C for 24 h (d).

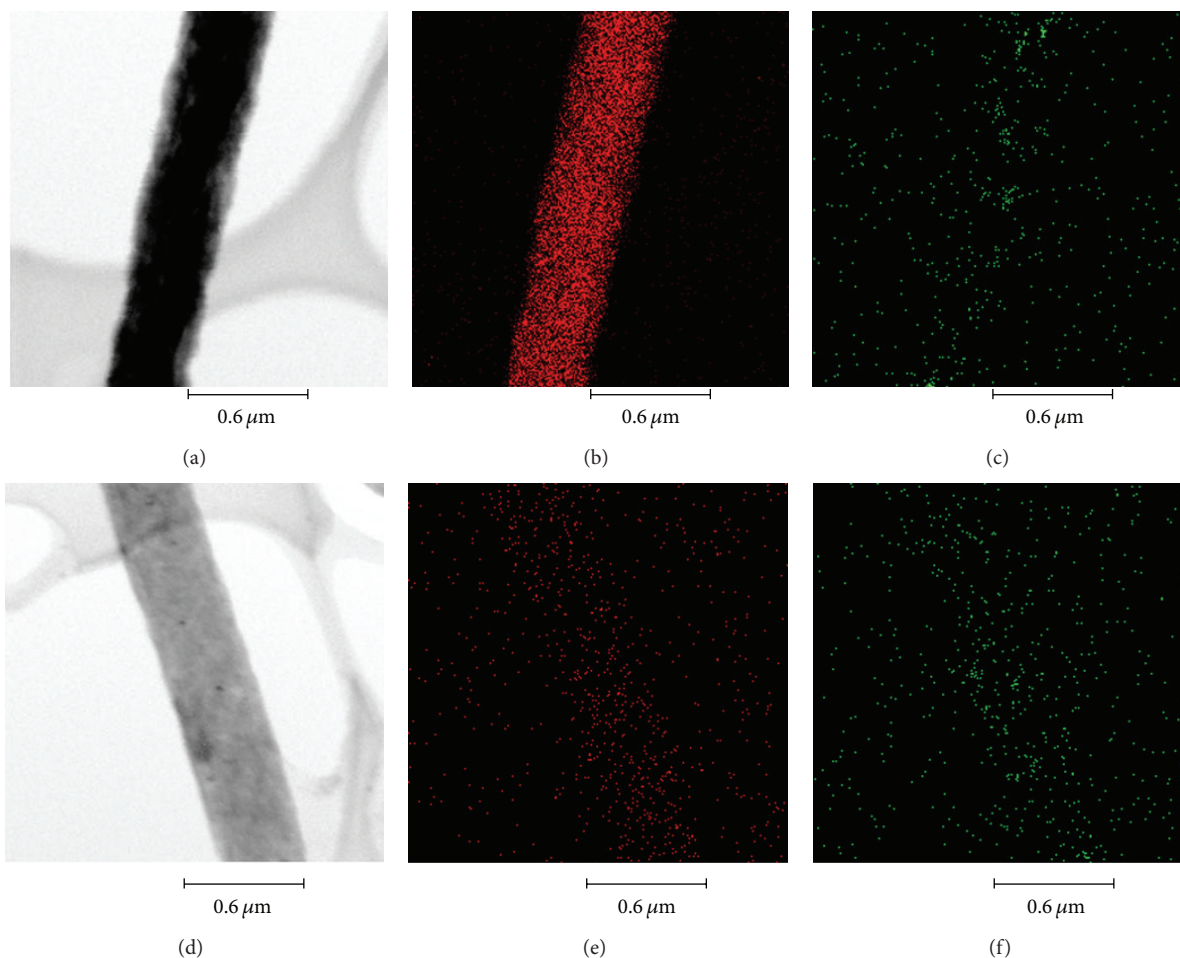


FIGURE 3: STEM images (a and d) and element mapping by EDX spectroscopy of Si (b and e) and Co (c and f) in the fibers before and after NaOH treatment at 80°C for 24 h, respectively.

in Figures 3(a) and 3(b), it was found that after the CVD reaction, the fibers contained a large amount of silica NPs. From an appreciable decrease in the Si signals, the silica NPs were shown to have been substantially removed by the NaOH treatment (Figures 3(b) and 3(e)). As shown in Figures 3(c) and 3(f), conversely, the signals for Co were too weak to detect its location or any difference after the NaOH treatment.

**3.2. Pore Structural Characterization.** The pore structures of the carbon fibers were determined by the nitrogen adsorption/desorption method. The isotherm observed for the fibers after the NaOH treatment had a type-H1 hysteresis loop (Figure 4(a)) [12], which was not observed for the fibers before the treatment, while the capillary condensation occurred at high relative pressures ( $P/P_0 = 0.85\text{--}0.97$ ). Additionally, from the corresponding pore size distributions of the fibers calculated by the BJH method, it was shown that the NaOH treatment increased mainly the quantity of mesopores (2–50 nm) and partially the quantity of macropores (>50 nm) in the fibers (Figure 4(b)). Table 1 summarizes the BET surface area and pore volume distributions of the fibers after the CVD and NaOH treatment. The BET surface area of

the fibers increased approximately 4 times after the NaOH treatment. Notably, the mesopore volume, in particular, greatly increased from 0.26 to 1.33 cm<sup>3</sup>/g through the NaOH treatment. These results indicate that the 15 nm silica NPs loaded into the fibers acted as templates for pores in the resultant fibers. The total pore volume also increased from 0.37 to 1.67 cm<sup>3</sup>/g, which is comparable with that of carbon aerogels [13, 14] and larger than that of carbon nanotubes synthesized by acetylene decomposition on cobalt-supported silica [14]. The highly porous fibrous structure may be useful in applications as catalyst supports and water cleaning, such as oil spill cleanup [10].

**3.3. Effect of CVD Reaction Time on Sheet Resistivity.** The sheet resistivity of the fibers was measured to evaluate the amount of carbon deposition, as influenced by CVD reaction time. As shown in Figure 5, for 15 min reaction, the fibers displayed high resistivity, acting as insulators. By prolonging the reaction time from 15 min to 1 h, the obtained fibers became conductive, with a sheet resistivity of  $477 \pm 66.4 \Omega/\square$ , and further reaction for 5 h lowered the resistivity to  $56.3 \pm 1.47 \Omega/\square$ . Finally, the sheet resistivity of the fibers, after 24 h

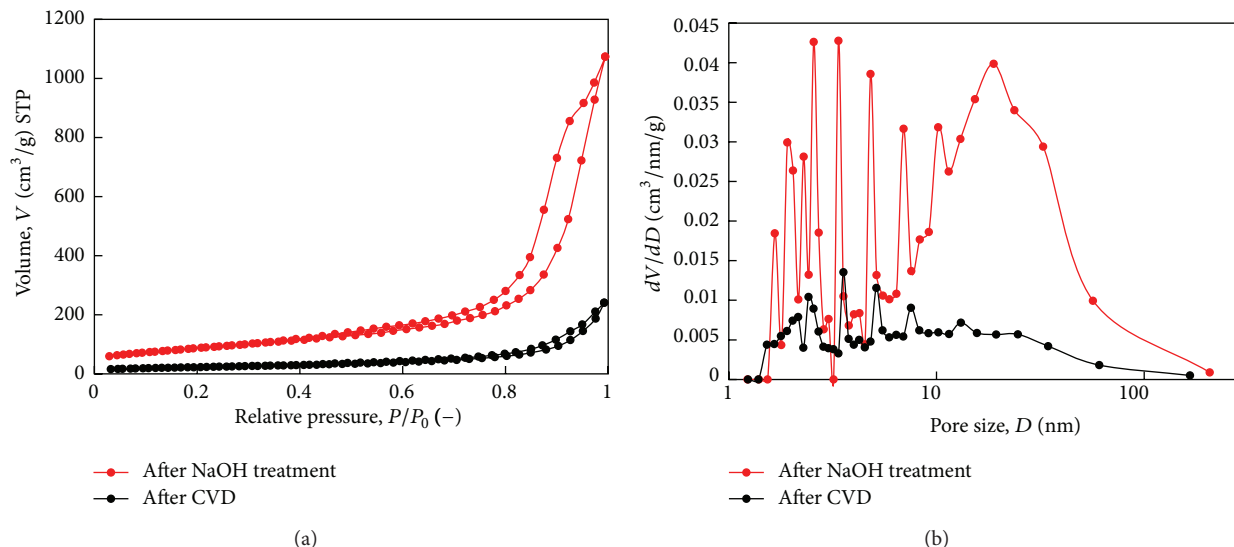


FIGURE 4: Nitrogen adsorption/desorption isotherms (a) and pore size distributions (b) for the fibers after CVD reaction at  $600^\circ\text{C}$  for 24 h and after NaOH treatment at  $80^\circ\text{C}$  for 24 h. STP: standard temperature and pressure (1 atm,  $0^\circ\text{C}$ ).

TABLE 1: Surface area and pore volume distributions of the fibers.

	$S_{\text{BET}}$ ( $\text{m}^2/\text{g}$ )	$V_{\text{micro}}^{\text{a}}$ ( $\text{cm}^3/\text{g}$ )	$V_{\text{meso}}^{\text{b}}$ ( $\text{cm}^3/\text{g}$ )	$V_{\text{macro}}^{\text{c}}$ ( $\text{cm}^3/\text{g}$ )	$V_{\text{total}}$ ( $\text{cm}^3/\text{g}$ )
Fibers after CVD	82	ND	0.26	0.11	0.37
Fibers after NaOH treatment	318	0.02	1.33	0.32	1.67

<sup>a</sup>Volume of micropores (<2 nm). <sup>b</sup>Volume of mesopores (2–50 nm). <sup>c</sup>Volume of macropores (>50 nm). ND: not detectable.

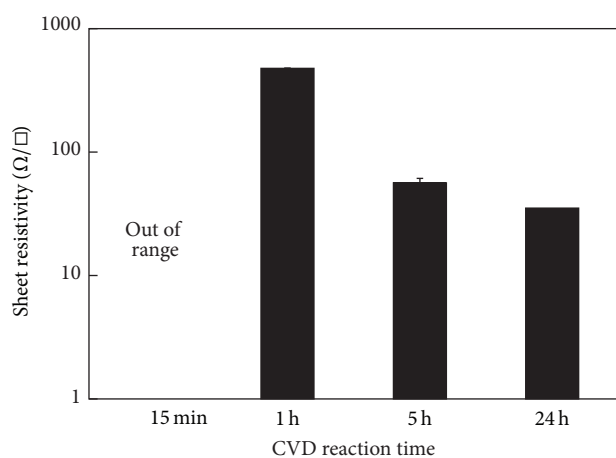


FIGURE 5: Effect of CVD reaction time on sheet resistivity of the fibers after CVD reaction at  $600^\circ\text{C}$  and NaOH treatment at  $80^\circ\text{C}$  for 24 h.

CVD, was  $35.1 \pm 4.82 \Omega/\square$ , which was similar to that of the fibers after 5 h CVD reaction. Considered together with the TEM image of the fibers that had undergone the CVD reaction (Figure 2(c)), these results indicate that 5 h CVD

reaction was sufficient to accumulate carbon deposits in/on the fibers under the conditions examined in the current study. Although these values of sheet resistivity are higher than those of carbonized PAN-based carbon fibers reported in the literature [6], it is difficult to compare sheet resistivity because of differences in material properties such as pore size and porosity. As the preparation process was not fully optimized in the current study, there is a possibility that sheet resistivity can be decreased by tailoring the electrospun fibers and CVD conditions.

**3.4. Raman Spectroscopic Analysis.** Raman spectroscopy is a powerful tool used to evaluate the quality and degree of crystallinity of vapor-grown carbon materials [12]. Figure 6 shows the Raman spectrum of fibers fabricated by the CVD reaction for 24 h and subsequent NaOH treatment. The pair of bands at  $1358$  and  $1581 \text{ cm}^{-1}$ , designating the D and G bands, respectively, are the most diagnostically relevant features. The D/G intensity, which strongly depends on the structure of the carbon, was 1.02 for the prepared fibers. This result indicates that the carbon deposits in/on the fabricated fibers possessed a low degree of crystallinity, although they had a more crystalline nature than charcoal and coke [12].

## 4. Conclusions

Ultrafine carbon fibers with a nanoporous structure were fabricated by a template method using silica NP-containing fibers, electrospun from a PVA-based aqueous solution. Black, conductive fibers were obtained by the CVD reaction under methanol vapor for a minimum of 5 h. TEM observation demonstrated that, after silica removal, the fabricated fibers had a structure originating from the silica NPs. The nitrogen adsorption/desorption method showed that the carbon fibers mainly contained mesopores (2–50 nm) and

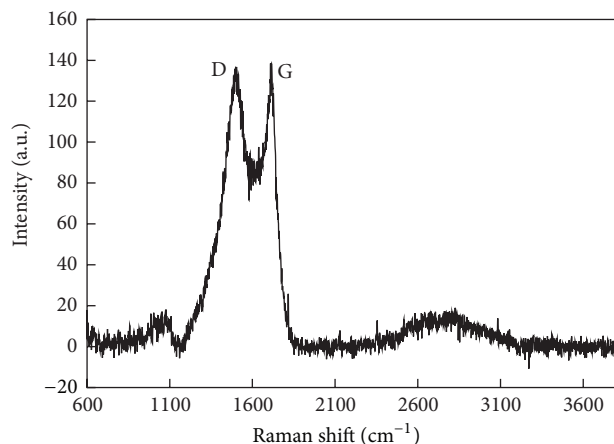


FIGURE 6: Raman spectrum of the fibers after CVD reaction at 600°C for 24 h.

macropores (>50 nm). The total surface area and total pore volume of the fibers after silica removal were 318 m<sup>2</sup>/g and 1.67 cm<sup>3</sup>/g, respectively. EDX analysis equipped with TEM confirmed the removal of silica from the fibers by the NaOH treatment at 80°C. The sheet resistivity of the fabricated fibers was relatively high compared with that reported for PAN-based fibers carbonized at 800°C. Raman spectroscopy showed that the prepared carbon fibers were more crystalline than natural carbonaceous materials.

## Conflict of Interests

The authors declare that there is no conflict of interests regarding the publication of this paper.

## Acknowledgments

The authors express their appreciation to Professor H. Yasuda and Dr. T. Sakata, Research Center for Ultra-High Voltage Electron Microscopy, Osaka University, for kind assistance in TEM experiments. The authors also express their appreciation to Dr. N. Nishiyama and Drs. H. Umakoshi and K. Suga, Graduate School of Engineering Science, Osaka University, for giving the facilities for nitrogen adsorption/desorption isotherm measurements and Raman spectroscopy analysis, respectively. This study was in part supported by the Kansai Research Foundation for Technology Promotion, Japan. One of the authors (Koichi Sawada) is grateful for financial support from a Grant-in-Aid for JSPS Fellows (no. 25.1614).

## References

- [1] F. Rodríguez-Reinoso, "The role of carbon materials in heterogeneous catalysis," *Carbon*, vol. 36, no. 3, pp. 159–175, 1998.
- [2] G. S. Chai, S. B. Yoon, J.-S. Yu, J.-H. Choi, and Y.-E. Sung, "Ordered porous carbons with tunable pore sizes as catalyst supports in direct methanol fuel cell," *Journal of Physical Chemistry B*, vol. 108, no. 22, pp. 7074–7079, 2004.
- [3] S. Sotiropoulou, V. Gavalas, V. Vamvakaki, and N. A. Chaniotakis, "Novel carbon materials in biosensor systems," *Biosensors and Bioelectronics*, vol. 18, no. 2-3, pp. 211–215, 2002.
- [4] C. Lu, Y.-L. Chung, and K.-F. Chang, "Adsorption of trihalomethanes from water with carbon nanotubes," *Water Research*, vol. 39, no. 6, pp. 1183–1189, 2005.
- [5] C. H. Ao and S. C. Lee, "Indoor air purification by photocatalyst TiO<sub>2</sub> immobilized on an activated carbon filter installed in an air cleaner," *Chemical Engineering Science*, vol. 60, no. 1, pp. 103–109, 2005.
- [6] M. Inagaki, Y. Yang, and F. Kang, "Carbon nanofibers prepared via electrospinning," *Advanced Materials*, vol. 24, no. 19, pp. 2547–2566, 2012.
- [7] Y. Yang, A. Centrone, L. Chen, F. Simeon, T. Alan Hatton, and G. C. Rutledge, "Highly porous electrospun polyvinylidene fluoride (PVDF)-based carbon fiber," *Carbon*, vol. 49, no. 11, pp. 3395–3403, 2011.
- [8] N. N. Bui, B. H. Kim, K. S. Yang, M. E. D. Cruz, and J. P. Ferraris, "Activated carbon fibers from electrospinning of polyacrylonitrile/pitch blends," *Carbon*, vol. 47, pp. 2528–2555, 2009.
- [9] C. Kim, Y. I. Jeong, B. T. N. Ngoc et al., "Synthesis and characterization of porous carbon nanofibers with hollow cores through the thermal treatment of electrospun copolymeric nanofiber webs," *Small*, vol. 3, no. 1, pp. 91–95, 2007.
- [10] H. Liu, C. Y. Cao, F. F. Wei et al., "Fabrication of macroporous/mesoporous carbon nanofiber using CaCO<sub>3</sub> nanoparticles as dual purpose template and its application as catalyst support," *The Journal of Physical Chemistry C*, vol. 117, pp. 21426–21432, 2013.
- [11] Z. P. Huang, D. Z. Wang, J. G. Wen, M. Sennett, H. Gibson, and Z. F. Ren, "Effect of nickel, iron and cobalt on growth of aligned carbon nanotubes," *Applied Physics A: Materials Science and Processing*, vol. 74, no. 3, pp. 387–391, 2002.
- [12] D. Zhao, J. Feng, Q. Huo et al., "Triblock copolymer syntheses of mesoporous silica with periodic 50 to 300 angstrom pores," *Science*, vol. 279, no. 5350, pp. 548–552, 1998.
- [13] Y. Hanzawa, H. Hatori, N. Yoshizawa, and Y. Yamada, "Structural changes in carbon aerogels with high temperature treatment," *Carbon*, vol. 40, no. 4, pp. 575–581, 2002.
- [14] E. Frackowiak and F. Béguin, "Carbon materials for the electrochemical storage of energy in capacitors," *Carbon*, vol. 39, no. 6, pp. 937–950, 2001.

## Research Article

# CLSVOF Method to Study the Formation Process of Taylor Cone in Crater-Like Electrospinning of Nanofibers

Yong Liu,<sup>1,2</sup> Jia Li,<sup>2</sup> Yu Tian,<sup>3</sup> Xia Yu,<sup>2</sup> Jian Liu,<sup>4</sup> and Bao-Ming Zhou<sup>1,2</sup>

<sup>1</sup> Key Laboratory of Advanced Textile Composites, Ministry of Education of China, Tianjin Polytechnic University, 399 West Binshui Road, Tianjin 300387, China

<sup>2</sup> School of Textiles, Tianjin Polytechnic University, 399 West Binshui Road, Tianjin 300387, China

<sup>3</sup> School of Science, Tianjin Polytechnic University, 399 West Binshui Road, Tianjin 300387, China

<sup>4</sup> Department of Textiles, Zhejiang Fashion Institute of Technology, No. 495 Fenghua Road, Ningbo, Zhejiang 31521, China

Correspondence should be addressed to Yong Liu; liuyong@tjpu.edu.cn

Received 24 February 2014; Revised 3 May 2014; Accepted 5 May 2014; Published 11 June 2014

Academic Editor: Aihua He

Copyright © 2014 Yong Liu et al. This is an open access article distributed under the Creative Commons Attribution License, which permits unrestricted use, distribution, and reproduction in any medium, provided the original work is properly cited.

The application of two-phase computational fluid dynamics (CFD) for simulating crater-like Taylor cone formation dynamics in a viscous liquid is a challenging task. An interface coupled level set/volume-of-fluid (CLSVOF) method and the governing equations based on Navier-Stokes equations were employed to simulate the crater-like Taylor cone formation process. The computational results of the dynamics of crater-like Taylor cone slowly formed on a free liquid surface produced by a submerged nozzle in a viscous liquid were presented in this paper. Some experiments with different air pressures were carried out to evaluate the simulation results. The results from both CFD and experimental observations were compared and analyzed. The numerical results were consistent with the experimental results. Our study showed that the CLSVOF method gave convincing results, and the computational method is robust to extreme variations in interfacial topology.

## 1. Introduction

Electrospinning is a simple, versatile, and effective approach to fabricate nanofibers from various synthetic and natural polymers [1–5]. To date, various nanofibers produced by electrospinning have been applied successfully in many fields, for example, tissue engineering, biotechnology, environmental engineering, filters, and sensors [6–10].

A traditional and typical electrospinning setup, which has a thin needle as a spinneret, still has some limitations due to the relatively low yield of the nanofibers. Recently, many novel free-liquid electrospinning techniques, such as needleless electrospinning [11], roller electrospinning [12], wire coil electrospinning [13], porous-tube electrospinning [14], and bubble electrospinning [15, 16], have been invented and have the potential to solve the current problem. Crater-like electrospinning, which creates crater-like solution blowup as a Taylor cone, is also a novel electrospinning process developed

on the basis of bubble-electrospinning by our group [17]. This electrospinning process has shown feasibility and potential application for mass production of nanofibers [18].

The crater-like electrospinning system consists of a vertical solution reservoir with a gas tube feeding from the reservoir bottom, like a bubble-electrospinning system described in many literatures [15]. One of the differences between the two electrospinning processes is that the crater-like Taylor cone is continuous, but the bubble Taylor cone is not. As shown in Figure 1, multiple jets were ejected from a bubble or crater-like Taylor cone. The former had a process of breaking and producing a new bubble again, while the latter could maintain stable spinning, which is considered as the main reason of a higher yield of nanofibers in this process.

In previous studies, the effects of different process parameters on the fabrication of nanofibers in crater-like electrospinning have been investigated [19, 20]. Recently, a multiphysics coupled FEM method was tentatively suggested

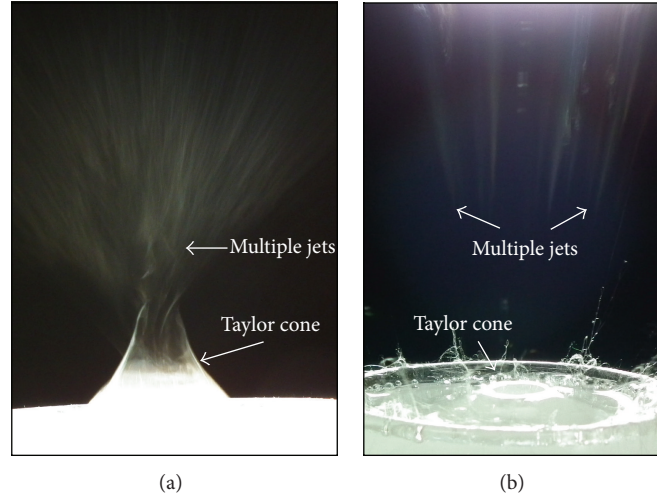


FIGURE 1: Photos of bubble electrospinning (a) and crater-like electrospinning (b).

to simulate the formation of crater-like Taylor Cone [21]. However, there is little literature in which the crater-like solution blowup structure has been studied systematically. The reason might be that the distributed quantities in the fluid field and extreme variations in interfacial topology are difficult to be measured. As a result, the application of two-phase computational fluid dynamics (CFD) for simulating crater-like Taylor cone formation dynamics in a viscous liquid is a challenging task.

In the past decades, various numerical methods have been developed to simulate the two-phase flow problem, such as front tracking method [22], marker particle method [23], VOF method [24], and the level set (LS) method [25]. The VOF method forms a building block of computations involving two fluids separated by a sharp interface. The VOF method satisfies compliance with mass conservation extremely well, but sometimes it is difficult to capture the geometric properties of the complicated interface [26]. The LS method was another interface-capturing method, which was first introduced by Osher and Sethian [25]. This method captures the interface very accurately, but in some cases it may violate mass conservation [26]. To achieve mass conservation as well as capture the interface accurately, the CLSVOF method, in which the LS method was coupled with the VOF method, was identified as a better method [27]. In the CLSVOF method, the LS function is used only to compute the geometric properties at the interface, while the void fraction is calculated using the VOF method. Compared with other methods, CLSVOF method can effectively overcome the calculation errors.

In this paper, we presented an interface coupled level set/volume-of-fluid (CLSVOF) method for investigating the forming process of crater-like Taylor cone in crater-like electrospinning process. According to the numerical results, the formation mechanism and the formation dynamics of the crater-like Taylor cone in a viscous liquid could be understood for deep explanation of the process.

## 2. Computational Methods

**2.1. Governing Equations.** Generally, for two incompressible and immiscible fluids separated by a moving surface, the Navier-Stokes equations were formulated to describe the motion of both fluids. The whole fluid fills a domain, which may be decomposed into any number of subdomains filled with the individual phases. For the interface between domains, some quantities, such as velocities, are required to be continuous, whereas others, such as pressure, are required to have specific jumps [28]. The discontinuities in physical properties such as density, viscosity, and surface tension at the interface can be treated in different ways; accordingly, the governing equations are reformulated into two useful types: whole-domain formulations and jump-condition formulations [28, 29].

**2.1.1. Navier-Stokes Equation: Whole-Domain Formulation.** The whole fluid domain can be divided into several subdomains which are occupied by individual phases. At the interface, the discontinuous physical properties, such as density, viscosity, and surface tension, can be smoothed over a transition region of finite thickness. Thus, the whole flow domain can be described by a single set of momentum and continuity equations within the one-field formulation approach, where different fluid properties are considered in each individual phase. Appropriate stress conditions at the interface between different phases are enforced implicitly. With the assumption that the fluid properties are constant in both phases, the mass and momentum conservation equations for the incompressible Newtonian fluids for the liquid and air phases can be written as

$$\nabla \cdot \vec{V} = 0, \quad (1)$$

$$\rho \left( \frac{\partial \vec{V}}{\partial t} + \nabla \cdot (\vec{V} \vec{V}) \right) = -\nabla P + 2\nabla \cdot \mu \mathbf{s} + \rho \vec{g} + \vec{F}_b, \quad (2)$$

where  $\vec{V}$  is the velocity,  $\rho$  the solution density,  $p$  the pressure,  $\vec{g}$  the acceleration of gravity,  $\vec{F}_b$  the body force,  $\mu$  the dynamic viscosity, and  $s$  the strain rate tensor. There are two physical properties of the bulk phases that may have discontinuities across phase boundaries. The strain rate tensor  $s$  can be given by

$$s = \frac{1}{2} \left[ \left( \nabla \vec{V} \right) + \left( \nabla \vec{V} \right)^T \right]. \quad (3)$$

The effective density  $\rho$  and viscosity  $\mu$  at each grid point can be expressed as

$$\begin{aligned} \rho &= \rho_g (1 - H) + \rho_l H, \\ \mu &= \mu_g (1 - H) + \mu_l H, \end{aligned} \quad (4)$$

where subscripts  $g$  and  $l$  represent gas and liquid, respectively;  $H$  is the Heaviside function to prevent numerical instability arising from steep density gradients [29, 30], defined as

$$H = \begin{cases} 1 & \phi > \varepsilon, \\ 0 & \phi \leq \varepsilon, \\ \frac{1}{2} + \frac{\phi}{2\varepsilon} + \frac{1}{2\pi} \left[ \sin \left( \frac{\pi\phi}{\varepsilon} \right) \right] & |\phi| \leq \varepsilon, \end{cases} \quad (5)$$

where  $\phi$  is the level set function and  $\varepsilon$  is the interface numerical thickness, which we have taken in our simulations as  $1.5\Delta x$  ( $\Delta x$  refers to the size of a mesh cell). By using the smoothed Heaviside function, one effectively assigns the interface a fixed finite thickness of a small parameter of the order  $\varepsilon$ , over which the phase properties are interpolated [26].

Equation (2) can be discretized as [29]

$$\begin{aligned} \rho^n \frac{\vec{V}^{n+1} - \vec{V}^n}{\delta t} &= -\nabla \cdot \left( \vec{V} \vec{V} \right)^n \rho^n - \nabla P^{n+1} \\ &+ \nabla \cdot (2\mu s)^n + \rho^n \vec{g}^n + \vec{F}_b^n, \end{aligned} \quad (6)$$

where the superscripts  $n$  and  $n + 1$  denote the value of the variable at consecutive time steps and  $\delta$  is a delta function concentrated at the interface. In the above equation, the pressure  $P$  is an implicit term. Other physical quantities, such as gravity, surface tension, and viscosity, are well approximated with  $t^n$  values.

### 2.1.2. Navier-Stokes Equation: Jump-Condition Formulation.

The discontinuous quantities, including density, viscosity, and surface tension, at the domain interface are treated in a continuum, where another useful formulation of the momentum-balance equation, jump-condition formulation, can be used.

The jump conditions at the interface include the pressure boundary condition written in tensor form as [29]

$$p_v - p + \sigma \kappa = -2\mu n_k \frac{\partial u_k}{\partial n} \quad (7)$$

for the normal direction, where  $\sigma$  is the surface tension coefficient and  $\kappa$  the curvature of the interface. And the velocity boundary condition is

$$\mu \left( t_i \frac{\partial u_i}{\partial n} + n_k \frac{\partial u_k}{\partial s} \right) = \frac{\partial \sigma}{\partial s} \quad (8)$$

for the tangential direction, where  $\partial/\partial s$  and  $\partial/\partial n$  are the surface and normal derivatives, respectively. For a constant surface tension coefficient, the term on the right-hand side of (8) will be zero.

In the fluid domain, the Navier-Stokes equation can be written as

$$\frac{\partial \vec{V}}{\partial t} \rho + \nabla \cdot \left( \vec{V} \vec{V} \right) \rho = -\nabla p + 2\nabla \cdot \mu s + \rho \vec{g} \quad (9)$$

and the continuity equation remains the same as (1). Equation (9) is then discretized as

$$\frac{\vec{V}^{n+1} - \vec{V}^n}{\delta t} \rho^n = -\nabla \cdot \left( \vec{V} \vec{V} \right)^n \rho^n - \nabla P^{n+1} + \nabla \cdot (2\mu s)^n + \rho^n \vec{g}^n. \quad (10)$$

When proper jump conditions were applied at the interface, (13) could be solved by the same two-step projection method as discussed in [29].

**2.2. Interface Tracking.** The problem in the work is the formation of crater-like solution blowup with large flow distortions and topological changes, for which the Eulerian-based methods are better suited [29]. Two Eulerian-based methods, the volume-of-fluid (VOF) method and the level set (LS) method, have been widely used in this field. The two methods both use phase functions to track the interface implicitly: volume fraction for the VOF method and distance function for the LS method. One of the advantages of the two methods is that they can easily deal with flow problems with large topological changes and interface deformations such as liquid ligament breakup and bubble merging and bursting, which is particularly well suited to this study. However, each method has its own weaknesses. For example, the characteristics of level set determine its flexibility to describe changes in topology and boundary capture, but in the process of solving a serious loss of quality, resulting in decreased accuracy, while VOF lacks accuracy on the normal and curvature calculations. In order to eliminate such weaknesses of the two methods, the coupled level set and volume-of-fluid (CLSVOF) method was employed in this study.

**2.3. CLSVOF Method.** The function of the CLSVOF method is to combine the advantages of the LS method with the VOF method. A flow chart for the CLSVOF algorithm is shown in Figure 2. Generally, the interface is reconstructed from the VOF function and the interface normal vector computed from the LS function. On the basis of the above reconstructed interface, the level set functions are redistanced to achieve mass conservation. By combining the advantages of VOF

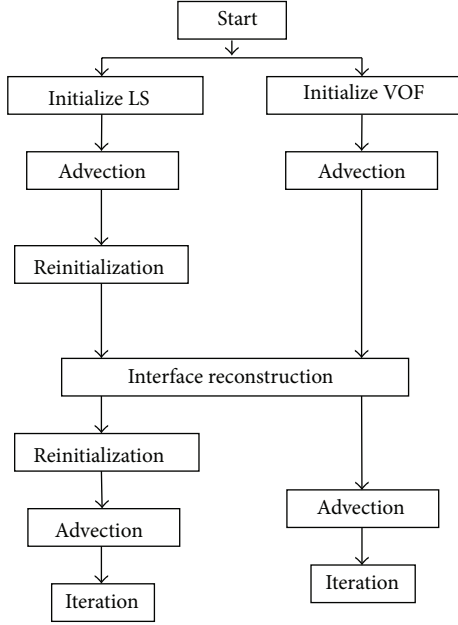


FIGURE 2: A flow-chart of CLSVOF method.

and LS, the CLSVOF method is capable of computing the normal and curvature more accurately while maintaining mass conservation. The coupling of the LS and VOF methods occurs at the interface reconstruction and the redistancing of the level set function.

**2.3.1. Volume-of-Fluid Method.** In the volume-of-fluid method, the interface is tracked by the VOF function, which is defined as the liquid volume fraction in a cell with its value between zero and one in a surface cell and at zero and one in air and liquid, respectively. One has

$$F(\vec{x}, t) = \begin{cases} 1 & \text{in the fluid} \\ 0 < F < 1 & \text{at the interface} \\ 0 & \text{in the void.} \end{cases} \quad (11)$$

An example for the VOF functions representing a delta-shaped region is shown in Figure 3.

In Figure 3, the number in each cell represents the volume fraction occupied by the liquid. The void fraction  $F$  is introduced as the volumetric fraction of the liquid inside a control volume (cell), with the void fraction taking the values 0 for pure gas cell, 1 for pure liquid cell, and between 0 and 1 for a two-phase cell. The VOF functions can be written as

$$\frac{\partial F}{\partial t} + \nabla \cdot (\vec{V}F) = 0. \quad (12)$$

Equation (12) is rewritten in the conservative form:

$$\frac{\partial F}{\partial t} + \nabla \cdot (\vec{V}F) = F(\nabla \cdot \vec{V}). \quad (13)$$

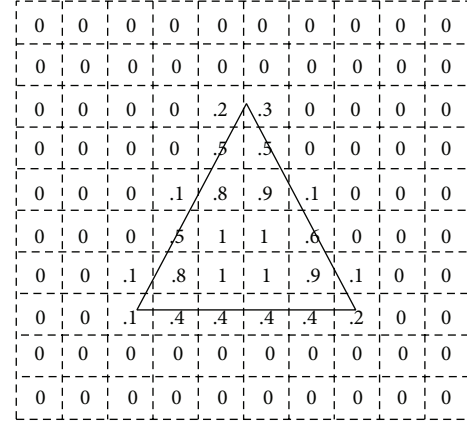
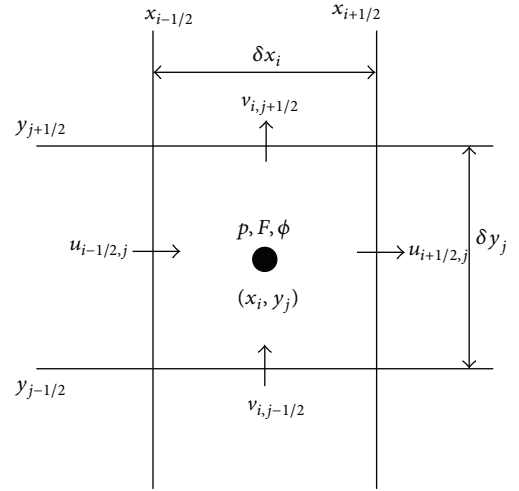


FIGURE 3: A sample VOF data on the mesh representing a triangular interface.

FIGURE 4: Diagram of the discrete variables,  $u$ ,  $p$ ,  $F$ , and  $\phi$ , in relation to the computational cell.

Equation (13) is discretized temporally and decomposed into two fractional steps [29]:

$$\begin{aligned} \frac{\tilde{F} - F^n}{\delta t} + \frac{\partial}{\partial x} (uF^n) &= \tilde{F} \frac{\partial u}{\partial x}, \\ \frac{F^{n+1} - \tilde{F}}{\delta t} + \frac{\partial}{\partial y} (v\tilde{F}) &= F^{n+1} \frac{\partial v}{\partial y}, \end{aligned} \quad (14)$$

where  $\tilde{F}$  is the intermediate VOF function. On the staggered grid, the VOF function,  $F$ , is located at the cell center and velocities,  $u$  and  $v$ , are stored at the cell edges, as shown in Figure 4. In Figure 4, the  $x$ - and  $y$ -velocities are located at the vertical and horizontal cell faces, respectively, and the pressure, the VOF function, and the level set function are stored at the cell centers.

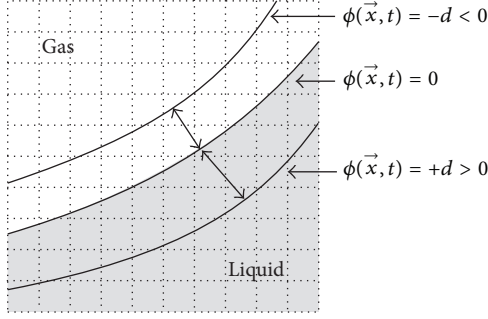


FIGURE 5: Two-phase cells of the LS function.

Discretizing the above equations spatially and integrating over a computational cell  $(i, j)$  yield [29]

$$\begin{aligned} \tilde{F}_{i,j} &= \frac{F_{i,j}^n \delta x_i \delta y_j - \delta t \delta y_j (\text{flux}_{i+(1/2),j} - \text{flux}_{i-(1/2),j})}{\delta x_i \delta y_j - \delta t \delta y_j (u_{i+(1/2),j} - u_{i-(1/2),j})}, \\ F_{i,j}^{n+1} &= \frac{\tilde{F}_{i,j} \delta x_i \delta y_j - \delta t \delta x_i (\text{flux}_{i,j+(1/2)} - \text{flux}_{i,j-(1/2)})}{\delta x_i \delta y_j - \delta t \delta x_i (v_{i,j+(1/2)} - v_{i,j-(1/2)})}, \end{aligned} \quad (15)$$

where  $\text{flux}_{i\pm(1/2),j} = (uF^n)_{i\pm(1/2),j}$  and  $\text{flux}_{i,j\pm(1/2)} = (v\tilde{F})_{i,j\pm(1/2)}$ . They denote VOF fluxes across the edges of the computational cell.

**2.3.2. Level Set Method.** In the LS method, a smooth function  $\phi$  is used to represent a signed distance function whose magnitude equals the shortest distance from the interface. The function  $\phi(\vec{x}, t)$ , at a point with position vector  $\vec{x}$  and at a time instant  $t$ , assumes values as the following:

$$\phi(\vec{x}, t) = \begin{cases} > 0 & \text{in the liquid region} \\ = 0 & \text{at the interface} \\ < 0 & \text{in the gas region.} \end{cases} \quad (16)$$

Liquid regions are regions in which  $\phi(\vec{x}, t) > 0$ , while gas regions are regions in which  $\phi(\vec{x}, t) < 0$ . The interface is implicitly represented by the set of points in which  $\phi(\vec{x}, t) = 0$ . One of the advantages of the LS method is its simplicity, especially when computing the curvature  $\kappa$  of the interface. Typically the level set function  $\phi(\vec{x}, t)$  is maintained as the signed distance to the interface; that is,  $\phi(\vec{x}, t) = -d$  in the gas and  $\phi(\vec{x}, t) = +d$  in the liquid, where  $\phi(\vec{x}, t)$  is the shortest distance from the point  $\vec{x}$  to the interface at time  $t$ . Two-phase cells of the LS function were shown in Figure 5.

The LS function data corresponding to a delta-shaped region are shown in Figure 6. All the LS values are located at the cell center and assigned as the shortest distance to the interface. The LS function is initialized as a distance function because of its important property; namely,  $|\nabla\phi| = 1$ , which can be used to make a number of simplifications.

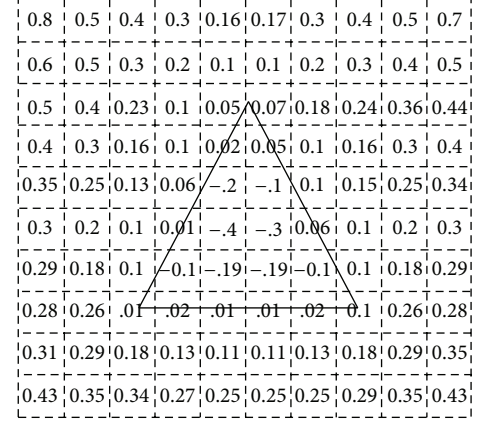


FIGURE 6: Level set function values corresponding to a delta-shaped region over a square grid.

After initialization, the LS function is moved with the flow field according to the following advection equation:

$$\frac{\partial\phi}{\partial t} + (\vec{V} \cdot \nabla)\phi = 0. \quad (17)$$

Since the LS function is smooth and continuous, the discretization of (17) is much more straightforward and some simple advection schemes can be used. However, in order to reduce numerical errors, the level set function must be reinitialized, which can be achieved by obtaining a steady-state solution of the following equation [29]:

$$\frac{\partial\phi}{\partial t} + (\vec{w} \cdot \nabla)\phi = \frac{\phi_0}{\sqrt{\phi_0^2 + h^2}}, \quad (18)$$

where  $\phi_0$  is the LS function of the previous time step,  $t$  the artificial time,  $h$  the grid spacing, and  $\vec{w}$  the propagating velocity normal to the interface with unity magnitude, given by

$$\vec{w} = \frac{\phi_0}{\sqrt{\phi_0^2 + h^2}} \left( \frac{\nabla\phi}{|\nabla\phi|} \right). \quad (19)$$

After the reinitialization process, the level set function will return to a distance function. In order to guarantee mass conservation, the LS functions must be redistance by calculating the distance from the cell center to the reconstructed interface before being used.

**2.3.3. Interface Reconstruction.** There are two purposes of the interface reconstruction: one is to calculate the VOF fluxes across each computational cell with an interface and the other is to redistance the LS function for achieving mass conservation [29]. The interface within each cell is approximated by a straight line segment the orientation of which is given by the normal vector. The properly oriented interface is then located in the cell such that the area (volume) is determined from the VOF function.

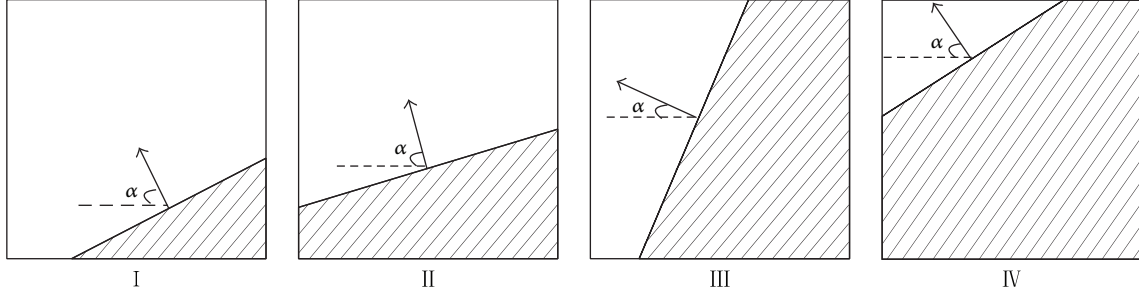


FIGURE 7: Four configurations for the interface reconstruction in computational cell.

In the CLSVOF method, the interface normal vector and the curvature can be calculated using LS function in all two-phase cells given by

$$\begin{aligned}\vec{n} &= \frac{\nabla\phi}{|\nabla\phi|} = \nabla\phi, \\ \kappa &= \nabla \cdot \frac{\nabla\phi}{|\nabla\phi|}.\end{aligned}\quad (20)$$

This is different from the usual discontinuous VOF functions. The orientation angle of the interface is then defined as

$$\alpha = \tan^{-1}\left(\frac{n_y}{n_x}\right) \quad (0 < \alpha \leq 2\pi), \quad (21)$$

where  $\alpha$  is the angle that the outward pointing unit surface normal makes with the positive  $x$ -axis. There are 16 possible cases for the interface shape in the piecewise linear interface construction algorithm. For  $n_x > 0$  and  $n_y > 0$ , the multitude of possible interface configurations is reduced and there exist 4 cases to be considered, as shown in Figure 7. The line segment is moved along the normal direction to fit the shadow area (volume) with the VOF value in the cell.

The dashed area (volume) can be calculated by the following  $n$ -sided area (volume) formula:

$$A_{xy} = \frac{1}{2} \sum_{i=1}^n (x_i y_{i+1} - x_{i+1} y_i), \quad (22)$$

for the two-dimensional case, and

$$V_{rz} = \frac{1}{6} \sum_{i=1}^n (r_i + r_{i+1})(r_i z_{i+1} - r_{i+1} z_i), \quad (23)$$

for the axisymmetric case. Once the calculated area (volume) matches the VOF value at the cell, the coordinates of endpoints of the line segment are determined and the reconstruction of the interface is completed. Then, the fluxes for the VOF advection can be evaluated based on the reconstructed interface [29]. Details of this procedure can be found in [31, 32].

**2.3.4. Reinitialization of the Level Set Function.** At each time step after finding the updated LS function  $\phi^{n+1}$  and the VOF function,  $F^{n+1}$ , the LS function must be reinitialized

to the exact signed normal distance from the reconstructed interface by coupling the LS function to the volume fraction in order to achieve mass conservation. The reinitialization of the LS function includes initial determination of the sign of the LS function and the subsequent calculation of the shortest distance from the cell centers to the reconstructed interface through a geometric process.

For the two-dimensional case, the sign of the LS function,  $S^\phi$ , is given by [33]

$$S^\phi = \text{sign}(F - 0.5), \quad (24)$$

where sign denotes a function that returns the sign of the numeric argument.  $F$  is the VOF function for the two-dimensional case.

Next, the magnitude of the LS function is determined to find the closest point on an interfacial cell to the neighboring cell centers. Generally, there are two cases for all the interfacial cells. One is  $F = 0$  or 1 for single-phase cells, and the other is  $0 < F < 1$  for interfacial cells. As shown in Figure 8(a), if the cell  $(i', j')$  is filled with liquid, the shortest distances are calculated simply by connecting the centers of the neighboring cells to the corners or face centroids of cell  $(i', j')$ . In Figure 8(b), the shortest point on the shadowed area to point A is its projection point onto the line segment within cell  $(i', j')$  rather than the top right corner at all. For a more general case, as shown in Figure 8(b), for points A and B, the nearest distance is from the cell center to the projection point, like point A in Figure 8(b); for points C and D, the nearest point is the endpoint of the segment, and for the other points, the closest points on cell  $(i', j')$  are either corners or face centroids [29]. The details of reinitialization of the LS function followed the algorithm presented by [29, 33].

### 3. Computational Domain and Boundary Conditions

According to the characteristic of crater-like Taylor cone formation, a two-dimensional axisymmetric geometry model was established. Figure 9 illustrates the schematic view of the flow domain used in the two-dimensional simulation. In this case, an 18 wt% polyvinyl alcohol (PVA,  $\overline{M}_w = 30000 \text{ g/mol}$ )/distilled water solution was put into a custom-made quartz circular cylinder chamber with diameter  $D = 40.0 \text{ mm}$  and height  $H = 35 \text{ mm}$ . A gas tube with internal

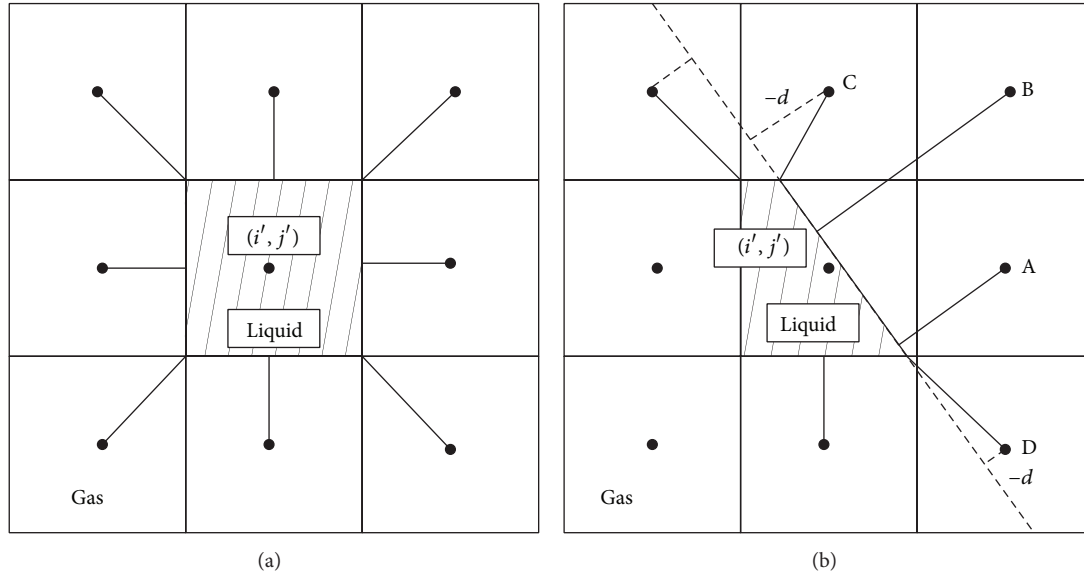


FIGURE 8: Schematic for reinitialization of the LS function.

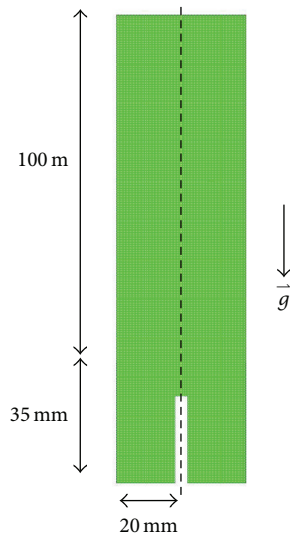


FIGURE 9: Illustration of the experimental zone.

diameter  $d = 2$  mm was mounted in the center bottom of the chamber. The distance was 100 mm between the collecting electrode and the surface of solution. The simulations were performed using the following parameters: the gas is set as the standard values of the air, the mass density of PVA  $\rho = 1100 \text{ Kg/m}^3$ , the viscosity of PVA solution  $\mu = 0.87 \text{ Pa}\cdot\text{S}$ , the surface tension  $\sigma = 0.04 \text{ N/m}$ , and the gas pressure  $P = 4\text{--}50 \text{ KPa}$ . In our experiments, the liquid surface is higher than the jet for 4 mm at the initial state. The pressure on the other free surface is set as 0 Pa. No-slip boundary conditions are used at all walls. The direction of gravity is along the vertical direction as shown in Figure 9.

The pressure-implicit with splitting of operators (PISO) pressure-velocity coupling scheme was used to calculate the transient two-phase fluid flow, and the iterative time step is set to  $10^{-6}$  S to ensure the accurate results of crater formation.

## 4. Results and Discussions

**4.1. The Formation of Crater-Like Taylor Cone.** When the inlet pressure is set as 4 kPa, the transient simulated results of 0–216 ms are shown in Figure 10. At the gas pressure, the simulated shape of Taylor cone was like a bubble. With the increase of the gas pressure, the shape of Taylor cone changed. When the gas pressure was over 10 kPa, the frequency of bubble occurrence decreased. The transient shapes of Taylor cone were much more crater-like blowup. The above simulated results were consistent with the experimental results. In the simulated results, there are many tiny bubbles or drops which might be stretched into the charged jets in the experiments.

**4.2. The Effect of Gas Pressure on the Formation Period of Crater-Like Taylor Cone.** Both our experimental results and numerical simulation results showed that there existed a formation period of crater-like Taylor cone. The simulated results also showed that the crater-like Taylor cone formation period also changed with the increase of gas pressure. In this case, the Taylor cone, which underwent a life-cycle process of growing and bursting, is not steady. When the gas pressure was 4 kPa, there was a big bubble, as Taylor cone, on the solution surface and the life-cycle period of Taylor cone was about 216 ms. When the gas pressure was 10 kPa, the formation period dramatically reduced to about 68 ms. And the occurrence of bubble will be significantly reduced, as shown in Figure 11.

Along with the continued increase of gas pressure, the crater-like Taylor cone formation period decreased.

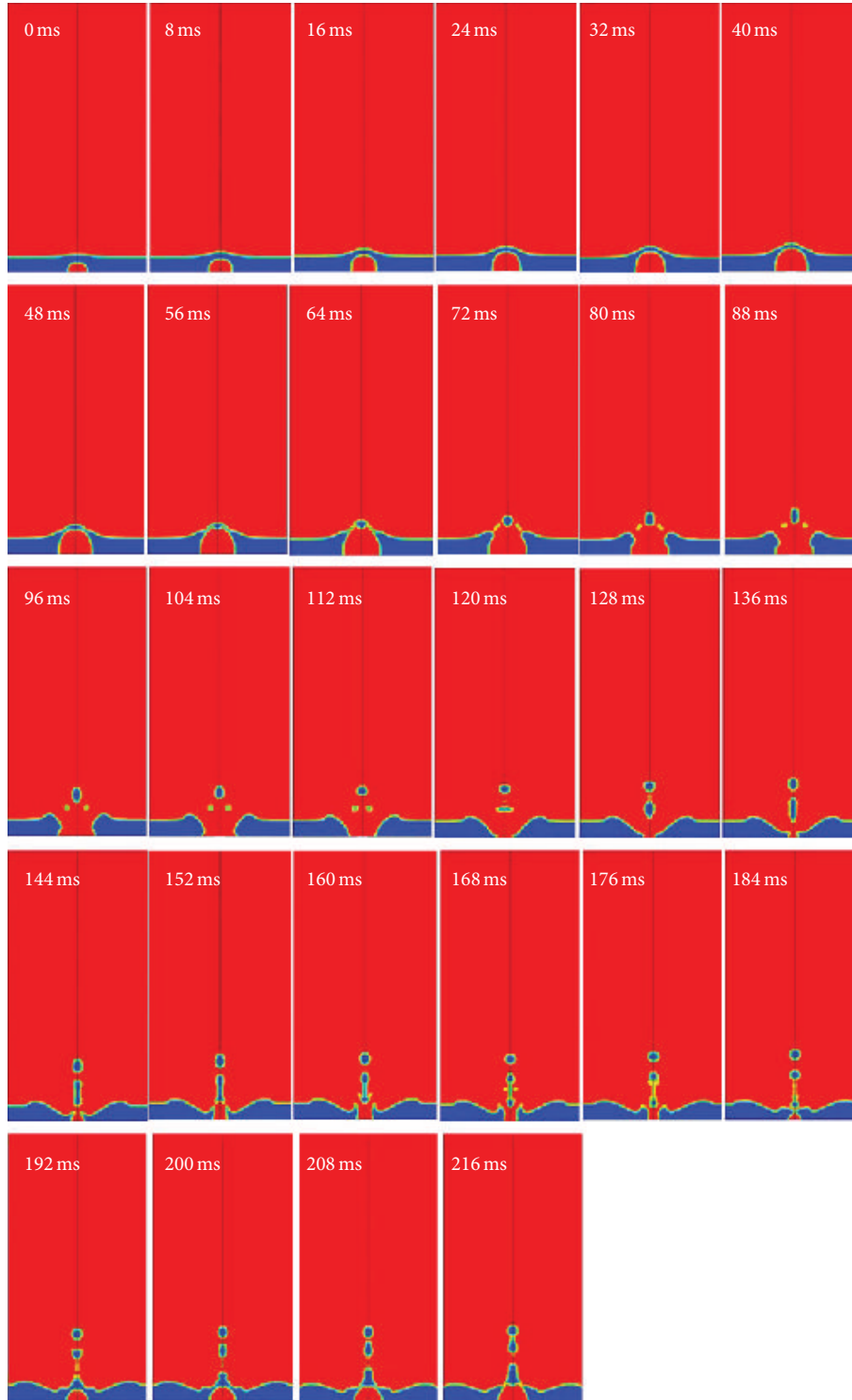


FIGURE 10: The simulated results of crater-like Taylor cone formation at the gas pressure 4 kPa.

Additionally, the occurrence of bubble also decreased with increasing gas pressure. For example, the simulated results of 25 kPa were shown in Figure 12. The life-cycle period of crater-like Taylor cone formation was 52 ms and bubble did not appear during the period, which showed that the crater-like Taylor cone formed completely. When the air

pressure reached 16, 35, and 50 kPa, the formation periods obtained from the simulated results were 56, 40, and 28 ms, respectively.

The reason for the decrease of the formation period might be that there was more amount of gas passed through the solution at the same period of time that the gas pressure

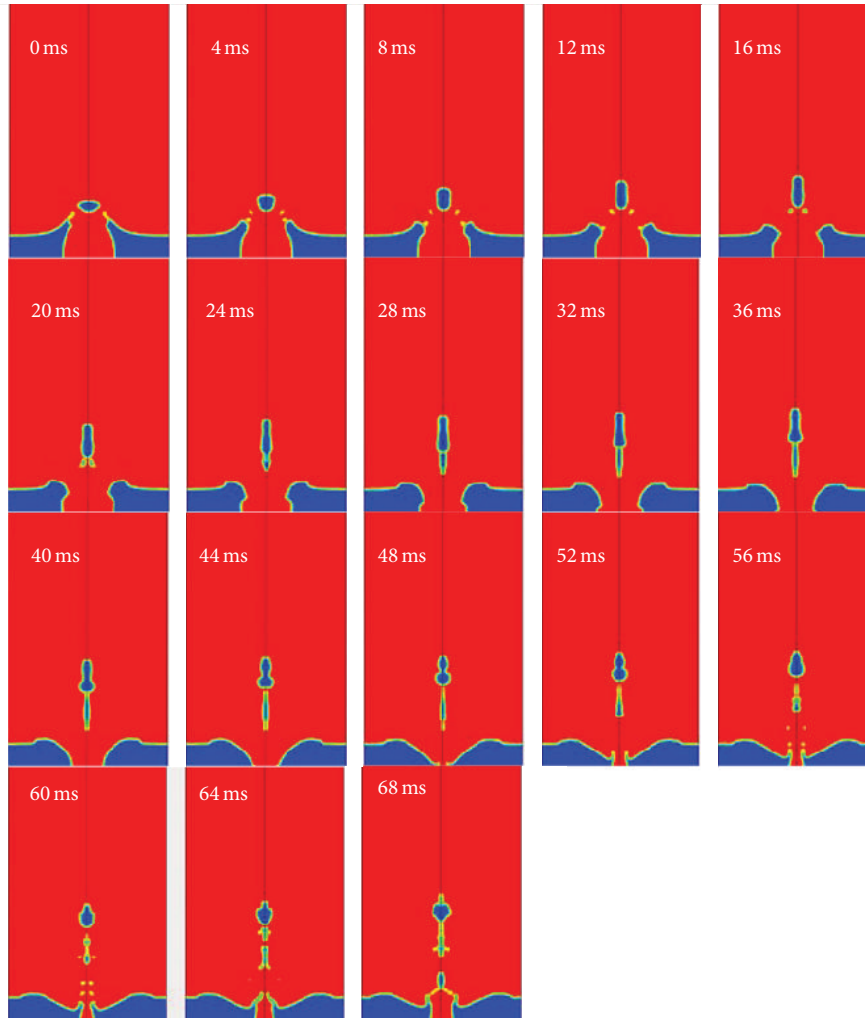


FIGURE 11: The simulated results of crater-like Taylor cone formation at the gas pressure 10 kPa.

was increased. The experimental results agree well with the simulated results, as shown in Figure 13, which indicates that the numerical model is validated to study the formation of crater-like Taylor cone.

**4.3. The Effect of Gas Pressure on the Height of Crater-Like Taylor Cone.** Besides the life-cycle period, the effect of gas pressure on the height of crater-like Taylor cone was also studied. Here the height of crater-like Taylor cone represents the maximum height from the solution surface to the tip of the blowup. The solution's depth between the solution surface and the tip of gas tube was kept constant, and the applied voltage was 0 kV. The simulations were performed at different gas pressures. According to the simulated results, the height of crater-like Taylor cone increased with the increase of gas pressure, which agreed well with the experimental results. However, the relationship between the gas pressure and the height of Taylor cone did not remain constant along the increase of gas pressure. When the gas pressure was over 30 kPa, the growth rate of height has decreased or stopped, as shown in Figure 14.

**4.4. The Effect of Solution Depth on the Height of Crater-Like Taylor Cone.** In the process of crater-like Taylor cone electrospinning, the solution depth between the solution surface and the tip of gas tube is another important factor that affects the height of Taylor cone. According to our previous experiments, the morphologies of nanofibers can also be influenced by the solution depth. In order to further verify the validation of the numerical method, the height of crater-like Taylor cone was calculated at different gas pressure. In our simulations, the inlet pressure was fixed at 25 kPa and the applied voltage 0 kV. The numerical results showed that the height of crater-like Taylor cone decreased with the increase of solution depth, which is in keeping with the experimental results, as shown in Figure 15. The reason for this might be that the higher the solution depth, the greater the weight of the overlying fluid, which requires more gas pressure to form the crater-like Taylor cone.

## 5. Conclusion

In this paper we suggested a numerical approach, CLSVOF method, to numerically simulate the formation of crater-like

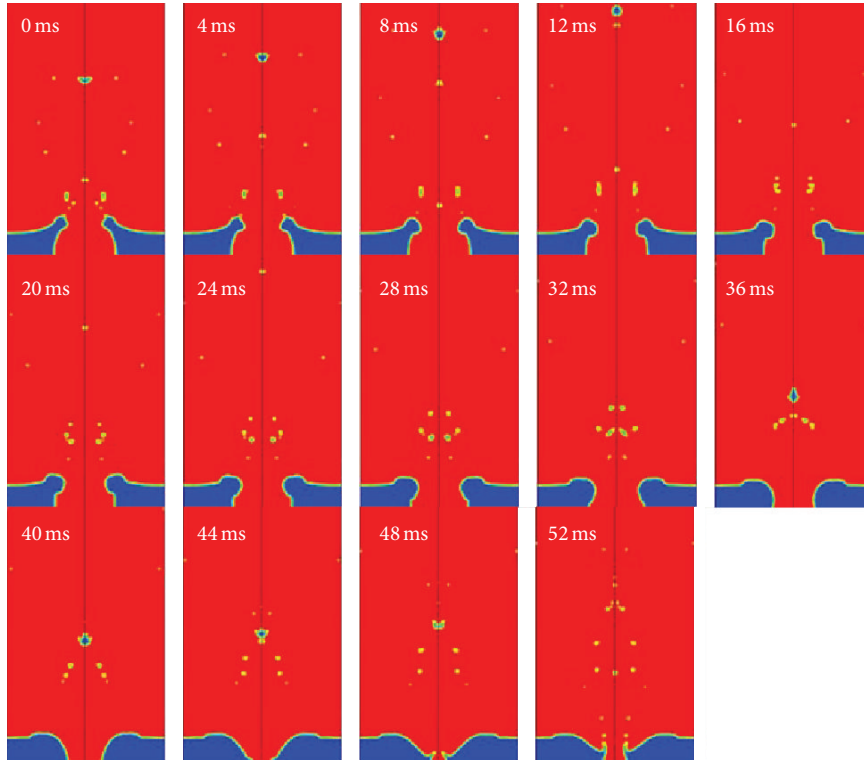


FIGURE 12: The formation of crater while the inlet pressure is 25 kPa.

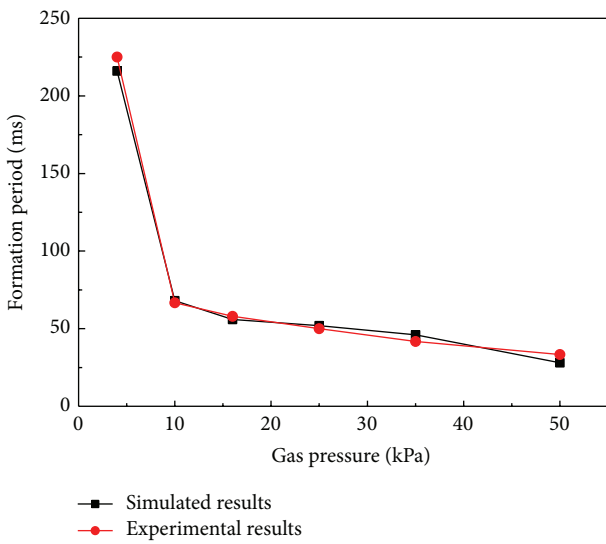


FIGURE 13: The relationship between gas pressure and the formation period.

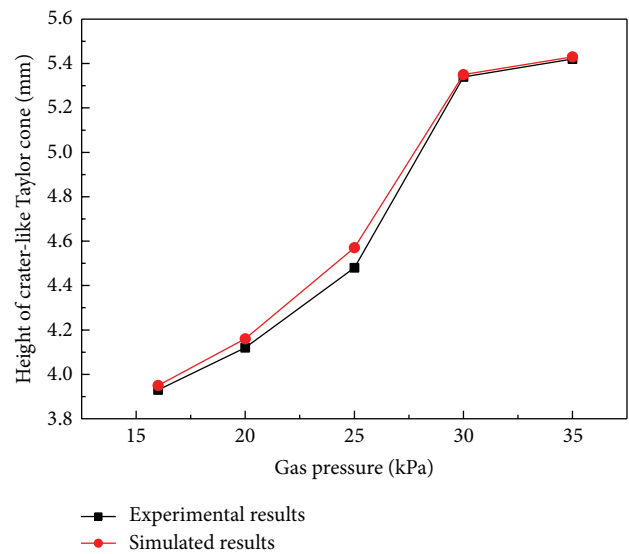


FIGURE 14: The effect of gas pressure on the height of crater-like Taylor cone.

Taylor cone electrospinning process. Numerical simulation was performed for two-dimensional uncompressed flow in axisymmetric coordinates. The numerical results showed that the formation period of crater-like Taylor cone decreased with the increasing gas pressure. The height of crater-like Taylor cone increased with the increase of gas pressure,

but the height decreased as the solution depth increased. The numerical results are consistent with the experimental results. The numerical method could be helpful to understand the mechanism of electrospinning process and improve the production rate of nanofibers.

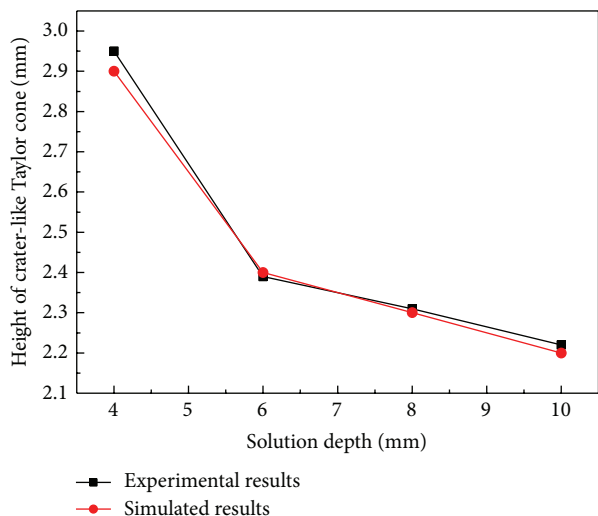


FIGURE 15: The effect of solution depth on the height of crater-like Taylor cone.

## Conflict of Interests

The authors declare that there is no conflict of interests regarding the publication of this paper.

## Acknowledgments

The present work is supported by National Natural Science Foundation of China under Grant no. 51003073, Foundation for the Author of National Excellent Doctoral Dissertation of China (no. 201255), Program for New Century Excellent Talents in University (NCET-12-1063), National Science Foundation of Tianjin (no. 14JCYBJC17600), Ningbo Natural Science Foundation (no. 2013A610016), and Foundation for Training Program of Young and Middle-Aged Innovative Talents in Higher Education of Tianjin, China. The third author, Dr. Yu Tian, is responsible for the computational methods.

## References

- [1] H. Nie, A. He, W. Wu et al., "Effect of poly(ethylene oxide) with different molecular weights on the electrospinnability of sodium alginate," *Polymer*, vol. 50, no. 20, pp. 4926–4934, 2009.
- [2] K. Liu, C. D. Ertley, and D. H. Reneker, "Interpretation and use of glints from an electrospinning jet of polymer solutions," *Polymer*, vol. 53, no. 19, pp. 4241–4253, 2012.
- [3] X. Wang, B. Ding, and B. Li, "Biomimetic electrospun nanofibrous structures of electrospun nanofibers for tissue engineering," *Materials Today*, vol. 16, no. 6, pp. 229–241, 2013.
- [4] J. H. He, Y. Liu, L. F. Mo, Y. Q. Wan, and L. Xu, *Electrospun Nanofibres and Their Applications*, Smithers Rapra Technology, Shropshire, UK, 2008.
- [5] Y. Liu, J.-H. He, J.-Y. Yu, and H.-M. Zeng, "Controlling numbers and sizes of beads in electrospun nanofibers," *Polymer International*, vol. 57, no. 4, pp. 632–636, 2008.
- [6] H. Nie, J. Li, A. He, S. Xu, Q. Jiang, and C. C. Han, "Carrier system of chemical drugs and isotope from gelatin electrospun nanofibrous membranes," *Biomacromolecules*, vol. 11, no. 8, pp. 2190–2194, 2010.
- [7] Y. Si, X. Tang, J. Ge et al., "In-situ synthesis of flexible magnetic  $\gamma$ -Fe<sub>2</sub>O<sub>3</sub>@SiO<sub>2</sub> nanofibrous membranes," *Nanoscale*, vol. 6, no. 4, pp. 2102–2105, 2014.
- [8] Y. Si, X. Wang, Y. Li et al., "Label-free colorimetric detection of mercury (II) in aqueous media using hierarchical nanostructured conjugated polymers," *Journal of Materials Chemistry A*, vol. 2, no. 3, pp. 645–652, 2014.
- [9] R. Wang, S. Guan, A. Sato et al., "Nanofibrous microfiltration membranes capable of removing bacteria, viruses and heavy metal ions," *Journal of Membrane Science*, vol. 446, no. 1, pp. 376–382, 2013.
- [10] Y. Liu, R. Wang, H. Ma, B. S. Hsiao, and B. Chu, "High-flux microfiltration filters based on electrospun polyvinylalcohol nanofibrous membranes," *Polymer*, vol. 54, no. 2, pp. 548–556, 2013.
- [11] A. L. Yarin and E. Zussman, "Upward needleless electrospinning of multiple nanofibers," *Polymer*, vol. 45, no. 9, pp. 2977–2980, 2004.
- [12] F. Cengiz-Çallioğlu, O. Jirsak, and M. Dayik, "Investigation into the relationships between independent and dependent parameters in roller electrospinning of polyurethane," *Textile Research Journal*, vol. 83, no. 7, pp. 718–729, 2013.
- [13] X. Wang, H. Niu, X. Wang, and T. Lin, "Needleless electrospinning of uniform nanofibers using spiral coil spinnerets," *Journal of Nanomaterials*, vol. 2012, Article ID 785920, 9 pages, 2012.
- [14] J. S. Varabhas, G. G. Chase, and D. H. Reneker, "Electrospun nanofibers from a porous hollow tube," *Polymer*, vol. 49, no. 19, pp. 4226–4229, 2008.
- [15] Y. Liu and J.-H. He, "Bubble electrospinning for mass production of nanofibers," *International Journal of Nonlinear Sciences and Numerical Simulation*, vol. 8, no. 3, pp. 393–396, 2007.
- [16] Y. Liu, L. Dong, J. Fan, R. Wang, and J.-Y. Yu, "Effect of applied voltage on diameter and morphology of ultrafine fibers in bubble electrospinning," *Journal of Applied Polymer Science*, vol. 120, no. 1, pp. 592–598, 2011.
- [17] Y. Liu, W. Liang, W. Shou, Y. Su, and R. Wang, "Effect of temperature on the crater-like electrospinning process," *Heat Transfer Research*, vol. 44, no. 5, pp. 447–454, 2013.
- [18] Y.-Y. Wang, Y. Liu, W. Liang, M. Ma, and R. Wang, "Fabrication of nanofibers via Crater-like electrospinning," *Advanced Materials Research*, vol. 332–334, pp. 1257–1260, 2011.
- [19] Y. Liu, Y.-Y. Wang, W.-M. Kang, R. Wang, and B.-W. Cheng, "Crater-like electrospinning of PVA nanofibers, part 1, effect of processing parameters on the morphology of nanofibers," *Advanced Science Letters*, vol. 10, pp. 624–627, 2012.
- [20] Y. Liu, Y.-Y. Wang, W.-M. Kang, R. Wang, and B.-W. Cheng, "Crater-like electrospinning of PVA nanofibers, part 2, minimizing the diameter of nanofibers using response surface methodology," *Advanced Science Letters*, vol. 10, pp. 593–596, 2012.
- [21] Y. Liu, J. Li, Y. Tian, J. Liu, and J. Fan, "Multi-physics coupled FEM method to simulate the formation of Crater-like Taylor cone in electrospinning of nanofibers," *Journal of Nano Research*, vol. 27, pp. 153–162, 2014.
- [22] G. Tryggvason, B. Bunner, A. Esmaeeli et al., "A front-tracking method for the computations of multiphase flow," *Journal of Computational Physics*, vol. 169, no. 2, pp. 708–759, 2001.
- [23] J. E. Welch, F. H. Harlow, J. P. Shannon, and B. J. Daly, "The MAC Method: a computing technique for solving viscous incompressible transient fluid flow problems involving free surfaces,"

- Los Alamos Scientific Laboratory Report, Los Alamos, NM, USA, 1966.
- [24] C. W. Hirt and B. D. Nichols, "Volume of fluid (VOF) method for the dynamics of free boundaries," *Journal of Computational Physics*, vol. 39, no. 1, pp. 201–225, 1981.
- [25] S. Osher and J. A. Sethian, "Fronts propagating with curvature-dependent speed: algorithms based on Hamilton-Jacobi formulations," *Journal of Computational Physics*, vol. 79, no. 1, pp. 12–49, 1988.
- [26] B. Ray, G. Biswas, A. Sharma, and S. W. J. Welch, "CLSVOF method to study consecutive drop impact on liquid pool," *International Journal of Numerical Methods for Heat and Fluid Flow*, vol. 23, no. 1, pp. 143–158, 2013.
- [27] D. L. Sun and W. Q. Tao, "A coupled volume-of-fluid and level set (VOSET) method for computing incompressible two-phase flows," *International Journal of Heat and Mass Transfer*, vol. 53, no. 4, pp. 645–655, 2010.
- [28] R. Scardovelli and S. Zaleski, "Direct numerical simulation of free-surface and interfacial flow," *Annual Review of Fluid Mechanics*, vol. 31, pp. 567–603, 1999.
- [29] Z. Wang, *Numerical study on capillarity- dominant free surface and interfacial flows [Ph.D. thesis]*, The University of Texas, Arlington, Va, USA, 2006.
- [30] M. Sussman, P. Smereka, and S. Osher, "A level set approach for computing solutions to incompressible two-phase flow," *Journal of Computational Physics*, vol. 114, no. 1, pp. 146–159, 1994.
- [31] G. Son, "Efficient implementation of a coupled level-set and volume-of-fluid method for three-dimensional incompressible two-phase flows," *Numerical Heat Transfer, B: Fundamentals*, vol. 43, no. 6, pp. 549–565, 2003.
- [32] M. Sussman and E. G. Puckett, "A coupled level set and volume-of-fluid method for computing 3D and axisymmetric incompressible two-phase flows," *Journal of Computational Physics*, vol. 162, no. 2, pp. 301–337, 2000.
- [33] G. Son and N. Hur, "A coupled level set and volume-of-fluid method for the buoyancy-driven motion of fluid particles," *Numerical Heat Transfer, B: Fundamentals*, vol. 42, no. 6, pp. 523–542, 2002.

## Research Article

# Electrohydrodynamic Direct-Write Orderly Micro/Nanofibrous Structure on Flexible Insulating Substrate

Jiang-Yi Zheng, Hai-Yan Liu, Xiang Wang, Yang Zhao, Wei-Wei Huang, Gao-Feng Zheng, and Dao-Heng Sun

*Department of Mechanical and Electrical Engineering, Xiamen University, Xiamen 361005, China*

Correspondence should be addressed to Gao-Feng Zheng; 65404580@qq.com

Received 13 February 2014; Revised 5 May 2014; Accepted 5 May 2014; Published 26 May 2014

Academic Editor: Huarong Nie

Copyright © 2014 Jiang-Yi Zheng et al. This is an open access article distributed under the Creative Commons Attribution License, which permits unrestricted use, distribution, and reproduction in any medium, provided the original work is properly cited.

AC pulse-modulated electrohydrodynamic direct-writing (EDW) was utilized to direct-write orderly micro/nanofibrous structure on the flexible insulating polyethylene terephthalate (PET) substrate. During the EDW process, AC electrical field induced charges to reciprocate along the jet and decreased the charge repulsive force that applied on charged jet. Thanks to the smaller charge repulsive force, stable straight jet can be built up to direct-write orderly micro/nanofibrous structures on the insulating substrate. The minimum motion velocity required to direct-write straight line fibrous structure on insulating PET substrate was 700 mm/s. Moreover, the influences of AC voltage amplitude, frequency, and duty cycle ratio on the line width of fibrous structures were investigated. This work proposes a novel solution to overcome the inherent charge repulsion emerging on the insulating substrate, and promotes the application of EDW technology on the flexible electronics.

## 1. Introduction

With the unique advantages, flexible electronics attracts significant interest from all over the world and has wide application prospects in the fields of information, energy, health, microsensors, and national defense [1–3]. To date, the functional patterns on flexible electronics can be deposited by sputter coating [4], inkjet printing [5], and airbrush spraying [6]. Thanks to features of low cost, low waste, noncontact, and good materials compatibility, inkjet printing has been regarded as one of the most effective technologies to realize the large-scale manufacturing of flexible electronic devices without stencil plate and etching process [7, 8].

Electrohydrodynamic direct-write (EDW) technique is a novel inkjet technology based on the principle of near-field electrospinning (NFES) [9], in which the stable straight charged jet is used to fabricate orderly micro/nanostructure. EDW used electrical field to drive charged jet injection from the tip of Taylor cone below the spinneret, and the diameter of charged jet is significantly smaller than the inner diameter of the spinneret. At present, EDW technology has displayed great application potential in many fields. Chang et al.

[10] direct-write straight PVDF nanofiber with diameter of 500 nm~6.5  $\mu$ m to fabricate high energy polymeric nanogenerator. Wang et al. [11] direct-write ZnO nanofibers to fabricate field-effect transistor. Kim et al. [12] used EDW to fabricate TiO<sub>2</sub> nanofibers as ultrasensitive chemiresistors.

However, there are still some problems that prevent EDW technique for industrial applications. A critical one is that EDW on insulating substrate, especially flexible polymer substrate such as polyethylene terephthalate (PET) and polyimide (PI), is still a challenge. DC electrical field is used as the energy source to stretch viscoelastic solution in commonly during EDW process, by which charged jet can be ejected from the tip of Taylor cone [13]. Liquid jet also carried away the charge from the spinneret. As the liquid jet is deposited on the collector, charges are also transferred to collector. The charges accumulated on collector surface change the electrical field distribution and provide Coulomb repulsive force on the following jet. Owing to the short distance between spinneret and collector, Coulomb repulsive force from accumulated charges plays a key role in the deposition behaviors of EDW jet [14]. The polymer substrate, for example, PET substrate, has low conductivity and large charge

relaxation time. The accumulated charges on PET substrate require longer relaxation time to leak from polymer substrate to ground. On the other hand, polymer substrate would be polarized by the electrical field and would provide an excess of repulsive force on the following charged jet. The large Coulomb repulsive force blocks the stable ejection and pattern deposition of EDW charged jet on polymer substrate. Polymer thin film is one of the multipurpose flexible base-ments for flexible electronics. At present, direct-writing of orderly micro/nanostructures on flexible polymer substrate have become the key for the application research of EDW technology.

Alternating electrical field changes the charge transfer characteristics in the charged liquid jet and provides a good way to reduce the interferences from charge repulsion [15, 16]. AC electrical field also induces the charge transfer along the surface of insulate substrate and prevents polarization inside the insulating substrate [17]. Alternating electrical field may be a good method to promote the application of EDW technology on the flexible electronics.

In this paper, AC pulse voltage is introduced to study the deposition behaviors of EDW charged jet on the PET substrate. The effects of AC electrical fields on the rheology and injection process of viscoelastic solution were also investigated. And then, orderly nanofiber can be direct-written on the PET substrate under AC electrical field.

## 2. Experiment Details

The schematic diagram of EDW apparatus was illustrated in Figure 1, where a high AC power source (DW-P503-LACDE, China) and a high DC power source (DW-P403-IAC, China) were used, respectively, to provide electrical field for the ejection of EDW jet. The anode of power source was connected to the stainless nozzle and the cathode was connected to a grounded PET substrate. The grounded PET substrate (the insert in Figure 1(a)) was fixed on a motion platform (Parker Linear Motor, USA), which consisted of an EDW module and a control module. The maximum velocity of linear motor was 5 m/s; the motion track and velocity of collector can be controlled by the host computer. Stainless nozzle (inner diameter was 210  $\mu\text{m}$  and outer diameter was 400  $\mu\text{m}$ ) was used as spinneret and the distance between spinneret and collector was in the range of 2~10 mm. Polymer solution was continuously delivered to the spinneret by a syringe pump (Harvard II Pico Plus, USA) at a flow rate of 50  $\mu\text{L/hr}$ . A CCD camera (Sony SSC-DC80, Japan) and a high speed camera (GX-1, Japan) were used to observe the ejection and deposition process. Polyethylene oxide (PEO,  $M_w = 300,000$  g/mol) solution in a mixed solvent of water and ethanol ( $v : v = 3 : 1$ ) was used as an experimental material. Before the experiments, the PET substrate was cleaned in deionized water and acetone and then dried by a hot air blower.

Figure 1(b) demonstrates the typical waveform of AC pulse voltage applied in the present work. The morphology of patterned micro/nanostructures was examined by using an optical microscope (Mitutoyo, Japan) and a scanning electron microscope (LEO 1530 Gemini, Germany).

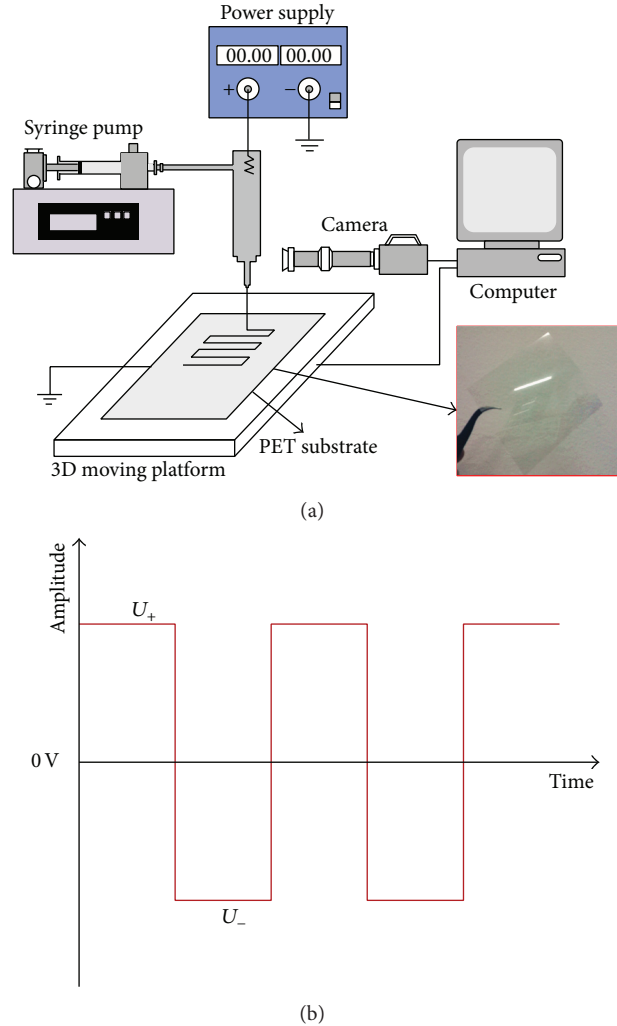


FIGURE 1: (a) The schematic diagram of EDW experimental setup; (b) wave shape of AC pulse voltage.

## 3. Results and Discussion

Firstly, nanofibers deposited on a fixed insulating PET substrate under AC and DC electrical fields were investigated. In these experiments, the concentration of PEO solution  $C$ , the distance between spinneret and insulated substrate  $H$ , and the solution supply rate  $Q$  were 14 wt%, 10 mm, and 50  $\mu\text{L/hr}$ , respectively.

It is difficult to direct-write patterns on insulating substrate, for example, PET substrate, by using EDW with DC electrical field applied. Figure 2(a) shows nanofibers collected on the PET substrate under a constant DC voltage of 4 kV. During EDW process, the liquid jet ejected from Taylor cone under the electrical field force. When the jet is deposited on substrate, charge carried by the liquid would leak through substrate to ground. Owing to the insulating PET substrate and lower charge leakage rate and large charge relaxation time, more charges would accumulate on the substrate and apply Coulomb repulsive force on the following jet. Due to the

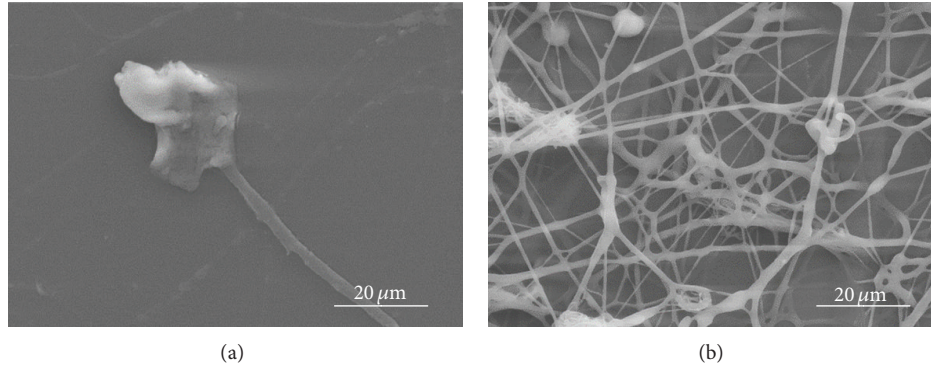


FIGURE 2: Micro/nanostructures deposited on PET insulate substrate under DC and AC electrical fields. (a) Nanofibers deposited on the PET substrate under the DC electrical field, experimental condition:  $U = 4$  kV,  $H = 10$  mm,  $C = 14$  wt%, and  $Q = 50$   $\mu$ L/hr; (b) nanofibers deposited on the PET substrate under the AC electrical field, experimental condition:  $U_- = -4$  kV,  $U_+ = 4$  kV,  $f_{app} = 500$  Hz,  $\rho = 50\%$ ,  $H = 10$  mm,  $C = 14$  wt%, and  $Q = 50$   $\mu$ L/hr.

Coulomb repulsive force, charged jets are repelled from deposition zone below spinneret. Therefore, fewer nanofibers can be deposited on the polymer substrate. By applying AC electrical field, we successfully obtained PEO nanofibers on the PET substrate, as shown in Figure 2(b). The voltage frequency  $f_{app}$ , duty cycle ratio  $\rho$ , negative amplitude  $U_-$ , and positive amplitude  $U_+$  of AC power source were 500 Hz, 50%,  $-4$  kV, and 4 kV, respectively. Contrary to the DC electrical field applied, there were plenty of nanofibers generated on the substrate just below the spinneret. AC electrical field changes the charge transfer characteristics in the charged jet and reduces the Coulomb repulsive force from the residual charges that accumulated on deposited nanofiber and PET substrate. Thus more nanofibers can be collected on PET under AC electrical field. The collection time of EDW nanofibers for each sample shown in Figure 2 was 10 s.

A stable straight jet is beneficial for the direct-writing of orderly micro/nanostructures. Because of the short distance between spinneret and substrate in EDW, the residual charge accumulated on the insulating substrate would play an important role on the motion deposition process of charged jet. In the applied DC electrical field case, the Coulomb repulsion force, which stemmed from the residual charge accumulated on PET substrate, made the jet deviate from the desired straight motion track, as shown in Figure 3(a). The fact that charged jet cannot be deposited on the PET substrate under the DC electrical field hinders the potential applications of EDW technology on flexible electronic manufacturing.

Due to the large Coulomb repulsive force from the insulating substrate, stable jet cannot be built up to direct-write uniform structures. Figure 3(b) shows the “direct-written” micro/nanostructures under DC electrical field. These fibrous structures were randomly oriented on the PET substrate and the diameter had a large distribution range due to the larger repulsive force and unstable stretching. In EDW process, with the short distance between spinneret and collector, the charged jet was repelled by the deposited ones and surpassed the constraint of the jet inner stress.

The alternating of positive and negative voltages would induce charge transferred upward and downward along the

jet, which reduced the Coulomb repulsive force applied on the following jet. With the help of AC electrical field, stable straight jet between spinneret and collector can be generated to direct-write continuous uniform micro/nanofibrous structures. The alternating polarity which stemmed from AC electrical field reduces the inherent instability of electrospinning jet [18, 19] and provides an excellent way to increase the stability of charged jet between the spinneret and insulating substrate. Figure 3(c) shows that the charged jet ejected from the spinneret kept in a straight track without splitting and whipping, under an AC electrical field. The voltage frequency  $f_{app}$ , duty cycle ratio  $\rho$ , negative amplitude  $U_-$ , and positive amplitude  $U_+$  of AC power source used in the experiment were 500 Hz, 50%,  $-2.3$  kV, and 2.3 kV, respectively. The direct-written uniform fibrous structure can be direct-written as spiral pattern along the motion track of collector, as shown in Figure 3(d).

The deposition behaviors of charged jet on the insulating substrate were further investigated. As discussed in previous works, the velocity of substrate  $v_{col}$  was a key factor that defined the deposition and the diameter of direct-written fibrous structures [13, 20]. As shown in Figure 4, when motion velocity of substrate  $v_{col}$  increased from 50 mm/s to 1500 mm/s, the deposition pattern of direct-written fibrous structure changed from waved shape to straight line structure. The negative amplitude  $U_-$  and positive amplitude  $U_+$  of AC power source were  $-4$  kV and 4 kV, respectively. The motion track and velocity of collector were controlled by the host computer and the distance between parallel lines in the direct-written pattern was 70  $\mu$ m. When motion velocity of substrate  $v_{col}$  was larger than 700 mm/s, the whipping of charged jet can be overcome by the stretching force that stemmed from motion substrate. Due to the Coulomb repulsive force, the minimum motion velocity required to direct-write straight line fibrous structure on insulating PET substrate was larger than that on conductive or semiconductive substrate [21].

To obtain stable charged jet in EDW, proper parameters of AC electrical field including the voltage amplitude, voltage frequency, and duty cycle ratio were required and the effect

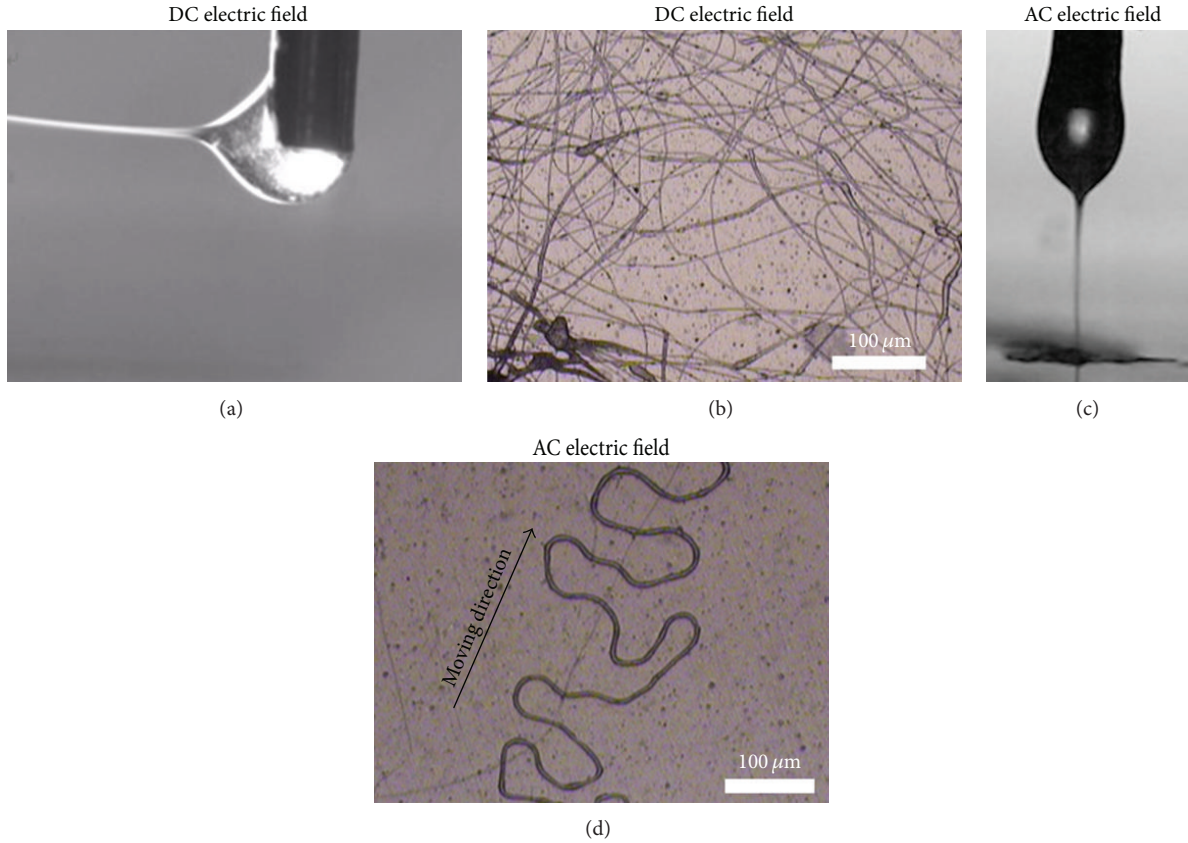


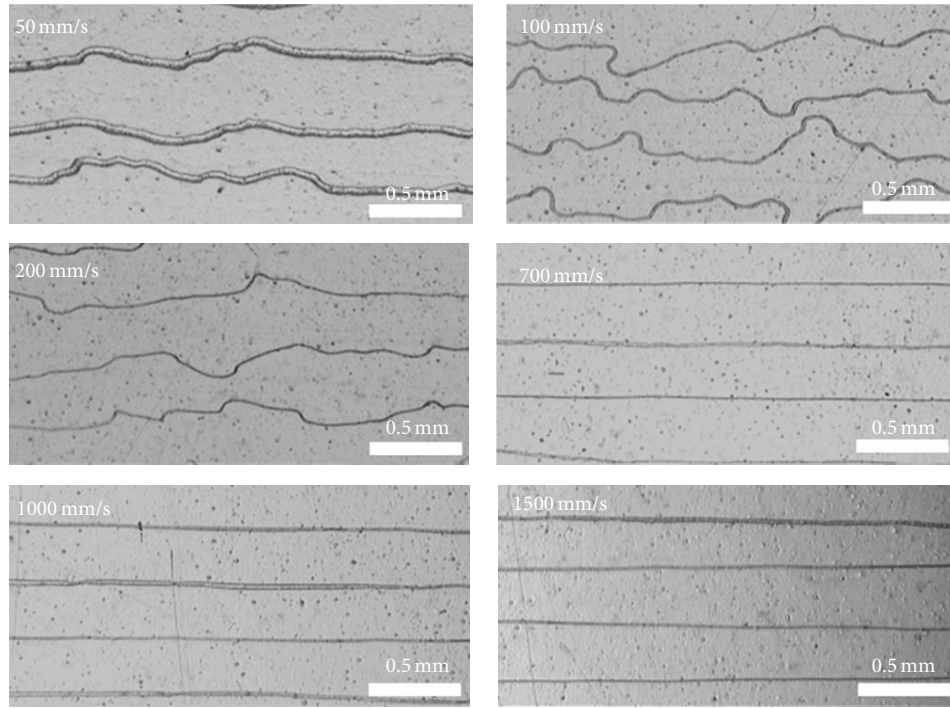
FIGURE 3: (a) Charged jet deviates from the straight motion track under DC electrical field; (b) nonuniform fibrous structure deposited on insulating PET substrate under DC electrical field. Experimental condition:  $U = 3$  kV,  $H = 2$  mm,  $Q = 50$   $\mu$ L/hr, and  $C = 14$  wt%; (c) stable straight jet under AC electrical field on the insulating substrate; (d) uniform fibrous structure direct-written on insulating PET substrate. Experimental condition:  $C = 14$  wt%,  $U_- = -2.3$  kV,  $U_+ = 2.3$  kV,  $f_{app} = 500$  Hz,  $\rho = 50\%$ ,  $H = 2$  mm,  $Q = 50$   $\mu$ L/hr, and  $v_{col} = 5$  mm/s.

of these parameters was also investigated further. To study the effect of AC voltage on the EDW patterns, we fixed the positive amplitude  $U_+$  at 3 kV and performed various negative amplitudes while the other parameters were set as  $v_{col} = 20$  mm/s,  $H = 2$  mm,  $f_{app} = 750$  Hz,  $\delta = 50\%$ , and  $Q = 50$   $\mu$ L/hr. Figure 5 shows that the average line width of EDW patterns increased with the increasing of negative voltage amplitude and reached its maximum value when the negative voltage amplitude equals the positive ones. The opposite trend appeared as the negative voltage amplitude succeeding the positive ones. The amount of free charge on the jet depends on the applied voltage in EDW. When the negative voltage amplitude equals the positive voltage ones, the equivalent charge density and electrical field force reach the minimum value, as the smaller electrical field force and stretch ratio lead to larger line width.

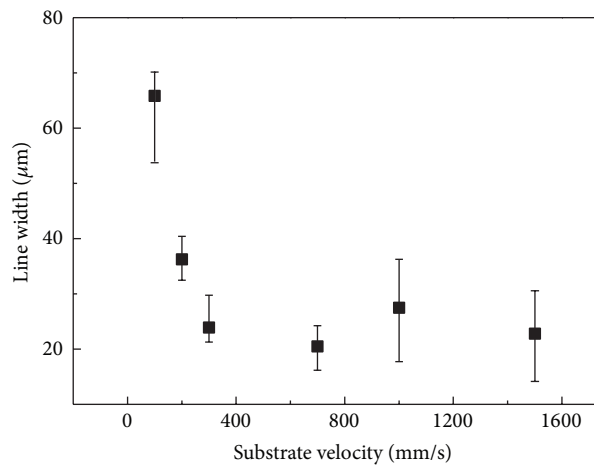
Figure 6 demonstrates the relationship between the AC voltage frequency  $f_{app}$  and the EDW patterns. The experimental parameters were set as  $C = 14$  wt%,  $U_- = -1.5$  kV,  $U_+ = 3.5$  kV,  $\rho = 50\%$ ,  $H = 2$  mm, and  $Q = 50$   $\mu$ L/hr. It can be seen that the average line width increased from 18  $\mu$ m to 33  $\mu$ m when increasing the AC voltage frequency  $f_{app}$  from 0 Hz to 750 Hz, due to the equivalent electrical field force

which decreased with the increase of voltage frequency. Then, line width reached the minimum value when AC voltage frequency  $f_{app}$  was 750 Hz. When AC voltage frequency  $f_{app}$  was larger than 750 Hz, average line width decreased with the increase of voltage frequency  $f_{app}$ . The relaxation time scale of liquid jet was larger than that of electrical field. With the high AC voltage frequency  $f_{app}$ , liquid jet did not have enough time to shrink back. Thus, equivalent stretch force increased with the increase of AC voltage frequency  $f_{app}$ , which helped to decrease the line width.

Figure 7 illustrates the effect of duty cycle ratio on the line width of EDW fibrous patterns. The experimental parameters were set as  $C = 14$  wt%,  $U_- = -1.5$  kV,  $U_+ = 3.5$  kV,  $f_{app} = 750$  Hz,  $H = 2$  mm, and  $Q = 50$   $\mu$ L/hr. As the duty cycle ratio  $\rho$  increased from 30% to 50%, the average line width enlarged from 22  $\mu$ m to 36  $\mu$ m. When the duty cycle ratio  $\rho$  was larger than 50%, the average line width decreased from 36  $\mu$ m to 14  $\mu$ m while the duty cycle ratio increased from 50% to 80%. The equivalent charge density and electrical field force reached the minimum value when duty cycle ratio  $\rho$  was 50%, such that the average line width reached its maximum value.



(a)



(b)

FIGURE 4: Micro/nanofibrous structure direct-written on insulate PET substrate under AC electrical field. The motion velocity of substrate was (a)  $v_{\text{col}} = 50$  mm/s; (b)  $v_{\text{col}} = 100$  mm/s; (c)  $v_{\text{col}} = 200$  mm/s; (d)  $v_{\text{col}} = 700$  mm/s; (e)  $v_{\text{col}} = 1000$  mm/s; and (f)  $v_{\text{col}} = 1500$  mm/s. Experimental condition:  $C = 14$  wt%,  $U_- = -4$  kV,  $U_+ = 4$  kV,  $f_{\text{app}} = 500$  Hz,  $\rho = 50\%$ ,  $H = 2$  mm, and  $Q = 50$   $\mu\text{L/hr}$ .

#### 4. Conclusion

This paper reported an effective AC EDW approach to direct-write orderly micro/nanofibrous structures on the flexible insulating PET substrate. AC electrical field changed the charge transfer characteristics along the jet and decreased the Coulomb repulsive force applied on the following charged jet. And, then, injection stability of charged jet can be enhanced to build up stable straight jet under AC electrical field. With the help of stable straight jet under AC electrical field, parallel microfibrous structures can be direct-written on insulating

PET substrate. The minimum motion velocity of substrate required to direct-write straight line fibrous on insulating PET substrate was 700 mm/s. Line width of direct-written fibrous structure was in the range of  $10 \mu\text{m} \sim 40 \mu\text{m}$ . The line width reached its maximum value, when the negative voltage amplitude equals the positive ones ( $U_- = U_+$ ), AC voltage frequency  $f_{\text{app}} = 750$  Hz, and duty cycle ratio  $\rho = 50\%$ . This work provides an excellent way to increase the EDW controlling technology and accelerates the industrial application in the field of flexible electronic.

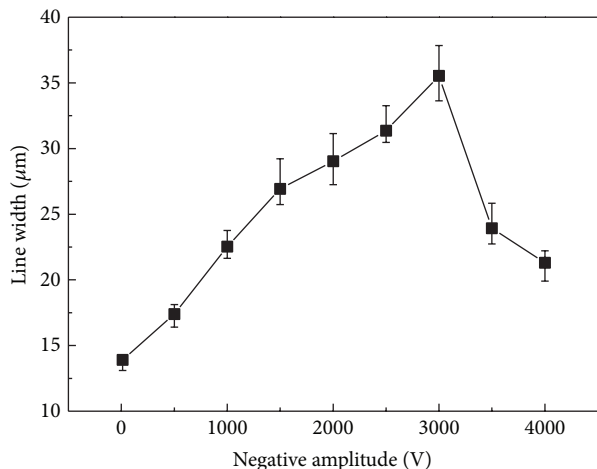


FIGURE 5: The relationship between line width and negative voltage amplitude. Experimental condition:  $C = 14$  wt%,  $U_+ = 3$  kV,  $f_{app} = 750$  Hz,  $\rho = 50\%$ ,  $H = 2$  mm, and  $Q = 50$   $\mu$ L/hr.

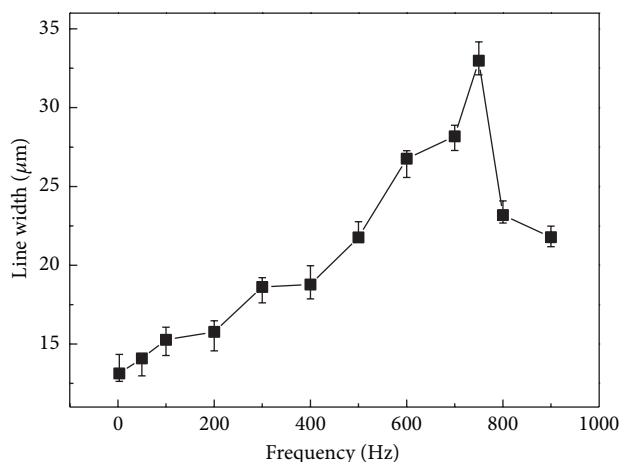


FIGURE 6: The relationship between line width and negative voltage amplitude. Experimental condition:  $C = 14$  wt%,  $U_- = -1.5$  kV,  $U_+ = 3.5$  kV,  $\rho = 50\%$ ,  $H = 2$  mm, and  $Q = 50$   $\mu$ L/hr.

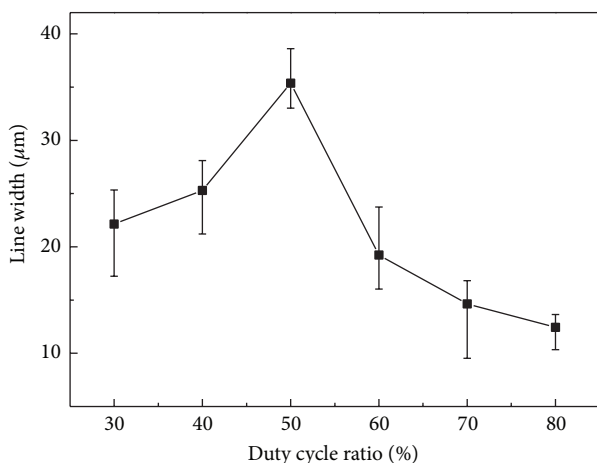


FIGURE 7: The relationship between line width and negative voltage amplitude. Experimental condition:  $C = 14$  wt%,  $U_- = -1.5$  kV,  $U_+ = 3.5$  kV,  $f_{app} = 750$  Hz,  $H = 2$  mm, and  $Q = 50$   $\mu$ L/hr.

## Conflict of Interests

The authors declare that there is no conflict of interests regarding the publication of this paper.

## Acknowledgments

This work is supported by the National Natural Science Foundation of China (nos. 51305371 and 51305373), the Natural Science Foundation of Fujian Province (Grant no. 2013J05083), and the Ph.D. Programs Foundation of Ministry of Education of China (no. 20120121120035).

## References

- [1] J. Upadhyay, R. Das, S. Rao et al., "Manufacturing and characterisation of PMMA-graphene oxide (GO) nanocomposite sandwich films with electrospun nano-fibre core," *Journal of Achievements in Materials and Manufacturing*, vol. 55, no. 2, pp. 835–840, 2012.
- [2] W. M. Choi, T. Tam, and N. B. Trung, "Fabrication of sub-micrometer graphene ribbon using electrospun nanofiber," *Journal of Materials Science*, vol. 49, no. 3, pp. 1240–1245, 2013.
- [3] N. Zhu, W. Liu, M. Xue et al., "Graphene as a conductive additive to enhance the high-rate capabilities of electrospun  $\text{Li}_4\text{Ti}_5\text{O}_{12}$  for lithium-ion batteries," *Electrochimica Acta*, vol. 55, no. 20, pp. 5813–5818, 2010.
- [4] Q. Wang, Y. Du, Q. Feng et al., "Nanostructures and surface nanomechanical properties of polyacrylonitrile/graphene oxide composite nanofibers by electrospinning," *Journal of Applied Polymer Science*, vol. 128, no. 2, pp. 1152–1157, 2013.
- [5] Y. Zhang, Y. Wang, J. Jia, and J. Wang, "Nonenzymatic glucose sensor based on graphene oxide and electrospun NiO nanofibers," *Sensors and Actuators B*, vol. 171-172, pp. 580–587, 2012.
- [6] Y.-L. Huang, A. Baji, H.-W. Tien et al., "Self-assembly of graphene onto electrospun polyamide 66 nanofibers as transparent conductive thin films," *Nanotechnology*, vol. 22, no. 47, Article ID 475603, 2011.
- [7] H. Minemawari, T. Yamada, H. Matsui et al., "Inkjet printing of single-crystal films," *Nature*, vol. 475, no. 7356, pp. 364–367, 2011.
- [8] S. H. Ko, H. Pan, C. P. Grigoropoulos, C. K. Luscombe, J. M. J. Fréchet, and D. Poulidakos, "All-inkjet-printed flexible electronics fabrication on a polymer substrate by low-temperature high-resolution selective laser sintering of metal nanoparticles," *Nanotechnology*, vol. 18, no. 34, Article ID 345202, 2007.
- [9] D. Sun, C. Chang, S. Li, and L. Lin, "Near-field electrospinning," *Nano Letters*, vol. 6, no. 4, pp. 839–842, 2006.
- [10] C. Chang, V. H. Tran, J. Wang, Y.-K. Fuh, and L. Lin, "Direct-write piezoelectric polymeric nanogenerator with high energy conversion efficiency," *Nano Letters*, vol. 10, no. 2, pp. 726–731, 2010.
- [11] X. Wang, G. Zheng, G. He et al., "Electrohydrodynamic direct-writing ZnO nanofibers for device applications," *Materials Letters*, vol. 109, pp. 58–61, 2013.
- [12] I.-D. Kim, A. Rothschild, B. H. Lee, D. Y. Kim, S. M. Jo, and H. L. Tuller, "Ultrasensitive chemiresistors based on electrospun  $\text{TiO}_2$  nanofibers," *Nano Letters*, vol. 6, no. 9, pp. 2009–2013, 2006.

- [13] G. Zheng, W. Li, X. Wang, D. Wu, D. Sun, and L. Lin, "Precision deposition of a nanofibre by near-field electrospinning," *Journal of Physics D*, vol. 43, no. 41, Article ID 415501, 2010.
- [14] H. Wang, G. F. Zheng, W. W. Li et al., "Direct-writing organic three-dimensional nanofibrous structure," *Applied Physics A*, vol. 102, no. 2, pp. 457–461, 2011.
- [15] R. Kessick, J. Fenn, and G. Tepper, "The use of AC potentials in electrospaying and electrospinning processes," *Polymer*, vol. 45, no. 9, pp. 2981–2984, 2004.
- [16] S. Ghashghaie, A. M. Bazargan, M. E. Ganji et al., "An investigation on the behavior of electrospun ZnO nanofibers under the application of low frequency AC electric fields," *Journal of Materials Science: Materials in Electronics*, vol. 22, no. 9, pp. 1303–1307, 2011.
- [17] H. Mu, G. Zhang, S. Suzuki, and Y. Tanaka, "Surface charge distribution of polymeric insulating materials under HVAC," *Proceedings of the Chinese Society of Electrical Engineering*, vol. 30, no. 31, pp. 130–136, 2010.
- [18] S. Sarkar, S. Deevi, and G. Tepper, "Biased AC electrospinning of aligned polymer nanofibers," *Macromolecular Rapid Communications*, vol. 28, no. 9, pp. 1034–1039, 2007.
- [19] F. O. Ochanda, M. A. Samaha, H. V. Tafreshi, G. C. Tepper, and M. Gad-El-Hak, "Fabrication of superhydrophobic fiber coatings by DC-biased AC-electrospinning," *Journal of Applied Polymer Science*, vol. 123, no. 2, pp. 1112–1119, 2012.
- [20] Y. Huang, L. Xu, G. Zheng, Z. Liu, and D. Sun, "Experiment on EHD printing under DC high voltage," *Chinese Journal of Sensors and Actuators*, vol. 23, no. 7, pp. 918–921, 2010.
- [21] W.-W. Li, G.-F. Zheng, X. Wang, and D.-H. Sun, "Position deposition of electrospinning direct-writing nanofiber on pattern substrate," *Optics and Precision Engineering*, vol. 18, no. 10, pp. 2231–2238, 2010.

## Research Article

# Alternating Current Electrohydrodynamic Printing of Microdroplets

Gao-Feng Zheng,<sup>1</sup> Hai-Yan Liu,<sup>1</sup> Rong Xu,<sup>1</sup> Xiang Wang,<sup>1</sup> Juan Liu,<sup>1</sup> Han Wang,<sup>2</sup> and Dao-Heng Sun<sup>1</sup>

<sup>1</sup> Department of Mechanical and Electrical Engineering, Xiamen University, Xiamen 361005, China

<sup>2</sup> Guangdong Provincial Key Laboratory of Micro/Nano Manufacturing Technology and Equipment, Guangdong University of Technology, Guangzhou 510006, China

Correspondence should be addressed to Juan Liu; [cecyluu@xmu.edu.cn](mailto:cecyluu@xmu.edu.cn)

Received 9 February 2014; Revised 3 May 2014; Accepted 5 May 2014; Published 26 May 2014

Academic Editor: Huarong Nie

Copyright © 2014 Gao-Feng Zheng et al. This is an open access article distributed under the Creative Commons Attribution License, which permits unrestricted use, distribution, and reproduction in any medium, provided the original work is properly cited.

This paper discusses the technology of orderly printing of microdroplets by means of electrohydrodynamic print (EHDP) with alternating current (AC). The AC electric field induces charges to reciprocate in the electrohydrodynamic charged jet and generates periodic alternation of electric field force, which facilitates the breakup of charged jets and injection of microdroplets. Microdroplets with a diameter of 100~300  $\mu\text{m}$  can be printed with a frequency of 5~25 Hz via AC EHDP. Effects of process parameters on the microdroplet injection behaviors were investigated. A higher frequency of applied AC voltage led to a higher deposition frequency, but smaller diameters of printed droplets. Deposition frequency and droplet diameters increased with the increase of duty cycle and solution supply rate. AC pulse voltage has provided a novel way to study the control technology in EHDP, which would accelerate the application of inkjet printing in the field of micro/nanosystem production.

## 1. Introduction

Owing to advantages of bendableness, low cost, robustness, and lower power consumption [1], flexible electronics have great potential application in the fields of information [2, 3], energy [4–6], lithium-ion [7, 8], health [9], and micro/nano system [10, 11], among others. Utilization of organic functional materials and flexible substrates are the trademarks for flexible electronics which, however, are incompatible with conventional IC fabrication technology [12] and call for novel fabrication methods [13, 14]. As a high efficiency, low-cost, low-waste, and noncontact fabrication process, inkjet printing has been regarded as one of the most potential technologies for large scale manufacturing of flexible and organic electronics [15, 16]. Inkjet printing does not need stencil-plate and etching process; therefore, electronic devices with complex patterns or three-dimensional structures can be printed directly and quickly [17, 18].

Conventional inkjet printing technologies, which rely on inner pressure generated by thermal bubbles or the piezoelectric pump, have limitations in reducing the droplet size and line width of printed patterns [19]. Electrohydrodynamic print (EHDP) utilizes external electric field force to stretch viscoelastic solution. EHDP jet was ejected from the tip of Taylor cone under the spinneret [20–22]. The diameter of the EHDP jet is independent of the inner diameter of the spinneret, which is a great advantage to reduce the size of printed micro/nanostructures. Near field electrospinning [23] (NFES) takes the advantage of stable straight jet outside the spinneret to produce precise deposition of printed micro/nanostructures. According to NFES theory, micro/nanodroplets [24] can be deposited accurately on the collector through the EHDP technology, the same as nanofibers [25, 26].

Not only direct current (DC) high voltage sources, but also multistep pulse voltage sources [27] and alternating

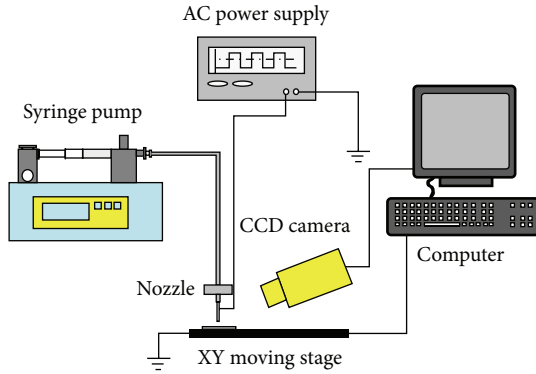


FIGURE 1: Schematic diagram of AC electrohydrodynamic printing experiment setup.

current (AC) voltage sources [28] can be used as the high voltage sources for EHDP. Espín et al. [29] discovered that, under AC electric fields, the maximum growth rate and corresponding wave number can be expressed as a function of the oscillation amplitude and frequency. Larsen et al. [30] disclosed a patent that employs an AC voltage source in the EHDP apparatus to improve the control technology of fiber and particle printing. Kessick et al. [31] reported that the AC high voltage source changes the charge transfer characteristics of the EHDP jet and reduces charge repulsive force between the solution jet and the substrate, which improves the positioning precision of printed micro/nanostructures. Ghashghaie et al. [32] reported that AC electric field induces charges to redistribute on the substrate, which helps the parallel deposition of ZnO nanofibers. Nguyen [28] used single AC electrode to print silver paste pattern that overcame the jet drawback of conventional DC EHDP and found out that AC voltage also was propitious for increasing the deposition frequency. The control technology of AC EHDP under near field was different from that of conventional DC EHDP. Thus, further studies on the injection and deposition behaviors of microdroplets under AC electric field should be carried out.

In this paper, AC pulse voltage was utilized to print microdroplets, and the injection and deposition behaviors of charged droplets were studied. We also discuss the effects of process parameters on the morphology, diameter, and deposition frequency of printed microdroplets.

## 2. Experiment Details

The schematic diagram of experimental setup was illustrated in Figure 1, where high AC power sources (DW-P503-LACDE, China) were used to generate electric field. A silicon wafer used as grounded collector was fixed on an X-Y motion stage (Googol GXY1515GT4, China). The motion velocity of the collector ranged from 2 mm/s to 40 mm/s, and motion track can be controlled by the host computer. Stainless nozzle (inner diameter = 62  $\mu\text{m}$ , outer diameter = 90  $\mu\text{m}$ ) was used as the EHDP spinneret, and the distance from spinneret to the collector was 2 mm. Polymer solution was continuously

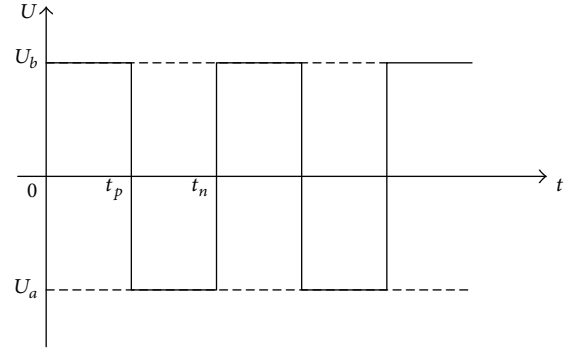


FIGURE 2: Wave shape of AC pulse voltage.

delivered to the spinneret by a syringe pump (Harvard 11 Pico Plus, USA). A CCD camera (uEyeRe UI-2250-C, German) was used to observe and record the injection and deposition process of the EHDP jet. The droplet size can be measured through the CCD pictures with scale with the help of image processing software ImageJ. Polyethylene oxide (PEO,  $M_w = 300,000$  g/mol) solution in mixed solvent of deionized water and ethanol ( $v/v = 60/40$ ) was used as injection materials. The concentration of PEO solution ranged from 1 wt% to 5 wt%. Before starting the experiment, the silicon wafer substrate was ultrasonically cleaned in the mixed solution of deionized water and acetone for 20 min; and then the cleaned silicon wafer was dried by a hot air blower. The wave shape of AC pulse voltage used in the experiments was shown in Figure 2;  $U_a$  and  $U_b$  referred to the negative amplitude and positive amplitude of AC pulse voltage, respectively. The effects of AC pulse voltage on the EHDP injection process were studied by varying the voltage amplitude, the duty cycle, and the frequency.

In these experiments, the deposition frequency of microdroplet was defined as  $f_{\text{dep}} = v_{\text{col}}/l$ , where  $v_{\text{col}}$  was the collector motion velocity (unit for the collector motion velocity was mm/s) and  $l$  was the center-to-center distance between two adjacent printed droplets (unit for the distance was mm). Both the average center-to-center distance  $l$  and the printed droplet diameter  $D_{\text{dep}}$  were calculated from 50 data points, respectively.

## 3. Results and Discussions

The injection and deposition behaviors of AC EHDP droplets were studied further to improve the control technology of microdroplet injection. A series of experiments were performed to investigate the effect of AC voltage amplitude  $U_a$ , duty cycle ratio  $\rho$ , frequency  $f_{\text{app}}$ , and solution supply flow rate  $Q$  on the microdroplet injection behaviors.

**3.1. AC Voltage Amplitude.** The effect of applied voltage amplitude on the injection process was studied first. The concentration of PEO solution  $C$ , AC voltage frequency  $f_{\text{app}}$ , duty cycle ratio  $\rho$ , and solution supply rate  $Q$  were 3 wt%, 20 Hz, 50%, and 30  $\mu\text{L/hr}$ , respectively. Experimental results showed that  $U_b = 2.8$  kV could build up the stable

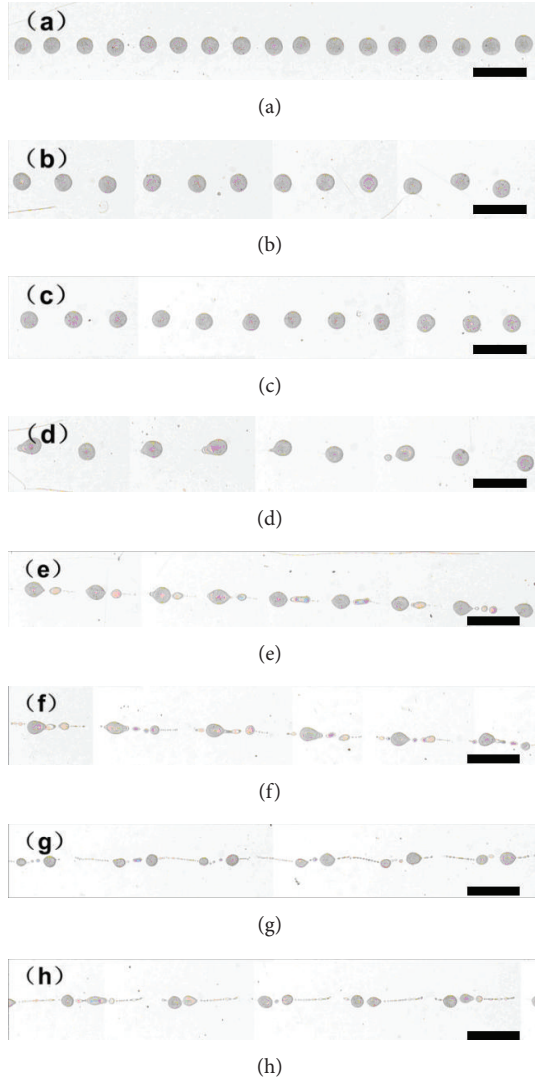


FIGURE 3: Printed droplets under AC voltage with different negative AC voltage amplitude  $U_a$ . Negative AC voltage amplitude and collector motion velocity were (a)  $U_a = 0$  kV,  $v_{col} = 10$  mm/s; (b)  $U_a = 0.5$  kV,  $v_{col} = 14$  mm/s; (c)  $U_a = 0.75$  kV,  $v_{col} = 14$  mm/s; (d)  $U_a = 1$  kV,  $v_{col} = 20$  mm/s; (e)  $U_a = 1.25$  kV,  $v_{col} = 20$  mm/s; (f)  $U_a = 1.5$  kV,  $v_{col} = 30$  mm/s; (g)  $U_a = 1.75$  V,  $v_{col} = 30$  mm/s; (h)  $U_a = 2$  kV,  $v_{col} = 30$  mm/s. The scale bar is  $1000 \mu\text{m}$ .

cone-jet injection. During the experimental process, the positive AC voltage amplitude  $U_b$  was fixed at  $2.8$  kV, and then the negative AC voltage amplitude  $U_a$  was varied to study the effect of applied voltage amplitude on the AC EHDP injection process. Droplets printed under different negative AC voltage amplitude  $U_a$  were showed in Figure 3. In order to capture clear pictures of printed droplets, the collector motion velocity  $v_{col}$  was controlled to adjust the space between two adjacent printed droplets according to the deposition frequency  $f_{dep}$ . EHDP jet had been broken into microdrops before deposition on the collector, so the collector motion velocity would not affect the deposition frequency and the volume of EHDP droplets [33].

Negative voltage generated a reverse force and the charged jet shrank back, which helped the EHDP jet break into droplets. When the negative AC voltage amplitude was lower than  $1$  kV, droplets can be printed without satellite dots, as shown in Figures 3(a)~3(c). When the negative AC voltage amplitude  $U_a$  varied from  $0$  to  $1$  kV, the average droplet diameter  $D_{dep}$  and the deposition frequency  $f_{dep}$  remained relatively constant.  $D_{dep}$  and  $f_{dep}$  of printed droplets were  $250 \mu\text{m}$  and  $24$  Hz, respectively. When the negative AC voltage amplitude  $U_a$  increased further, the charged jet was drawn back by the reverse electric field force more quickly. The higher recovery rate caused the jet to break into more satellite dots due to the larger Weber number. Satellite dots were deposited along the collector motion track, as shown in Figures 3(d)~3(h). The number of satellite dots between two adjacent printed droplets increased along with the negative AC voltage amplitude  $U_a$ , due to the larger reverse force and speed. The printed droplet diameter decreased with the increase of negative AC voltage amplitude  $U_a$ , due to the constant solution supply rate  $Q$  and a higher deposition frequency  $f_{dep}$ . On the other hand, the Coulomb repulsive force among the liquid droplet was another reason for the satellite dots. According to the theory simulation, positive voltage period would induce positive charge assembled on the surface of polymer jet, but negative voltage would induce positive charge. The surface charge density increased with the increase of applied voltage amplitude [34, 35]. Theory simulation results showed that surface charge density of liquid jet increased from  $1.28 \text{ C/m}^2$  to  $80.8 \text{ C/m}^2$ , when applied voltage amplitude increased from  $0.5$  kV to  $2$  kV. Larger surface charge density also increased the Coulomb repulsive force among the liquid droplet, which promoted the breakup of charged droplet.

**3.2. Duty Cycle Ratio.** The microdroplets printed under different duty cycle  $\rho$  of  $20\sim 70$  wt% were shown in Figure 4. The negative AC voltage amplitude  $U_a$ , positive AC voltage amplitude  $U_b$ , AC voltage frequency  $f_{app}$ , PEO solution concentration  $C$ , and solution supply rate  $Q$  were  $1.0$  kV,  $2.8$  kV,  $20$  Hz,  $4$  wt%, and  $60 \mu\text{L/hr}$ , respectively. The positive AC voltage played the role to stretch the viscoelastic solution to produce the charged jet. The charged jet was stretched and accelerated toward the collector by the positive electric field force. A higher duty cycle  $\rho$  led to longer charging time, larger charge density, and higher motion speed of EHDP jet, which would help the jet break up into microdroplets.

The deposition frequency  $f_{dep}$  and the droplet diameter  $D_{dep}$  increased with the increase of the duty cycle  $\rho$ ; the relationship was shown in Figure 5. The droplet diameter  $D_{dep}$  increased from  $150$  to  $190 \mu\text{m}$  due to longer stretching time under the positive voltage, when the duty cycle  $\rho$  increased from  $20$  to  $70\%$ . As shown in Figure 5, the deposition frequency  $f_{dep} = 10$  Hz was one half of the AC voltage frequency  $f_{app}$ , when duty cycle  $\rho$  was smaller than  $60\%$ . The deposition frequency could be rewritten as  $f_{dep} = f_{app}/2$ . However, when the duty cycle  $\rho$  increased to  $70\%$ , the deposition frequency  $f_{dep}$  increased sharply to  $15$  Hz, where  $f_{dep} = 3/4 f_{app}$ .

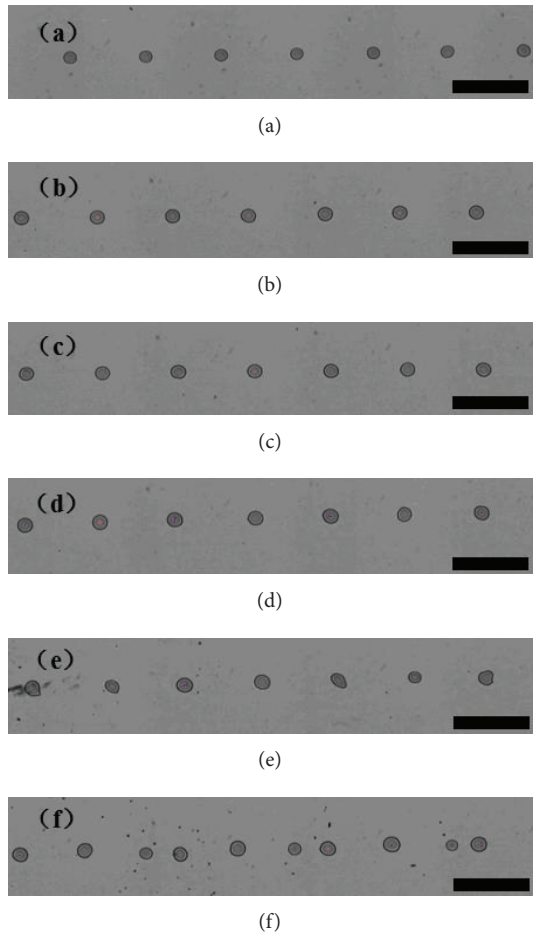


FIGURE 4: Printed droplets under AC voltage with different duty cycle  $\rho$ . Duty cycles were (a)  $\rho = 20\%$ ; (b)  $\rho = 30\%$ ; (c)  $\rho = 40\%$ ; (d)  $\rho = 50\%$ ; (e)  $\rho = 60\%$ ; (f)  $\rho = 70\%$ . The collector motion speed was  $v_{\text{col}} = 10 \text{ mm/s}$ . The scale bar is  $1000 \mu\text{m}$ .

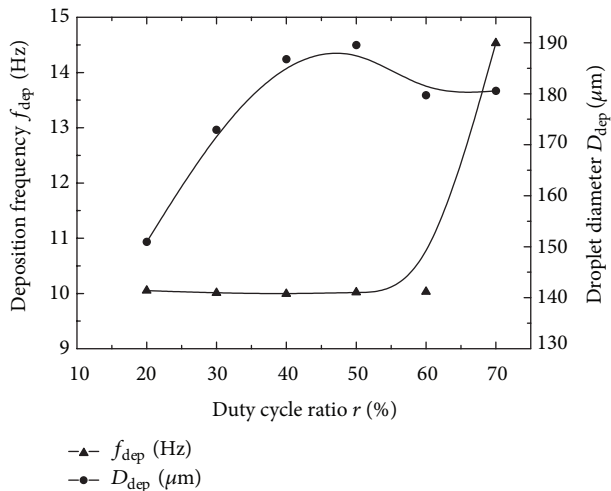


FIGURE 5: The relationship between deposition frequency  $f_{\text{dep}}$ , droplet diameter  $D_{\text{dep}}$ , and duty cycle  $\rho$ .

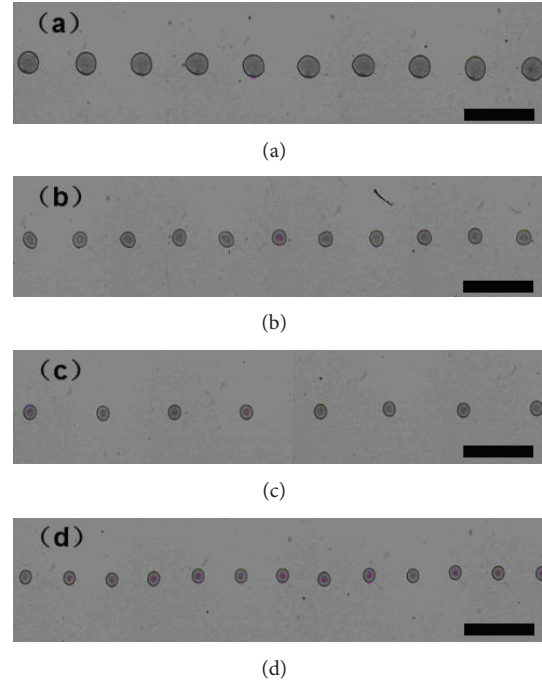


FIGURE 6: Printed droplets under AC voltage with different applied AC voltage frequency  $f_{\text{app}}$ . AC voltage frequency and collector motion velocity were (a)  $f_{\text{app}} = 10 \text{ Hz}$ ,  $v_{\text{col}} = 4 \text{ mm/s}$ ; (b)  $f_{\text{app}} = 30 \text{ Hz}$ ,  $v_{\text{col}} = 10 \text{ mm/s}$ ; (c)  $f_{\text{app}} = 50 \text{ Hz}$ ,  $v_{\text{col}} = 10 \text{ mm/s}$ ; (d)  $f_{\text{app}} = 70 \text{ Hz}$ ,  $v_{\text{col}} = 10 \text{ mm/s}$ . The scale bar is  $1000 \mu\text{m}$ .

**3.3. AC Voltage Frequency.** The printed droplets deposited on the silicon collector with different AC voltage frequency  $f_{\text{app}}$  of 10~70 Hz were shown in Figure 6. The PEO solution concentration  $C$ , solution supply rate  $Q$ , duty cycle  $\rho$ , negative AC voltage amplitude  $U_a$ , and positive AC voltage amplitude  $U_b$  were 4 wt%, 20  $\mu\text{L/hr}$ , 50%, 1.0 kV, and 2.8 kV, respectively. Higher frequency shortened the period of electric field alternation and accelerated breakup of microdroplets from the jet. Due to the constant solution supply rate, the droplet diameter  $D_{\text{dep}}$  decreased with the increase of deposition frequency. As the applied AC voltage frequency  $f_{\text{app}}$  increased from 10 to 70 Hz, the deposition frequency  $f_{\text{dep}}$  increased from 5 to 18 Hz and the droplet diameter  $D_{\text{dep}}$  decreased from 280 to 150  $\mu\text{m}$ ; the relationship was plotted in Figure 7.

**3.4. Solution Supply Rate.** The printed droplets under different solution supply rate  $Q$  were presented in Figure 8. The PEO solution concentration  $C$ , duty cycle  $\rho$ , AC voltage frequency  $f_{\text{app}}$ , negative AC voltage amplitude  $U_a$ , and positive AC voltage amplitude  $U_b$  were 4 wt%, 50%, 20 Hz, 2.0 kV, and 2.8 kV, respectively. A higher solution supply rate can provide adequate printing materials to ensure the high speed injection of microdroplets with a larger diameter. The relationship in Figure 9 indicated that deposition frequency  $f_{\text{dep}}$  increased from 10 to 22 Hz and the droplet diameter  $D_{\text{dep}}$  increased from 170 to 185  $\mu\text{m}$ , when solution supply rate  $Q$  increased from 20  $\mu\text{L/hr}$  to 60  $\mu\text{L/hr}$ .

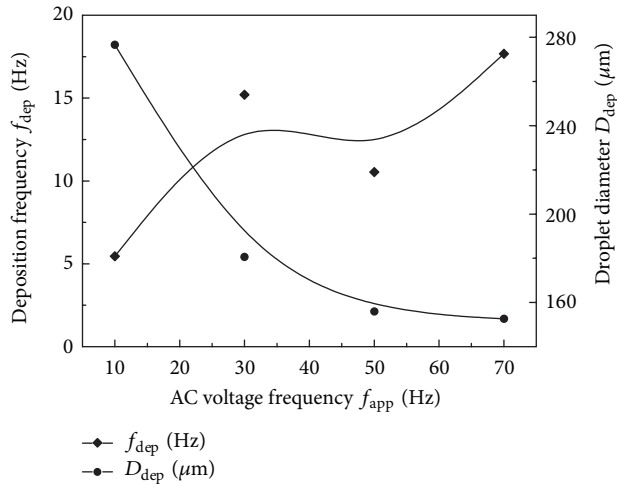


FIGURE 7: The relationship between deposition frequency  $f_{dep}$ , droplet diameter  $D_{dep}$ , and applied AC voltage frequency  $f_{app}$ .

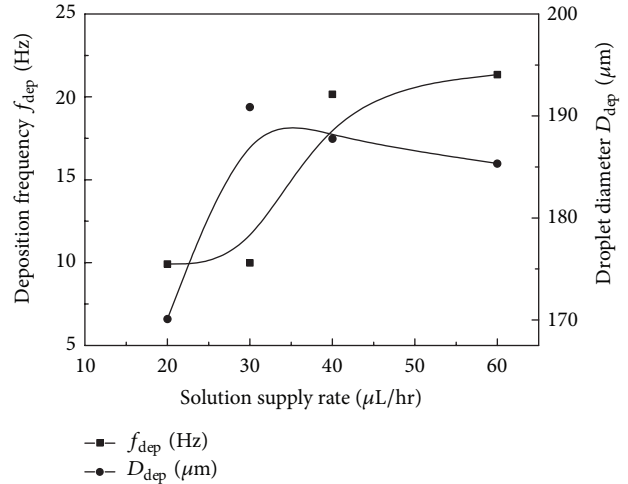


FIGURE 9: The relationship between deposition frequency  $f_{dep}$ , droplet diameter  $D_{dep}$ , and solution supply rate  $Q$ .

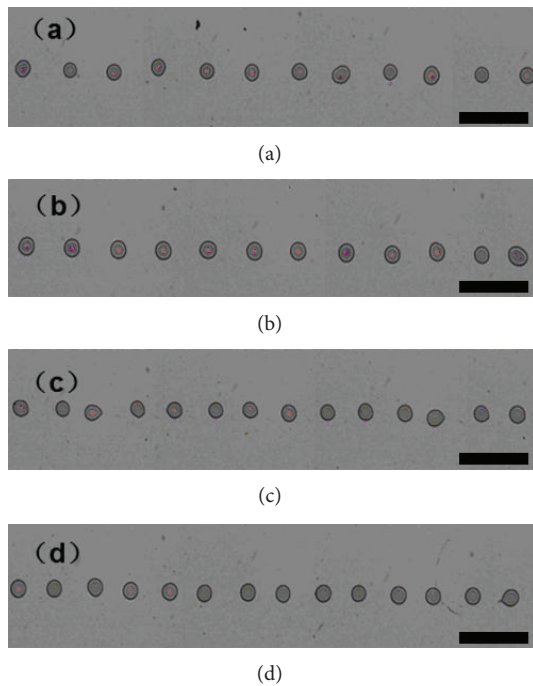


FIGURE 8: Printed droplets under AC voltage with different solution supply rate  $Q$ . Solution supply rate and collector motion speed were (a)  $Q = 20 \mu\text{L/hr}$ ,  $v_{col} = 6 \text{ mm/s}$ ; (b)  $Q = 30 \mu\text{L/hr}$ ,  $v_{col} = 6 \text{ mm/s}$ ; (c)  $Q = 50 \mu\text{L/hr}$ ,  $v_{col} = 10 \text{ mm/s}$ ; (d)  $Q = 70 \mu\text{L/hr}$ ,  $v_{col} = 10 \text{ mm/s}$ . The scale bar is  $1000 \mu\text{m}$ .

#### 4. Summary and Conclusion

A novel EHDP method based on AC pulse voltage was utilized to orderly print microdroplets with a diameter of  $100\sim 300 \mu\text{m}$  and a deposition frequency of  $5\sim 25 \text{ Hz}$ . AC pulse voltage led to the periodic alternation of electric field force applied on the charged jet. Positive voltage provided forward force to stretch the printing solution into fine jet and

motion toward the collector. Reverse force that generated the negative voltage caused the charged jet to shrink back, which helps the charged jet break up into microdroplets. When the negative voltage was higher than  $1 \text{ kV}$ , the larger Weber number of jet motion might cause the charged jet to break into satellite dots and be deposited along the collector motion track. The number of satellite dots between two adjacent printed droplets increased with the increase of negative AC voltage amplitude. The effects of process parameters on the deposition frequency and droplet diameter were also studied. The deposition frequency increased with the increase of AC voltage frequency, while the droplet diameter decreased due to the constant solution supply rate. The deposition frequency and droplet diameter increased with the increase of duty cycle, but decreased with the increase of the solution supply rate.

The AC electric field varied charge transformation behaviors and decreased the charge density in the EHDP jet. This has opened a new door to study the control technology and accelerate the industrial application of EHDP.

#### Conflict of Interests

The authors declare that there is no conflict of interests regarding the publication of this paper.

#### Acknowledgments

This work is supported by a project funded by the National Natural Science Foundation of China (Grant no. 51305373, 51305084), the Natural Science Foundation of Fujian Province (Grant no. 2013J05083), and the Opening Fund of Guangdong Provincial Key Laboratory of Micro-Nano Manufacturing Technology and Equipment (Grant no. GDMNML2013-01).

## References

- [1] P. Maury, D. Turkenburg, N. Stroeks et al., "Roll-to-roll UV imprint lithography for flexible electronics," *Microelectronic Engineering*, vol. 88, no. 8, pp. 2052–2055, 2011.
- [2] T. Sekitani, U. Zschieschang, H. Klauk, and T. Someya, "Flexible organic transistors and circuits with extreme bending stability," *Nature Materials*, vol. 9, no. 12, pp. 1015–1022, 2010.
- [3] N. Padma, S. Sen, S. N. Sawant, and R. Tokas, "A study on threshold voltage stability of low operating voltage organic thin-film transistors," *Journal of Physics D: Applied Physics*, vol. 46, no. 32, Article ID 325104, 2013.
- [4] Y. Li, "Molecular design of photovoltaic materials for polymer solar cells: toward suitable electronic energy levels and broad absorption," *Accounts of Chemical Research*, vol. 45, no. 5, pp. 723–733, 2012.
- [5] N. Gao, W. Q. Liu, S. Q. Ma, Z. L. Yan, and Y. Zhao, "Modification of epoxy resin with cycloaliphatic-epoxy oligosiloxane for Light-Emitting Diode (LED) encapsulation application," *Journal of Macromolecular Science B: Physics*, vol. 51, no. 8, pp. 1509–1524, 2012.
- [6] X. Xiao, T. Li, P. Yang et al., "Fiber-based all-solid-state flexible supercapacitors for self-powered systems," *ACS Nano*, vol. 6, no. 10, pp. 9200–9206, 2012.
- [7] E. S. Kim, S. H. Kim, and C. H. Lee, "Electrospinning of polylactide fibers containing silver nanoparticles," *Macromolecular Research*, vol. 18, no. 3, pp. 215–221, 2010.
- [8] S. Y. Lee, K. H. Choi, W. S. Choi et al., "Progress in flexible energy storage and conversion systems, with a focus on cable-type lithium-ion batteries," *Energy and Environmental Science*, vol. 6, no. 8, pp. 2414–2423, 2013.
- [9] G. Schwartz, B. C. K. Tee, J. Mei et al., "Flexible polymer transistors with high pressure sensitivity for application in electronic skin and health monitoring," *Nature Communications*, vol. 4, article 1861, 2013.
- [10] J. H. Pikul, P. Graf, S. Mishra et al., "High precision electrohydrodynamic printing of polymer onto microcantilever sensors," *IEEE Sensors Journal*, vol. 11, no. 10, pp. 2246–2253, 2011.
- [11] C. M. Xia, G. Y. Zhou, Y. Han, and L. T. Hou, "Photoluminescence of an  $\text{Yb}^{3+}/\text{Al}^{3+}$ -codoped microstructured optical fibre," *Chinese Physics B*, vol. 20, no. 8, Article ID 087802, 2011.
- [12] P. Z. Zhang, R. S. Li, X. J. Pan, and E. Q. Xie, "Fabrication of ZnO nanoparticles-embedded hydrogenated diamond-like carbon films by electrochemical deposition technique," *Chinese Physics B*, vol. 22, no. 5, Article ID 058106, 2013.
- [13] Q. Zheng, G. Fang, F. Cheng, H. Lei, P. Qin, and C. Zhan, "Low-temperature solution-processed graphene oxide derivative hole transport layer for organic solar cells," *Journal of Physics D: Applied Physics*, vol. 46, no. 13, Article ID 135101, 2013.
- [14] H. Ko, R. Kapadia, K. Takei, T. Takahashi, X. Zhang, and A. Javey, "Multifunctional, flexible electronic systems based on engineered nanostructured materials," *Nanotechnology*, vol. 23, no. 34, Article ID 344001, 2012.
- [15] J. Lee, S. Chung, H. Song, S. Kim, and Y. Hong, "Lateral-crack-free, buckled, inkjet-printed silver electrodes on highly pre-stretched elastomeric substrates," *Journal of Physics D: Applied Physics*, vol. 46, no. 10, Article ID 105305, 2013.
- [16] J. J. Bai, X. M. Wu, Y. L. Hua et al., "Efficiency of a blue organic light-emitting diode enhanced by inserting charge control layers into the emission region," *Chinese Physics B*, vol. 22, no. 4, Article ID 047806, 2013.
- [17] B. D. Gates, "Materials science: flexible electronics," *Science*, vol. 323, no. 5921, pp. 1566–1567, 2009.
- [18] D. F. Duarte Campos, A. Blaeser, M. Weber et al., "Three-dimensional printing of stem cell-laden hydrogels submerged in a hydrophobic high-density fluid," *Biofabrication*, vol. 5, no. 1, Article ID 015003, 2013.
- [19] M. Singh, H. M. Haverinen, P. Dhagat, and G. E. Jabbour, "Inkjet printing-process and its applications," *Advanced Materials*, vol. 22, no. 6, pp. 673–685, 2010.
- [20] W. Li, G. Zheng, X. Wang et al., "Directly electrospun ultrafine nanofibres with Cu grid spinneret," *Journal of Physics D: Applied Physics*, vol. 44, no. 13, Article ID 135502, 2011.
- [21] J. Zheng, Y. Z. Long, B. Sun et al., "Polymer nanofibers prepared by low-voltage near-field electrospinning," *Chinese Physics B*, vol. 21, no. 4, Article ID 048102, 2012.
- [22] Z. H. Zhang, Y. Z. Long, H. X. Yin et al., "Electrospun fluorescein/polymer composite nanofibers and their photoluminescent properties," *Chinese Physics B*, vol. 21, no. 9, Article ID 097805, 2012.
- [23] D. Sun, C. Chang, S. Li, and L. Lin, "Near-field electrospinning," *Nano Letters*, vol. 6, no. 4, pp. 839–842, 2006.
- [24] L. Xu and D. Sun, "Electrohydrodynamic printing under applied pole-type nozzle configuration," *Applied Physics Letters*, vol. 102, no. 2, Article ID 024101, 2013.
- [25] W. W. Li, G. F. Zheng, X. Wang, and D. H. Sun, "Position deposition of electrospinning direct-writing nanofiber on pattern substrate," *Optics and Precision Engineering*, vol. 18, no. 10, pp. 2231–2238, 2010.
- [26] G. Zheng, W. Li, X. Wang, D. Wu, D. Sun, and L. Lin, "Precision deposition of a nanofibre by near-field electrospinning," *Journal of Physics D: Applied Physics*, vol. 43, no. 41, Article ID 415501, 2010.
- [27] K. H. Choi, A. Khan, K. Rahman, Y. H. Doh, D. S. Kim, and K. R. Kwan, "Effects of nozzles array configuration on cross-talk in multi-nozzle electrohydrodynamic inkjet printing head," *Journal of Electrostatics*, vol. 69, no. 4, pp. 380–387, 2011.
- [28] V. D. Nguyen and D. Byun, "Mechanism of electrohydrodynamic printing based on ac voltage without a nozzle electrode," *Applied Physics Letters*, vol. 94, no. 17, Article ID 173509, 2009.
- [29] L. Espín, A. Corbett, and S. Kumar, "Electrohydrodynamic instabilities in thin viscoelastic films—AC and DC fields," *Journal of Non-Newtonian Fluid Mechanics*, vol. 196, pp. 102–111, 2013.
- [30] G. Larsen, R. Spretz, R. Velarde-ortiz, D. Vu, and L. Nunez, "Systems for producing multilayered particles, fibers and sprays and methods for administering the same," US Patent US 20130017148, 2013.
- [31] R. Kessick, J. Fenn, and G. Tepper, "The use of AC potentials in electro-spraying and electrospinning processes," *Polymer*, vol. 45, no. 9, pp. 2981–2984, 2004.
- [32] S. Ghashghaie, A. M. Bazargan, M. E. Ganji et al., "An investigation on the behavior of electrospun ZnO nanofibers under the application of low frequency AC electric fields," *Journal of Materials Science: Materials in Electronics*, vol. 22, no. 9, pp. 1303–1307, 2011.
- [33] L. Xu, X. Wang, T. Lei, D. Sun, and L. Lin, "Electrohydrodynamic deposition of polymeric droplets under low-frequency pulsation," *Langmuir*, vol. 27, no. 10, pp. 6541–6548, 2011.

- [34] S. A. Theron, E. Zussman, and A. L. Yarin, "Experimental investigation of the governing parameters in the electrospinning of polymer solutions," *Polymer*, vol. 45, no. 6, pp. 2017–2030, 2004.
- [35] X. Sun, D. Jia, W. Kang, B. Cheng, and Y. Li, "Research on electrospinning process of pullulan nanofibers," *Applied Mechanics and Materials*, vol. 268, no. 1, pp. 198–201, 2013.

## Research Article

# Fabrication of Aligned Carbon Nanotube/Polycaprolactone/Gelatin Nanofibrous Matrices for Schwann Cell Immobilization

Shiao-Wen Tsai,<sup>1</sup> Chun-Chiang Huang,<sup>2</sup> Lih-Rou Rau,<sup>1</sup> and Fu-Yin Hsu<sup>2,3</sup>

<sup>1</sup> Graduate Institute of Biochemical and Biomedical Engineering, Chang-Gung University, Taoyuan 33333, Taiwan

<sup>2</sup> Institute of Bioscience and Biotechnology, National Taiwan Ocean University, Keelung 20224, Taiwan

<sup>3</sup> Department of Life Sciences, National Taiwan Ocean University, Keelung 20224, Taiwan

Correspondence should be addressed to Fu-Yin Hsu; [fyhsu5565@gmail.com](mailto:fyhsu5565@gmail.com)

Received 10 February 2014; Accepted 27 March 2014; Published 14 May 2014

Academic Editor: Ruigang Liu

Copyright © 2014 Shiao-Wen Tsai et al. This is an open access article distributed under the Creative Commons Attribution License, which permits unrestricted use, distribution, and reproduction in any medium, provided the original work is properly cited.

In this study, we utilized a mandrel rotating collector consisting of two parallel, electrically conductive pieces of tape to fabricate aligned electrospun polycaprolactone/gelatin (PG) and carbon nanotube/polycaprolactone/gelatin (PGC) nanofibrous matrices. Furthermore, we examined the biological performance of the PGC nanofibrous and film matrices using an *in vitro* culture of RT4-D6P2T rat Schwann cells. Using cell adhesion tests, we found that carbon nanotube inhibited Schwann cell attachment on PGC nanofibrous and film matrices. However, the proliferation rates of Schwann cells were higher when they were immobilized on PGC nanofibrous matrices compared to PGC film matrices. Using western blot analysis, we found that NRG1 and P0 protein expression levels were higher for cells immobilized on PGC nanofibrous matrices compared to PG nanofibrous matrices. However, the carbon nanotube inhibited NRG1 and P0 protein expression in cells immobilized on PGC film matrices. Moreover, the NRG1 and P0 protein expression levels were higher for cells immobilized on PGC nanofibrous matrices compared to PGC film matrices. We found that the matrix topography and composition influenced Schwann cell behavior.

## 1. Introduction

Nerve autografts are considered the “gold standard” for the repair of long gaps caused by nerve damage. These materials are harvested from another site in the body and are typically not rejected by the immune system. Nevertheless, the harvesting step requires an additional surgical procedure that can cause donor site morbidity and patient discomfort. Allografts, obtained from human cadavers or living donors, often are rejected by the host; thus, their efficiency, application, and availability are limited [1–3]. Nerve grafts made of natural and synthetic materials are thus a promising alternative for promoting successful nerve regeneration because they have the potential to overcome many of the drawbacks associated with autologous and allogeneic nerve grafting.

Polycaprolactone (PCL) has recently been used in a variety of tissue engineering applications because of its high toughness and cost efficiency [4]. However, cells exposed

to PCL do not behave favorably because PCL has lower hydrophilicity than natural ECM. Gelatin is obtained by partial hydrolysis of native collagen in acidic or alkaline environments. Gelatin exhibits excellent biocompatibility and biodegradability, and it has been widely used as a component in many biomedical materials, including wound dressings, drug release structures, and tissue-engineered bone, skin, cartilage, and nerve [5, 6]. Carbon nanotubes (CNTs) are promising for use in regenerative medicine due to their unique electrical, mechanical, chemical, and biological properties and their ease of combination with various biological compounds [7, 8]. When CNTs are incorporated into biopolymers, electrically conductive scaffolds that can support both Schwann cells and neurons can be synthesized [9].

Electrospinning can be readily utilized to fabricate ultra-fine fibers with average diameters ranging from the sub-micrometer to nanometer scale. Advantageously, fibrous

matrices that have been synthesized using electrospinning display high specific surface areas, high aspect ratios, and high porosity surfaces. More importantly, the topological structures of these matrices can mimic that of the extracellular matrix and enhance cell migration, proliferation, and differentiation [10, 11].

Aligned fibers prepared via electrospinning enhance Schwann cell maturation to a greater degree compared to randomly oriented fibers [12]. In the past, aligned fibers have been produced using a variety of methods [13, 14]. Li et al. fabricated aligned nanofibers using a collector consisting of two parallel, electrically conductive substrates separated by a gap [15]. Matthews et al. collected circumferentially aligned electrospun fibers on a mandrel rotating at a high speed [16]. In this paper, we discuss the fabrication of electrospun nanofibrous matrices in which the fibers are aligned along the longitudinal axis of a mandrel using a rotating collector containing two parallel, electrically conductive pieces of tape.

It is challenging and difficult to promote nervous system regeneration. However, the peripheral nervous system has an intrinsic ability to repair and regenerate axons; Schwann cells enhance such regeneration after damage occurs [17]. The aim of this study was to fabricate aligned carbon nanotube/polycaprolactone/gelatin nanofibrous matrices and investigate their potential as neurografts for peripheral nerve repair.

## 2. Materials and Methods

**2.1. Reagents.** Gelatin (type A) and polycaprolactone were purchased from the Sigma Aldrich Chemical Company (St. Louis, MO, USA). Carbon nanotubes were purchased from the Golden Innovation Business Co. Ltd. (New Taipei City, Taiwan). RT4-D6P2T rat Schwann cells were purchased from the BCRC (Bioresource Collection and Research Center, Hsinchu, Taiwan). Dulbecco's modified Eagle medium (DMEM), fetal bovine serum (FBS), and trypsin were purchased from GIBCO (Grand Island, NY, USA). All of the other chemicals used herein were of reagent grade unless stated otherwise.

**2.2. Acid-Oxidized CNTs.** The surfaces of the CNTs were functionalized according to the method delineated by Xiao et al. [18]. Briefly, 0.1 g of pristine CNTs was added to 20 mL of hydrochloric acid (36.5 wt%) and stirred for 2 hours at a moderate speed. Then, the CNTs were diluted with water, filtered, washed with deionized water, and dried under vacuum at 60°C overnight. Afterward, the pretreated CNTs were put into 15 mL of nitric acid (HNO<sub>3</sub>) (65 wt%) and heated at 140°C for 4 hours. The CNTs were subsequently cooled to room temperature; then the entire of acid-oxidized CNT process was repeated one time.

**2.3. Characterization of Acid-Oxidized CNTs.** ATR-FTIR spectra of pristine and acid-oxidized CNTs were obtained using a Bruker spectrometer. The spectra were obtained using 64 scans with a resolution of 4 cm<sup>-1</sup> in the range of 600–4000 cm<sup>-1</sup>.

**2.4. Preparation of CNT/Polycaprolactone/Gelatin Nanofibrous Matrices.** Gelatin and polycaprolactone powders (42.5 mg of each) were dissolved in 1 mL 1,1,1,3,3,3-hexafluoro-2-propanol (HFIP). Acid-oxidized CNTs were then added to the HFIP solution of polycaprolactone/gelatin and dissolved using vortexing until the solution became homogeneous. In preparation for electrospinning, the polymer solution was placed into a 5 mL syringe fitted with a needle (tip diameter = 0.96 mm) and attached to a syringe pump that provided a steady solution flow rate. A voltage was applied to the needle using a high voltage power supply; the tip-to-collector distance was fixed.

**2.5. Preparation of CNT/Polycaprolactone/Gelatin Films.** CNT/polycaprolactone/gelatin (PGC) thin films were prepared using the spin-coating method. The PGC solution was spin-coated onto cover glass (diameter = 10 mm) at 4000 rpm for 3 seconds. The films were dried in air at room temperature.

**2.6. Characterization of the Electrospun Nanofibers.** The morphologies of the PG and PGC fibers were examined by scanning electron microscopy (Hitachi S-4800). Briefly, the electrospun matrices were sputter-coated with gold and then visualized using a scanning electron microscope (accelerating voltage = 5 kV). The diameters of the fibers were determined manually from the SEM images using ImageJ (ImageJ software 1.42, National Institutes of Health, USA).

**2.7. Schwann Cell Culture on PG and PGC Matrices.** PG and PGC matrices were placed in 24-well tissue culture plates containing a suspension of RT4-D6P2T rat Schwann cells (BCRC no. 60508) ( $5 \times 10^4$  cells/well) in DMEM supplemented with 10% v/v FBS, 100 U/mL of penicillin, and 100 µg/mL of streptomycin. The cultures of these cell-seeded matrices were harvested after 4 hours so that cell attachment assays could be completed and on days 1, 3, 5, and 7 so that cell proliferation assays could be performed. Cell viabilities were determined using MTT assays. In each experiment, the amount of dye formed was immediately measured using a microplate reader (Biotek uQuant) (wavelength = 570 nm). At each time point, the number of cells attached to three matrices was measured.

**2.8. Fluorescent Staining of the Cytoskeleton.** The morphologies of the cells were examined by fluorescently staining their F-actin cytoskeletons with fluorescein isothiocyanate-(FITC-) conjugated phalloidin and their nuclei with DAPI. Cells were cultured for 1 day, fixed with 3.7% paraformaldehyde in phosphate buffer for 10 minutes, and washed twice with 0.02 M PBS (pH 7.4). The cells were then rinsed in PBS containing 0.1% Triton X-100 for 5 minutes. The samples were blocked with 1% bovine serum albumin (BSA) in PBS for 1 hour to reduce nonspecific background staining. After blocking, the BSA solution was aspirated, and the samples were incubated with 6.4 µM FITC-conjugated phalloidin for 20 minutes. The cells were then incubated with a solution of DAPI for 5 minutes to stain the DNA in the cells. The samples

TABLE 1: Sample notation, electrospinning parameters, and average diameters of random PG and PGC nanofibers.

Sample notation	Polycaprolactone concentration (mg/mL)	Gelatin concentration (mg/mL)	Carbon nanotube concentration (mg/mL)	Electrospinning parameters (applied voltage, working distance, and flow rate)	Average diameter $\pm$ standard deviation (nm)
PG	42.55	42.55	0	15 kV, 15 cm, 3.81 mL/hour	671 $\pm$ 145
PG3C	42.55	42.55	3.54	15 kV, 15 cm, 3.81 mL/hour	331 $\pm$ 111
PG5C	42.55	42.55	4.47	15 kV, 15 cm, 3.81 mL/hour	440 $\pm$ 140

were washed three times with PBS (for 5 minutes each) and analyzed using a fluorescence microscope.

**2.9. Immunoblotting Analysis.** Cells were seeded on PG and PGC matrices ( $3 \times 10^4$  cells/cm<sup>2</sup>, in media). Immunoblotting was performed to detect the Schwann cell-specific proteins neuregulin 1 (NRG1) and myelin protein zero (P0) after 3 days of culture. Cells were collected and lysed in lysis buffer. The supernatants were obtained by centrifugation ( $15,000 \times g$  for 10 minutes) at 4°C. The concentration of protein was analyzed using a Bradford Coomassie assay. The proteins (30  $\mu\text{g}/\mu\text{L}$ ) were fractionated by electrophoresis and electrotransferred to a polyvinylidene difluoride film (PVDF). Blocking was performed using 5% w/v nonfat milk, and primary antibodies were applied to the membrane overnight at 4°C. The primary antibodies were diluted with fresh blocking buffer to the designated concentration and applied to the membrane at 4°C overnight. Antibodies specific to NRG1 (Santa Cruz Biotechnology, Inc., sc-28916), P0 (Santa Cruz Biotechnology, Inc., sc-18531), and nucleophosmin B23 (Invitrogen 325200) were used. After incubation with a secondary antibody, the immunoreactive bands were visualized using enhanced chemiluminescence detection (Millipore WBKLS0500). Nucleophosmin B23 was used as the internal control.

### 3. Results and Discussion

The pristine CNTs were quite hydrophobic. Hence, the pristine CNTs precipitated from the HFIP solution. Nitric acid was used to introduce oxygen-containing functional groups, such as carboxylic acids and hydroxyls, onto the ends and defect sites of the CNT surfaces [19]. Figure 1 shows the ATR-FTIR spectra of pristine CNTs and acid-oxidized CNTs. The absorption peaks centered at  $1594 \text{ cm}^{-1}$  correspond to the asymmetric  $-\text{COO}-$  stretching bands. The absorption peaks at  $3443 \text{ cm}^{-1}$  correspond to the  $-\text{OH}$  stretch. We found that the acid-oxidized CNTs have better dispersibility in HFIP. The zeta potentials of the pristine CNTs and acid-oxidized CNTs were measured to be  $-5.05 \pm 0.56 \text{ mV}$  and  $-23.8 \pm 0.87 \text{ mV}$ , respectively.

Figure 2 shows transmission electron microscopy images of nanofibers containing PG and PGC. Individual CNTs were successfully embedded in the polycaprolactone/gelatin nanofibers, indicating that the original dispersion contained individual CNTs rather than CNT aggregates.

Under the same electrospinning conditions, the fiber diameters were  $671 \pm 145 \text{ nm}$ ,  $331 \pm 111 \text{ nm}$ , and  $440 \pm 140 \text{ nm}$

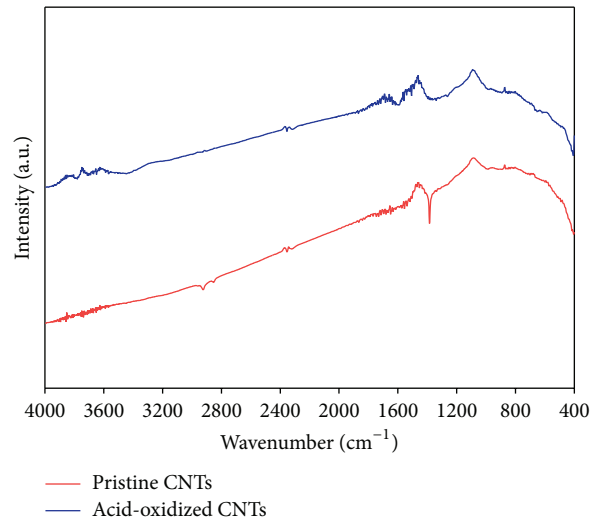


FIGURE 1: ATR-FTIR spectra of pristine CNTs and acid-oxidized CNTs.

for PG, PG3C, and PG5C matrices, respectively (Table 1 and Figure 3). The diameters of the fibers decreased and then increased as the concentration of CNTs was increased. The conductivity of the polymer was increased when the CNTs were added. Previously, we found that when the charge density on the surface of the electrospinning jet was increased, higher electrostatic forces were induced, resulting in the formation of smaller diameter fibers [20]. In addition, the viscosity of the polymer solution also affects the diameter of the nanofibers. The diameters of the electrospun fibers increased as the viscosity of the polymer solution increased [21]. The viscosity of the polymer solution also increased when CNTs were added. These factors likely explain why the mean fiber diameters decrease when lower CNTs concentrations are used and increase when higher CNTs concentrations are used.

A schematic of the experimental setup used to align the fibers is shown in Figure 4(a). A cylinder collector was used to gather the aligned nanofibers. The radius of the cylinder collector was 7.6 cm, and the rotation speed of the mandrel was set to 13 rpm. The distance between the two pieces of parallel conductive carbon tape was 2 cm. A cross section of the cylinder collector is shown in Figure 4(b). The literature has demonstrated that the diameters of the electrospun fibers can affect cell behavior [22–24]. We fabricated aligned PG and aligned PGC fibers with similar diameters by adjusting the parameters of the experiment.

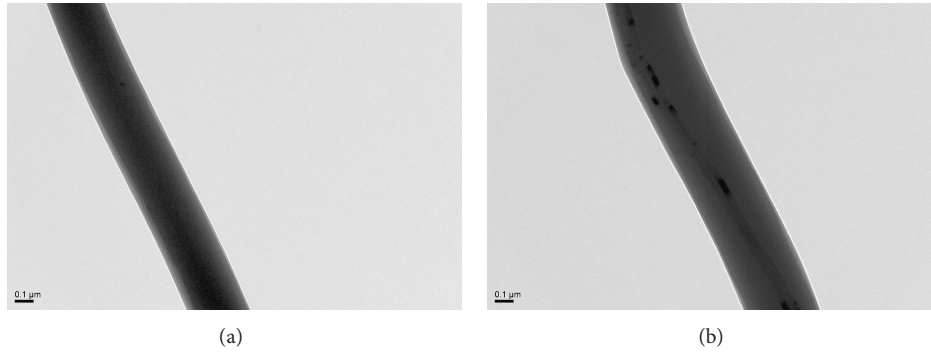


FIGURE 2: Transmission electron microscopy images of (a) a PG and (b) a PGC nanofiber.

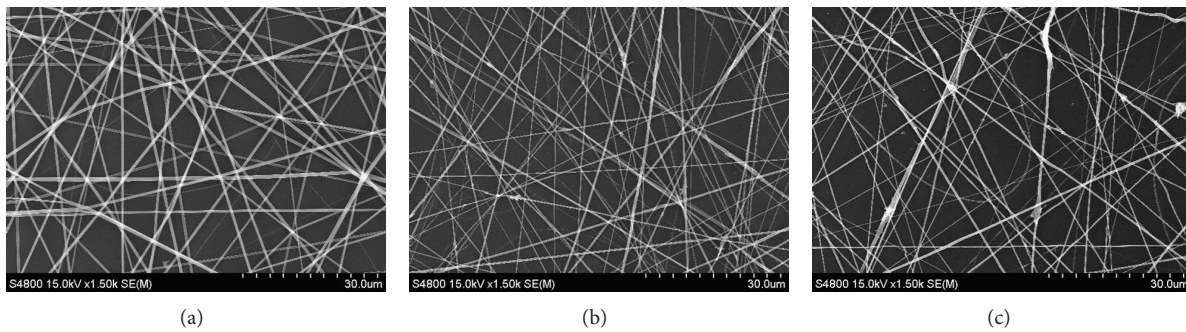


FIGURE 3: Scanning electron microscopy images of randomly oriented (a) PG, (b) PG3C, and (c) PG5C nanofibers.

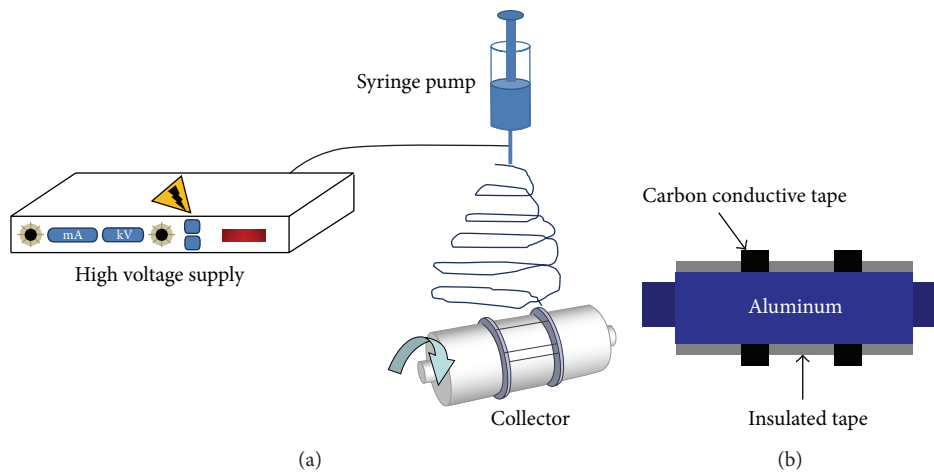


FIGURE 4: (a) Schematic illustration of the electrospinning setup. (b) Profile of the aligned nanofiber collector.

TABLE 2: Sample notation, electrospinning parameters, average diameters, and angular distributions of aligned PG and PGC nanofibers.

Sample notation	Polycaprolactone concentration (mg/mL)	Gelatin concentration (mg/mL)	Carbon nanotube concentration (mg/mL)	Electrospinning parameters (applied voltage, working distance, and flow rate)	Average diameter $\pm$ standard deviation (nm)	Angular distribution of aligned nanofibers (full width at half maximum, degrees)
PG	42.55	42.55	0	15 kV, 15 cm, 0.51 mL/hour	$785 \pm 155$	26
PG3C	42.55	42.55	3.54	20 kV, 15 cm, 0.76 mL/hour	$828 \pm 169$	21
PG5C	42.55	42.55	4.47	20 kV, 10 cm, 6.36 mL/hour	$710 \pm 156$	43

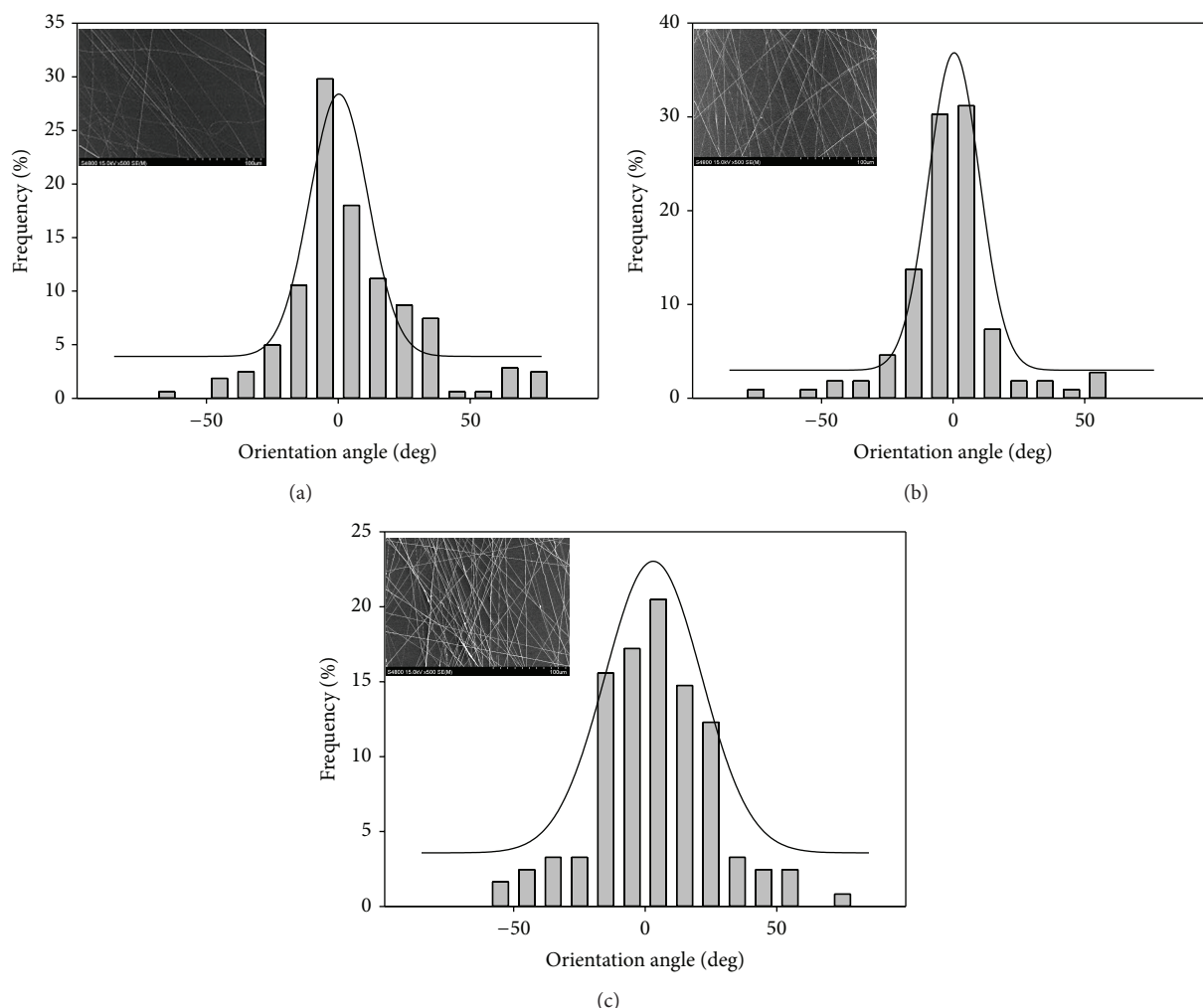


FIGURE 5: Distributions of the orientation angles between the long axes of the nanofibers and their expected directions: (a) PG, (b) PG3C, and (c) PG5C. The black lines are Gaussian fits to the data. These results were based on measurements of more than 100 nanofibers. The insets show scanning electron microscopy images of the corresponding nanofibers.

The diameters of the synthesized fibers were  $785 \pm 155$  nm,  $828 \pm 169$  nm, and  $710 \pm 156$  nm for the PG, PG3C, and PG5C systems, respectively (Figure 5 and Table 2). The diameters of these fibers were not significantly different ( $P > 0.05$ ). The average orientation angles of the nanofibers were measured using SEM. The angular distributions of the nanofibers were determined by fitting the relative frequencies of the angle between the long axes of the fibers and their expected direction for each sample to a Gaussian curve. The full width at half maximum (FWHM) values of these curves was  $26^\circ$ ,  $21^\circ$ , and  $43^\circ$  for the PG, PG3C, and PG5C samples, respectively (Figure 5). In the past, researchers have used high-speed ( $>500$  rpm) rotating cylinder collectors to fabricate aligned electrospun nanofibers [25, 26]. In this study, we fabricated aligned electrospun nanofibrous matrices at much slower speeds; the alignment direction of the nanofibers is along the longitudinal axis of the mandrel. However, we found that the CNTs influenced the alignment of the nanofibers.

Cell behaviors, including adhesion, spreading, proliferation, and differentiation, are sensitive to the surface topography and molecular composition of the matrix. To evaluate the effect of the CNTs on cell behavior, we incubated RT4-D6P2T rat Schwann cells on PG and PGC nanofiber and film matrices. The attachment and proliferation rates of the Schwann cells gradually decreased when the amount of CNTs was gradually increased when either PGC nanofiber matrices or PGC film matrices were used (Figure 6). Behan et al. [9] found that although CNTs have little effect on Schwann cell viability, they do inhibit their ability to proliferate. Kaiser et al. [27, 28] also demonstrated that CNTs can attach to integrin receptors and can therefore affect cell functions, such as adhesion, spreading, focal adhesion, and cytoskeletal development. Schwann cells proliferated more actively on PGC nanofiber matrices than on PGC film matrices. The CNTs likely disperse on the surface of the PGC film matrices and directly interfere with cell proliferation (Figure 7). However, the CNTs are embedded in the nanofibers of

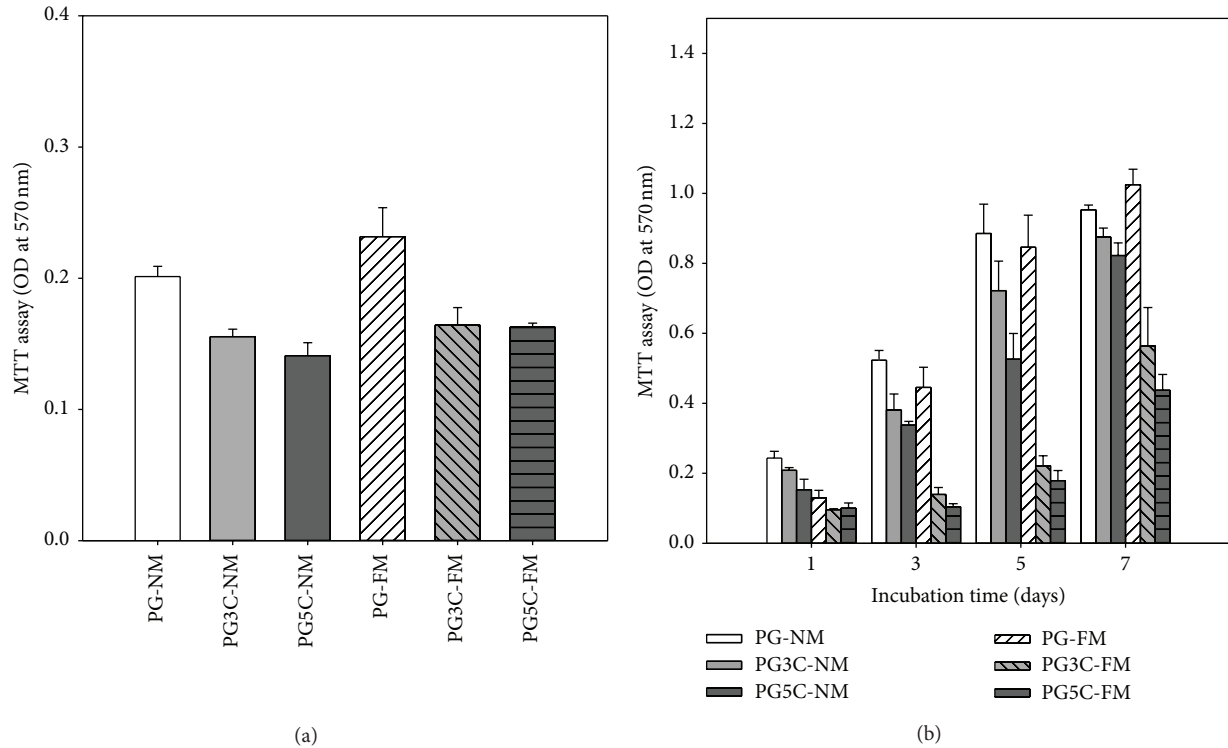


FIGURE 6: (a) The attachment of RT4-D6P2T Schwann cell lines on various matrices after 4 hours of culturing. (b) The viabilities of RT4-D6P2T Schwann cell lines on various matrices after up to 7 days of culture as assessed by the MTT method. Data are presented as the mean  $\pm$  SD ( $n = 6$ ).

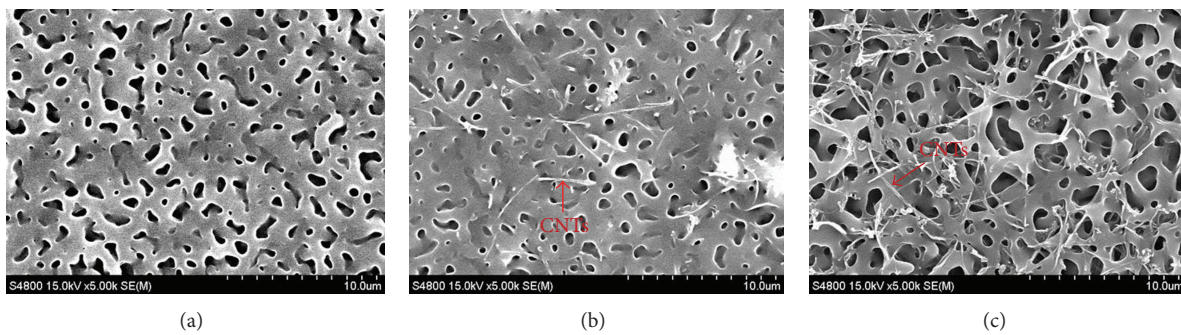


FIGURE 7: Scanning electron microscopy images of (a) PG, (b) PG3C, and (c) PG5C film matrices.

the PGC nanofibrous matrices, reducing their interaction with the Schwann cells.

The morphologies of the Schwann cells that adhered to the PG and PGC nanofiber and film matrices were investigated. Their actin cytoskeletons were stained with FITC-phalloidin and visualized using a fluorescence microscope. The Schwann cells aligned along the direction of the nanofibers with typical bipolar morphologies (Figures 8(a)–8(c)). However, Schwann cells attached to the film matrices in random directions (Figures 8(d)–8(f)).

Schwann cells are heavily involved in the peripheral nerve repair process. These cells synthesize and secrete important substances, such as myelin protein zero (P0) and neuregulin 1 (NRG1). NRG1 is essential for the myelination of axons

and the development of Schwann cells [29]. P0 is expressed by myelinating Schwann cells, and it is the major adhesive and structural protein of the myelin sheath surrounding peripheral nerves [30, 31]. Some studies have demonstrated that P0 promotes the regeneration of injured axons [32]. Using western blot analysis, we found that the NRG1 and P0 protein expression levels were higher for cells immobilized on the PGC nanofibrous matrices than for those immobilized on the PG nanofibrous matrices. However, the CNTs inhibited NRG1 and P0 protein expression in Schwann cells immobilized on the PGC film matrices. Moreover, the NRG1 and P0 protein expression levels were higher for cells immobilized on the PGC nanofibrous matrices than for those immobilized on the PGC film matrices (Figure 9). These results suggest that

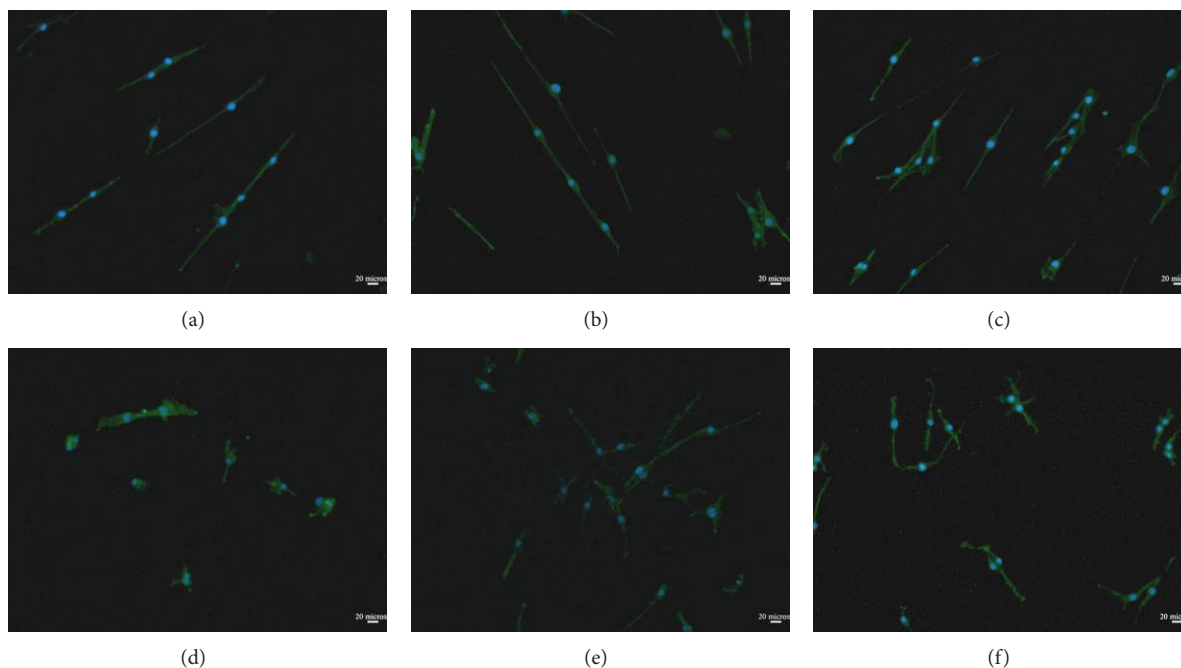


FIGURE 8: Fluorescent microscopy micrographs of RT4-D6P2T Schwann cell lines cultured for 1 hour on electrospun matrices of (a) PG-NM, (b) PG3C-NM, (c) PG5C-NM, (d) PG-FM, (e) PG3C-FM, and (f) PG5C-FM. NM: nanofibrous matrix; FM: film matrix.

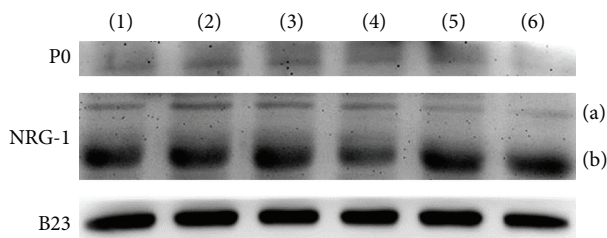


FIGURE 9: Western blot analyses of NRG1, P0, and B23 proteins in RT4-D6P2T Schwann cells cultured for 3 days. Line 1: PG-NM, Line 2: PG3C-NM, Line 3: PG5C-NM, Line 4: PG-FM, Line 5: PG3C-FM, and Line 6: PG5C-FM. NM: nanofibrous matrix; FM: film matrix. Nrg1: (a) neuregulin 1 precursor and (b) mature neuregulin 1.

Schwann cell maturation is favored on fibrous matrices, as opposed to film matrices, and that CNTs enhance Schwann cell maturation on PGC fibrous matrices.

#### 4. Conclusion

Schwann cells grown on aligned CNT/polycaprolactone/gelatin nanofibrous matrices show higher cell proliferation levels, align along the directionality of the nanofibres with typical bipolar morphologies, and exhibit higher levels of P0 protein expression compared to those grown on CNT/polycaprolactone/gelatin film matrices. These findings suggest that the CNT/polycaprolactone/gelatin nanofibrous matrices could potentially be used for the repair of injured peripheral nerves.

#### Conflict of Interests

The authors declare that there is no conflict of interests regarding the publication of this paper.

#### References

- [1] T. E. Trumble and F. G. Shon, "The physiology of nerve transplantation," *Hand Clinics*, vol. 16, no. 1, pp. 105–122, 2000.
- [2] P. J. Evans, R. Midha, and S. E. Mackinnon, "The peripheral nerve allograft: a comprehensive review of regeneration and neuroimmunology," *Progress in Neurobiology*, vol. 43, no. 3, pp. 187–233, 1994.
- [3] J. L. Platt, G. M. Vercellotti, A. P. Dalmaso et al., "Transplantation of discordant xenografts: a review of progress," *Immunology Today*, vol. 11, no. 12, pp. 450–457, 1990.
- [4] H. M. Lin, Y. H. Lin, and F. Y. Hsu, "Preparation and characterization of mesoporous bioactive glass/polycaprolactone nanofibrous matrix for bone tissues engineering," *Journal of Materials Science: Materials in Medicine*, vol. 23, no. 11, pp. 2619–2630, 2012.
- [5] H. M. Liou, L. R. Rau, C. C. Huang, M. R. Lu, and F. Y. Hsu, "Electrospun hyaluronan-gelatin nanofibrous matrix for nerve tissue engineering," *Journal of Nanomaterials*, vol. 2013, Article ID 613638, 9 pages, 2013.
- [6] J. Zhan and P. Lan, "The review on electrospun gelatin fiber scaffold," *Journal of Research Updates in Polymer Science*, vol. 1, no. 2, pp. 59–71, 2012.
- [7] F. Mottaghitlab, M. Farokhi, A. Zaminy et al., "A biosynthetic nerve guide conduit based on silk/SWNT/fibronectin nanocomposite for peripheral nerve regeneration," *PLoS ONE*, vol. 8, no. 10, Article ID e74417, 2013.

- [8] A. Fabbro, M. Prato, and L. Ballerini, "Carbon nanotubes in neuroregeneration and repair," *Advanced Drug Delivery Reviews*, vol. 65, no. 15, pp. 2034–2044, 2013.
- [9] B. L. Behan, D. G. DeWitt, D. R. Bogdanowicz, A. N. Koppes, S. S. Bale, and D. M. Thompson, "Single-walled carbon nanotubes alter Schwann cell behavior differentially within 2D and 3D environments," *Journal of Biomedical Materials Research A*, vol. 96, no. 1, pp. 46–57, 2011.
- [10] S. Liao, B. Li, Z. Ma, H. Wei, C. Chan, and S. Ramakrishna, "Biomimetic electrospun nanofibers for tissue regeneration," *Biomedical Materials*, vol. 1, no. 3, pp. R45–R53, 2006.
- [11] D. R. Nisbet, J. S. Forsythe, W. Shen, D. I. Finkelstein, and M. K. Horne, "Review paper: a review of the cellular response on electrospun nanofibers for tissue engineering," *Journal of Biomaterials Applications*, vol. 24, no. 1, pp. 7–29, 2009.
- [12] S. Y. Chew, R. Mi, A. Hoke, and K. W. Leong, "The effect of the alignment of electrospun fibrous scaffolds on Schwann cell maturation," *Biomaterials*, vol. 29, no. 6, pp. 653–661, 2008.
- [13] P. Katta, M. Alessandro, R. D. Ramsier, and G. G. Chase, "Continuous electrospinning of aligned polymer nanofibers onto a wire drum collector," *Nano Letters*, vol. 4, no. 11, pp. 2215–2218, 2004.
- [14] W. E. Teo, M. Kotaki, X. M. Mo, and S. Ramakrishna, "Porous tubular structures with controlled fibre orientation using a modified electrospinning method," *Nanotechnology*, vol. 16, no. 6, pp. 918–924, 2005.
- [15] D. Li, Y. Wang, and Y. Xia, "Electrospinning of polymeric and ceramic nanofibers as uniaxially aligned arrays," *Nano Letters*, vol. 3, no. 8, pp. 1167–1171, 2003.
- [16] J. A. Matthews, G. E. Wnek, D. G. Simpson, and G. L. Bowlin, "Electrospinning of collagen nanofibers," *Biomacromolecules*, vol. 3, no. 2, pp. 232–238, 2002.
- [17] T. A. Ferguson and Y. J. Son, "Extrinsic and intrinsic determinants of nerve regeneration," *Journal of Tissue Engineering*, vol. 2, no. 1, Article ID 2041731411418392, 2011.
- [18] Y. Xiao, T. Gong, and S. Zhou, "The functionalization of multi-walled carbon nanotubes by in situ deposition of hydroxyapatite," *Biomaterials*, vol. 31, no. 19, pp. 5182–5190, 2010.
- [19] V. Datsyuk, M. Kalyva, K. Papagelis et al., "Chemical oxidation of multiwalled carbon nanotubes," *Carbon*, vol. 46, no. 6, pp. 833–840, 2008.
- [20] F. Y. Hsu, Y. S. Hung, H. M. Liou, and C. H. Shen, "Electrospun hyaluronate-collagen nanofibrous matrix and the effects of varying the concentration of hyaluronate on the characteristics of foreskin fibroblast cells," *Acta Biomaterialia*, vol. 6, no. 6, pp. 2140–2147, 2010.
- [21] C. Henriques, R. Vidinha, D. Botequim, J. P. Borges, and J. A. M. C. Silva, "A systematic study of solution and processing parameters on nanofiber morphology using a new electrospinning apparatus," *Journal of Nanoscience and Nanotechnology*, vol. 9, no. 6, pp. 3535–3545, 2009.
- [22] J. Wang, R. Ye, Y. Wei et al., "The effects of electrospun TSF nanofiber diameter and alignment on neuronal differentiation of human embryonic stem cells," *Journal of Biomedical Materials Research A*, vol. 100, no. 3, pp. 632–645, 2012.
- [23] Y. Liu, Y. Ji, K. Ghosh, R. A. F. Clark, L. Huang, and M. H. Rafailovich, "Effects of fiber orientation and diameter on the behavior of human dermal fibroblasts on electrospun PMMA scaffolds," *Journal of Biomedical Materials Research A*, vol. 90, no. 4, pp. 1092–1106, 2009.
- [24] H. B. Wang, M. E. Mullins, J. M. Cregg, C. W. McCarthy, and R. J. Gilbert, "Varying the diameter of aligned electrospun fibers alters neurite outgrowth and Schwann cell migration," *Acta Biomaterialia*, vol. 6, no. 8, pp. 2970–2978, 2010.
- [25] N. Bhattarai, D. Edmondson, O. Veisoh, F. A. Matsen, and M. Zhang, "Electrospun chitosan-based nanofibers and their cellular compatibility," *Biomaterials*, vol. 26, no. 31, pp. 6176–6184, 2005.
- [26] C. Vaquette, C. Kahn, C. Frochot et al., "Aligned poly(L-lactic-co-ε-caprolactone) electrospun microfibers and knitted structure: a novel composite scaffold for ligament tissue engineering," *Journal of Biomedical Materials Research A*, vol. 94, no. 4, pp. 1270–1282, 2010.
- [27] J. P. Kaiser, T. Buerki-Thurnherr, and P. Wick, "Influence of single walled carbon nanotubes at subtoxic concentrations on cell adhesion and other cell parameters of human epithelial cells," *Journal of King Saud University—Science*, vol. 25, no. 1, pp. 15–27, 2013.
- [28] J. Kaiser, P. Wick, P. Manser, P. Spohn, and A. Bruinink, "Single walled carbon nanotubes (SWCNT) affect cell physiology and cell architecture," *Journal of Materials Science: Materials in Medicine*, vol. 19, no. 4, pp. 1523–1527, 2008.
- [29] K. Nave and J. L. Salzer, "Axonal regulation of myelination by neuregulin 1," *Current Opinion in Neurobiology*, vol. 16, no. 5, pp. 492–500, 2006.
- [30] D. D'Urso, P. J. Brophy, S. M. Staugaitis et al., "Protein zero of peripheral nerve myelin: biosynthesis, membrane insertion, and evidence for homotypic interaction," *Neuron*, vol. 4, no. 3, pp. 449–460, 1990.
- [31] D. M. Menichella, E. J. Arroyo, R. Awatramani et al., "Protein Zero is necessary for E-cadherin-mediated adherens junction formation in Schwann cells," *Molecular and Cellular Neuroscience*, vol. 18, no. 6, pp. 606–618, 2001.
- [32] L. B. Spiryda, "Myelin protein zero and membrane adhesion," *Journal of Neuroscience Research*, vol. 54, no. 2, pp. 137–146, 1998.

## Research Article

# Tunable Structures and Properties of Electrospun Regenerated Silk Fibroin Mats Annealed in Water Vapor at Different Times and Temperatures

Xiangyu Huang,<sup>1</sup> Suna Fan,<sup>1</sup> Alhadi Ibrahim Mohammed Altayp,<sup>1</sup> Yaopeng Zhang,<sup>1</sup> Huili Shao,<sup>1</sup> Xuechao Hu,<sup>1</sup> Minkai Xie,<sup>2</sup> and Yuemin Xu<sup>2</sup>

<sup>1</sup> State Key Laboratory for Modification of Chemical Fibers and Polymer Materials, College of Materials Science and Engineering, Donghua University, Shanghai 201620, China

<sup>2</sup> Department of Urology, Shanghai Jiaotong University Affiliated Sixth People's Hospital, Shanghai 200233, China

Correspondence should be addressed to Yaopeng Zhang; zyp@dhu.edu.cn and Yuemin Xu; xuyuemin@263.com

Received 26 February 2014; Accepted 12 April 2014; Published 5 May 2014

Academic Editor: Huarong Nie

Copyright © 2014 Xiangyu Huang et al. This is an open access article distributed under the Creative Commons Attribution License, which permits unrestricted use, distribution, and reproduction in any medium, provided the original work is properly cited.

Regenerated silk fibroin (SF) mats were fabricated using electrospinning technique, followed by mild water vapor annealing to effectively tune the structures and improve the mechanical properties of the mats at different annealing times and temperatures. The breaking strength and the breaking energy of the mats treated with water vapor at 65°C for 12 h reached 6.0 MPa and 171.7 J/kg, respectively. The conformational transition of the SF mats was significantly influenced by the treating temperature, while the influence of time was comparatively limited. The influence is consistent with the time-temperature equivalent principle and would be helpful for the preparation of water-vapor-annealed silk-based biomaterials for various applications.

## 1. Introduction

Silk fibroin (SF), the main component of natural silks from *Bombyx mori* silkworms, has contributed to the outstanding mechanical properties, excellent biocompatibility, and controllable biodegradability of silks [1]. Recently, many SF-based materials have been developed in different forms for biomedical applications, such as scaffolds, hydrogels, porous sponges, tubes, microspheres, and fibers [2–10]. In these forms of SF, electrospun SF mats exhibit similar morphological structure to the native extracellular matrix (ECM), which may greatly promote the cell attachment and proliferation on this material [11, 12].

Before the electrospun SF mats are applied in tissue engineering, they always require certain types of posttreatment to enhance their mechanical properties and stability in water. Most of the reported posttreatment methods are based on the chemical agents, especially the aqueous alcoholic solutions [13, 14]. However, the organic solvents may cause potential negative effects on human bodies. The soaking

process may also lead to the loss of embedded drugs, thereby limiting the applications of SF mats in drug-delivery fields [15]. Recently, a posttreatment method using water vapor annealing to induce the conformational transition in SF has been investigated due to its mild processing conditions and elimination of organic solvents. Min et al. [16] proved the mild characteristic of water vapor treatment through investigating cell behavior on water-vapor-treated SF nanofibers. Jeong et al. [17] confirmed that water vapor could successfully stabilize the SF matrices as alcohol vapor. However, the results of water vapor treatment may significantly depend on the treating time and the temperature. Therefore, in order to control the structures and properties of SF via water vapor annealing, it is necessary to investigate the detailed influence of temperature and time on SF. Hu et al. reported a method of temperature-controlled water vapor annealing to control the structures and properties of SF films [18]. However, the detailed influences of annealing time and temperature on SF mats are rarely reported. Moreover, the average diameter of the electrospun fibers is much smaller than the thickness of

films, so that the influences of posttreatment process on the mats may be significantly different from those on the films.

In this study, we provide an effective and easy-conducting approach to fabricate electrospun regenerated SF mats with tunable structures through water vapor annealing at different times and temperatures. Improved mechanical properties are desired to be achieved for further biomedical applications.

## 2. Experimental

**2.1. Materials.** *B. mori* cocoons produced in Zhejiang Province, China, were used as raw material to extract SF. Analytical-grade sodium carbonate ( $\text{Na}_2\text{CO}_3$ ) and lithium bromide (LiBr) were obtained from Sinopharm Chemical Reagent Co., Ltd. (Shanghai, China) and Zhongli Industrial Co., Ltd. (Shanghai, China), respectively. Cellulose semipermeable membranes with a molecular weight cutoff of  $14000 \pm 2000$  D were purchased from Yuanju Co., Ltd. (Shanghai, China).

**2.2. Preparation of Silk Fibroin and Electrospun Mats.** The *B. mori* cocoons were boiled twice in 0.5 wt%  $\text{Na}_2\text{CO}_3$  solution to remove sericin. Degummed silks were then dissolved in 9.0 M LiBr aqueous solution at  $40^\circ\text{C}$  for 2 h and further dialyzed in deionized water at  $10^\circ\text{C}$  for 3 days according to the established procedures [19]. Ultimately, a purified 33 wt% SF solution was obtained through concentrating at  $10^\circ\text{C}$ .

The SF mats were fabricated by electrospinning using the purified 33 wt% SF solution and were randomly collected on a grounded collector with a spinneret-to-collector distance of 10 cm. During electrospinning, a high voltage of 20 kV was applied and a flow rate of spinning dope was maintained at 1.2 mL/h. The details of this process can be found in our previous literature [20].

**2.3. Water Vapor Annealing on SF Mats.** A constant temperature and humidity chamber (HCP 108, Memmert GmbH + Co. KG, Germany) was used in the posttreatment process. Relative humidity (RH) in the chamber was fixed at  $90 \pm 1\%$ . In the temperature-controlled series, samples were treated with water vapor for 3 h at different temperatures: 45, 55, 65, and  $75^\circ\text{C}$ . In the time-controlled series, samples were treated with water vapor at  $65^\circ\text{C}$  for different times: 0.5, 1, 3, 6, 9, 12, 15, 18, and 24 h. After posttreatment, samples were dried in a sealed container with desiccant for 48 h before further characterization.

**2.4. Characterization.** The morphology of the SF mats was examined by scanning electron microscopy (SEM; JSM-5600LV, JEOL, Japan). Diameters of the electrospun fibers were measured directly from their SEM images using Image Tool software based on at least 100 fibers.

The secondary structure of the electrospun fibers was characterized by a Raman spectrometer (LabRAM-1 B, Dilor, France) at a  $1\text{ cm}^{-1}$  resolution. All samples were irradiated by a He-Ne laser with a wavelength of 632.8 nm. Spectra were recorded in the range of  $900\text{--}1800\text{ cm}^{-1}$ .

Wide angle X-ray diffraction (WAXD) patterns were obtained at the BL15U1 beamline in Shanghai Synchrotron Radiation Facility (SSRF) at a wavelength of 0.07746 nm. The sample-to-detector distance was calibrated using lanthanum hexaboride ( $\text{LaB}_6$ ) as a standard to 187 mm. Each specimen was exposed for 30 s and the corresponding background was recorded simultaneously. Data analysis was carried out by FIT2D software. Then a method reported previously was applied to calculate the crystallinity of the SF mats according to the diffractograms [21].

An Instron 5969 material testing instrument (Instron Co., USA) was applied to investigate the mechanical properties of the mats at  $25 \pm 5^\circ\text{C}$  and  $50 \pm 5\%$  RH. Thickness of the samples was tested by a CH-1-S thickness gauge (Shanghai Liuling Instruments Co., China). All samples were cut into  $5\text{ mm} \times 40\text{ mm}$  pieces for tensile test, which was conducted with an extension rate of 1 mm/min and a gauge length of 20 mm. At least 10 specimens were tested for each mat sample.

## 3. Results and Discussion

**3.1. Morphology and Nanostructure of SF Mats.** Figure 1 shows typical morphologies and diameter distribution histograms of the electrospun SF mats which were obtained by water vapor annealing at different conditions. As-spun mat was also shown in the figure for comparison. All water-vapor-annealed samples and the as-spun sample present smooth surface morphologies. When compared with the alcohol-treated or postdrawn SF mats with rough surface [20, 22], the water-vapor-annealed samples with smooth surface show obvious advantages. This suggests that the water vapor annealing is quite a mild posttreating method which would not cause severe damages to the fiber surface. And the diameter distribution histograms show that the diameters of fibers increase with the temperature. This is probably attributed to the significant swelling of SF fibers in water vapor during annealing.

**3.2. Secondary Structures of SF Mats.** The secondary structure transition of the SF fibers occurs in the water vapor annealing process. Figure 2 shows the Raman spectra of the SF mats posttreated at different times and temperatures. The assignments of the major bands in the spectra were based on literatures [23, 24]. Spectra of the as-spun fibers exhibit obvious bands relate to  $\alpha$ -helix ( $1103\text{ cm}^{-1}$ ), random coil ( $1251, 946\text{ cm}^{-1}$ ), and  $\beta$ -turn ( $1675\text{ cm}^{-1}$ ), which are somehow obscure in the posttreated samples. In addition, intense bands at  $1666\text{ cm}^{-1}$ ,  $1230\text{ cm}^{-1}$ , and  $1085\text{ cm}^{-1}$  which correspond to  $\beta$ -sheet conformation are observed in the spectra of the posttreated fibers. The varied intensities of the characteristic peaks suggest that the time and temperature definitely affect the structural transition of SF mats in different degrees.

To further investigate the relationships between secondary structure of the SF mats and annealing condition, we conducted the quantitative analysis in amide I region of Raman spectra. As shown in Figure 3, with prolonged time or raised temperature, the  $\beta$ -sheet content significantly increases accompanied with decreased contents of  $\alpha$ -helix

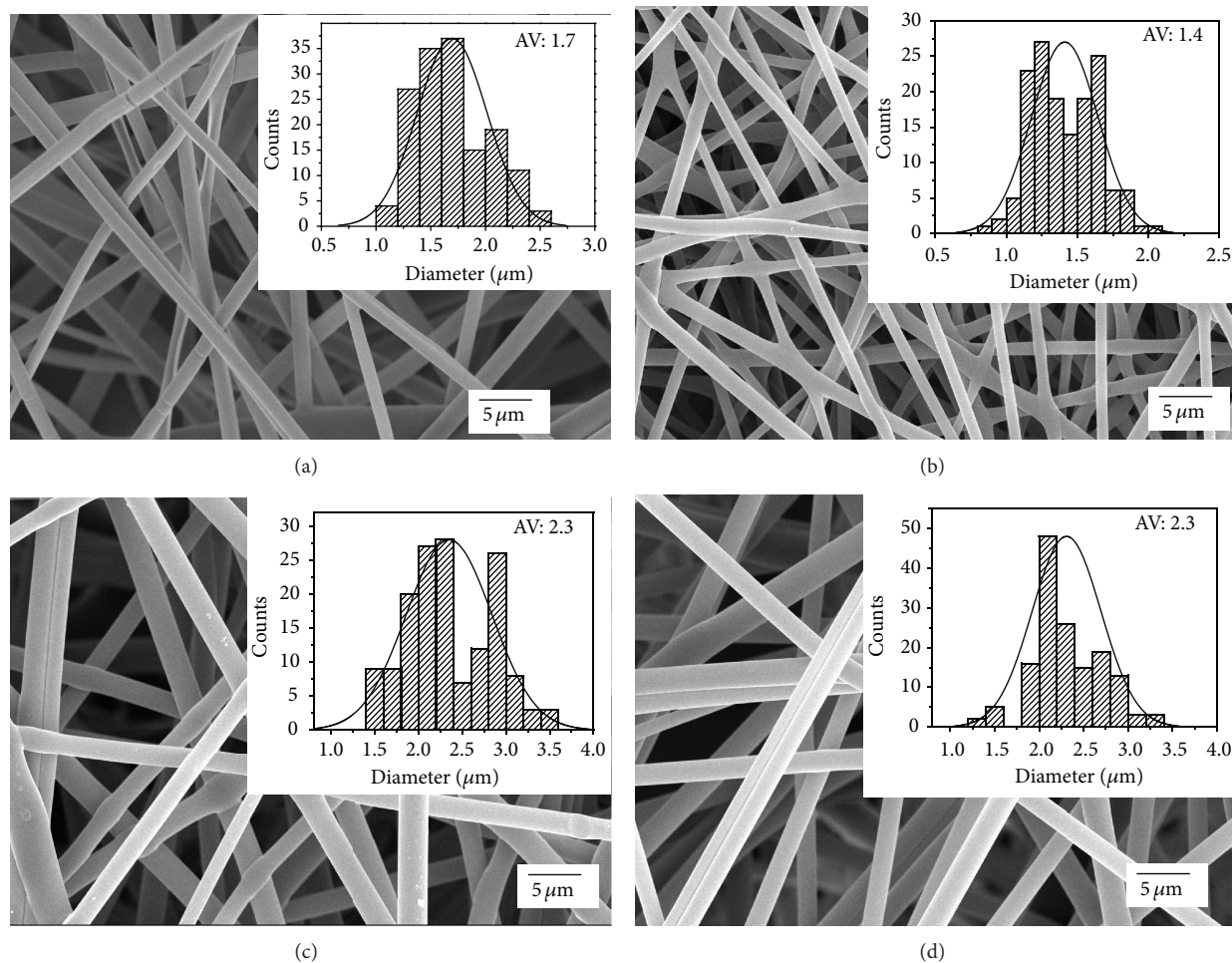


FIGURE 1: SEM images and diameter distribution histograms of water-vapor-annealed electrospun SF mats under different conditions: (a) as-spun; (b) 55°C-3 h; (c) 65°C-3 h; and (d) 65°C-9 h.

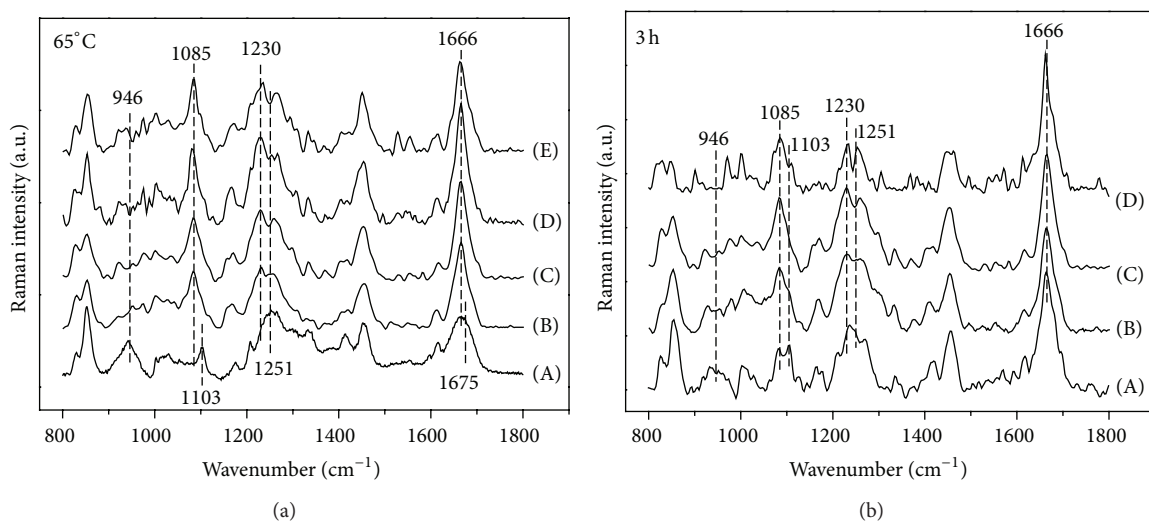


FIGURE 2: Raman spectra of electrospun SF fibers: (a) samples treated with water vapor at 65°C for different times: (A) as-spun, (B) 0.5 h, (C) 3 h, (D) 9 h, and (E) 24 h; (b) samples treated with water vapor for 3 h at different temperatures: (A) 45°C, (B) 55°C, (C) 65°C, and (D) 75°C.

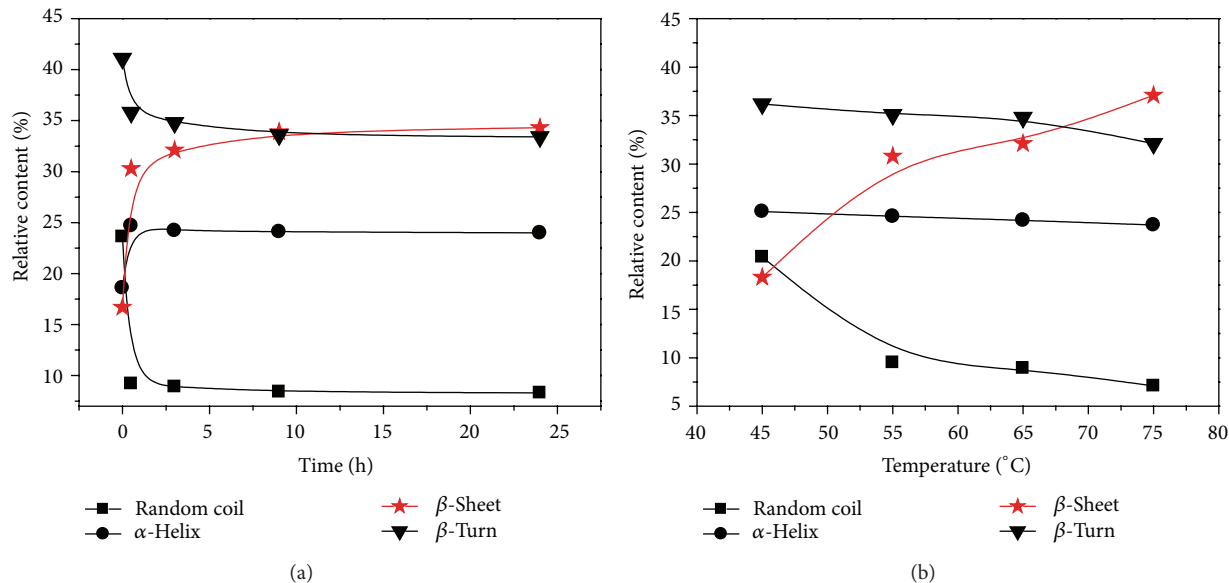


FIGURE 3: Quantitative analysis of the secondary structure components of electrospun SF fibers treated with water vapor at different conditions: (a) annealed at 65°C for different times; (b) annealed for 3 h at different temperatures.

(time > 0.5 h), random coil, and  $\beta$ -turn conformation. This suggests that SF mats with desired secondary structures can be achieved through controlling a single variable of either time or temperature during water vapor annealing. The SF mats annealed at 75°C for 3 h (37.1%) show an even higher  $\beta$ -sheet content than the mats treated at 65°C for 24 h (34.3%). This indicates that the increase of temperature may be more effective than time in inducing the conformation transition of SF. Apart from high temperature, water molecule is another indispensable factor in the formation of  $\beta$ -sheets. As proved by Hu et al. [25], the water-silk structure possesses a lower glass transition temperature than that of the pure dry silk. Therefore, during the water vapor annealing process, the high content of free water molecules may weaken the original intermolecular bonding force within SF and decrease the required energy for movements of amino acids [26]. Moreover, the high ambient temperature could provide more energy for the molecular movements. As a result, the high-temperature water vapor annealing successfully induces the conformational transition of SF. Mo et al. [27] also found that the formation of  $\beta$ -sheets in SF relates to the dissociation of hydrogen bonds between water and peptides and reformation of stronger hydrogen bonds between peptides themselves. Accordingly, we may be able to control the microstructure of SF materials accurately in a high-humidity environment by simply adjusting the ambient temperature.

**3.3. Crystalline Structure of SF Mats.** It has been reported that silk fibroin from the *B. mori* contains two forms of crystalline modifications, silk I and silk II, as well as the amorphous structure. Moreover, silk II is commonly considered to be constituted of  $\beta$ -sheets [28]. To further investigate the effects of water vapor annealing temperature and time on SF fibers, WAXD diffractograms (Figure 4) were obtained to

analyze the crystalline structure of SF according to Asakura's assignments [29]. Regardless of the temperature, all samples posttreated for different times (Figure 4(a)) exhibit apparent diffraction peaks at  $D$ -spacing of 0.226, 0.36, 0.43 nm which correspond to the reflection of silk II structure [30, 31]. Meanwhile, the characteristic reflection of amorphous structure at  $D$ -spacing of 0.407 nm is observed in the as-spun fibers, while it is absent in water-vapor-annealed fibers. It indicates that the crystallization rate of SF during water vapor annealing at 65°C is quite rapid. This relationship can be seen more obviously from Figure 5(a). During water vapor annealing at 65°C, the crystallinity of SF mats improves promptly from 35.5% to 47.3% within 1 h. However, when the annealing time prolongs from 1 to 24 h, the crystallinity keeps improving gradually and further reaches 52.2%. It can be concluded that time is an important factor to control the crystallization of SF mats during water vapor annealing and the rise of annealing time leads to a higher crystallinity. Nevertheless, the influence of time is rather limited, especially under a high ambient temperature.

Figure 4(b) shows the influence of temperature on SF mats during water vapor annealing. When the annealing time was fixed at 3 h, the characteristic reflection of silk I structure at  $D$ -spacing of 0.72 nm [32, 33] can be observed on the diffractograms at 45 and 55°C. At higher temperatures of 65 and 75°C, clear changes of the diffractograms occur. Not only silk I reflection at 0.72 nm disappears, but also silk II reflections become more intense with the increasing annealing temperature. It can be found from Figure 5(b) that the crystallinity of SF mats increases almost linearly from 45.1% to 51.5% with raising temperature from 45 to 75°C. The above results suggest that the temperature in water vapor annealing process could significantly influence the crystallization behavior of SF mats.

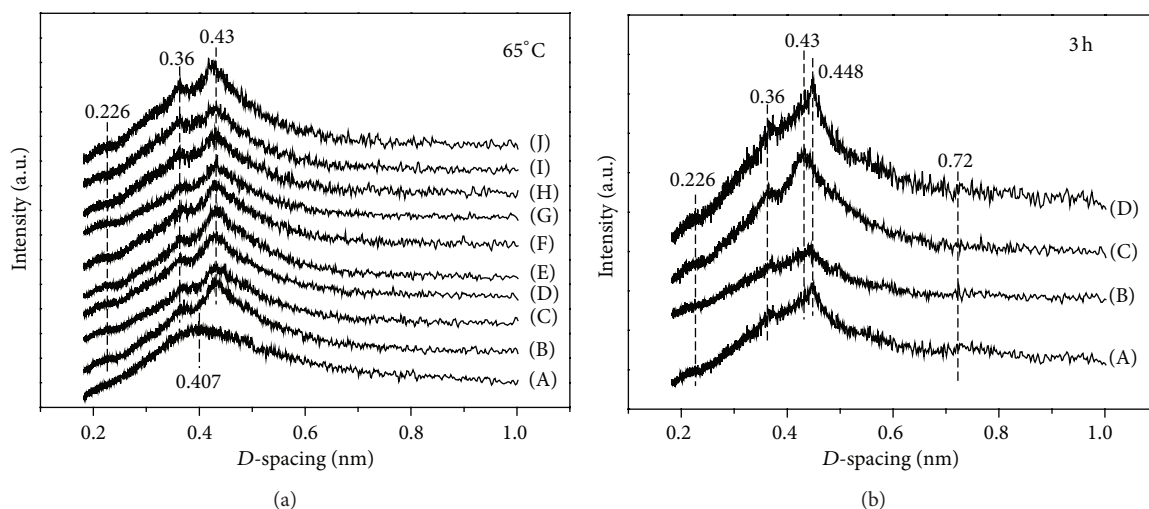


FIGURE 4: WAXD diffractograms of electrospun RSF fibers: (a) samples treated with water vapor at 65°C for different times: (A) as-spun, (B) 0.5 h, (C) 1 h, (D) 3 h, (E) 6 h, (F) 9 h, (G) 12 h, (H) 15 h, (I) 18 h, and (J) 24 h; (b) samples treated with water vapor for 3 h at different temperatures: (A) 45°C, (B) 55°C, (C) 65°C, and (D) 75°C.

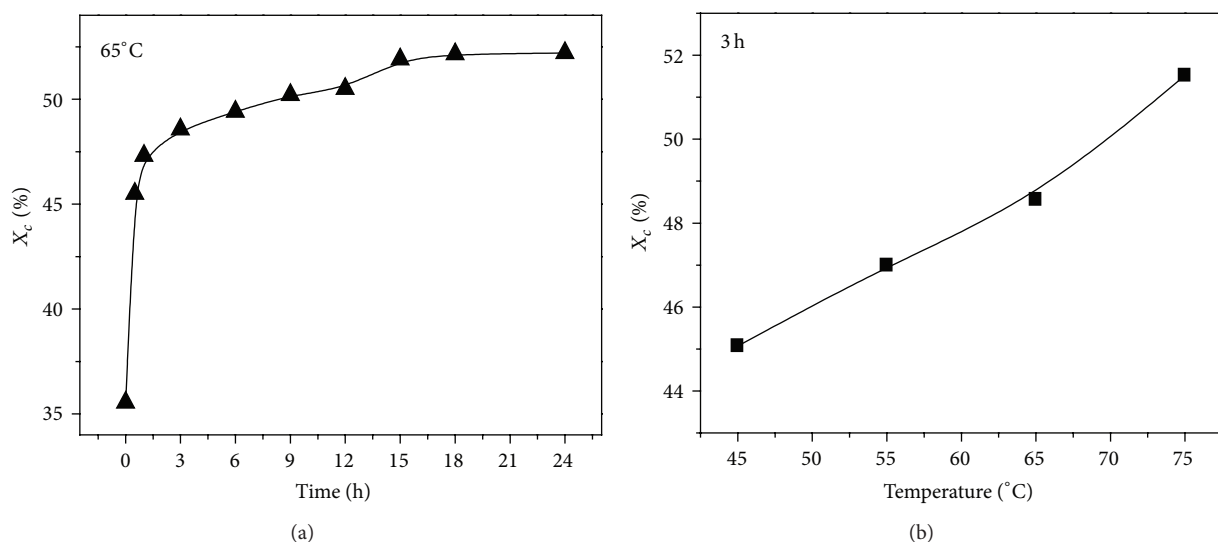


FIGURE 5: Crystallinities of electrospun RSF mats treated with water vapor: (a) at 65°C for different times; (b) for 3 h at different temperatures.

**3.4. Mechanical Properties of SF Mats.** The mechanical properties of the SF mats treated with water vapor at different temperatures and times are shown in Figure 6. It can be seen from Figure 6(a) that the breaking strength of the SF mats is greatly improved after annealing in water vapor at 65°C and gradually increases with prolonged treating time. When temperature rises, a more significant increasing trend of breaking strength can be found in Figure 6(b). The two curves of breaking strength in Figure 6 present great consistency with the corresponding crystallinity changes shown in Figure 5. This indicates that the potential SF materials with tunable properties and structures can be achieved by controlling the annealing time and temperature. Although the water-vapor-annealed SF mats do not have mechanical

properties comparable to those of the posttreated mats via uniaxial drawing in ethanol solution [20], the moderate characteristic of water vapor annealing is still quite attractive. The mild conditions would be favorable for drug loading and preparation of SF materials with enhanced and uniform mechanical properties [34]. When the mats are annealed at 65°C for 15 h, the breaking stress is improved to 6.0 MPa, which is about 4 times of the as-spun mats (1.8 MPa) [20]. The mats with similar properties could also be achieved within 3 h while raising the temperature to 75°C. This well exhibits the time-temperature equivalence, which may be attributed to the more energy that SF molecules absorbed for conformational transition in a longer annealing period or at a higher annealing temperature. From another aspect,

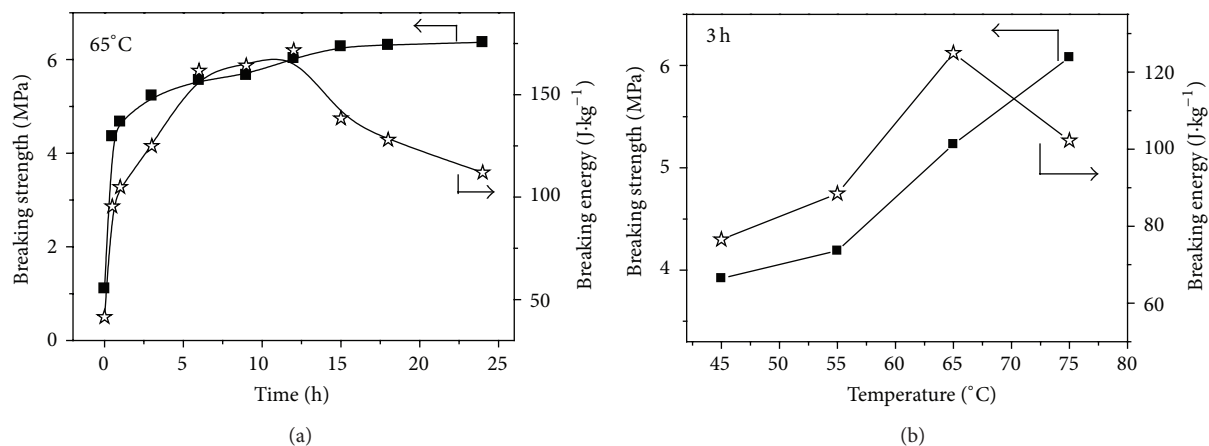


FIGURE 6: Breaking strength and breaking energy of electrospun RSF mats treated with water vapor: (a) at 65°C for different times; (b) for 3 h at different temperatures.

the motion of SF molecules is time dependent. The longer time could result in a more complete structure transition, namely, an increased content of the stable  $\beta$ -sheet structure in SF.

However, the breaking energy of the mats changes irregularly with annealing condition. It increases with annealing time or temperature first but decreases at an annealing time longer than 15 h in Figure 6(a) or at a temperature higher than 65°C in Figure 6(b). This may be attributed to the microstructure changes in SF fibers. With increasing treating time or temperature, the transformation from silk I to silk II is performed more completely. As the primary antiparallel  $\beta$ -sheet structure in silk II structure is more stable than the characterized  $\beta$ -turn type in silk I [35], the SF mats present a higher breaking elongation with increasing  $\beta$ -sheet content. When the crystallinity of SF mats is higher than 50%, the samples with low breaking strain become much brittle and the breaking energy decreases. This phenomenon is similar to the results of SF films [18].

#### 4. Conclusions

An effective and easy-conducting approach was developed to fabricate regenerated SF mats through water vapor annealing under different conditions of time and temperature. Water vapor can effectively induce the conformational transition of SF from random coil/ $\alpha$ -helix (silk I) to stable  $\beta$ -sheet (silk II) conformation and enhance the mechanical properties of the mats. The structures and properties of the SF mats significantly depend on the annealing time and temperature. Through improving the annealing temperature or prolonging the annealing time, we could achieve SF mats with tunable structures and enhanced mechanical properties. This water-based posttreatment provides a potential option to adjust the secondary structure and crystallinity of SF mats in mild conditions, thereby controlling the properties of SF mats for specific applications without using harmful chemicals. The water-vapor-annealed SF mats and other silk-based materials could be the promising candidates in biomedical

fields, including drug delivery, wound dressing, and tissue engineering.

#### Conflict of Interests

The authors declare that there is no conflict of interests regarding the publication of this paper.

#### Acknowledgments

This work is supported by the National Natural Science Foundation of China (21274018, 81170641), the Shanghai Rising Star Program (12QA1400100), the Innovation Program of the Shanghai Municipal Education Commission (12ZZ065), DHU Distinguished Young Professor Program (A201302), and the Fundamental Research Funds for the Central Universities.

#### References

- [1] D. L. Kaplan, "Silk polymers," in *Workshop on Silks: Biology, Structure, Properties, Genetics*, American Chemical Society, 1994.
- [2] S. Mobini, B. Hoyer, M. Solati-Hashjin et al., "Fabrication and characterization of regenerated silk scaffolds reinforced with natural silk fibers for bone tissue engineering," *Journal of Biomedical Materials Research A*, vol. 101, no. 8, pp. 2392–2404, 2013.
- [3] A. Seth, Y. G. Chung, E. S. Gil et al., "The performance of silk scaffolds in a rat model of augmentation cystoplasty," *Biomaterials*, vol. 34, no. 20, pp. 4758–4765, 2013.
- [4] T. Wang, L. I. Zhang, and X. j. He, "Preparation and characterization of a novel hybrid hydrogel composed of Bombyx mori fibroin and poly (n-isopropylacrylamide)," *Journal of Nanomaterials*, vol. 2013, Article ID 832710, 9 pages, 2013.
- [5] T. Zhong, Z. Xie, C. Deng, M. Chen, Y. Gao, and B. Zuo, "Copolymer-induced silk-based hydrogel with porous and nanofibrous structure," *Journal of Applied Polymer Science*, vol. 127, no. 3, pp. 2019–2024, 2013.

- [6] A. Sionkowska and A. Płancka, "Preparation and characterization of silk fibroin/chitosan composite sponges for tissue engineering," *Journal of Molecular Liquids*, vol. 178, pp. 5–14, 2013.
- [7] B. Marelli, A. Alessandrino, S. Farè, G. Freddi, D. Mantovani, and M. C. Tanzi, "Compliant electrospun silk fibroin tubes for small vessel bypass grafting," *Acta Biomaterialia*, vol. 6, no. 10, pp. 4019–4026, 2010.
- [8] X. Wang, E. Wenk, X. Zhang, L. Meinel, G. Vunjak-Novakovic, and D. L. Kaplan, "Growth factor gradients via microsphere delivery in biopolymer scaffolds for osteochondral tissue engineering," *Journal of Controlled Release*, vol. 134, no. 2, pp. 81–90, 2009.
- [9] Z. Zhu, Y. Kikuchi, K. Kojima et al., "Mechanical properties of regenerated bombyx mori silk fibers and recombinant silk fibers produced by transgenic silkworms," *Journal of Biomaterials Science, Polymer Edition*, vol. 21, no. 3, pp. 395–411, 2010.
- [10] Z. H. Zhu, K. Ohgo, and T. Asakura, "Preparation and characterization of regenerated Bombyx mori silk fibroin fiber with high strength," *Express Polymer Letters*, vol. 2, no. 12, pp. 885–889, 2008.
- [11] X. Zhang, M. R. Reagan, and D. L. Kaplan, "Electrospun silk biomaterial scaffolds for regenerative medicine," *Advanced Drug Delivery Reviews*, vol. 61, no. 12, pp. 988–1006, 2009.
- [12] B. M. Min, G. Lee, S. H. Kim, Y. S. Nam, T. S. Lee, and W. H. Park, "Electrospinning of silk fibroin nanofibers and its effect on the adhesion and spreading of normal human keratinocytes and fibroblasts in vitro," *Biomaterials*, vol. 25, no. 7–8, pp. 1289–1297, 2004.
- [13] G. M. Nogueira, A. C. D. Rodas, C. A. P. Leite et al., "Preparation and characterization of ethanol-treated silk fibroin dense membranes for biomaterials application using waste silk fibers as raw material," *Bioresource Technology*, vol. 101, no. 21, pp. 8446–8451, 2010.
- [14] A. L. Oliveira, L. Sun, H. J. Kim et al., "Aligned silk-based 3-D architectures for contact guidance in tissue engineering," *Acta Biomaterialia*, vol. 8, no. 4, pp. 1530–1542, 2012.
- [15] L. Fan, H. Wang, K. Zhang, C. He, Z. Cai, and X. Mo, "Regenerated silk fibroin nanofibrous matrices treated with 75% ethanol vapor for tissue-engineering applications," *Journal of Biomaterials Science, Polymer Edition*, vol. 23, no. 1–4, pp. 497–508, 2012.
- [16] B. M. Min, L. Jeong, K. Y. Lee, and W. H. Park, "Regenerated silk fibroin nanofibers: water vapor-induced structural changes and their effects on the behavior of normal human cells," *Macromolecular Bioscience*, vol. 6, no. 4, pp. 285–292, 2006.
- [17] L. Jeong, K. Y. Lee, J. W. Liu, and W. H. Park, "Time-resolved structural investigation of regenerated silk fibroin nanofibers treated with solvent vapor," *International Journal of Biological Macromolecules*, vol. 38, no. 2, pp. 140–144, 2006.
- [18] X. Hu, K. Shmelev, L. Sun et al., "Regulation of silk material structure by temperature-controlled water vapor annealing," *Biomacromolecules*, vol. 12, no. 5, pp. 1686–1696, 2011.
- [19] Y. Hang, Y. Zhang, Y. Jin, H. Shao, and X. Hu, "Preparation and characterization of electrospun silk fibroin/sericin blend fibers," *Journal of Materials Research*, vol. 26, no. 23, pp. 2931–2937, 2011.
- [20] S. Fan, Y. Zhang, H. Shao, and X. Hu, "Electrospun regenerated silk fibroin mats with enhanced mechanical properties," *International Journal of Biological Macromolecules*, vol. 56, pp. 83–88, 2013.
- [21] H. Pan, Y. Zhang, Y. Hang et al., "Significantly reinforced composite fibers electrospun from silk fibroin/carbon nanotube aqueous solutions," *Biomacromolecules*, vol. 13, no. 9, pp. 2859–2867, 2012.
- [22] W. Wei, Y. Zhang, Y. Zhao, H. Shao, and X. Hu, "Studies on the post-treatment of the dry-spun fibers from regenerated silk fibroin solution: Post-treatment agent and method," *Materials and Design*, vol. 36, pp. 816–822, 2012.
- [23] M. E. Rousseau, T. Lefèvre, L. Beaulieu, T. Asakura, and M. Pézolet, "Study of protein conformation and orientation in silk-worm and spider silk fibers using Raman microspectroscopy," *Biomacromolecules*, vol. 5, no. 6, pp. 2247–2257, 2004.
- [24] B. G. Frushour and J. L. Koenig, "Raman spectroscopic study of poly ( $\beta$  benzyl-L-aspartate) and sequential polypeptides," *Biopolymers*, vol. 14, no. 10, pp. 2115–2135, 1975.
- [25] X. Hu, D. Kaplan, and P. Cebe, "Dynamic protein-water relationships during  $\beta$ -sheet formation," *Macromolecules*, vol. 41, no. 11, pp. 3939–3948, 2008.
- [26] X. Hu, D. Kaplan, and P. Cebe, "Effect of water on the thermal properties of silk fibroin," *Thermochimica Acta*, vol. 461, no. 1–2, pp. 137–144, 2007.
- [27] C. Mo, P. Wu, X. Chen, and Z. Shao, "The effect of water on the conformation transition of Bombyx mori silk fibroin," *Vibrational Spectroscopy*, vol. 51, no. 1, pp. 105–109, 2009.
- [28] R. Fraser, *Conformation in Fibrous Proteins and Related Synthetic Polypeptides*, Elsevier Science, Amsterdam, The Netherlands, 2012.
- [29] T. Asakura, A. Kuzuhara, R. Tabeta, and H. Saitô, "Conformation characterization of Bombyx mori silk fibroin in the solid state by high-frequency  $^{13}\text{C}$  cross polarization-magic angle spinning NMR, x-ray diffraction, and infrared spectroscopy," *Macromolecules*, vol. 18, no. 10, pp. 1841–1845, 1985.
- [30] L. F. Drummy, D. M. Phillips, M. O. Stone, B. L. Farmer, and R. J. Naik, "Thermally induced  $\alpha$ -helix to  $\beta$ -sheet transition in regenerated silk fibers and films," *Biomacromolecules*, vol. 6, no. 6, pp. 3328–3333, 2005.
- [31] S. W. Ha, Y. H. Park, and S. M. Hudson, "Dissolution of bombyx mori silk fibroin in the calcium nitrate tetrahydrate-methanol system and aspects of wet spinning of fibroin solution," *Biomacromolecules*, vol. 4, no. 3, pp. 488–496, 2003.
- [32] O. Kratky, E. Schauenstein, and A. Sekora, "An unstable lattice in silk fibroin," *Nature*, vol. 165, no. 4191, pp. 319–320, 1950.
- [33] B. Lotz and H. D. Keith, "Crystal structure of poly(L-Ala-Gly)II. A model for silk I," *Journal of Molecular Biology*, vol. 61, no. 1, pp. 201–215, 1971.
- [34] B. Kundu, R. Rajkhowa, S. C. Kundu, and X. Wang, "Silk fibroin biomaterials for tissue regenerations," *Advanced Drug Delivery Reviews*, vol. 65, no. 4, pp. 457–470, 2013.
- [35] J. Ashida, K. Ohgo, K. Komatsu, A. Kubota, and T. Asakura, "Determination of the torsion angles of alanine and glycine residues of model compounds of spider silk (AGG)10 using solid-state NMR methods," *Journal of Biomolecular NMR*, vol. 25, no. 2, pp. 91–103, 2003.

## Research Article

# Effects of Electrode Reversal on the Distribution of Naproxen in the Electrospun Cellulose Acetate Nanofibers

Zhuang Li,<sup>1,2</sup> Hongliang Kang,<sup>1</sup> Ning Che,<sup>1,2</sup> Zhijing Liu,<sup>1,2</sup> Pingping Li,<sup>1,2</sup> Weiwei Li,<sup>1</sup> Chao Zhang,<sup>1,2</sup> Chun Cao,<sup>1,2</sup> Ruigang Liu,<sup>1</sup> and Yong Huang<sup>1,3</sup>

<sup>1</sup> State Key Laboratory of Polymer Physics and Chemistry, Beijing National Laboratory of Molecular Sciences, Institute of Chemistry, Chinese Academy of Sciences, Beijing 100190, China

<sup>2</sup> University of Chinese Academy of Sciences, Beijing 100049, China

<sup>3</sup> National Research Center for Engineering Plastics, Technical Institute of Physics & Chemistry, Chinese Academy of Sciences, Beijing 100190, China

Correspondence should be addressed to Ruigang Liu; [rgliu@iccas.ac.cn](mailto:rgliu@iccas.ac.cn) and Yong Huang; [yhuang@mail.ipc.ac.cn](mailto:yhuang@mail.ipc.ac.cn)

Received 8 January 2014; Revised 26 March 2014; Accepted 31 March 2014; Published 4 May 2014

Academic Editor: Huarong Nie

Copyright © 2014 Zhuang Li et al. This is an open access article distributed under the Creative Commons Attribution License, which permits unrestricted use, distribution, and reproduction in any medium, provided the original work is properly cited.

Naproxen (NAP)/cellulose acetate hybrid nanofibers were prepared by positive and reversed emitting electrodes electrospinning setups. The morphology and structure of the resultant nanofibers were characterized, and the NAP release behaviors were investigated. It was found that NAP dispersed in the CA matrix in molecular level, and no aggregation and dimers of NAP were found in the resultant NAP/CA hybrid nanofibers due to the formation of hydrogen bonds between NAP and CA. The nanofibers obtained by reversed emitting electrode electrospinning setup have a thicker diameter and a faster NAP release rate compared with those obtained by positive emitting electrode electrospinning setup. The faster drug release of NAP from nanofibers prepared by reversed emitting electrode electrospinning is due to the fact that the concentration of NAP molecules near the surface of the nanofibers is relatively higher than that of the nanofibers prepared by positive emitting electrode electrospinning setup. The effects of the electrode polarity on the distribution of drugs in nanofibers can be used to prepare hybrid electrospun fibers of different drug release rates, which may found applications in biomedical materials.

## 1. Introduction

Electrospinning is a cost effective and straightforward technique to produce nanofibers with diameters in the range of 50 nm to 5  $\mu$ m [1, 2]. The resultant nanofiber mats are attractive materials for their superior specific surface area and high porosity, which have promising applications in filter [3–6], catalyst [7–9], sensor [10–12], and biomedical materials [13–15]. In the process of electrospinning, a continuous charged jet is initiated when the electric field force exerted on the pendent drop exceeds its own surface tension. The flying jet then undergoes straight movement and whipping motion and finally solidifies on the collector as a nonwoven mat [16, 17]. Due to the complexity of electrohydrodynamics, the process of electrospinning was affected by various factors including solution properties, experimental parameters, and

environmental conditions [18, 19]. Among various process parameters, volumetric charge density, distance between nozzle and collector, initial jet radius, relaxation time, and solution viscosity have the most significant effects on the flying jet [20]. The polarity of the emitting electrode, say the one that is in contact with the polymer solution or melt, can be either positive or negative in electrospinning. Generally, the emitting electrode is positive. Meanwhile, electrospinning with negative emitting electrode has also been applied for preparing nanofibers, and the effects of the electric field morphology on the resultant nanofibers have been investigated [21–23]. It was found that the prepared nanofibers usually have larger diameter and pore size in the case of using negative emitting electrode, which is attributed to the relatively small Coulombic repulsion force on the flying jets [24].

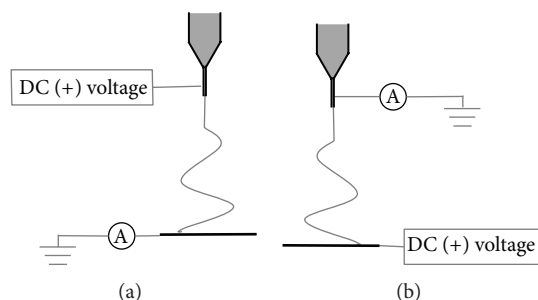


FIGURE 1: Schematic illustration of the electrospinning setup with (a) positive and (b) reversed emitting electrodes.

Due to the similarity to extracellular matrix (ECM), electrospun nanofibers loading various drugs and biomolecules have been used as wound dressing, surgical scaffold, and orthopedic materials [25–27]. The conventional method of producing these composite nanofibers was directly electrospinning the mixed solution of polymers and contents. It is reported that the loaded drugs were embedded in the polymer fibers and diffused out with a burst release in *in vitro* dissolution test, which is due to the interaction between the drugs and the polymer molecules [28, 29]. Naproxen (NAP) as an effective nonsteroidal anti-inflammatory drug is commonly used to treat the inflammation and pain of various wounds [30]. Owing to gastrointestinal irritancy caused by oral administration, NAP is more appropriate for topical application [31].

In this work, cellulose acetate (CA) nanofibers loaded with naproxen were prepared by electrospinning with positive and reversed emitting electrodes setups. CA and NAP mixed solution was used in the electrospinning. The morphology of the resultant nanofibers and the drug distribution were investigated and discussed.

## 2. Materials and Methods

**2.1. Materials.** Cellulose acetate (CA,  $M_r = 29$  kDa) was purchased from Sigma Aldrich (USA). Naproxen (NAP) was purchased from Alfa Aesar (USA). Highly purified water was prepared using Milli-Q Water Purification System (Millipore, USA). Dimethyl sulfoxide (DMSO) was supplied by Beijing Chemical Works and distilled before use. Other chemicals including acetone and *N, N*-dimethylacetamide (DMAc) are all of analytical grade and were used as received.

**2.2. Preparation of NAP-Loaded Nanofibers.** 19% (w/v) CA solution was prepared by dissolving CA in a mixed solution of acetone and DMAc (2:1, v/v). Then, 10 wt% NAP (based on the weight of CA) was added into the base CA solution to get the mixed solution for electrospinning. The conductivity of the CA solution and the NAP/CA mixed solution was measured using a conductivity meter (Rex DDS-307A, INESA, China).

Two setups with inverse emitting electrode polarity, say positive and reversed emitting electrodes, were used for electrospinning (Figure 1). The other parameters were the

same for the two setups. The inner diameter of the needle was 1.0 mm and the extruding rate was 0.25 mL/h. The applied voltage was 15 kV and the distance between the needle and the collector plate was 12 cm. All the electrospinning experiments were carried out at room temperature with a humidity of about 20–30%. The electric current of both electrospinning setups was determined using a multimeter (Fluke 15B, USA).

**2.3. Instruments and Characterization.** The morphology of the prepared fibers was observed on a field emission scanning electron microscopy (FESEM, JEOL 6700, Japan) operated at an accelerating voltage of 5 kV and current of 10  $\mu$ A. The samples were sputter-coated with a layer of platinum using a sputter-coater (Bal-Tec, SCD 500, Switzerland) before observation. All the images were taken in the secondary electron mode. Elemental analysis was performed on an energy dispersive X-ray spectrometer (EDS, EDAX-TSL, USA). Transmission electron microscopy (TEM) observation of the nanofibers was carried out on a field emission transmission electron microscopy (FETEM, 2200FS, JEOL, Japan). The samples were prepared by fixing copper grids on the collector and collecting fibers during the process of electrospinning. The operation voltage of TEM was set to 200 kV, and the images were recorded in the bright field mode.

Differential scanning calorimetry (DSC) experiments were carried out on DSC Q2000 (TA Instruments, USA) in the range of 20–200°C at the heating rate of 10°C/min in nitrogen atmosphere.

Wide angle X-ray diffraction (WAXD) experiments were carried out on a D/max 2500 X-ray diffraction meter (Rigaku, Japan).  $\text{CuK}\alpha$  X-ray ( $\lambda = 0.154$  nm) was used as the radiation source. Operation parameters were set at 40 kV and 200 mA and the data in the range of  $2\theta = 5$ –60° were recorded.

Fourier transform infrared spectroscopy (FTIR, EQUINOX55, Bruker, Germany) was used to characterize the fiber mats at a range of 400  $\text{cm}^{-1}$  to 4000  $\text{cm}^{-1}$  and a resolution of 2  $\text{cm}^{-1}$ .

UV-Vis spectrophotometer (TU-1901, Purkinje General, China) was used to determine the NAP concentration in the buffer solutions. The wavelength of the emitting UV-Vis light was selected as 262 nm.

**2.4. In Vitro Drug Release.** The *in vitro* drug release experiments of both NAP/CA nanofibers were carried out as follows. A certain amount of nanofibers were placed in a dialysis bag with molecular weight cutoff of 3.5 kDa. The dialysis bag was then immersed in a phosphate buffer solution with a desired volume. The temperature of the phosphate buffer solution (pH = 6.4) was set at  $37 \pm 0.5^\circ\text{C}$  to mimic the physiological conditions of human skin. The out medium was stirred continuously at 200 rpm and the NAP concentration in the out buffer solution was determined at desired time by UV-Vis absorbance.

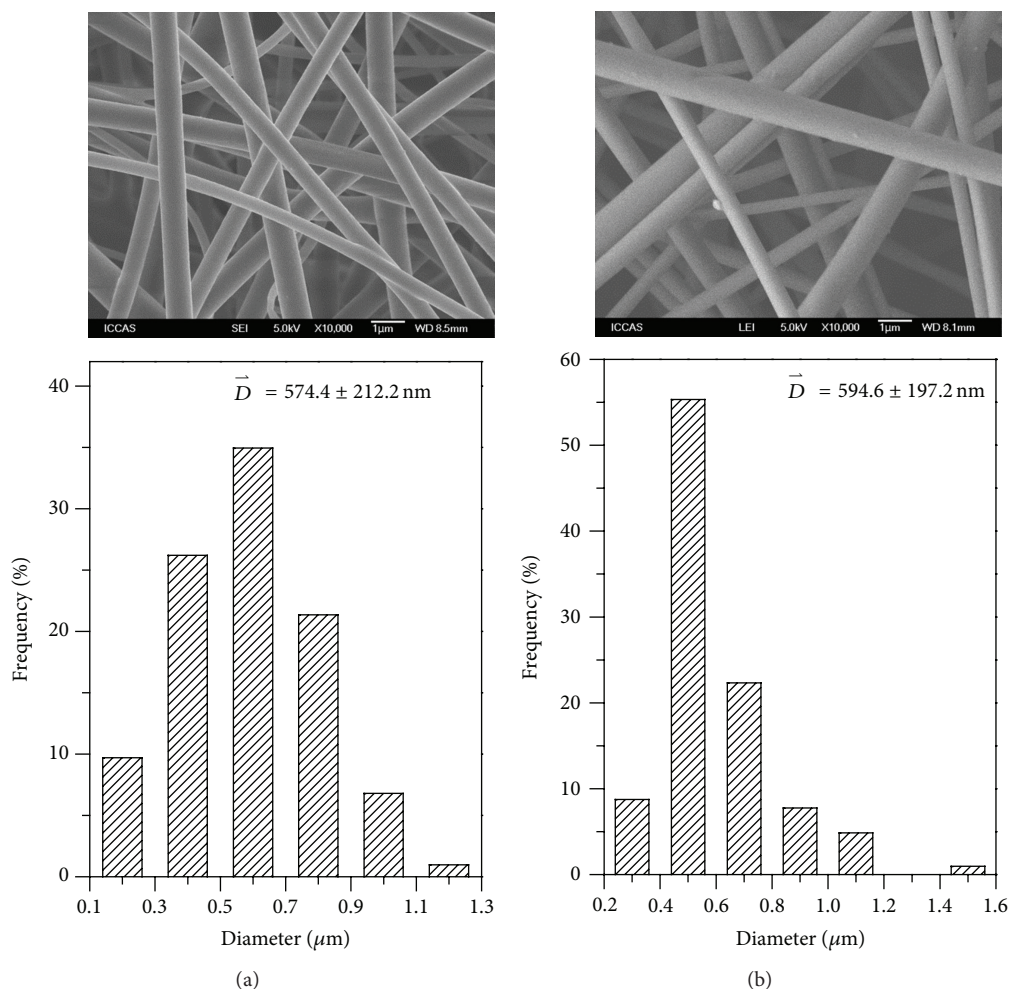


FIGURE 2: Typical SEM images and corresponding diameter distribution of the nanofibers prepared by (a) positive and (b) reversed emitting electrodes electrospinning setups.

The accumulative release of NAP from the nanofibers,  $P(\%)$ , was calculated using the following equation [32]:

$$P(\%) = \frac{C_n \times V_0 + \sum_{i=1}^{n-1} C_i \times V}{W}, \quad (1)$$

where  $C_n$  is the NAP concentration determined at number  $n$  and  $C_i$  is the NAP concentration determined at number  $i$ ;  $V_0$  is the volume of the buffer and  $V$  is the volume of the withdrawn sample; and  $W$  is the total amount of NAP in the fibers. Three parallel experiments were carried out and the mean value was plotted as a function of time.

### 3. Results and Discussion

**3.1. Preparation of NAP/CA Nanofibers.** NAP/CA hybrid nanofiber mats can be successfully prepared by both positive and reversed emitting electrode setups (Figure S1); see Figure S1 in Supplementary Material available online at <http://dx.doi.org/10.1155/2014/360658>. Figure 2 shows the typical SEM images of the NAP/CA nanofibers prepared by

electrospinning using positive and reversed emitting electrodes. The results indicate that the resultant nanofibers have similar morphology. The nanofibers have smooth surfaces and no particles can be observed, suggesting no NAP aggregations formed outside of the hybrid nanofibers. Statistics of the diameter of the nanofibers indicates that the nanofibers prepared by reversed emitting electrode electrospinning have a larger average diameter and a narrower diameter distribution ( $594.6 \pm 197.2$  nm) compared with those nanofibers prepared by using positive emitting electrode setup ( $574.4 \pm 212.2$  nm) (Figure 2). The difference could come from the difference in the working electric current for the positive and reversed emitting electrodes electrospinning setups. It was noted that the electric current of the jets for the reversed emitting electrode approach is about  $0.3\text{--}0.5 \mu\text{A}$  much lower than that of the positive emitting electrode approach ( $4.6\text{--}5.4 \mu\text{A}$ ). A lower working electric current corresponds to a lower charge density of the jet flow during electrospinning [33–35]. As a result, the electric field force stretching the jet as well as the electrostatic repulsion between the jets is accordingly smaller, leading to the relatively low stretching

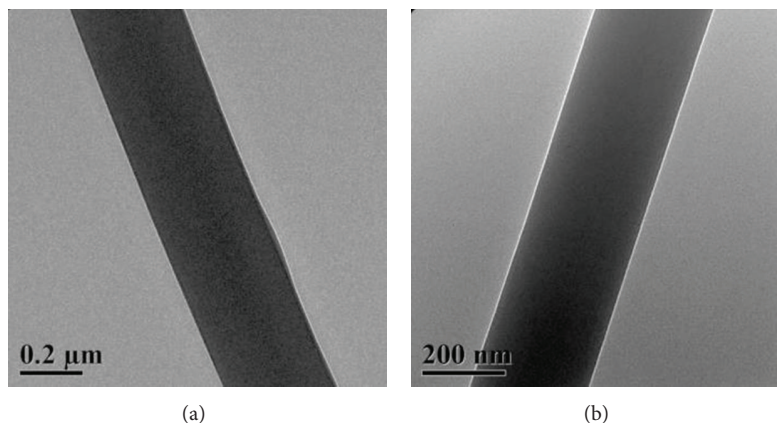


FIGURE 3: TEM images of nanofibers prepared by (a) positive and (b) reversed emitting electrodes electrospinning setups.

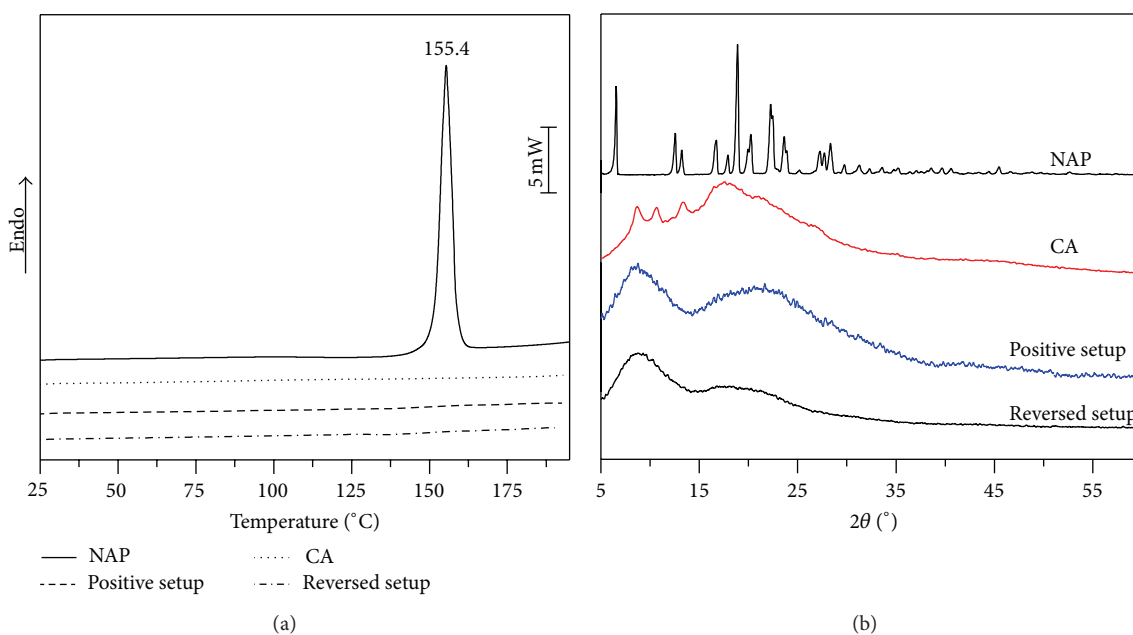


FIGURE 4: DSC traces (a) and XRD curves (b) of the NAP/CA nanofibers and correlated raw materials.

force on the jet and the thick diameter of the resultant nanofibers. TEM observation indicates that the nanofibers prepared by both positive and reversed emitting electrodes electrospinning setups have uniform structure (Figure 3), which suggests that NAP molecules are homogeneously dispersed in the CA matrixes.

**3.2. Dispersion of the NAP in the CA Matrix.** The solubility of hydrophobic drugs, such as NAP, is quite important for the improvement of the drug efficiency, which can be achieved by adding additives to reduce the crystallization of the drugs. Figure 4 shows the DSC and XRD curves of the NAP/CA hybrid nanofibers prepared by positive and reversed emitting electrodes electrospinning setups. Data of NAP and CA are also provided for comparison. The DSC results indicate that there is no melting peak of NAP crystal appearing on both NAP/CA nanofibers, suggesting no NAP crystal formed in

either of the nanofibers. The XRD results further confirmed that no NAP crystal exists in the nanofibers. These results are consistent with the TEM observations (Figure 3), in which no NAP crystal or aggregation can be observed.

For clarification of the interactions between the NAP and the CA matrix, FTIR experiments were carried out and the results are shown in Figure 5. The well-defined sharp absorption peak of pure NAP is at  $1728\text{ cm}^{-1}$ , which comes from the stretching vibration of the carbonyl groups. The absorption peak of carbonyl groups of pure CA locates at  $1753\text{ cm}^{-1}$ . For both hybrid nanofibers, the absorption peak of carbonyl groups locates at  $1743\text{ cm}^{-1}$ , indicating the interactions between the carbonyl groups from NAP and CA molecules [29, 36, 37]. Moreover, on the FTIR spectrum of NAP, the strong broad absorption peak at around  $3150\text{ cm}^{-1}$  is from the hydroxyl groups of NAP dimers as indicated in Figure 6. This peak disappeared in both hybrid nanofibers.

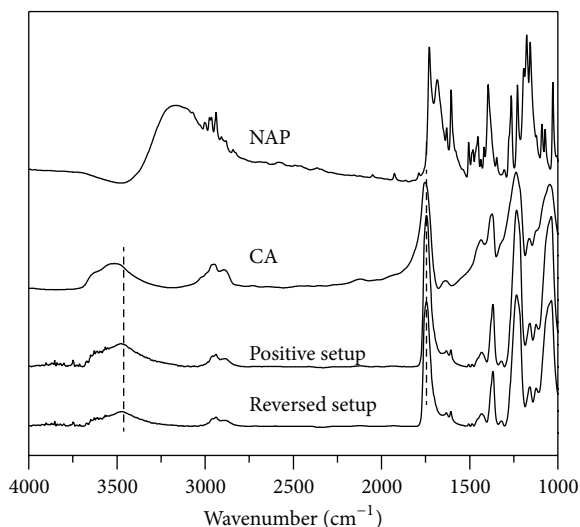


FIGURE 5: FTIR spectra of NAP-loaded nanofibers and correlated raw materials.

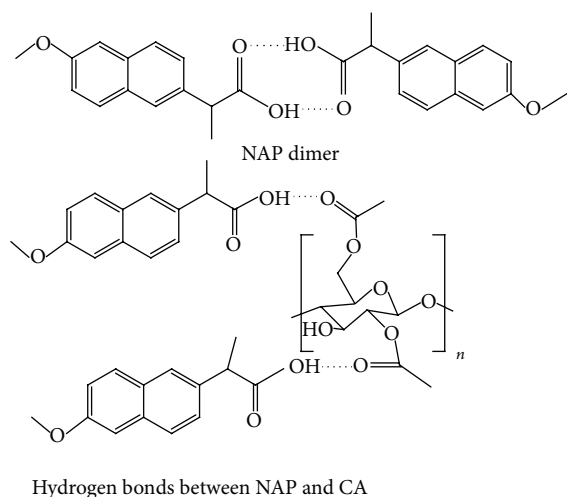


FIGURE 6: The hydrogen bonding of NAP dimer and NAP/CA.

Meanwhile, the absorption peak from the  $-OH$  groups in CA at around  $3520\text{ cm}^{-1}$  red shifts to around  $3470\text{ cm}^{-1}$  due to the formation of hydrogen bonds between NAP and CA molecules. Above results confirm that NAP mixed with CA in molecular level in the resultant NAP/CA hybrid nanofibers. The interactions between NAP and CA molecules can efficiently prevent the crystallization of NAP, which is helpful for the enhancement of the solubility of NAP.

**3.3. Distribution of NAP in the CA Matrix.** NAP contents in the hybrid nanofibers prepared by positive and reversed emitting electrodes electrospinning setups are similar to each other. The actual NAP content is 8.89 wt% and 8.94 wt% for nanofibers prepared by positive and reversed emitting electrodes electrospinning setups, respectively. The data are similar to the feeding NAP content in the NAP/CA solution (9.09 wt%), indicating that there is no NAP loss during the

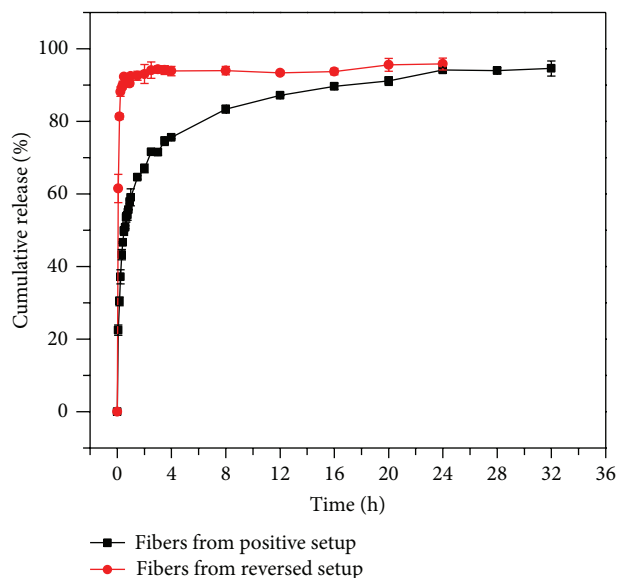


FIGURE 7: In vitro NAP release of the NAP/CA hybrid nanofibers prepared by positive and reversed emitting electrodes electrospinning setups.

preparation of the nanofibers. The in vitro NAP release profiles of the nanofibers are shown in Figure 7. Three parallel experiments were carried out and the average data and the error bar are depicted. The results showed that the NAP release of the nanofibers prepared by reversed emitting electrode electrospinning setup is much faster than that of the nanofibers prepared by the positive emitting electrode electrospinning setup (Figure 2). As reported in the literatures, the release rate of the same drug from electrospun nanofibers of the same matrix depends on the diameter of the nanofibers. The drug releasing rate of the nanofibers with thicker diameter is slower than that of the nanofibers with thinner diameter [29, 36, 37]. However, in the present work, the drug releasing rate of the NAP/CA nanofibers (diameter of  $574.4 \pm 212.2\text{ nm}$ ) prepared from the positive emitting electrode approach is slower than that of the nanofibers (diameter of  $594.6 \pm 197.2\text{ nm}$ ) prepared from the reversed emitting electrode approach (Figure 7), which is different from the literatures in [29, 36, 37]. The difference in the NAP release behaviors of the NAP/CA hybrid nanofibers suggests that the distribution of NAP in the nanofibers prepared by the positive and reversed emitting electrodes electrospinning approaches could be different. The fast NAP release of the nanofibers prepared by reversed emitting electrode electrospinning setup could be attributed to the fact that the NAP molecules were enriched near the surface of the nanofibers during the electrospinning. In order to approve the difference in the content of NAP near the surface of the nanofibers, EDS experiments were carried out and the data are listed in Table 1. It was found that the oxygen content in fibers prepared from the positive emitting electrode is higher than that in the nanofibers prepared from reversed approach. Considering that EDS provides exact element compositions of the nanofiber surface within depth of 5–10 nm and that the

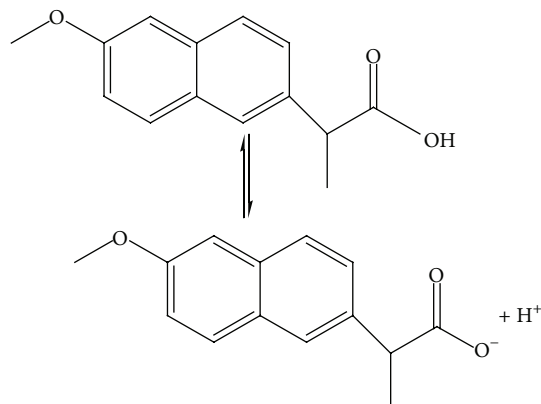


FIGURE 8: The ionization of NAP in the solution.

TABLE 1: Element C and O in different fibers and the raw materials.

Materials	C/wt%	O/wt%
CA*	51.72	4828
NAP*	77.78	22.22
Fibers from positive setup	67.92	32.08
Fibers from reversed setup	80.34	19.66

\*The weight fraction was calculated from its molecular formula.

oxygen content in CA is higher than that in NAP (Table 1), the EDS results suggested that NAP was enriched near the surface of the nanofibers prepared from the reversed emitting electrode, which is consistent with the conclusion derived from the NAP release profile of both nanofibers.

NAP molecules have carboxyl groups and could be ionized in CA/acetone/DMAc solution (Figure 8). The conductivities of the CA and NAP/CA solutions with acetone/DMAc mixed solvent are 0.765 and 0.857 mS/m, respectively, confirming the ionization of NAP molecules in the mixed solution. During the electrospinning process, the electric field enhanced the dissociation and any structure capable of being ionized would experience a separation of charges [38]. With a positive emitting electrode electrospinning setup, the reversed ions will migrate to the inner surface of the needle and vice versa, resulting in the core part of the solution fluid with an excess of mobile charges that can respond to the electrostatic stress of the opposite electrode. In the case of the electrospinning of the NAP/CA solution with positive emitting electrode setup, the electron with smaller mass moves to the needle surface much faster than the proton with bigger mass in the case of reversed emitting electrode electrospinning setup (Figure 9), resulting in the positive flying jet with more net charges than the reversed jet, which is confirmed by the difference in the working electric current during the positive (4.6–5.4  $\mu\text{A}$ ) and reversed (0.3–0.5  $\mu\text{A}$ ) emitting electrodes electrospinning in the present work. It is widely accepted that the net charge moves to the surface of the flying jet and the drift velocity of ions inside the jet is about 0.1 m/s [33, 39, 40]. Therefore, the negatively charged NAP could move to the surface of the jet in the reversed emitting electrode electrospinning, which leads to the higher

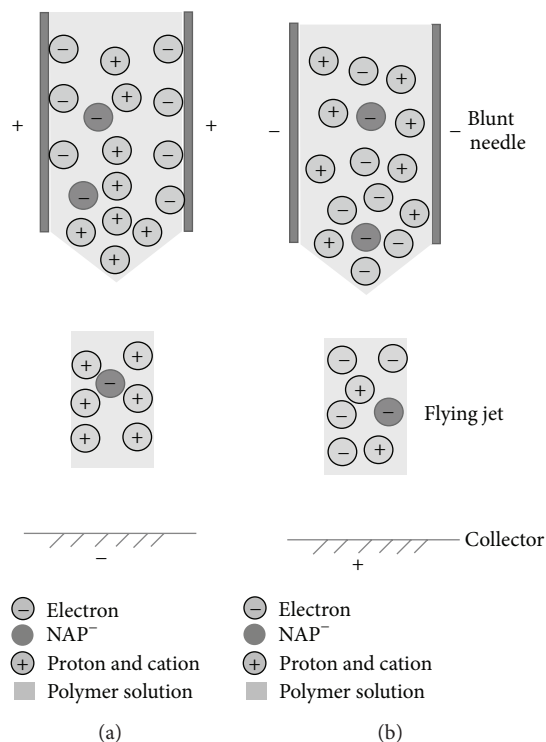


FIGURE 9: NAP distribution in the jets of (a) positive and (b) reversed emitting electrodes electrospinning setups.

NAP content near the surface of the prepared nanofibers. Therefore, the release rate of the NAP is faster from the nanofibers prepared by reversed emitting electrode electrospinning setup than from those nanofibers prepared by positive emitting electrode electrospinning setup. Considering the distribution of the loaded NAP caused by the emitting electrode polarity, drugs of different ionization properties can be embedded in the polymer matrixes of nanofibers with relatively controlled distribution by modulating the emitting electrode polarity, which could be used to prepare biomedical materials for various applications, such as wound dressings and surgical scaffolds.

#### 4. Conclusions

NAP/CA hybrid nanofibers were prepared by both positive and reversed emitting electrodes electrospinning setups. The nanofibers prepared by reversed emitting electrode electrospinning setup have relatively thicker diameter than those prepared by positive emitting electrode electrospinning setup. NAP is dispersed in the CA matrix in molecular level without formation of NAP aggregation and dimer. Nanofibers prepared by the reversed emitting electrode electrospinning setup have a larger amount of NAP in the surface layer, which resulted in the faster NAP release compared with the nanofibers prepared by positive emitting electrode electrospinning setup. This finding is important in producing hybrid nanofibers with drugs of different ionization property

through blend electrospinning, which may have various drug release behaviors and then be used as biomedical materials.

## Supporting Information

Nanofiber mats prepared by positive and reversed emitting electrodes electrospinning were shown in Figure S1.

## Conflict of Interests

The authors declare that there is no conflict of interests regarding the publication of this paper.

## Acknowledgments

This work was supported by the National Natural Science Foundation of China (nos. 21174150 and 21174156) and the Knowledge Innovation Program of the Chinese Academy of Sciences (no. KJCX2-YW-H19).

## References

- [1] J. Doshi and D. H. Reneker, "Electrospinning process and applications of electrospun fibers," *Journal of Electrostatics*, vol. 35, no. 2-3, pp. 151-160, 1995.
- [2] A. Greiner and J. H. Wendorff, "Electrospinning: a fascinating method for the preparation of ultrathin fibers," *Angewandte Chemie International Edition*, vol. 46, no. 30, pp. 5670-5703, 2007.
- [3] L. Chen, L. Bromberg, T. A. Hatton, and G. C. Rutledge, "Catalytic hydrolysis of p-nitrophenyl acetate by electrospun polyacrylamidoxime nanofibers," *Polymer*, vol. 48, no. 16, pp. 4675-4682, 2007.
- [4] L. Chen, L. Bromberg, H. Schreuder-Gibson, J. Walker, T. A. Hatton, and G. C. Rutledge, "Chemical protection fabrics via surface oximation of electrospun polyacrylonitrile fiber mats," *Journal of Materials Chemistry*, vol. 19, no. 16, pp. 2432-2438, 2009.
- [5] J. Shi, L. Wang, F. Zhang et al., "Incorporating protein gradient into electrospun nanofibers as scaffolds for tissue engineering," *ACS Applied Materials & Interfaces*, vol. 2, no. 4, pp. 1025-1030, 2010.
- [6] Y. Tian, M. Wu, R. Liu et al., "Electrospun membrane of cellulose acetate for heavy metal ion adsorption in water treatment," *Carbohydrate Polymers*, vol. 83, no. 2, pp. 743-748, 2011.
- [7] H. Kang, Y. Zhu, X. Yang, Y. Jing, A. Lengalova, and C. Li, "A novel catalyst based on electrospun silver-doped silica fibers with ribbon morphology," *Journal of Colloid and Interface Science*, vol. 341, no. 2, pp. 303-310, 2010.
- [8] Z. Zhang, C. Shao, Y. Sun et al., "Tubular nanocomposite catalysts based on size-controlled and highly dispersed silver nanoparticles assembled on electrospun silica nanotubes for catalytic reduction of 4-nitrophenol," *Journal of Materials Chemistry*, vol. 22, no. 4, pp. 1387-1395, 2012.
- [9] Y. Huang, H. Ma, S. Wang et al., "Efficient catalytic reduction of hexavalent chromium using palladium nanoparticle-immobilized electrospun polymer nanofibers," *ACS Applied Materials & Interfaces*, vol. 4, no. 6, pp. 3054-3061, 2012.
- [10] Y. Long, H. Chen, Y. Yang et al., "Electrospun nanofibrous film doped with a conjugated polymer for DNT fluorescence sensor," *Macromolecules*, vol. 42, no. 17, pp. 6501-6509, 2009.
- [11] X. W. Mao, F. Simeon, G. C. Rutledge, and T. A. Hatton, "Electrospun carbon nanofiber webs with controlled density of states for sensor applications," *Advanced Materials*, vol. 25, no. 9, pp. 1309-1314, 2013.
- [12] G. D. Fu, L. Q. Xu, F. Yao et al., "Smart nanofibers from combined living radical polymerization, "click chemistry", and electrospinning," *ACS Applied Materials & Interfaces*, vol. 1, no. 2, pp. 239-243, 2009.
- [13] H.-J. Jin, S. V. Fridrikh, G. C. Rutledge, and D. L. Kaplan, "Electrospinning Bombyx mori silk with poly(ethylene oxide)," *Biomacromolecules*, vol. 3, no. 6, pp. 1233-1239, 2002.
- [14] M. Wang, H.-J. Jin, D. L. Kaplan, and G. C. Rutledge, "Mechanical properties of electrospun silk fibers," *Macromolecules*, vol. 37, no. 18, pp. 6856-6864, 2004.
- [15] H. Bai, J. Ju, Y. Zheng, and L. Jiang, "Functional fibers with unique wettability inspired by spider silks," *Advanced Materials*, vol. 24, no. 20, pp. 2786-2791, 2012.
- [16] M. M. Hohman, M. Shin, G. Rutledge, and M. P. Brenner, "Electrospinning and electrically forced jets. II. Applications," *Physics of Fluids*, vol. 13, no. 8, pp. 2221-2236, 2001.
- [17] M. M. Hohman, M. Shin, G. Rutledge, and M. P. Brenner, "Electrospinning and electrically forced jets. I. Stability theory," *Physics of Fluids*, vol. 13, no. 8, pp. 2201-2220, 2001.
- [18] S. Sukigara, M. Gandhi, J. Ayutsede, M. Micklus, and F. Ko, "Regeneration of Bombyx mori silk by electrospinning—part 1: processing parameters and geometric properties," *Polymer*, vol. 44, no. 19, pp. 5721-5727, 2003.
- [19] S.-H. Tan, R. Inai, M. Kotaki, and S. Ramakrishna, "Systematic parameter study for ultra-fine fiber fabrication via electrospinning process," *Polymer*, vol. 46, no. 16, pp. 6128-6134, 2005.
- [20] C. J. Thompson, G. G. Chase, A. L. Yarin, and D. H. Reneker, "Effects of parameters on nanofiber diameter determined from electrospinning model," *Polymer*, vol. 48, no. 23, pp. 6913-6922, 2007.
- [21] M. Chowdhury and G. K. Stylios, "Analysis of the effect of experimental parameters on the morphology of electrospun polyethylene oxide nanofibres and on their thermal properties," *Journal of the Textile Institute*, vol. 103, no. 2, pp. 124-138, 2012.
- [22] A. Kilic, F. Oruc, and A. Demir, "Effects of polarity on electrospinning process," *Textile Research Journal*, vol. 78, no. 6, pp. 532-539, 2008.
- [23] P. Supaphol, C. Mit-Uppatham, and M. Nithitanakul, "Ultrafine electrospun polyamide-6 fibers: effect of emitting electrode polarity on morphology and average fiber diameter," *Journal of Polymer Science B: Polymer Physics*, vol. 43, no. 24, pp. 3699-3712, 2005.
- [24] U. Ali, X. Wang, and T. Lin, "Effect of nozzle polarity and connection on electrospinning of polyacrylonitrile nanofibers," *Journal of the Textile Institute*, vol. 103, no. 11, pp. 1160-1168, 2012.
- [25] J. Lin, C. Li, Y. Zhao, J. Hu, and L.-M. Zhang, "Co-electrospun nanofibrous membranes of collagen and zein for wound healing," *ACS Applied Materials & Interfaces*, vol. 4, no. 2, pp. 1050-1057, 2012.
- [26] C. Tang, A. E. Ozcam, B. Stout, and S. A. Khan, "Effect of pH on protein distribution in electrospun PVA/BSA composite nanofibers," *Biomacromolecules*, vol. 13, no. 5, pp. 1269-1278, 2012.

- [27] R. A. Thakur, C. A. Florek, J. Kohn, and B. B. Michniak, "Electrospun nanofibrous polymeric scaffold with targeted drug release profiles for potential application as wound dressing," *International Journal of Pharmaceutics*, vol. 364, no. 1, pp. 87–93, 2008.
- [28] S. Tungprapa, I. Jangchud, and P. Supaphol, "Release characteristics of four model drugs from drug-loaded electrospun cellulose acetate fiber mats," *Polymer*, vol. 48, no. 17, pp. 5030–5041, 2007.
- [29] D.-G. Yu, X.-Y. Li, X. Wang, W. Chian, Y.-Z. Liao, and Y. Li, "Zero-order drug release acetate nanofibers prepared using coaxial electrospinning," *Cellulose*, vol. 20, no. 1, pp. 379–389, 2012.
- [30] C. Derry, S. Derry, R. A. Moore, and H. J. McQuay, "Single dose oral naproxen and naproxen sodium for acute postoperative pain in adults," *Cochrane Database of Systematic Reviews*, no. 1, Article ID CD004234, 2009.
- [31] M.-N. Giraud, C. Motta, J. J. Romero, G. Bommelaer, and L. M. Lichtenberger, "Interaction of indomethacin and naproxen with gastric surface-active phospholipids: a possible mechanism for the gastric toxicity of nonsteroidal anti-inflammatory drugs (NSAIDs)," *Biochemical Pharmacology*, vol. 57, no. 3, pp. 247–254, 1999.
- [32] K. E. S. Locock, T. D. Michl, J. D. P. Valentin et al., "Guanylated polymethacrylates: a class of potent antimicrobial polymers with low hemolytic activity," *Biomacromolecules*, vol. 14, no. 11, pp. 4021–4031, 2013.
- [33] Y. M. Shin, M. M. Hohman, M. P. Brenner, and G. C. Rutledge, "Experimental characterization of electrospinning: the electrically forced jet and instabilities," *Polymer*, vol. 42, no. 25, pp. 9955–9967, 2001.
- [34] S. A. Theron, E. Zussman, and A. L. Yarin, "Experimental investigation of the governing parameters in the electrospinning of polymer solutions," *Polymer*, vol. 45, no. 6, pp. 2017–2030, 2004.
- [35] W.-E. Teo, R. Inai, and S. Ramakrishna, "Technological advances in electrospinning of nanofibers," *Science and Technology of Advanced Materials*, vol. 12, no. 1, Article ID 013002, 2011.
- [36] D. G. Yu, X. Wang, X. Y. Li, W. Chian, Y. Li, and Y. Z. Liao, "Electrospun biphasic drug release polyvinylpyrrolidone/ethyl cellulose core/sheath nanofibers," *Acta Biomaterialia*, vol. 9, no. 3, pp. 5665–5672, 2013.
- [37] D.-G. Yu, J.-H. Yu, L. Chen, G.-R. Williams, and X. Wang, "Modified coaxial electrospinning for the preparation of high-quality ketoprofen-loaded cellulose acetate nanofibers," *Carbohydrate Polymers*, vol. 90, no. 2, pp. 1016–1023, 2012.
- [38] G. Collins, J. Federici, Y. Imura, and L. H. Catalani, "Charge generation, charge transport, and residual charge in the electrospinning of polymers: a review of issues and complications," *Journal of Applied Physics*, vol. 111, no. 4, Article ID 044701, 2012.
- [39] D. H. Reneker, A. L. Yarin, H. Fong, and S. Koombhongse, "Bending instability of electrically charged liquid jets of polymer solutions in electrospinning," *Journal of Applied Physics*, vol. 87, no. 9 I, pp. 4531–4547, 2000.
- [40] Z. Zha, S. L. Leung, Z. Dai, and X. Wu, "Centering of organic-inorganic hybrid liposomal cerasomes in electrospun gelatin nanofibers," *Applied Physics Letters*, vol. 100, no. 3, Article ID 033702, 3 pages, 2012.

## Research Article

# Assessment of Morphology, Activity, and Infiltration of Astrocytes on Marine EPS-Imbedded Electrospun PCL Nanofiber

Seul Ki Min, Cho Rong Kim, Sung Hoon Kim, and Hwa Sung Shin

*Department of Biological Engineering, Inha University, Incheon 402-751, Republic of Korea*

Correspondence should be addressed to Hwa Sung Shin; [hsshin@inha.ac.kr](mailto:hsshin@inha.ac.kr)

Received 22 December 2013; Revised 11 March 2014; Accepted 26 March 2014; Published 14 April 2014

Academic Editor: Ruigang Liu

Copyright © 2014 Seul Ki Min et al. This is an open access article distributed under the Creative Commons Attribution License, which permits unrestricted use, distribution, and reproduction in any medium, provided the original work is properly cited.

Tissue engineering using a biomaterial including bioactive compounds has been researched as a way to restore injured neural systems. Extracellular polymeric substances (EPS) extracted from marine seaweeds have been known to produce positive effects on physiological activities in human tissues. In this study, an electrospun nanofiber containing brown seaweed EPS was proven to be a candidate biomaterial for neural tissue engineering. Glial fibrillary acidic protein (GFAP) as a specific marker protein increased in the astrocytes cultured on the polycaprolactone (PCL) nanofiber containing EPS (EPS-PCL nanofiber), compared with PCL nanofiber. The upregulation of GFAP indicates that the EPS-PCL nanofiber induced astrocyte activation, which supports physiological agents favorable to restore injured neural tissue. Astrocytes could infiltrate into the EPS-PCL nanofiber mat without toxicity, comparable to PCL nanofiber. These results imply that EPS-PCL nanofiber could be a useful biomaterial to regulate astrocyte activity at a molecular level and could be considered as a novel therapeutic material for neural tissue engineering.

## 1. Introduction

Regarding central nervous system (CNS) injuries, astrocytes are one of many glial cells that are important in supporting neural systems to operate correctly [1, 2]. Following some reports, astrocytes are regarded as curative agents in therapy of CNS injuries [3], while they are also known to interfere with neural regeneration [4, 5]. The mechanism to explain the astrocyte effect on neuronal systems is connected to various growth factors, cytokines, proteoglycans, and other tissues [6–12]. Especially, GFAP is an important biomarker to determine the state of astrocytes, which is involved in the CNS injury response and plays a critical role in neural tissue organization. For example, GFAP has been known as an essential protein for construction of cerebral white matter and normal myelination [13].

Three typical ways have been used to treat CNS injuries: drug delivery, cell therapy, and tissue engineering. Medication has been administered mainly in a solution or liposome vesicle to the injured site or in the blood stream [14]. Various

bioactive substances from natural resources have been tried in studies of neurological disorders [15]. Seaweed-originated polysaccharides also have demonstrated abilities to regulate neurons and glial cells [16]. However, a recent development of drug delivery systems using biomaterials for drug control release has encountered several problems such as drug instability, side effects, and low controllability. In the case of cell therapy including stem cells, injected cells must reside correctly in the target injured tissue and follow-up events such as survival, differentiation, and curing activities must be understood and controlled. Unfortunately an injected cell's fate in an implanted state is rarely controllable. Therefore, as in drug delivery, cell therapy has also been actively administered in conjunction with biomaterials in order to better control the injected cell's fate while benefiting the injured nerve tissue. Namely, a neural tissue engineering approach is highlighted in terms of control of drugs and cell therapy within the injured tissue.

Biomaterials for neural tissue engineering should be thin, flexible, porous, biocompatible, biodegradable, compliant,

neuroinductive, and neuroconductive. Various types of scaffolds have been developed including nanofibers, sintered matrices, nanofoams, hydrogels, and nanotubes. Among these, hydrogels and nanofibers have recently been underscored for their peculiar advantages [17, 18]. They show potential to facilitate nerve regeneration by providing ECM-like environments and structures favorable to cells and tissues. Hydrogels can be easily injected into the cavity of the injured tissue with low tension but may need frequent changing and are hard to sterilize. However, nanofibers are relatively easy to sterilize and can also guide axonal growth direction even though injection into a tissue is not easy compared to hydrogels.

Nanofibers with polysaccharides for neuron cells have been actively researched. However, glial cells have been rarely studied in relation to nanofiber, especially, at a molecular level, even though glial cells are highly involved in subsequent events following CNS injury. Therefore, this work was to ascertain the availability of brown seaweed-derived EPS incorporated into polycaprolactone (EPS-PCL) nanofiber as a therapeutic nanomedicine in CNS injuries by observing GFAP expression and astrocyte infiltration into the nanofiber mat.

## 2. Materials and Methods

**2.1. Extraction of EPS and Fabrication of Electrospun Nanofiber Mats.** EPS derived from brown seaweed, *Undaria pinnatifida*, were obtained based on the hot water extraction method of Fujiki et al. [19]. Briefly, a dried brown seaweed was ground to small pieces, mixed in distilled water at 100 g/L, and autoclaved at 121°C for 30 min. Then, the pieces of seaweed were removed by filtering. EPS were precipitated by an excess of ethanol and obtained by centrifugation at 14,000 ×g for 20 min. The precipitated EPS were dissolved in 0.5 mM EDTA solution and dialyzed by dialysis membrane to remove salt. Dialyzed EPS were lyophilized to make a powder form. Finally the obtained EPS sample was stored at -20°C until use. To prepare polymer solution for electrospinning, 15% (wt/v) of PCL (Mn 80,000; Sigma-Aldrich, USA) was dissolved in mixture of tetrahydrofuran (THF, Junsei, Japan) and N,N-dimethylformamide (DMF, Junsei, Japan) with a ratio of 7:3 (v/v). A PCL solution containing EPS from *Undaria pinnatifida* was prepared by adding 0.5% (wt/v) EPS in a PCL polymer solution. Electrospun nanofiber mats were fabricated using an electrospinning apparatus [20] consisting of a syringe pump (KDS100, KD Scientific, USA), high voltage supply, and a flatted collector. Two kinds of solution were electrospun with the following conditions. Flow rate of solution was at 2 mL/hr. The distance from needle tip to aluminum collector was 16 cm under a 14 kV. A sample of the electrospun nanofiber mats was stored in vacuum to remove the organic solvent completely and placed under UV light to ensure sterility before cell culturing.

**2.2. Characterization of Electrospun Nanofiber.** The morphology of electrospun nanofiber was examined using field emission scanning emission microscope (FE-SEM, Hitachi

S-4200, Japan). In order to obtain SEM images, nanofiber mats were coated by a Pt sputter. Each image was taken under an accelerating voltage of 10 kV. The diameter of electrospun nanofiber was determined from SEM images using Image J (National Institutes of Health, USA). 200 spots of diameter were measured to calculate average and standard deviations for statistical analysis. The hydrophobicity of PCL and EPS-PCL nanofiber mats was determined by contact angle analyzer (S-EO Phoenix touch, Korea) using 3 μL distilled water as probe liquid on 5 spots of each sample. To observe the pattern of EPS composition of EPS-PCL nanofiber, transmission electron microscopy (TEM, Hitachi H-7600, Japan) was operated at 80 kV. Nanofibers for TEM images were electrospun on copper grids.

**2.3. Isolation of Primary Astrocytes.** Primary astrocytes were isolated from the cerebra of 1 day old *Sprague-Dawley* rats (SAMTACO, Korea) as previously described [21]. The cerebra tissues extracted from neonatal rats were minced using a Pasteur pipette and then filtered through a 0.7 mm cell strainer. The cells in filtrate were counted using a hemocytometer and  $2 \times 10^7$  cells were seeded on a T-75 flask (SPL, Korea). After incubation for 7 days in an incubator with 5% CO<sub>2</sub> at 37°C, the cells were shaken at 200 rpm for 24 hrs. Nonadherent cells were removed by centrifugating the supernatant and then the cultured medium was fed back to cells in the T-75 flask with fresh medium with a ratio of 2:8. Once mixed cells go through all of the above process, only astrocytes will be remained.

**2.4. Western Blot for GFAP Analysis.** The expression of GFAP was measured by a western blot. GFAP are typical intermediate filaments derived from activated astrocytes in the CNS. Astrocytes were cultured for 5 days on tissue culture polystyrene (TCPS), PCL, and EPS-PCL nanofibers, followed by washing with PBS and adding RIPA lysis buffer. The harvested total protein was quantified by a BCA protein assay kit. For electrophoresis, the quantified protein was loaded into a 12% acrylamide gel and separated by its molecular weight. The resultant SDS-PAGE gel was transferred to a PVDF membrane, followed by incubation for 6 hrs in TBS with 10% skim milk to block non-specific protein binding at 4°C. Primary antibody (rabbit anti-GFAP polyclonal IgG antibodies, ab7260, Abcam) was diluted with TBS supplemented with 10% skim milk at a ratio of 1:50000 and then reacted on the transferred membrane for 4 h at 4°C. After washing three times with TBST for 5 min, secondary antibody (goat anti-rabbit IgG-HRP, sc-2004, Santa Cruz), which was diluted with TBS supplemented with 10% skim milk, was reacted for 1 h at room temperature. The membrane was washed three times with TBST for 5 min, and finally, the reaction parts with ECL solution were detected on the film. These development steps were performed in a dark room.

**2.5. Immunostaining of GFAP of Astrocytes Cultured on Nanofiber.** Electrospun nanofibers were blocked for 1 hour using 1% BSA in PBST. After blocking, the cells were soaked in the PBST with 1% BSA and rabbit anti-GFAP polyclonal

IgG antibodies (1:5000, ab7260, Abcam) overnight at 4°C. The sample was washed with PBS three times each for 5 min and then reacted with goat anti-rabbit secondary antibody-Texas Red (1:5000, ab6800, Abcam) dissolved in PBST with 1% BSA for 1 hr at room temperature. Afterwards, the samples were washed with PBS three times for 5 min. To ascertain each cell, we used Hoechst 33342 which stained all cell nuclei for 1 min. Double stained samples were observed under confocal laser scanning microscope (LSM 510 META, USA).

**2.6. Evaluation of the Infiltration of Astrocytes.** For a cross-section assay to observe infiltration of cells, nanofibers should be thick enough for cell migration. For a cross-section assay, collected nanofibers must be over 200 nm. Primary astrocytes were seeded at  $3 \times 10^4$  cells per well on a 24-well plate. 5 days after astrocytes were seeded into the nanofibers, the culture media were removed and the nanofibers were washed with chilled PBS (pH 7.4), treated with 4% paraformaldehyde at RT for 20 min to fix the astrocytes cultured on the nanofiber, and washed twice with PBS. They were then dehydrated by ethanol/deionized water (10%, 20%, and 30%) in order. This astrocyte-cultured mat measured at  $1 \times 1 \text{ cm}^2$  was cut out and rapidly frozen at  $-20^\circ\text{C}$  with OCT (optimal cutting temperature) compounds (Tissue-Tek, Europe). Next, these were sectioned at  $50 \mu\text{m}$  widths, attached to coating slide glasses (SUPER FROST, MATSUNAMI, Japan), and washed by PBS (pH 7.4) 2 times. After that, H&E staining was performed to confirm astrocyte infiltration.

### 3. Results

**3.1. Characterization of EPS-PCL Nanofiber.** Images of PCL and EPS-containing PCL nanofibers were taken using SEM and TEM to characterize morphology and confirm the existence of EPS. Comparing Figures 1(a) with 1(b), the EPS particle was confirmed to be incorporated into the EPS-PCL nanofiber. During extracting EPS, proteins and alginic acid were removed by heating and precipitation, respectively. Small molecules were also eliminated by dialysis step. Thus, following a reference [22], the isolated EPS is thought to consist of laminarin and fucoidan as main components. Fucoidan is a sulfated polysaccharide which is stained by alcian blue. In order to ascertain its presence and distribution, the EPS-PCL nanofiber was stained by alcian blue. As seen in Figure 1(b), sulfated polysaccharides can be seen to be homogeneously distributed over the EPS-PCL nanofiber. Both nanofibers exhibited similar cylindrical morphologies and diameter distribution (Figures 1(c)–1(f)). PCL and EPS-PCL nanofibers had a thickness of  $560.56 \pm 107.66$  and  $551.41 \pm 107.65$  nm in diameter, respectively. Contact angle was measured to investigate the effect of EPS incorporation on hydrophilicity of EPS-PCL nanofiber (Figures 1(c) and 1(d)). PCL and EPS-PCL nanofibers showed  $129.29 \pm 2.45^\circ$  and  $135.27 \pm 2.04^\circ$  of contact angle, respectively. Topography and surface energy both can influence contact angle cooperatively. However, since topography is similar to both nanofibers, EPS can be considered to affect the increased hydrophilicity of EPS-PCL nanofiber.

**3.2. GFAP Expression of Astrocytes on EPS-PCL Nanofiber.** In order to assess whether EPS activates astrocytes, the expression level of GFAP in astrocytes was measured on PCL and EPS-PCL nanofibers by western blot. As shown in Figure 2, GFAP was more expressed on EPS-PCL nanofiber than on PCL nanofiber. It means that although there is less expression than on TCPS, where two-dimensionally cultured conditions were simulated as an injury [23], EPS, as well as the dimensional similarity of nanofiber to ECM, induced the astrocytes to become more activated.

**3.3. Morphology of Astrocytes on PCL and EPS-PCL Nanofiber Mats.** SEM images were taken to observe cell morphologies and evaluate adhesion of astrocytes on the nanofiber (Figure 3). The appearance of cells in a particular environment is known to have a certain shape (e.g., polygonal shape in normal brain and stellate shape in injury environment). Upon larger magnification, astrocytes are shown to adhere tightly to three-dimensional nanofibers, regardless of existence of EPS. But, there is no significant difference in morphologies between PCL and EPS-PCL nanofibers.

In order to investigate GFAP pattern inside astrocytes on nanofibers, astrocyte morphologies immunostained with GFAP were compared between PCL nanofiber and EPS-PCL nanofiber (Figure 4). But, cells in this research did not form a regular morphology. Astrocytes on PCL and EPS-PCL nanofibers both express GFAP correctly but significant differences were not detected in the confocal images.

**3.4. Infiltration Effect of Astrocytes Cultured on Nanofiber.** A thick nanofiber on which astrocytes were cultured for 5 days was cross-sectionalized by using Cryostat (Leica CM-1800, USA) so that astrocytes infiltration can be observed (Figure 5). The cross-section was stained with hematoxylin and eosin (H&E) to find astrocyte positions in the nanofiber. First of all, infiltration of astrocytes tested the case of culture on PCL nanofiber as control. It was easy and has no cytotoxicity (data not shown). As in Figure 5, it was found that the cells infiltrated deeper into EPS-PCL nanofiber. That is because, regardless of the depth, there seemed to be more pores to offset the compression pressure than expected. This means that media and nutrients could be provided easily, which is such an important fact to use biomaterials in tissue engineering; cells should be alive in the implanted scaffold. Both the figures suggested a potential that the topography of the nanofiber was able to induce cell infiltration.

### 4. Discussion

As well as supporting the neuronal physical structure, astrocytes help neural plasticity and synapse-formation [24, 25]. In addition, in an acute CNS injury, astrocytes have been reported to contribute to neuroregeneration by regulating immunity, reinstating homeostasis, affording neurotrophic factors, reconstructing the damaged lesion, and protecting spared neural tissue [26]. For these reasons, astrocytes have widely been studied as a curing agent for CNS injuries. The objective of this research was to investigate whether EPS-PCL

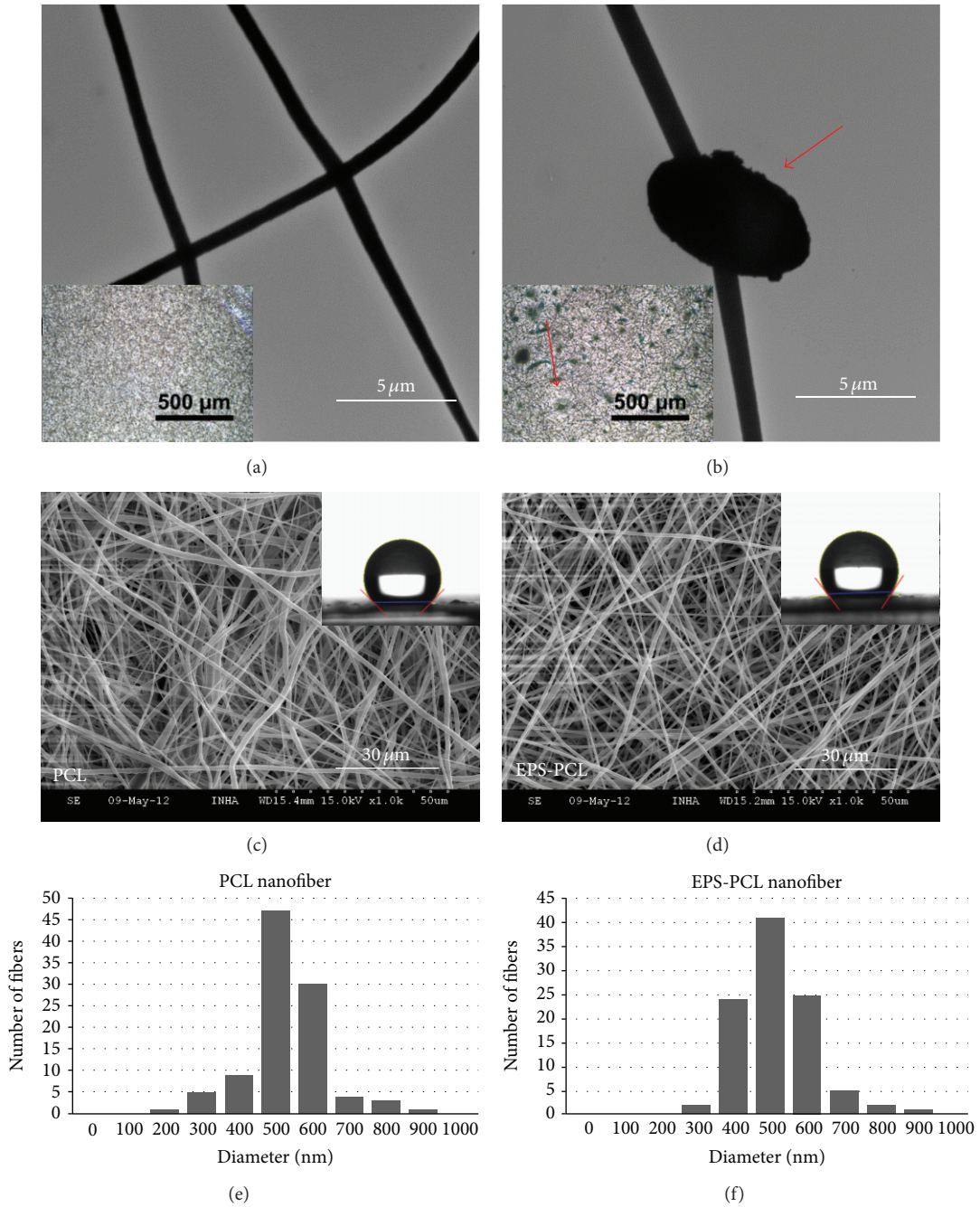


FIGURE 1

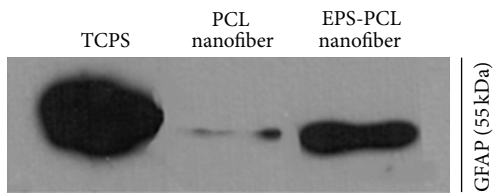


FIGURE 2

nanofiber is a favorable scaffold for astrocytic tissue engineering in CNS injuries by observing molecular behaviors,

morphological change, and infiltration of astrocytes on EPS-PCL nanofiber.

EPS-PCL nanofiber may promote biochemical effects to astrocytes. In this work, we at most tried to investigate the biochemical effects of EPS-PCL nanofiber. In this sense, it is important to make PCL and EPS-PCL nanofibers gain similar morphologies so that morphological variations would rarely influence astrocyte activity. Thus, in order to minimize structural variations between PCL and EPS-PCL nanofibers, we optimized electrospinning conditions to make similar diameters in both nanofibers. Meaning, there was almost no topography difference between PCL and EPS-PCL nanofibers.

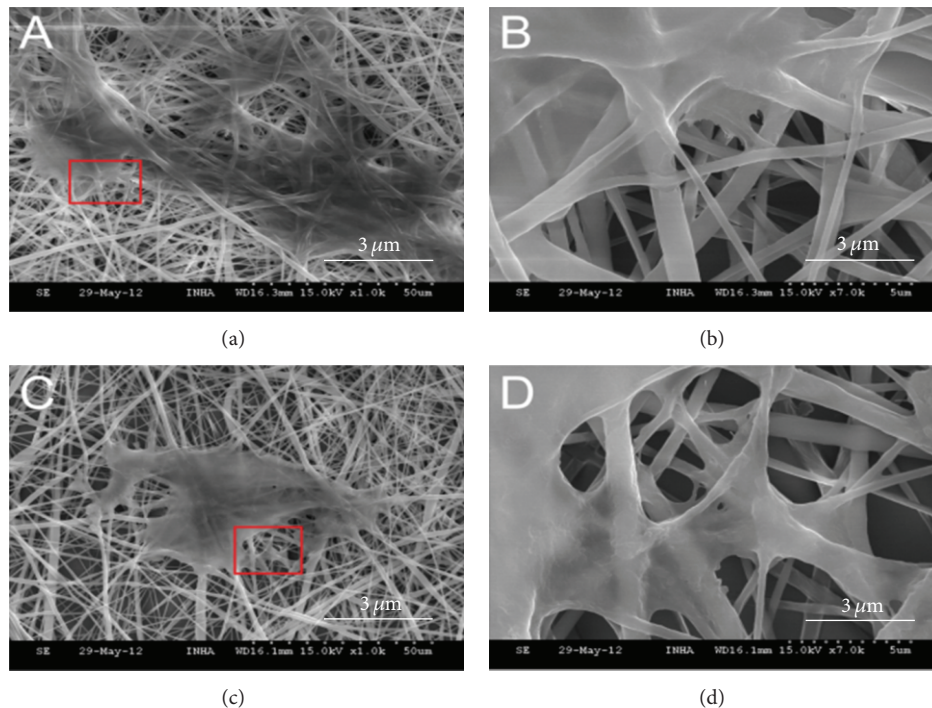


FIGURE 3

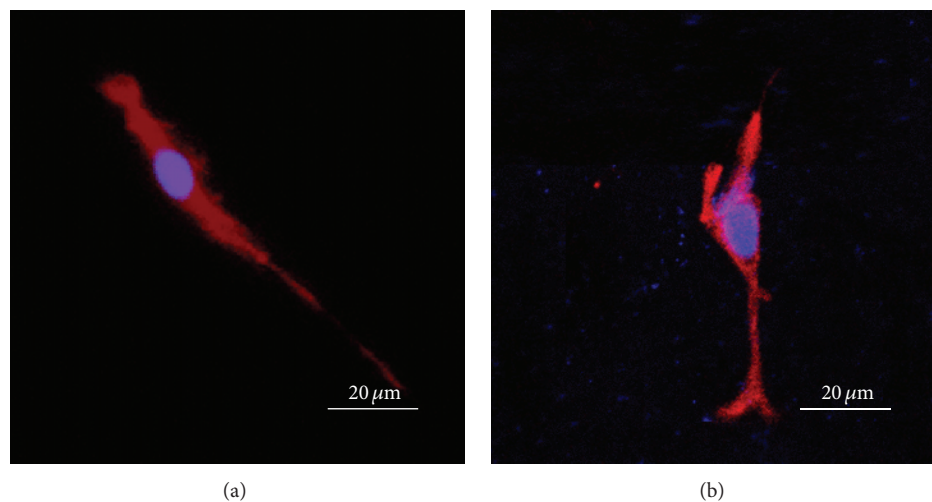


FIGURE 4

Polysaccharide which is extracted by hot water extraction and filtration methods is mainly composed of laminarin and fucoidan. Fucoidan is a sulfated polysaccharide which can be stained by alcian blue. Taking a look at alcian blue in Figure 1(b), the sulfated polysaccharide of EPS was stained within the PCL nanofiber. The distribution of EPS was sporadic over the PCL nanofiber mat. That is because solubility differences between EPS and PCL make them immiscible. Choosing an appropriate solution such as an ionic liquid, EPS and PCL polymers could be homogeneously miscible. However, for this experiment, the existence of EPS in the PCL nanofiber can be assured to be a sufficient condition to investigate its effect on astrocyte activity. By adding EPS into

PCL nanofiber, the surface energy of the EPS-PCL nanofiber increased because EPS is composed of macromolecules with charges. However, aside from this hydrophilicity, the fiber diameter and morphology were set to be similar between both nanofibers.

GFAP is a biomarker that represents astrocyte activation. In order to maintain hypertrophic processes of cells, astrocytes upregulate GFAP levels in an activated state [27, 28]. Once upregulated, GFAP-activated astrocytes produce neurotrophic factors to help neural tissue protection and regeneration [29–31]. Astrocytes cultured on EPS-PCL nanofiber were activated with higher expression of GFAP in our study. This indicates that EPS were a factor in influencing astrocyte



FIGURE 5

activity. In our previous study, while EPS were added in the culture medium, astrocyte viability was influenced (data not shown). In this sense, EPS molecules could be released from the immersed nanofiber and they contributed to a biochemical effect to astrocyte activities.

Astrocytes become reactive when hypoxia, ischemia, or seizures induce brain tissue damage [32]. It has been known that astrocytes *in vivo* took specific shapes depending on the circumstances. Resting astrocytes transform their morphologies into a stellate shape when they are activated [33]. But astrocytes on PCL and EPS-PCL nanofibers appeared as irregular morphologies from Figure 4. Topography, surface chemistry, and biochemical properties of a cell culture substrate are main causes to determine the adhesion and morphological change of a cell. From the experimental result of astrocyte morphology, surface chemistry and biochemical effects did not have a huge impact on astrocyte morphology, but similar topography instead predominates in astrocyte morphology, considering the similar and irregular shapes of astrocytes regardless of EPS incorporation. Moreover, as reported in previous research from our group, morphological difference of astrocytes was not shown on PCL nanofiber or a biochemical material such as *spirulina* added PCL nanofiber [34].

One of the important factors for materials to be used in tissue engineering is whether cells would be able to infiltrate into the materials such as electrospun nanofibers. It was demonstrated that cells on both PCL and EPS-PCL nanofibers infiltrated into the nanofibers with no significant differences in the level of infiltration. Considering astrocytes infiltrated and through EPS-PCL nanofiber pores and maintained alive state, EPS incorporated into PCL nanofiber is told not to give cytotoxicity to 3D growth of astrocytes through the nanofiber mat. In order for a scaffold to be used in neural tissue engineering, it should help cells grow and survive in a 3-dimensional environment, promoting axonal regrowth and guidance and reestablishment of a functional neural network [23]. Since EPS-PCL nanofiber did not show cytotoxic effect to astrocyte infiltration and viability in the 3D environment of the nanofiber, it is told to be adequate as a scaffold in astrocyte tissue engineering.

When the artificially constructed astrocyte tissue is implanted into a CNS injury, it must support neuronal regeneration. For this purpose, astrocytes first should show good

viability, proliferation, and activated markers when seeded on the scaffold. In this sense, EPS-PCL nanofiber is a good candidate to support neuronal protection and regeneration judging from the experimental results previously described. In addition, following that laminarin and fucoidan are both already known to modulate immune responses of microglia [35, 36], PCL nanofiber containing laminarin and fucoidan could be a potential biomaterial for neural tissue engineering that can promote astrocyte survival and activation favorable to axonal regeneration and guidance while suppressing inflammation events by the other cells such as microglia.

## 5. Conclusions

There have been several studies about nanofibers and polysaccharides applied to astrocytes, but cooperative effects of nanofibers containing polysaccharides on astrocytes have rarely been researched, and in particular, molecular studies have not yet been reported. In this research, EPS derived from marine brown seaweed, *Undaria pinnatifida*, were studied over astrocyte activation in view of the topography and biochemical effect of the nanofiber. Cellular morphologies were similar irrespective of the presence of EPS in the nanofiber. This is presumed to be because similar topographies, PCL and EPS-PCL nanofibers, predominate astrocyte morphology. GFAP expression was higher on EPS-PCL nanofiber, which means astrocytes were more activated on EPS-PCL nanofiber. Finally, astrocytes could easily infiltrate into EPS-PCL nanofiber from the seeding surface to the lower part of the fiber mats without toxicity.

Biomaterials must facilitate astrocytes to express sufficient neurotrophic factors to constitute a favorable environment for neural regeneration when applied to the injured CNS and also to have a structure through which astrocytes can easily infiltrate. Considering the experimental results of astrocyte activation and infiltration described above as well as the fact that laminarin and fucoidan modulate inflammatory events of microglia and protect axons in an Alzheimer's environment [35], EPS-PCL nanofiber could be thought to be a suitable material for neural tissue engineering. However, in order to verify the effectiveness of EPS-PCL nanofiber, further studies are needed about expression levels of other neurotrophic factors, cytokines and also biological studies *ex vivo* or *in vivo*.

## Conflict of Interests

The authors declare that there is no conflict of interests regarding the publication of this paper.

## Acknowledgments

This research was supported by the Marine Biotechnology Program funded by the Ministry of Land, Transport and Maritime Affairs, Korea, and by the INHA University research grant.

## References

- [1] N. J. Maragakis and J. D. Rothstein, "Mechanisms of Disease: astrocytes in neurodegenerative disease," *Nature Clinical Practice Neurology*, vol. 2, no. 12, pp. 679–689, 2006.
- [2] M. V. Sofroniew and H. V. Vinters, "Astrocytes: biology and pathology," *Acta Neuropathologica*, vol. 119, no. 1, pp. 7–35, 2010.
- [3] X. Sheng, N. Zhang, S. Song et al., "Morphological transformation and proliferation of rat astrocytes as induced by sulfated polysaccharides from the sea cucumber *Stichopus japonicus*," *Neuroscience Letters*, vol. 503, no. 1, pp. 37–42, 2011.
- [4] J. S. Rudge and J. Silver, "Inhibition of neurite outgrowth on astroglial scars in vitro," *The Journal of Neuroscience*, vol. 10, no. 11, pp. 3594–3603, 1990.
- [5] G. Yiu and Z. He, "Glial inhibition of CNS axon regeneration," *Nature Reviews Neuroscience*, vol. 7, no. 8, pp. 617–627, 2006.
- [6] A. Buffo, C. Rolando, and S. Ceruti, "Astrocytes in the damaged brain: molecular and cellular insights into their reactive response and healing potential," *Biochemical Pharmacology*, vol. 79, no. 2, pp. 77–89, 2010.
- [7] J. P. Schwartz and N. Nishiyama, "Neurotrophic factor gene expression in astrocytes during development and following injury," *Brain Research Bulletin*, vol. 35, no. 5-6, pp. 403–407, 1994.
- [8] J. E. Merrill and E. N. Benveniste, "Cytokines in inflammatory brain lesions: helpful and harmful," *Trends in Neurosciences*, vol. 19, no. 8, pp. 331–338, 1996.
- [9] A. Logan, M. Berry, A. M. Gonzalez, S. A. Frautschy, M. B. Sporn, and A. Baird, "Effects of transforming growth factor  $\beta$ 1 on scar production in the injured central nervous system of the rat," *European Journal of Neuroscience*, vol. 6, no. 3, pp. 355–363, 1994.
- [10] Y. Takamiya, S. Kohsaka, and S. Toya, "Possible association of platelet-derived growth factor (PDGF) with the appearance of reactive astrocytes following brain injury in situ," *Brain Research*, vol. 383, no. 1-2, pp. 305–309, 1986.
- [11] S. Strauss, U. Otten, B. Joggerst, K. Plüss, and B. Volk, "Increased levels of nerve growth factor (NGF) protein and mRNA and reactive gliosis following kainic acid injection into the rat striatum," *Neuroscience Letters*, vol. 168, no. 1-2, pp. 193–196, 1994.
- [12] S. W. Levison, M. H. Ducceschi, G. M. Young, and T. L. Wood, "Acute exposure to CNTF in vivo induces multiple components of reactive gliosis," *Experimental Neurology*, vol. 141, no. 2, pp. 256–268, 1996.
- [13] W. Liedtke, W. Edelmann, P. L. Bieri et al., "GFAP is necessary for the integrity of CNS white matter architecture and long-term maintenance of myelination," *Neuron*, vol. 17, no. 4, pp. 607–615, 1996.
- [14] H. E. Schaeffer and D. L. Krohn, "Liposomes in topical drug delivery," *Investigative Ophthalmology and Visual Science*, vol. 22, no. 2, pp. 220–227, 1982.
- [15] D. Alonso, A. Castro, and A. Martinez, "Marine compounds for the therapeutic treatment of neurological disorders," *Expert Opinion on Therapeutic Patents*, vol. 15, no. 10, pp. 1377–1386, 2005.
- [16] K. Kataoka, Y. Suzuki, M. Kitada et al., "Alginate, a bioresorbable material derived from brown seaweed, enhances elongation of amputated axons of spinal cord in infant rats," *Journal of Biomedical Materials Research*, vol. 54, pp. 373–384, 2001.
- [17] Z. Ma, M. Kotaki, R. Inai, and S. Ramakrishna, "Potential of nanofiber matrix as tissue-engineering scaffolds," *Tissue Engineering*, vol. 11, no. 1-2, pp. 101–109, 2005.
- [18] K. Y. Lee and D. J. Mooney, "Hydrogels for tissue engineering," *Chemical Reviews*, vol. 101, no. 7, pp. 1869–1879, 2001.
- [19] K. Fujiki, H. Matsuyama, and T. Yano, "Effect of hot-water extracts from marine algae on resistance of carp and yellowtail against bacterial infections," *Science Bulletin of the Faculty of Agriculture-Kyushu University*, vol. 47, 1993.
- [20] S. H. Kim, C. Shin, S. K. Min, S.-M. Jung, and H. S. Shin, "In vitro evaluation of the effects of electrospun PCL nanofiber mats containing the microalgae *Spirulina* (*Arthrospira*) extract on primary astrocytes," *Colloids and Surfaces B: Biointerfaces*, vol. 90, no. 1, pp. 113–118, 2012.
- [21] S. Fedoroff and A. Richardson, *Protocols For Neural Cell Culture*, Humana Press, 2001.
- [22] P. McDonnell, S. Figat, and J. V. Odoherly, "The effect of dietary laminarin and fucoidan in the diet of the weanling piglet on performance, selected faecal microbial populations and volatile fatty acid concentrations," *Animal*, vol. 4, no. 4, pp. 579–585, 2010.
- [23] E. East, J. P. Golding, and J. B. Phillips, "A versatile 3D culture model facilitates monitoring of astrocytes undergoing reactive gliosis," *Journal of Tissue Engineering and Regenerative Medicine*, vol. 3, no. 8, pp. 634–646, 2009.
- [24] M. Slezak and F. W. Pfrieger, "New roles for astrocytes: regulation of CNS synaptogenesis," *Trends in Neurosciences*, vol. 26, no. 10, pp. 531–535, 2003.
- [25] M. Pekny, U. Wilhelmsson, Y. R. Bogestål, and M. Pekna, "The role of astrocytes and complement system in neural plasticity," in *International Review of Neurobiology*, M. T. C. Giacinto Bagetta and A. L. Stuart, Eds., pp. 95–111, Academic Press, 2007.
- [26] J. L. Ridet, S. K. Malhotra, A. Privat, and F. H. Gage, "Reactive astrocytes: cellular and molecular cues to biological function," *Trends in Neurosciences*, vol. 20, no. 12, pp. 570–577, 1997.
- [27] L. F. Eng, R. S. Ghirnikar, and Y. L. Lee, "Glial fibrillary acidic protein: GFAP-Thirty-One Years (1969–2000)," *Neurochemical Research*, vol. 25, no. 9-10, pp. 1439–1451, 2000.
- [28] S. Brahmachari, Y. K. Fung, and K. Pahan, "Induction of glial fibrillary acidic protein expression in astrocytes by nitric oxide," *The Journal of Neuroscience*, vol. 26, no. 18, pp. 4930–4939, 2006.
- [29] M.-Y. Lee, C.-J. Kim, S.-L. Shin, S.-H. Moon, and M.-H. Chun, "Increased ciliary neurotrophic factor expression in reactive astrocytes following spinal cord injury in the rat," *Neuroscience Letters*, vol. 255, no. 2, pp. 79–82, 1998.
- [30] N. M. Oyesiku, J. N. Wilcox, and D. J. Wigston, "Changes in expression of ciliary neurotrophic factor (CNTF) and CNTF-receptor  $\alpha$  after spinal cord injury," *Journal of Neurobiology*, vol. 32, pp. 251–261, 1997.
- [31] M. A. Kahn, J. A. Ellison, G. J. Speight, and J. De Vellis, "CNTF regulation of astrogliosis and the activation of microglia in the developing rat central nervous system," *Brain Research*, vol. 685, no. 1-2, pp. 55–67, 1995.
- [32] K. Abe and M. Misawa, "Astrocyte stellation induced by Rho kinase inhibitors in culture," *Developmental Brain Research*, vol. 143, no. 1, pp. 99–104, 2003.
- [33] T. Endo, "Glycans and glycan-binding proteins in brain: galectin-1-induced expression of neurotrophic factors in astrocytes," *Current Drug Targets*, vol. 6, no. 4, pp. 427–436, 2005.
- [34] S. K. Min, C. R. Kim, S. M. Jung, and H. S. Shin, "Astrocyte behavior and GFAP expression on *Spirulina* extract-incorporated PCL nanofiber," *Journal of Biomedical Materials Research Part A*, vol. 101, pp. 3467–3473, 2013.

- [35] V. B. Shah, D. L. Williams, and L. Keshvara, " $\beta$ -Glucan attenuates TLR2- and TLR4-mediated cytokine production by microglia," *Neuroscience Letters*, vol. 458, no. 3, pp. 111–115, 2009.
- [36] V. B. Shah, Y. Huang, R. Keshwara, T. Ozment-Skelton, D. L. Williams, and L. Keshvara, " $\beta$ -glucan activates microglia without inducing cytokine production in dectin-1-dependent manner," *Journal of Immunology*, vol. 180, no. 5, pp. 2777–2785, 2008.

## Research Article

# Coaxial Electrospinning with Mixed Solvents: From Flat to Round Eudragit L100 Nanofibers for Better Colon-Targeted Sustained Drug Release Profiles

Deng-Guang Yu,<sup>1</sup> Ying Xu,<sup>1,2</sup> Zan Li,<sup>1</sup> Lin-Ping Du,<sup>1</sup> Ben-Guo Zhao,<sup>1</sup> and Xia Wang<sup>1</sup>

<sup>1</sup> School of Materials Science & Engineering, University of Shanghai for Science and Technology, 516 Jungong Road, Yangpu District, Shanghai 200093, China

<sup>2</sup> School of Environment and Architecture, University of Shanghai for Science and Technology, Shanghai 200093, China

Correspondence should be addressed to Deng-Guang Yu; ydg017@usst.edu.cn and Xia Wang; wangxia@usst.edu.cn

Received 6 December 2013; Revised 26 January 2014; Accepted 4 March 2014; Published 27 March 2014

Academic Editor: Aihua He

Copyright © 2014 Deng-Guang Yu et al. This is an open access article distributed under the Creative Commons Attribution License, which permits unrestricted use, distribution, and reproduction in any medium, provided the original work is properly cited.

A modified coaxial electrospinning process was developed for creating drug-loaded composite nanofibers. Using a mixed solvent of ethanol and N,N-dimethylacetamide as a sheath fluid, the electrospinning of a codissolving solution of diclofenac sodium (DS) and Eudragit L100 (EL100) could run smoothly and continuously without any clogging. A series of analyses were undertaken to characterize the resultant nanofibers from both the modified coaxial process and a one-fluid electrospinning in terms of their morphology, physical form of the components, and their functional performance. Compared with those from the one-fluid electrospinning, the DS-loaded EL100 fibers from the modified coaxial process were rounder and smoother and possessed higher quality in terms of diameter and distribution with the DS existing in the EL100 matrix in an amorphous state; they also provided a better colon-targeted sustained drug release profile with a longer release time period. The modified coaxial process not only can smooth the electrospinning process to prevent clogging of spinneret, but also is a useful tool to tailor the shape of electrospun nanofibers and thus endow them improved functions.

## 1. Introduction

The physical properties, such as shape, size, mechanical properties, surface texture, and compartmentalization, profoundly impact the function of a nanobiomaterial and thus raise important questions for the design of its next generation [1]. Electrospinning is a facile method for generating fibers at micro-/nanoscale [2–7]. Often, electrospun nanofibers of some typical pharmaceutical polymers (such as cellulose acetate, Eudragit series, and zein) exhibit a flat morphology, which is undesired for providing sustained drug release profiles because the flat morphology aggravates the initial burst release effect and results in a shorter time sustained release [8–10]. Although a great effort has been paid to generate novel fiber structure (such as core-shell and side-by-side) and obtain nanofibers with thinner diameters [11, 12], few studies have been reported to manipulate the nanofibers' shape and their functional performance.

Coaxial electrospinning is a power tool for generating core-sheath nanofibers through manipulating two fluids using a concentric spinneret [13, 14]. Traditionally, the shell solution is critical and the selected sheath fluid should be electrospinnable by itself to facilitate core-shell structure formation, whereas the core fluid can either be electrospinnable or not [15]. Yu et al. have broken this concept by developing a modified coaxial electrospinning that is characterized by the usage of liquids lacking electrospinnability as shell fluids [16–18]. Because there are many types of “unspinnable” liquids (including solvents, solutions of little chemical molecules, dilute polymer solutions, suspensions, and emulsions) that can be managed to act as sheath fluids for conducting the modified coaxial process, thus this advanced technology has greatly expanded the capability of the traditional coaxial one in generating a series of new possibilities. Some examples include manipulating the size of self-assembled nanoparticles [16]; preparing ultrafine fibers from concentrated polymer

solutions thought to be unspinnable previously [17]; improving the quality of nanofibers systematically [18]; and coating drug-loaded nanofibers with a blank release-retarded polymer layer for achieving zero-order drug release profiles [8, 9].

Here, different from above-mentioned applications, the modified coaxial electrospinning was exploited as a useful tool for manipulating the shape of resultant nanofibers and improving their functional performance of colon-targeted sustained release. Eudragit L-100 (EL100), a well-known methacrylate-based copolymer developed by the Röhm Company in Germany and a common excipient used in the pharmaceutical field, was exploited as the filament-forming matrix here. It has been widely used for the formulation of different oral dosage forms (e.g., tablet coating, tablet matrix, microspheres, and nanoparticles) for colon-targeted drug delivery [19]. Diclofenac sodium (DS), a nonsteroidal anti-inflammatory drug (NSAID), was used as a model drug. It is taken or applied to reduce inflammation and as an analgesic reducing pain in certain conditions, supplied as or contained in medications under a variety of trade names [20].

## 2. Experimental

**2.1. Materials.** EL100 was supplied by Rohm GmbH & Co. KG (Darmstadt, Germany). DS was purchased from Hubei Biocause Pharmaceutical Co., Ltd. (Hubei, China). Methylene blue, N,N-dimethylacetamide (DMAc), and anhydrous ethanol were provided by Sinopharm Chemical Reagent Co., Ltd. (Shanghai, China). Water was double distilled just before use. All other chemicals and reagents were of analytical grade.

**2.2. Preparation.** A codissolving solution of EL100 and DS was prepared and used as the core fluid, which consisted of 15% (w/v) EL100 and 2% (w/v) DS in a mixture of ethanol : DMAc (with a volume ratio of 9 : 1), meaning 11.8% of DS in the solid products. The sheath mixed solvents contained DMAc and ethanol at a volume ratio of 30 : 70. The prepared nanofibers are referred to as F2. To observe the electrospinning process, 5 ppm methylene blue was added to the core solution.

A homemade concentric spinneret was used to conduct the coaxial electrospinning processes. Two syringe pumps (KDS100 and KDS200, Cole-Parmer, IL, USA) and a high-voltage power supply (ZGF 60 Kv/2 mA<sup>-1</sup>, Shanghai Sute Corp., Shanghai, China) were used for electrospinning, which was performed under ambient conditions (25 ± 2°C; 57% ± 6% relative humidity). The coaxial electrospinning processes were recorded using a digital video recorder (PowerShot A490, Canon, Tokyo, Japan). After optimization, the applied voltage was fixed at 15 kV and the fibers were collected on an aluminum foil 20 cm from the spinneret.

Using the same apparatus of coaxial electrospinning and under the same conditions, a one-fluid electrospinning of the core solutions was implemented through adjusting the flow rate of the sheath fluid to 0 mL/h. The prepared nanofibers are referred to as F1, which was investigated as a control.

**2.3. Characterization.** The morphology of the nanofibers was examined using an S-4800 field-emission scanning electron

microscope (FESEM, Hitachi, Tokyo, Japan). Prior to examination, the samples were platinum sputter-coated under nitrogen atmosphere to render them electrically conductive. The average fiber diameter was determined by measuring their sizes in FESEM images at more than 100 different places using NIH Image J software (National Institutes of Health, MD, USA). Cross-sections of the fiber mats were prepared by placing them in liquid nitrogen and manually breaking them before platinum coating. The topographies of raw material particles and drug-loaded nanofibers were observed under cross-polarized light using an XP-700 polarized optical microscope (Shanghai Changfang Optical Instrument Co. Ltd., Shanghai, China).

XRD patterns were obtained over the 2θ range of 5° to 60° on a D/Max-BR diffractometer (Rigaku, Tokyo, Japan) with Cu Kα radiation at 40 mV and 30 mA. Attenuated total reflectance Fourier transform infrared (ATR-FTIR) analysis was carried out on a Nicolet-Nexus 670 FTIR spectrometer (Nicolet Instrument Corporation, Madison, USA) over the range 500–4000 cm<sup>-1</sup> and at a resolution of 2 cm<sup>-1</sup>.

The *in vitro* dissolution of drug-loaded nanofibers was performed according to the Chinese Pharmacopoeia (2005 Edn.), a paddle method using a RCZ-8A dissolution apparatus (Tianjin University Radio Factory, China). All experiments were conducted at 37°C and 50 rpm in 900 mL pH 1.5 HCl solutions for 2 h, followed by 5 h in 900 mL of phosphate buffer (PBS, pH 6.8, 0.1 mol/L). At predetermined time intervals, aliquots of 5.0 mL were withdrawn for sampling and replaced by an equal volume of the same solutions to maintain a constant volume. After filtration through a membrane (0.45 μm), the sample solutions were analyzed at a wavelength of 276 nm by a UV spectrophotometer (UV-2102PC, Unico Instrument Co. Ltd., Shanghai, China). DS dissolved at specified time periods was plotted as percentage released versus time. All measurements were performed six times, and results were reported as the mean value ± S.D.

## 3. Results and Discussion

**3.1. The Modified Coaxial Electrospinning.** A schematic diagram of the modified coaxial electrospinning process is shown in Figure 1(a). The homemade spinneret used in this work has outer and inner diameters of 1.2 and 0.3 mm, respectively, (Figure 1(b)). A typical clogging phenomenon that has taken place in the traditional one-fluid electrospinning is shown in Figure 2(a). The easy evaporation of ethanol made a semisolid substance hang on the spinneret to deteriorate the process. The semisolid “skin” had to be removed frequently and manually to keep the electrospinning process going.

Digital images about the modified coaxial electrospinning are shown in Figures 2(b)–2(d). After some preexperiments, a sheath-to-core flow rate ratio of 0.3 was selected for the preparation of drug-loaded nanofibers F2. Under the selected conditions, a fluid jet trajectory similar to that observed in a single-fluid electrospinning was created. This comprised a straight thinning jet emitted from a compound Taylor cone, followed by a bending and whipping instability region with loops of increasing size (Figure 2(c)). The compound Taylor cone is shown in Figure 2(d), which has clearly

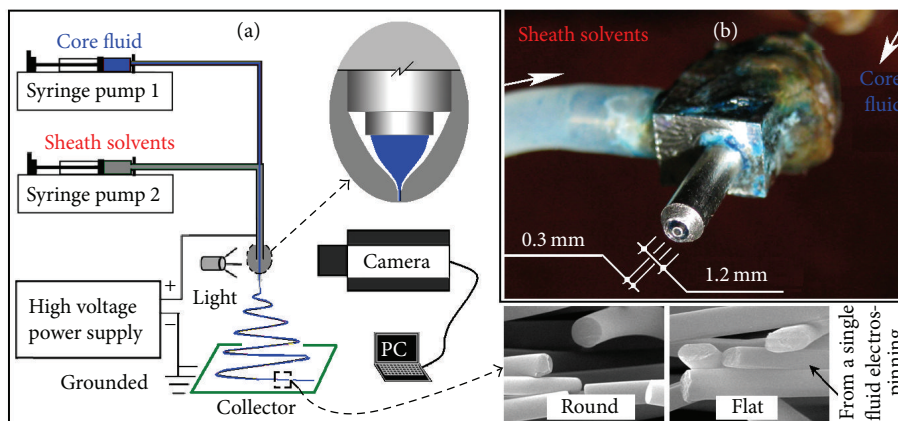


FIGURE 1: The schematic diagram of the modified coaxial electrospinning (a) and the homemade concentric spinneret (b).

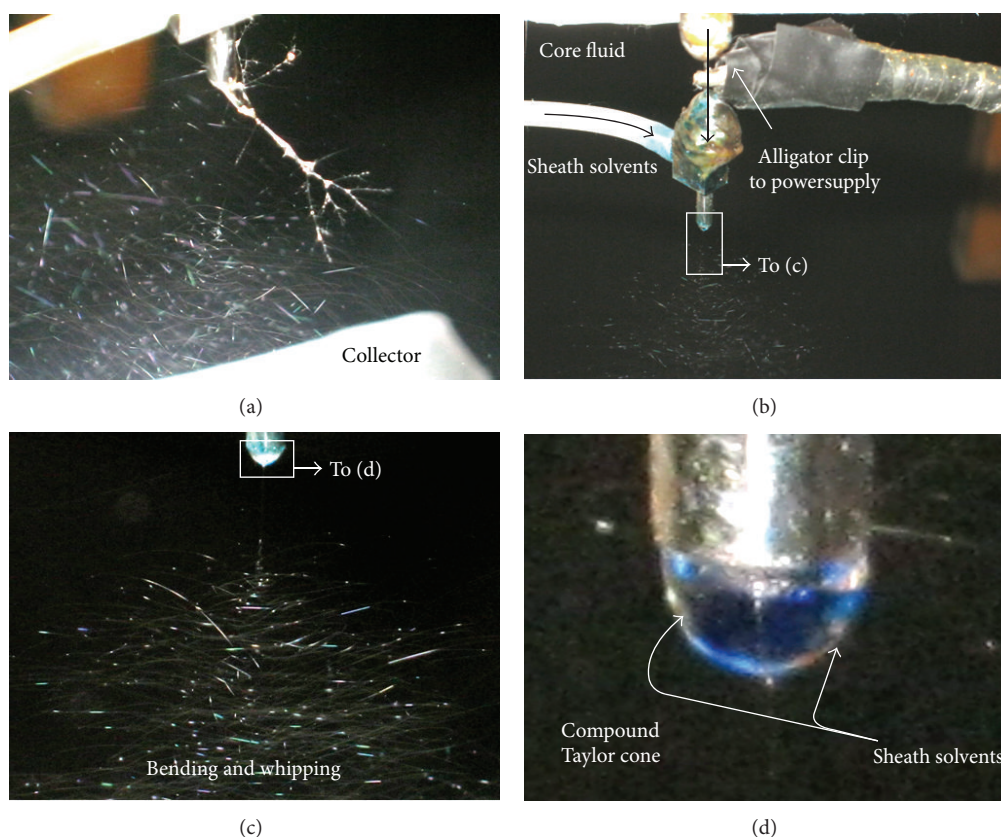


FIGURE 2: Observations of the traditional single fluid electrospinning (a) and the modified coaxial process ((b) to (d)).

internal and external structure, as indicated by the blue color of methylene blue. The modified coaxial process could be undertaken continuously without any user intervention.

**3.2. Morphology.** The morphologies of surface (Figures 3(a) and 3(b)) and cross-section (Figures 3(c) and 3(d)) of the nanofibers F1 obtained from the one-fluid electrospinning are given in Figure 3. Clearly, the fibers showed a flat morphology and had an average width of  $1280 \pm 330$  nm. In sharp contrast, the nanofibers F2 from the modified coaxial processes had

rounder and smoother morphologies with a smaller diameter and narrower size distribution of  $650 \pm 130$  nm, as exhibited by both the surface (Figures 4(a) and 4(b)) and cross-section images (Figures 4(c) and 4(d)).

The traditional one-fluid electrospinning shares characteristics of both electrospinning and conventional solution dry spinning. During the process, ethanol evaporated very quickly. This would make the electrospinning process very sensitive to small changes in the environment and thus resulted in nanofibers with a wide range of sizes and also

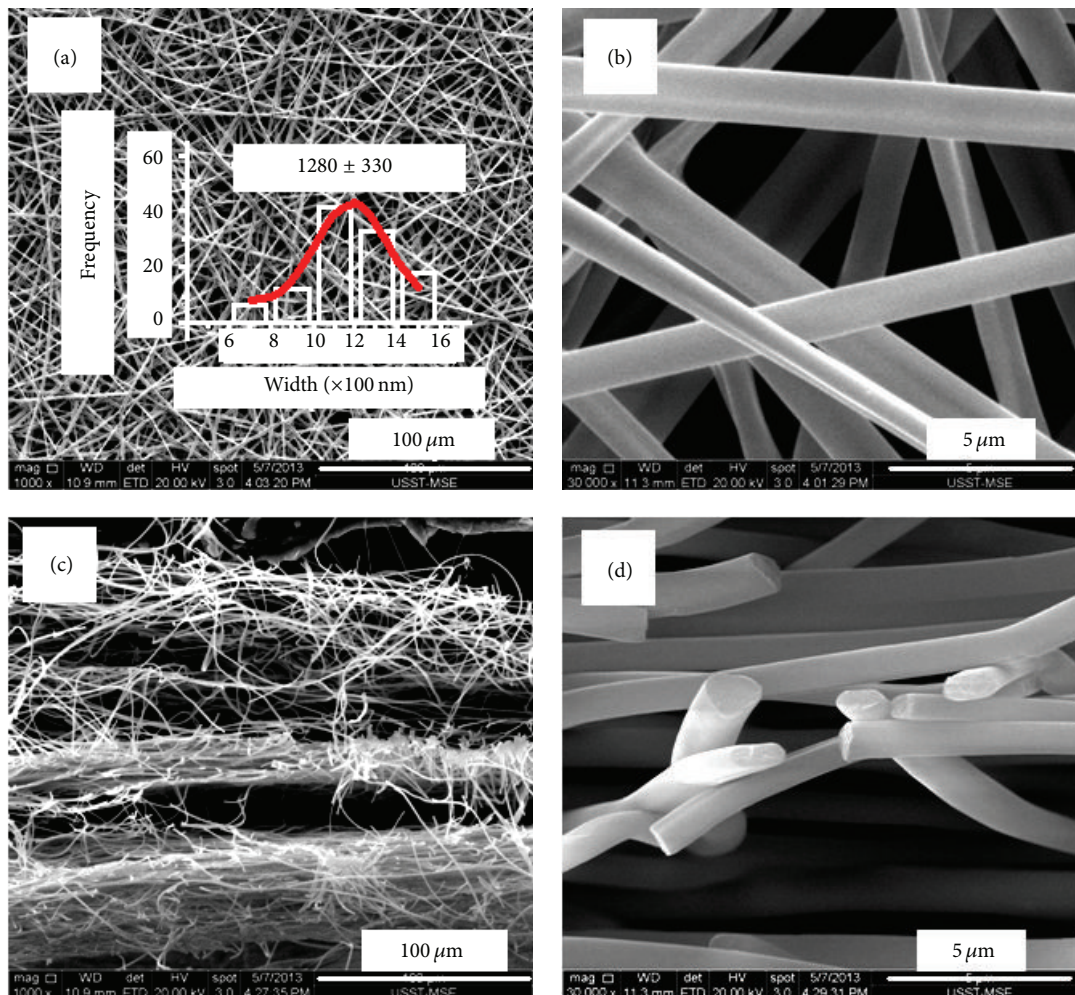


FIGURE 3: Surface and cross-section morphologies of FI nanofibers from the traditional electrospinning.

generate a solid “skin” on the surfaces of collected fibers with some solvent still trapped inside the fiber bodies. After spinning, the solvent contained in the fibers diffused out into the atmosphere, and the resulting barometric pressure distorted the cylindrical fibers to the flat morphology, whereas the modified coaxial process shares characteristics of both electrospinning and conventional solution wet spinning to some extent. It could provide a stable and robust core-sheath interface for the core EL100-DS solution when it was drawn in the electrical field. This not only enables the core solutions to have a longer time period of electrical drawing force in the fluid phase [16, 18] but also protects them from the disturbance of environmental changes. During their evaporation, the sheath solvents render a stable Knudsen layer permitting gradual and smooth mass transfer of the solvents from the core fluid jets to the atmosphere and precluding the formation of a surface semisolid “skin” [21]. Thus, the modified process can produce DS-loaded EL100 nanofibers with rounder morphology, smaller diameters, and more uniform structures.

**3.3. Physical Status and Compatibility of Components.** The presence of numerous distinct peaks in the XRD patterns of the fibers suggested that DS was present as crystalline material with characteristic diffraction peaks, as also demonstrated by the colorful images of their crude particles under polarized light (Figure 5(a)). EL100 exhibits only a hump characteristic of amorphous forms. There are no peaks of crystalline DS detectable in the XRD patterns of the nanofibers F1 and F2, indicating that all the DS encapsulated in the nanofibers no longer presented as a crystalline material regardless of the different electrospinning processes. Unlike the observations on crystalline DS particles, EL100 and the nanofibers showed no bright colors, suggesting that EL100 and the nanofibers were amorphous (Figure 5(a)). These results concurred that DS molecules were highly distributed in the EL100 matrix and were present in a composite manner where the original structure of the pure, crystalline material was lost.

Compared to the spectra of pure DS and EL100, there are significant changes in the spectra of the nanofibers F1

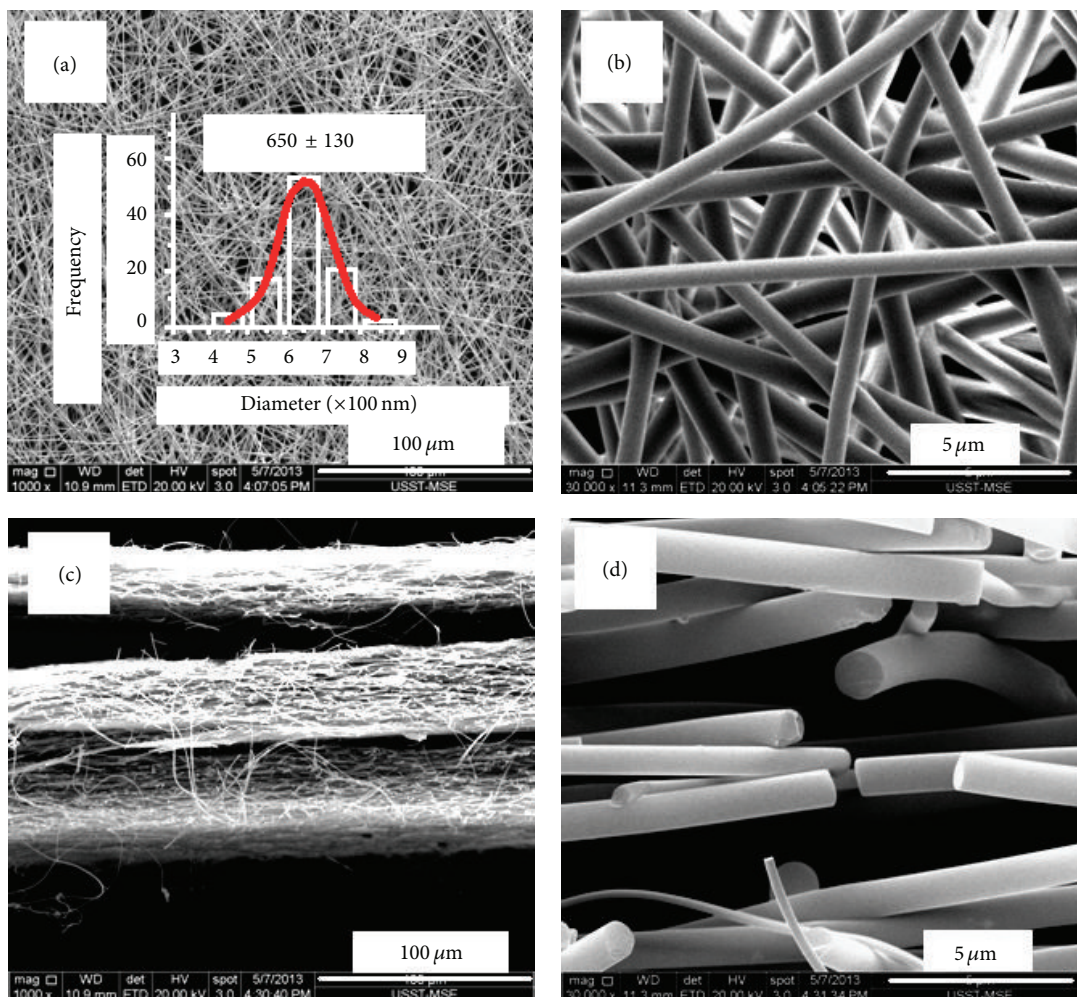


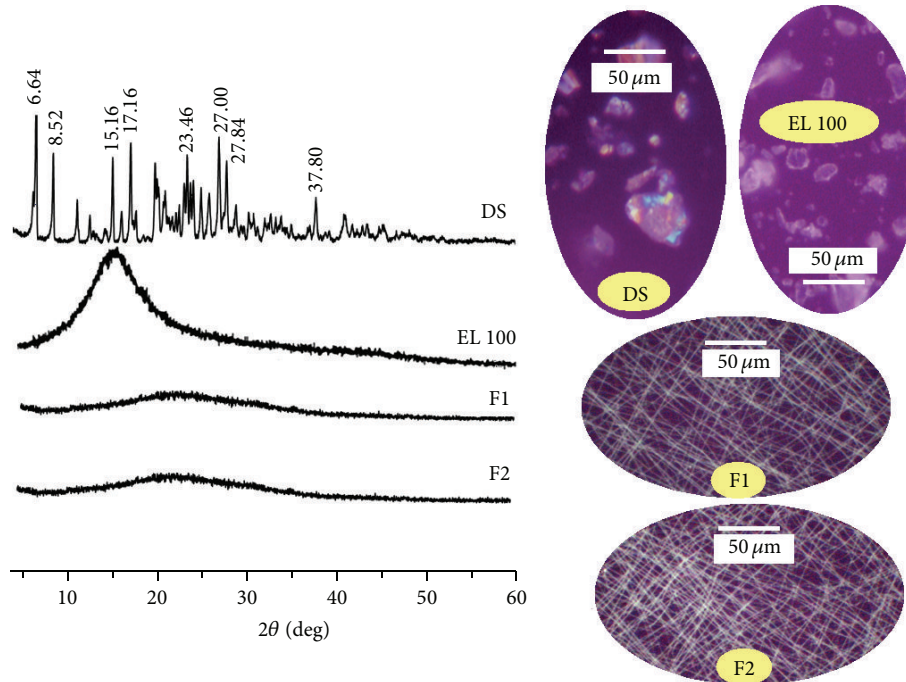
FIGURE 4: Surface and cross-section morphologies of F2 nanofibers from the coaxial process.

and F2 (Figure 5(b)), including (1) the characteristic peaks of the carbonyl groups of EL100 (C=O stretch vibration) at  $1735\text{ cm}^{-1}$  that have shifted to  $1732\text{ cm}^{-1}$ ; (2) the disappearance of the characteristic peaks of the phenyl group of DS (C=C stretch vibration) at  $1577\text{ cm}^{-1}$  and the disappearance of the substituted phenyl group stretch at  $747\text{ cm}^{-1}$ . All these changes can be attributed to hydrogen bonding between DS and EL 100, including (1) between C=O of DS and O-H of EL 100 and (2) between the C=O of EL 100 and the N-H of DS. The latter hydrogen bonding disrupts the  $p\text{-}\pi$  conjugation in the DS molecules generated between the aromatic ring and secondary amino group which has an isolated electron pair at the N atom and thus accounts for the disappearance of characteristic peaks of DS in the composite nanofibers. The interactions between the DS and EL100 may promote them to combine at a molecular level in the nanofibers, reflecting the good compatibility between them, and would be favorable to the stability of the medicated nanofibers to prevent solid phase separation.

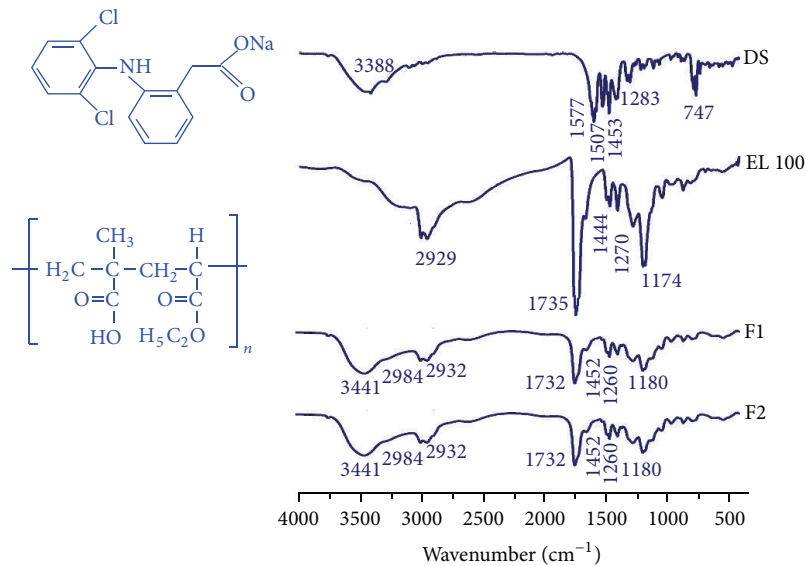
**3.4. In Vitro Dissolution Tests.** To evaluate DS release profiles from the medicated nanofibers, *in vitro* dissolution tests were carried out under acidic conditions in pH 1.5 HCl for

2 h and subsequently at pH 6.8 in PBS for 5 h to mimic gastrointestinal conditions. The drug release profiles of the nanofibers are shown in Figure 6(a). In pH 1.5 HCl solutions the *in vitro* drug release rates were very slow, with no more than 5% of the loaded drug released from both the samples in 2 h (Figure 6(a)). Both DS and EL 100 are insoluble in an acid environment; the very small release of drugs from the fibers should reflect the drug content presented on the medicated nanofiber surface.

At a pH of 6.8, both the nanofibers F1 and F2 exhibited a sustained drug release profile. However, nanofibers F2 from the modified coaxial process provided a better sustained release profile with a longer time period. Compared to nanofibers F2, nanofibers F1 had (1) a larger burst release in the 3rd hr (i.e., 55.7% to 41.2%) which is disadvantageous to sustained release; (2) a shorter time when 50% of the contained drug was freed (i.e., 2.8 hr to 3.4 hr); and (3) a longer time period of the undesired “tailing off” release (i.e., only released 1.9% after the 5th hr). Both nanofibers F1 and F2 were nanocomposites with the drug DS homogeneously distributed on the polymer matrix EL100. The sustained drug release profiles should be attributed to their difference in physical shapes, which determined the diffusion or erosion



(a)



(b)

FIGURE 5: XRD patterns (a) and ATR-FTIR spectra (b) of the components and their composite nanofibers.

distance for water diffusing into the nanofibers and the drug diffusing into the dissolution medium. Shown in Figure 6(b) is a schematic diagram of the drug DS to explain how the drug goes into the dissolution medium from the nanofibers. Although F1 had a larger width than F2, the drug went into the medium always by the shortest way. The thickness of the flat nanofibers F1 was the determined factor to control the drug release. Because of a flat morphology, the longest diffusion distance ( $R_1$ , 280 nm by estimate from their FESEM images) of the nanofibers F1 was smaller than the diameters of F2

( $R_2 = D_2/2$ ) and thus exhibited a poorer colon-targeted sustained drug release profile.

To further investigate the drug controlled release mechanism, the drug release profiles from the nanofibers F1 and F2 were analyzed using the Peppas equation [22]:

$$Q = kt^n, \quad (1)$$

where  $Q$  is the drug release percentage,  $t$  is the release time,  $k$  is a constant reflecting the structural and geometric characteristics of the fibers, and  $n$  is an exponent that indicates

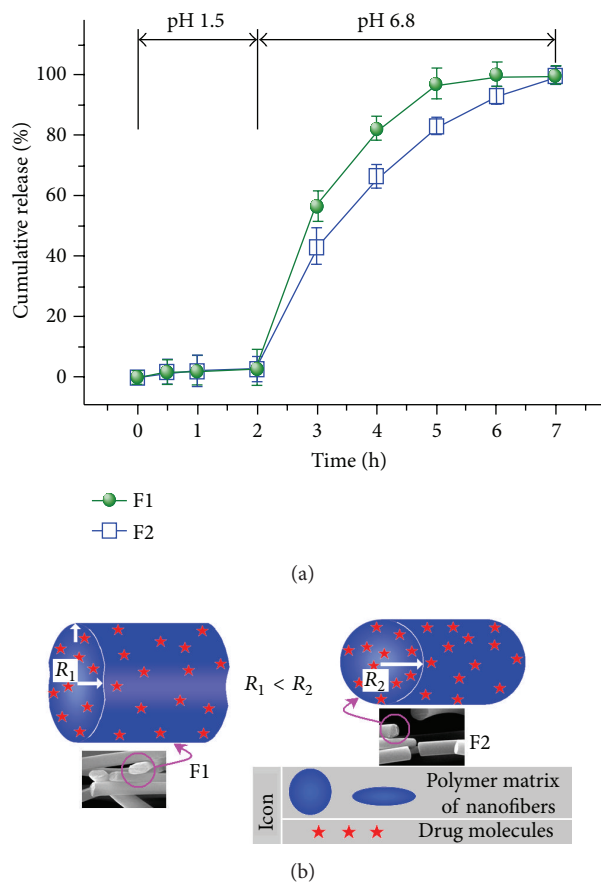


FIGURE 6: *In vitro* drug dissolution profiles ( $n = 6$ ) (a) and a schematic diagram of the drug release distance (b).

the drug release mechanism. The results for nanofibers F1 and F2 yield  $Q_1 = 15.78t_1^{0.98}$  ( $R_1^2 = 0.9771$ ) and  $Q_2 = 19.13t_2^{0.84}$  ( $R_2^2 = 0.9845$ ), respectively. Exponent values of 0.98 and 0.84 (a value of  $n$  between 0.5 and 1) indicate that the drug releases from F1 and F2 were similarly controlled *via* a non-Fickian diffusion mechanism; that is, the drug release from the nanofibers was controlled by a combination of diffusion and erosion mechanisms. At a pH of 6.8, both EL100 and DS are soluble. However, their dissolution behaviors are different. The dissolution polymer always takes relatively longer time because they usually involve the processes of absorption of water, swelling, and disentanglement before they are free in the dissolution media. However, DS dissolves more quickly than EL 100 as a little chemical molecule. It can dissolve with EL100 synchronously *via* erosion mechanism. It can also enter into the dissolution media through channels that would develop during the dissolution process along the nanofibers from the surface to the inside of the fiber, that is, *via* a diffusion mechanism. There is no difference of drug controlled release mechanisms, which means that it is the nanofibers' shapes that produced the different colon-targeted sustained release profiles between nanofibers F1 and F2.

## 4. Conclusion

A modified coaxial electrospinning process in which only an unspinnable mixed solvent system was used as a sheath fluid has been successfully developed to produce medicated EL100 nanofibers. FESEM observations revealed that the modified coaxial electrospinning process is an effective method for manipulating the nanofibers' shape and structural uniformity. The use of the surrounding solvents facilitated the drawing of the core DS/EL100 codissolving fluid jet, producing round composite fibers with a finer average size of  $650 \pm 130$  nm under a sheath-to-core flow rate ratio of 0.1, whereas the fibers from the one-fluid electrospinning process had a flat morphology with an average width of  $1280 \pm 330$  nm. However, both fiber types were similar in that the drug DS dispersed in an amorphous state in the filament-forming matrix EL100 and could be freed in a sustained manner through a combination of erosion and diffusion mechanisms in a neutral condition. Nonetheless, the fibers from the modified process exhibited a better colon-targeted sustained release performance than those from the single fluid electrospinning process in terms of release time period. The modified coaxial electrospinning process reported herein clearly extends the capability of electrospinning to fabricate functional polymer fibers with better structure and morphology and enhanced functional performance.

## Conflict of Interests

The authors declare that there is no conflict of interests regarding the publication of this paper.

## Acknowledgments

This work was supported by the National Science Foundation of China (nos. 51373101 and 51373100), the Natural Science Foundation of Shanghai (no. 13ZR1428900), the Key Project of the Shanghai Municipal Education Commission (no. 13ZZ113), and the Innovation Project of the College Student Fund Committee (no. SH2013167).

## References

- [1] S. Mitragotri and J. Lahann, "Physical approaches to biomaterial design," *Nature Materials*, vol. 8, no. 1, pp. 15–23, 2009.
- [2] T. Lin and X. Wang, *Encyclopedia of Nanoscience and Nanotechnology*, Edited by H. S. Nalwa, American Scientific, Los Angeles, Calif, USA, 2nd edition, 2011.
- [3] N. Vitchuli, Q. Shi, J. Nowak et al., "Atmospheric plasma application to improve adhesion of electrospun nanofibers onto protective fabric," *Journal of Adhesion Science and Technology*, vol. 27, no. 8, pp. 924–938, 2013.
- [4] J. Fang, H. Niu, H. Wang, X. Wang, and T. Lin, "Enhanced mechanical energy harvesting using needleless electrospun poly(vinylidene fluoride) nanofibre web," *Energy & Environmental Science*, vol. 6, no. 7, pp. 2196–2202, 2013.
- [5] J. Fang, X. Wang, and T. Lin, "Nanofibrous *p-n* junction and its rectifying characteristics," *Journal of Nanomaterials*, vol. 2013, Article ID 758395, 7 pages, 2013.
- [6] Y. Li, B. Guo, L. Ji et al., "Structure control and performance improvement of carbon nanofibers containing a dispersion of

- silicon nanoparticles for energy storage,” *Carbon*, vol. 51, pp. 185–194, 2013.
- [7] X.-Y. Li, X. Wang, D.-G. Yu et al., “Electrospun borneol-PVP nanocomposites,” *Journal of Nanomaterials*, vol. 2012, Article ID 731382, 8 pages, 2012.
- [8] D.-G. Yu, W. Chian, X. Wang, X.-Y. Li, Y. Li, and Y.-Z. Liao, “Linear drug release membrane prepared by a modified coaxial electrospinning process,” *Journal of Membrane Sciences*, vol. 428, no. 2, pp. 150–156, 2013.
- [9] D.-G. Yu, X.-Y. Li, X. Wang, W. Chian, Y.-Z. Liao, and Y. Li, “Zero-order drug release cellulose acetate nanofibers prepared using coaxial electrospinning,” *Cellulose*, vol. 20, no. 1, pp. 379–389, 2013.
- [10] D. G. Yu, X. Wang, X. Y. Li, W. Chian, Y. Li, and Y. Z. Liao, “Electrospun biphasic drug release polyvinylpyrrolidone/ethyl cellulose core/shell nanofibers,” *Acta Biomaterialia*, vol. 9, no. 3, pp. 5665–5672, 2013.
- [11] D.-G. Yu, G. R. Williams, X. Wang, X. K. Liu, H. L. Li, and S. W. A. Bligh, “Coaxial electrospinning using a concentric Teflon spinneret to prepare biphasic-release nanofibers of helicid,” *RSC Advances*, vol. 3, no. 39, pp. 17775–17783, 2013.
- [12] K.-H. Roh, D. C. Martin, and J. Lahann, “Biphasic Janus particles with nanoscale anisotropy,” *Nature Materials*, vol. 4, no. 10, pp. 759–763, 2005.
- [13] S. Agarwal, A. Greiner, and J. H. Wendorff, “Functional materials by electrospinning of polymers,” *Progress in Polymer Science*, vol. 38, no. 6, pp. 963–991, 2013.
- [14] C. J. Luo, S. D. Stoyanov, E. Stride, E. Pelan, and M. Ediris-inghe, “Electrospinning versus fibre production methods: from specifics to technological convergence,” *Chemistry Society Reviews*, vol. 41, no. 13, pp. 4708–4735, 2012.
- [15] A. K. Moghe and B. S. Gupta, “Co-axial electrospinning for nanofiber structures: preparation and applications,” *Polymer Reviews*, vol. 48, no. 2, pp. 353–377, 2008.
- [16] D.-G. Yu, L.-M. Zhu, C. Branford-White, S. W. A. Bligh, and K. N. White, “Coaxial electrospinning with organic solvent for controlling the size of self-assembled nanoparticles,” *Chemical Communications*, vol. 47, no. 4, pp. 1216–1218, 2011.
- [17] D.-G. Yu, C. J. Branford-White, N. P. Chatterton et al., “Electrospinning of concentrated polymer solutions,” *Macromolecules*, vol. 43, no. 24, pp. 10743–10746, 2010.
- [18] D.-G. Yu, C. Branford-White, S. W. A. Bligh, K. White, N. P. Chatterton, and L.-M. Zhu, “Improving polymer nanofiber quality using a modified co-axial electrospinning process,” *Macromolecular Rapid Communications*, vol. 32, no. 9-10, pp. 744–750, 2011.
- [19] D.-G. Yu, G. R. Williams, X. Wang, X.-K. Liu, H.-L. Li, and S. W. A. Bligh, “Dual drug release nanocomposites prepared using a combination of electrospraying and electrospinning,” *RSC Advances*, vol. 3, no. 14, pp. 4652–4658, 2013.
- [20] X.-X. Shen, D.-G. Yu, L.-M. Zhu, C. Branford-White, K. White, and N. P. Chatterton, “Electrospun diclofenac sodium loaded Eudragit L 100–55 nanofibers for colon-targeted drug delivery,” *International Journal of Pharmaceutics*, vol. 408, no. 1-2, pp. 200–207, 2011.
- [21] D.-G. Yu, J.-H. Yu, L. Chen, G. R. Williams, and X. Wang, “Modified coaxial electrospinning for the preparation of high-quality ketoprofen-loaded cellulose acetate nanofibers,” *Carbohydrate Polymers*, vol. 90, no. 2, pp. 1016–1023, 2012.
- [22] N. A. Peppas, “Analysis of Fickian and non-Fickian drug release from polymers,” *Pharmaceutica Acta Helveticae*, vol. 60, no. 4, pp. 110–111, 1985.